



UNIVERSITÀ DEGLI STUDI DI
CASSINO E DEL LAZIO MERIDIONALE

Corso di Dottorato in
Metodi, modelli e tecnologie per l'ingegneria
curriculum Ingegneria Civile

Ciclo XXXV

Urban scale assessment of buildings' liquefaction
vulnerability

SSD: ICAR - 07

Coordinatore del Corso
Chiar.mo Prof. Fabrizio Marignetti

Dottoranda
Anna Baris

Supervisore
Chiar.mo Prof. Giuseppe Modoni

ACKNOWLEDGEMENTS

This work has been carried out in the framework of the project: “Accordo di collaborazione tra Regione Emilia-Romagna, Amministrazione Comunale di Terre del Reno, Consiglio Nazionale delle Ricerche – Istituto di Geologia Ambientale e Geoingegneria, Università degli Studi di Cassino e del Lazio Meridionale Dipartimento di Ingegneria Civile e Meccanica, finalizzato a definire una strategia multilivello per valutare il rischio da liquefazione in presenza di argini e situazioni geologiche e morfologiche complesse”. The author wishes to acknowledge Emilia-Romagna Region, CNR-IGAG and Municipality of Terre del Reno for their support to the project.

ABSTRACT

The extensive injury caused to buildings by liquefaction during past earthquakes, with the uneven spatial distribution of damage, raises the need for rapid predictive tools, applicable at a large scale, that comprehensively account for the properties of earthquake, subsoil and structure. A method is herein proposed to quantify the angular distortion of framed low-rise buildings based on a simple characterization of the above factors. The analysis moves from past literature criteria introduced to quantify the vulnerability of buildings under static conditions and extends their applicability to liquefaction assessment integrating parametric two-dimensional numerical analyses with recent literature predictive formulas and machine learning inference. The numerical calculation, performed for variable stratigraphic and mechanical characteristics of the subsoil, ground motion and equivalent flexural stiffness of the foundation, quantifies the role of each factor on the absolute settlement and angular distortion. Then the dependency on the different factors of the angular distortion is inferred with an artificial neural network (ANN), grouping parameters to limit the number of input variables and express results with charts that make prediction more accessible.

TABLE OF CONTENTS

ABSTRACT.....	I
List of Figures.....	V
List of Tables.....	X
INTRODUCTION.....	1
Chapter 1. Seismic Risk assessment: Overall Approach and Framework of Methodology	5
1.1 Motivation.....	5
1.2 History and overall approach of Risk Assessment.....	7
1.3 Principles for Seismic Risk Assessment.....	12
1.3.1 Seismic hazard analysis.....	16
1.3.2 Seismic vulnerability analysis.....	18
1.3.3 Exposure.....	18
1.4 Scale and Resolution of Risk Studies.....	20
Chapter 2. Seismic Liquefaction: phenomenon and hazard assessment.....	23
2.1 Susceptibility.....	26
2.1.1 Geological factors controlling liquefaction susceptibility.....	27
2.1.2 Geotechnical factors controlling liquefaction susceptibility.....	29
2.2 Triggering.....	33
2.3 Liquefaction-induced surficial manifestations.....	37
2.3.1 LPI: Liquefaction Potential Index.....	41
2.3.2 Settlement (W_v) Indicator.....	41
2.3.3 Volumetric Densification (Zhang <i>et al.</i> , 2002).....	42
2.3.4 LSN: Liquefaction Severity Number.....	43
2.3.5 LPIISH: LPI Ishihara inspired.....	44
2.3.6 IAM: Induced dAmage parameter.....	45
2.3.7 GLSN: generalized severity number to predict liquefaction damage with lateral spreading.....	46
Chapter 3. Vulnerability assessment.....	49
3.1 Intensity scales.....	51
3.2 Damage States.....	59
3.3 Seismic vulnerability assessment.....	59
3.3.1 Empirical methods.....	59
3.3.2 Analytical methods.....	64

3.3.3	Hybrid methods	66
3.4	Liquefaction vulnerability assessment	67
3.4.1	Karamitros <i>et al.</i> (2013)	69
3.4.2	Bray & Macedo (2017)	71
3.4.3	Bullock <i>et al.</i> (2018).....	72
3.4.4	Bullock <i>et al.</i> (2019)	74
3.4.5	Fotopoulou <i>et al.</i> (2018).....	77
Chapter 4.	Subsoil Characterization at Urban Scale	80
4.1	Methodology.....	81
4.1.1	Definition of stratigraphic units	82
4.1.2	Soil boundaries discontinuities	82
4.1.3	Stratigraphic recognition with AI.....	86
4.2	Considerations	86
Chapter 5.	Liquefaction Vulnerability of Buildings: the proposed tool for a preliminary assessment	88
5.1	Abstract.....	88
5.2	Numerical analysis	88
5.2.1	Definition of the model	88
5.2.2	Parametric study	93
5.2.3	Sensitivity study	95
5.2.4	Role of superstructure inertia	100
5.3	Prediction of settlement with the Bullock <i>et al.</i> (2018) formula	101
5.4	Prediction of angular distortion	103
Chapter 6.	The case study of Terre del Reno (FE)	109
6.1	Abstract.....	109
6.2	The 2012 Emilia-Romagna seismic sequence	109
6.3	The Municipality of Terre del Reno	112
6.3.1	Geological setting.....	113
6.3.2	Liquefaction-induced surficial manifestations	116
6.3.3	Urban development and damage on buildings	117
6.4	Geodatabase.....	120
6.5	Subsoil characterization with statistical methods and AI.....	123
6.5.1	Definition of stratigraphic units in the municipality of the Terre del Reno	124
6.5.2	CPT profiles processing	125
6.5.3	Training and application of the Artificial intelligence algorithm ..	125

6.5.4	3D subsoil stratigraphic reconstruction.....	128
6.6	Angular distortion assessment.....	129
6.7	Validation	133
6.8	Analysis of results	136
CONCLUSIONS		138
Appendix A.....		141
Appendix B.....		145
Appendix C.....		150
Appendix D.....		171
References.....		175

LIST OF FIGURES

Figure 1.1- Total deaths from Earthquake Disasters, 1900 to 2021 (EM-DAT)	6
Figure 1.2 - Objective of the SENDAI Framework and priorities for action (UNISDR, 2015).....	11
Figure 1.3 - The causal chain from basic research disciplines to preventive actions through earthquake loss estimation (adapted from Bungum and Lang, 2010).....	13
Figure 1.4 - Performance-based earthquake engineering (PBEE) cascade methodology proposed by the Pacific Earthquake Engineering Research (PEER) Center (modified after Cornell and Krawinkler, 2000).	15
Figure 1.5 - Different levels of the study area’s size. The extent of the study area affects the study’s resolution and efforts to make (adapted after Lang, 2012).....	21
Figure 1.6 - Different ways to demarcate the geographical units (geounits). The size of the geounits affect the study’s resolution and level of effort required (adapted from Lang and Aldea, 2011).....	22
Figure 2.1 - Liquefaction evidences over Europe (extracted from the deliverable D2.4 of LiquefACT Project).....	26
Figure 2.2 - (a) Normalized CPT Soil Behavior Type (SBTn) chart, $Q_t - F_r$ (Robertson, 1990, updated by Robertson, 2010 and 2015); (b) Schematic flowchart to evaluate the Soil Behaviour Type index (Robertson, 1998).....	31
Figure 2.3 - Scheme of the procedure to implement the CRR-fitted method and equivalent soil profile classification criteria.	32
Figure 2.4 - Flowchart of the Boulanger & Idriss (2008, 2010) SPT-based procedure for liquefaction triggering analysis.;Flowchart of the Boulanger & Idriss (2014) CPT-based procedure (b).....	36
Figure 2.5 - Flowchart of the Andrus & Stokoe (2000) procedure for liquefaction triggering evaluation.	37
Figure 2.6 - Sand Boils from 2011 Christchurch, New Zealand Earthquake (Musson, 2011).	38
Figure 2.7 - Effect of lateral spreading on the roadway after the 2011 earthquake series in Christchurch (New Zealand).	38
Figure 2.8 - Differential settlement on building (Taipei in Taiwan, 2010).....	39

Figure 2.9 - Loss of Bearing Capacity due to Soil Liquefaction from Niigata, Japan 1964 Earthquake (Niigata Earthquake, 1964).....	39
Figure 2.10 - Post liquefaction maximum cyclic shear strain (b) as function of relative density and Liquefaction Safety Factor (FS) (modified from Ishihara & Yoshimine, 1992).....	47
Figure 3.1 - Choices for the vulnerability assessment procedure (adapted from Calvi et al., 2006).	51
Figure 3.2 - Vulnerability classes in EMS-98.....	53
Figure 3.3 - Damage classification for masonry buildings in the European Macroseismic Scale.	53
Figure 3.4 - Damage classification for reinforced concrete buildings in the European Macroseismic Scale.	54
Figure 3.5 - Modified Mercalli intensity scale: level of shaking and description of damage.	55
Figure 3.6 - Modified Mercalli intensity scale: people's perception and effects on environment.	56
Figure 3.7 - Human perception and reaction according to JMA scale.....	57
Figure 3.8 - Effects on wooden houses (a) and reinforced concrete buildings (b) according to JMA scale.....	58
Figure 3.9 - Influence on infrastructures and utilities according to JMA scale. ...	58
Figure 3.10 - Structural damage States (adapted from Rajkumari et al., 2022)....	59
Figure 3.11 – Example of empirical fragility curves for RC building typologies proposed by Rosti et al. (2021). Numbers in the legend refer to the sample size.....	63
Figure 3.12 -Vulnerability functions to relate damage factor (d) and peak ground acceleration (PGA) for different values of vulnerability index (Iv) (adapted from Guagenti and Petrini, 1989).	64
Figure 3.13 - Flowchart to describe the components of the calculation of analytical vulnerability curves and damage probability matrices (modified after Dumova-Jovanoska, 2004).	65
Figure 3.14 - Liquefaction-induced displacement mechanisms: a) volumetric strains caused by water flow in response to transient gradients; b) partial bearing failure due to soil softening; and c) SSI-induced building ratcheting during earthquake loading (from Dashti and Bray 2013).	68
Figure 3.15 - Flowchart of the framework for vulnerability assessment of RC frame buildings subjected to liquefaction-induced differential displacements (from Fotopoulou et al., 2018).	78

Figure 3.16 - Fragility curves formulated by Fotopoulou et al. (2018) for the (a) 2-storey, (b) 4-storey and (c) 9-storey frame buildings subjected to differential settlements due to liquefaction (from Fotopoulou et al., 2018).....	79
Figure 4.1 - Proposed methodology for the subsoil stratigraphic recognition.....	81
Figure 4.2 - Definition of the two subsets of relevant parameters along the vertical axis of CPT test (from Spacagna et al, 2015).	83
Figure 4.3 – Spherical variogram.....	84
Figure 4.4 - Example of sectioned CPT profile.	85
Figure 5.1 - Layout of the implemented numerical model.....	89
Figure 5.2 - Shear modulus degradation and damping curves numerically and experimentally (Fioravante et al., 2013 and Sinatra and Foti, 2015) obtained for the different subsoil layers.....	91
Figure 5.3 - Results of the numerical liquefaction tests in terms of a) deviatoric stress against axial strain curves; b) deviatoric stress against main effective stress curves; c) liquefaction curves.	92
Figure 5.4 - Typical output and definition of the characteristic variables.	94
Figure 5.5 - Absolute versus mean settlement obtained in all numerical analyses.	96
Figure 5.6 - Absolute settlement (a), differential settlement (b), and angular distortion (c) for variable thicknesses of the crust (HC) (calculation has been performed assigning the Emilia Romagna earthquake, HL=6m, Dr=40%, su=50kPa, B=10m, q=50kPa, EI=0 MN*m).	97
Figure 5.7 - Absolute settlement (a), differential settlement (b), and angular distortion (c) for variable undrained shear strength (su) of the crust (calculation has been performed assigning the Emilia Romagna earthquake, HL=6m, HC =4m, Dr=40%, B=10m, q=50kPa, EI=0 MN*m).	97
Figure 5.8 - Absolute settlement (a), differential settlement (b), and angular distortion (c) for variable thickness of liquefiable layer (HL) (calculation has been performed assigning the Emilia Romagna earthquake, HC =4m, Dr=40%, su=50kPa, B=10m, q=50kPa, EI=0 M).	98
Figure 5.9 - Absolute settlement (a), differential settlement (b), and angular distortion (c) for variable relative density (Dr) of the liquefiable layer (calculation has been performed assigning the Emilia Romagna earthquake, HL=6m, HC =4m, su=50kPa, B=10m, q=50kPa, EI=0 MN*m).	98
Figure 5.10 - Absolute settlement (a), differential settlement (b), and angular distortion (c) for variable relative foundation loads (q) (calculation has been performed	

assigning the Emilia Romagna earthquake, HL=6m, HC =4m, Dr=40%, su=50kPa, B=10 m, EI=0 MN*m).	99
Figure 5.11 - Absolute settlement (a), differential settlement (b), and angular distortion (c) for variable relative foundation width (B) (calculation has been performed assigning the Emilia Romagna earthquake, HL=6m, HC =4m, Dr=40%, su=50kPa, q=50kPa, EI=0 MN*m).	99
Figure 5.12 - Absolute settlement (a), differential settlement (b), and angular distortion (c) for variable stiffness (EI) (calculation has been performed assigning the Emilia Romagna earthquake, HL=6m, HC =4m, Dr=40%, su=50kPa, q=50kPa, B=10).	99
Figure 5.13 - Effect of superstructure in terms of ratio (ρ) between foundation movements computed with the model contemplating superstructure inertia and the corresponding results of the basic analysis (a); plot box of effect of H/B ratio for each foundation movement.	101
Figure 5.14 - Mean settlements predicted with the numerical calculation vs median settlements computed with the Bullock et al. (2018) semi-empirical method.....	103
Figure 5.15 - Key evidence from the parametric study: ground horizontal strain vs angular distortion overlapped to the plot of Boscardin and Cording (1989).	104
Figure 5.16 - Angular distortion vs maximum absolute settlement overlapped to the plot of Grant et al. (1974).	105
Figure 5.17 - Structure of the artificial neural network (a), regression (b), statistical analysis and frequency distribution of error (c).	107
Figure 5.18 - Example of β prediction with ANN.	108
Figure 6.1 - Map reporting the epicentres of the Emilia Romagna 2012 seismic sequence (INGV database).	110
Figure 6.2 - Liquefaction ground evidences after the 2012 Emilia Earthquake Sequence.	111
Figure 6.3 - The municipality of Terre del Reno (FE): main districts and Digital Elevation Model.....	112
Figure 6.4 - a) In the map, the paleochannels and the different types of alluvial deposits are shown; b) geomorphology of the study area.....	114
Figure 6.5 - Geological cross section WNW-ESE through the San Carlo area, (Martelli, 2012).	115
Figure 6.6 - Liquefaction ground observations after the 2012 Emilia Earthquake Sequence.	116

Figure 6.7 – Urban development of the municipality of Terre del Reno: aerial detail on the districts of Sant’Agostino (a) , San Carlo (b) and Mirabello (c).	118
Figure 6.8 - Location of the damaged buildings in the municipality of Terre del Reno.	119
Figure 6.9 - Statistical analysis of the costs of reconstruction for the three districts of Terre del Reno.	120
Figure 6.10 - Spatial distribution of the "PERL" geognostic surveys database, the acronym in the legenda are consistent with the guidelines for seismic microzonation.	122
Figure 6.11 - statistical distribution of the available survey in terms of typology (a), period of realization (b) and depth (c).	123
Figure 6.12 - Efficiency of the proposed LDA algorithm.....	127
Figure 6.13 - Application of the LDA algorithm on the surveys disseminated all over the area of San Carlo.....	127
Figure 6.14 - Detail of the liquefiable volumes (in yellow) in the 3D stratigraphic reconstruction of the subsoil of San Carlo, performed with Isatis software.	129
Figure 6.15 - Forecasted liquefaction induced angular distortion in the district of San Carlo.....	131
Figure 6.16 - Liquefaction induced surficial manifestations and fractures in the district of San Carlo.	132
Figure 6.17 - Liquefaction induced damages on buildings in the district of San Carlo.....	132
Figure 6.18 - Receiver Operating Curve (ROC) method.	134
Figure 6.19 - Receiver Operating Curve test between damages on buildings and forecasted angular distortion, settlement computed with Bullock et al. (2018) and settlement indicator proposed by Zhang et al. (2002).	135
Figure 6.20 - Receiver Operating Curve test between liquefaction-induced surficial manifestations and free-field settlement indicator proposed by Zhang et al. (2002).	136

LIST OF TABLES

Table 1.1 - Terminology coded during the 1979 UNDRO conference for natural disaster definition and comparison with the past terms.....	9
Table 1.2 - List of critical infrastructures.....	19
Table 2.1 - Liquefaction susceptibility of sedimentary deposits (Youd and Perkins, 1978).....	28
Table 2.2 - Level of liquefaction susceptibility defined at the scale of in-situ test (“CMS”- University of Ferrara, 2014).....	30
Table 2.3 - Liquefaction severity indexes proposed in literature.....	40
Table 2.4 – LPI based risk classes	41
Table 2.5 - The following additional constraints are applied to the volumetric densification calculations using the equations given in Appendix A of Zhang et al. (2002).....	43
Table 2.6 - LSN Ranges and observed land effects (NGS, 2016).....	44
Table 2.7 - Suggested limit states for rigid body settlements due to earthquake induced ground deformation (modified after Chiaradonna et al., 2020).	46
Table 3.1- Damage Probability Matrix Proposed by Whitman et al. (1973).	60
Table 3.2 - Coefficient values for the empirical model	75
Table 3.3 - Coefficients for the semiempirical model of residual tilt (from Bullock et al., 2019)	76
Table 5.1 - Subsoil parameters assigned in the calculation.	92
Table 5.2 - Parameters for sensitivity analyses.....	95
Table 5.3 - Selected seismic input.	95
Table 5.4 - Input parameters for the application of Bullock et al. (2018) semi-empirical formula.....	102
Table 5.5 - ANOVA test showing the statistical significance of the relation between variables and angular distortion.	106
Table 6.1 – Required input parameter for the assessment of the liquefaction induced angular distortion with the proposed ANN.....	131
Table 6.2 - AUC values.....	135

INTRODUCTION

Seismic liquefaction continuously stimulates the interest of the geotechnical community in promoting experimental, theoretical studies and field observations that clarify the factors ruling susceptibility of soil, triggering (e.g., Ishihara, 1996; Youd *et al.*, 2001; Seed *et al.*, 2003; Bray and Sancio, 2006; Boulanger and Idriss, 2014) and chained mechanisms (Iwasaki *et al.*, 1978; van Ballegooy *et al.*, 2014; Chiaradonna *et al.*, 2020; Cubrinovski *et al.*, 2017). For buildings and infrastructures, studies are oriented at predicting damage (Bird *et al.*, 2005; Bray and Macedo, 2017; Karamitros *et al.*, 2013; Bullock *et al.*, 2018; Castiglia *et al.*, 2020; Baris *et al.*, 2021) or at conceiving mitigative solutions (Flora *et al.*, 2021; Salvatore *et al.*, 2020), motivated by the concern of stakeholders for the huge economic and social impact of liquefaction recorded in past seismic events.

An overall estimate is provided by Daniell *et al.* (2012) who disaggregated primary (shaking) and secondary causes (tsunami, fire, landslides, liquefaction, fault rupture, and other type losses) over a global record of nearly seven thousand earthquakes from 1900 to 2012. These authors found liquefaction responsible for about 2.2% of the direct economic losses, globally estimated at 2.24 trillion US dollars, this fraction becoming 3.6 % when considering total losses, i.e. direct plus indirect damage. This relatively small percentage could drive to underestimate the relevance of liquefaction, but the numerous examples that occurred in urbanized systems prove that the physical damage together with the prolonged impracticableness of buildings and infrastructures undermines the recovery of normal living conditions and may lead to the complete abandonment of the place (Macaulay, 2009; CSAPEISLA, 2016). Literature reports plenty of examples of destructive effects caused by liquefaction on urban areas (San Francisco 1960 - Youd and Hoose, 1978; Kobe 1995 - Chung, 1995; Kocaeli 1999 - Cetin *et al.*, 2002; Christchurch 2010-2011 - Cubrinovski *et al.* 2011, Bray *et al.* 2014, Paoletta *et al.*, 2020; Urayasu 2011 - Yasuda *et al.*, 2012; Baris *et al.*, 2021; Emilia-Romagna 2012 - Fioravante *et al.*, 2013). The soil-foundation-structure interaction strongly rules this phenomenon (Bray *et al.*, 2014). Fully coupled analyses of liquefaction and shaking are rather complex and require a very accurate definition of the input variables, difficult to achieve when performing serial analyses like in large-

scale assessment. Bird *et al.* (2006) propose a simpler solution that decouples and recombines the effects of shaking and liquefaction for a prescribed event. The first compulsory step is the definition of a demand variable, i.e. the most expressive quantity that characterizes physical damage. Foundation movement is classically subdivided into the following components: mean settlement, rigid rotation and angular distortion. Rotation is of paramount importance for high-rise buildings and towers, prEN 1997-1 (2004), both in static and seismic cases. Poulos *et al.* (2001) converge on identifying the angular distortion as the paramount demand variable for low-rise buildings (1-3 stories, Fotopoulou *et al.*, 2018), fixing thresholds equal to 1/500, 1/300 or 1/150 for respectively light, visible cracking, and structural damage of framed buildings in the static case. A similar assumption is made by previous studies that considered the effect caused by the self-weight of buildings (e.g. Skempton and MacDonald, 1956; Bjerrum, 1963; Meyerhof, 1953; Burland and Wroth, 1974; Burland *et al.*, 1977; Wahls 1981). Boscardin and Cording (1989) studied the effects of excavation and defined the damage level as a function of angular distortion and horizontal tensile strain, the two quantities related to each other for the different sources of movement. This step is simplified by Grant *et al.* (1974) that propose to statistically estimate angular distortion as the upper bound from a relation with absolute settlements measured on buildings founded on cohesive or cohesionless soils with rafts, strips or isolated footings.

For liquefaction assessment of low-rise buildings, Bird *et al.* (2006) distinguish the case of rigid from flexible foundation, with absolute settlements being the principal damage factor for the former, differential settlement for the latter case. In this circumstance, differential settlements induced by liquefaction on framed buildings cause a drift of columns that the authors propose to cumulate with that produced by shaking. Fotopoulou *et al.* (2018) also adopted the differential settlement as a demand variable in their probabilistic definition of vulnerability for low-grade structures. In general, the structural damage induced by foundation movements on a building depends on the stiffness and fragility of the structure-foundation system, these factors are connected with the typology, extension, and height of the building. A continuous transition, rather than a net separation between rigid and flexible structures, would better describe the variety of possible structural typologies.

For liquefaction, several methods are proposed to predict absolute settlements. The state-of-the-art practice for this evaluation largely relies on empirical procedures developed to estimate post-liquefaction, one-dimensional consolidation settlement in free-field conditions (e.g., Tokimatsu and Seed, 1987; Ishihara and Yoshimine, 1992).

According to Ishii and Tokimatsu (1988), this assumption can be reasonably accepted only if the width of the foundation is at least twice or three times larger than the thickness of the liquefiable soil layer. However, the main limitation of these empirical procedures is that none of them considers the soil-structure interaction and the resulting complex mechanisms, for example, the SSI-induced building ratcheting during earthquake loading (Dashti and Bray, 2013). Based on the results of numerical analyses and attributing liquefaction-induced settlements to the seismic excitation characteristics and the post-shaking degraded static factor of safety, Karamitros *et al.* (2013) provide a simplified analytical formula for the estimation of absolute settlement of strip and rectangular footings with a clay crust. Such settlement is associated with a "sliding-block" type of punching failure through the clay crust and within the liquefied sand layer. Bray and Macedo (2017) performed a large number of parametric numerical analyses and proposed to express the total settlement as a sum of three contributions respectively induced by shear, volume deformation and sand ejecta. In particular, the shear-induced rate is related to several properties, including the unitary contact pressure on the foundation, the thickness of the liquefiable layer and the lower planimetric dimension of the building footprint and the cumulative absolute velocity (Campbell & Bozorgnia, 2011). Performing rich and various parametric numerical, fully coupled three-dimensional analyses of the soil–structure interaction, Bullock *et al.* (2018) define a relation to predicting the statistical distribution of settlements for shallow-founded structures on liquefiable soil induced by volumetric and distortional strains. This formula has the advantage of capturing the role of most soil, ground motion and building properties.

The present research aims to develop a procedure for rapid and preliminary screening of the buildings' liquefaction vulnerability at an urban scale. The proposed methodology is mainly articulated in two phases: first, an extensive subsoil characterization is carried out with a procedure based on geostatistical tools and artificial intelligence algorithms; then, an artificial neural network for the calculation of the liquefaction-induced angular distortion on shallow-founded low-rise buildings is developed.

The proposed analyses are based on an extensive and complete study for the definition of a procedure for the subsoil characterization. *Chapter 4* exposes the data-driven analysis for the subsoil stratigraphic recognition combining geostatistical tools and AI algorithms. The procedure is calibrated and validated on the case study of Terre del Reno (Italy), homogeneously covered by about 2500 geognostic surveys available in the "PERL" database (Varone *et al.*, 2022 - submitted). "PERL" (stand for

“Protocollo Emilia-Romagna Liquefazione”) is research project, carried out by the Emilia Romagna Region (RER), CNR-IGAG and UniCas-DiCeM, aiming to provide a reliable procedure for liquefaction risk assessment and a seismic microzonation.

Chapter 5 describes the analysis procedure that leads to the definition of the tool for the prediction of the angular distortion in foundation, applicable for the preliminary screening of risk at a large scale, e.g. city, and districts. To this aim, a large number of two-dimensional coupled numerical analyses are performed, parametrically varying the stratigraphic and mechanical conditions of the subsoil, the ground motion characteristics and the equivalent structural properties of the building.

Last, procedure are applied and validated on the case study of Terre del Reno (FE, Emilia-Romagna, Italy).

Chapter 1. SEISMIC RISK

ASSESSMENT:

OVERALL APPROACH AND

FRAMEWORK OF METHODOLOGY

1.1 Motivation

The huge impact caused by past earthquakes has raised the need for approach and methodology to perform seismic risk assessment analyses. The EM-DAT International Disaster Database provided by the Centre for Research on the Epidemiology of Disasters (CRED) at the Catholic University in Louvain (Belgium) collects natural disasters all over the world from 1900. From a technical viewpoint, a phenomenon is assessed as a disaster, and thus incorporated into EM-DAT, if at least one of the following criteria is satisfied:

- 10 or more reported killed people;
- 100 or more reported affected people;
- declaration of a state of emergency;
- call for international assistance.

In the EM-DAT, earthquakes are individuated as the second cause of death due to natural disasters after weather-related problems, such as drought. In particular, from 1900 to 2021, earthquakes caused about 3 million deaths in the world (Figure 1.1); the Asian continent is most affected by this natural hazard.

In the last two decades, the number of deaths is approximately 750000 deaths globally (CRED & UNISDR, 2018), being responsible for more than half of all deaths related to natural disasters (around 1.3 million). The high number of deaths between 1998-2017 is strongly influenced by the 2004 Indian Ocean Tsunami, the 2008 Wenchuan (China) Earthquake, the 2010 Haiti Earthquake, and the 2011 Tohoku (Japan) Earthquake.

Seismic Risk assessment:
Overall Approach and Framework of Methodology

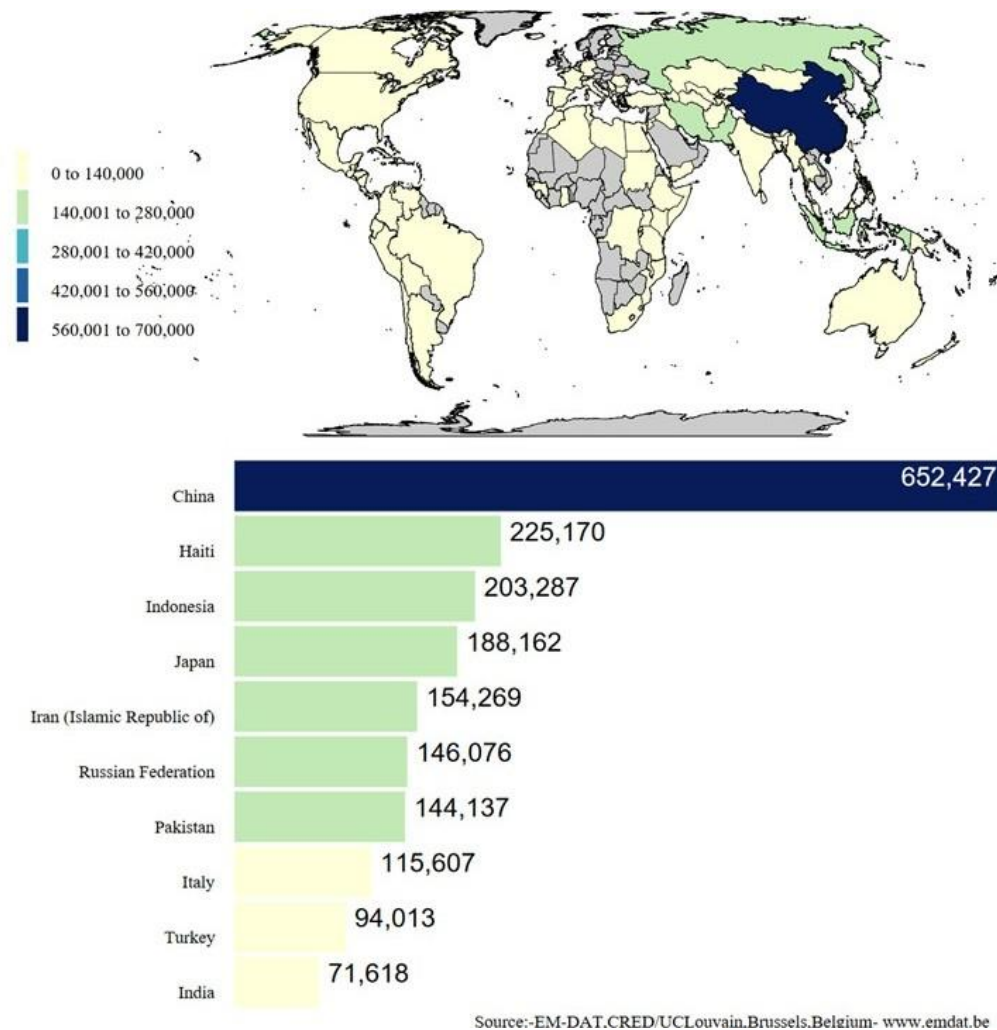


Figure 1.1- Total deaths from Earthquake Disasters, 1900 to 2021 (EM-DAT)

From the reports of past earthquakes, the EM-DAT, and UNISDR catalogs, it is clear that these events affect a very large population, not only in terms of deaths, but also of displaced, or evacuated during the emergency phase of the disaster, injured, homeless. Furthermore, the number of total affected people is not only related to the ground movement, but also to secondary natural hazards, such as tsunamis (i.e. Tohoku Earthquake, Sumatra-Andaman earthquake) or seismic liquefaction in sands or quick clays (i.e. Port-au-Prince Earthquake; Tohoku Earthquake; New Zealand seismic sequence in 2011; the 2012 Emilia-Romagna earthquake, in Italy).

An overall estimate is provided by Daniell *et al.* (2012) who disaggregated primary (shaking) and secondary causes (tsunami, fire, landslides, liquefaction, fault rupture, and other type losses) over a global record of nearly seven thousand earthquakes from 1900 to 2012. In particular, these authors found that liquefaction is responsible for

about 2.2% of the direct economic losses, globally estimated at 2.24 trillion US dollars, this fraction becoming 3.6 % when considering total losses, i.e. direct plus indirect damage. This relatively small percentage could misleadingly drive to underestimating the relevance of liquefaction. On the other hand, the numerous examples that occurred in urbanized systems prove that the physical damage together with the prolonged impracticability of buildings and infrastructures can be overwhelming, as it undermines the recovery of normal living conditions and may lead to the complete abandonment of the place (Macaulay *et al.*, 2009; CSAPEISLA, 2016).

Literature reports plenty of examples of destructive effects caused by liquefaction on urban areas (San Francisco 1960 - Youd and Hoose, 1978; Kobe 1995 - Chung, 1996; Kocaeli 1999 - Cetin *et al.*, 2002; Christchurch 2010-2011 - Cubrinovski *et al.* 2011, Bray *et al.* 2014, Paoletta *et al.*, 2020; Urayasu 2011 - Yasuda *et al.*, 2012; Paris *et al.*, 2021; Emilia-Romagna 2012 - Fioravante *et al.*, 2013).

Long-term effects on the communities and societal aspects connected to the rebuilt and the restoration of the functionality of damaged structures and infrastructures should not be neglected since this process may take years until the pre-disaster conditions are restored. The destructive impact on society, in terms of structural damages, loss of service functionality, deaths and injuries continuously stimulates the interest of the scientific community in promoting the development of a univocal methodology widely and worldwide applicable to evaluate the risk against natural hazards and averting or mitigating new losses. The need for a common procedure in risk assessment has been raised since the 1970s in the International Community and has been coded for the first time during the United Nations Disaster Relief Office (UNDRO) conference of 1979. In the following paragraphs and chapters, an overview will be presented on the conceptual basis for the seismic risk assessment, focusing on the procedure proposed for the evaluation of the secondary seismic effect of liquefaction.

1.2 History and overall approach of Risk Assessment

In 1971, the Office of the UN Disaster Relief Co-ordinator (UNDRO) was established to help deal with natural disasters, mitigate destruction, and fill the gap of International disaster relief assistance haphazard, un-coordinated, and not always conducted as a managerial and developmental as well as humanitarian task. UNDRO's mandate, established after several years of debate, is to mobilize, direct and coordinate international relief efforts and promote disaster prevention, planning and preparedness.

Seismic Risk assessment:
Overall Approach and Framework of Methodology

The Joint Inspection Unit evaluated UNDR0's programme with emphasis on the 1976-80 period in which its staff and activities have been substantially strengthened (Allen *et al.*, 1980). Furthermore, there was no univocal terminology to describe risk before 1979.

Mr Fournier d'Albe of UNESCO in his paper on *Earthquake Prediction and Risk Management* (1979) uses the term risk to denote the possibility or probability of loss and defines this as the product of seismic hazard, vulnerability and value. In this case, vulnerability is a measure of the proportion of the value which may be expected to be lost as the result of a given earthquake. Instead, the same UNDR0 members and coordinators used to define vulnerability (or disaster risk) as the product of the values of the terms natural hazard risk and damage probability (UNDR0, 1979). The lack of a coded language made the management and mitigation of emergencies even more difficult. In order to avoid misunderstandings, during the United Nations Disaster Relief Office (UNDR0) conference of 1979, a set of terms (Table 1.1) for use in disaster studies which will be widely understood and accepted was defined.

The meeting proposed therefore that the following terms and definitions be used:

- NATURAL HAZARD: the probability of occurrence, within a specific period in a given area, of a potentially damaging natural phenomenon;
- VULNERABILITY: the degree of loss to a given element at risk or set of such elements resulting from the occurrence of a natural phenomenon of a given magnitude and expressed on a scale from 0 (no damage) to 1 (total loss);
- ELEMENTS AT RISK or EXPOSURE: the population, buildings and civil engineering works, economic activities, public services, utilities and infrastructure at risk in a given area;
- SPECIFIC RISK: the expected degree of loss due to a particular natural phenomenon and as a function of both natural hazard and vulnerability;
- RISK: the expected number of lives lost, persons injured, damage to property and disruption of economic activity due to a particular natural phenomenon, and consequently the product of specific risk and elements at risk.

More generally, the United Nations International Strategy for Disaster Reduction "UNISDR" (UN, 2009) defines risk as the combination of the probability of an event and its negative consequences, in a way that emphasizes both the concept of chance, possibility (e.g., the risk of an accident) as well the potential losses, for a given cause, location and period.

Seismic Risk assessment:
Overall Approach and Framework of Methodology

Table 1.1 - Terminology coded during the 1979 UNDRO conference for natural disaster definition and comparison with the past terms.

UNDRO (before 1979)	UNESCO	UNDRO (proposed after 1979)
Risk	Hazard	Natural hazard
Damage	Vulnerability	Vulnerability
Vulnerability	-	Specific risk
-	Value	Element at risk or Exposure
-	Risk	Risk

In its simplest way, risk can be expressed with the product of three factors that encompass the concepts:

$$Risk = Hazard \times Vulnerability \times Exposure \quad (1.1)$$

Over the years a general tendency towards higher-resolution risk analyses has been observed. In most cases, the resolution of the risk analysis follows the resolution of the hazard and exposure datasets used as input. Frequently, these have the same resolution, and where this is not the case the tendency is to either resample the lower-resolution datasets to the higher resolution or vice versa.

Archives of historical data of past natural disasters, georeferenced subsoil investigations, geological maps, land use maps, pluviometric and satellite measurements are a fundamental resources to carrying out these analyzes. Besides, the concentration of human and economic activities in cities generates an increasing interest in the use of underground space as an environmentally friendly solution to enhance the quality of life and boost competitiveness (ACUUS, 2018).

A key factor for both scopes is the knowledge of subsoil, today encouraged by the capability to store, process, and quickly analyze large amounts of geo-referenced data. Not only information drives decision making but, it moreover, promotes the data-driven culture to assist operators in performing better and, in a further scenario, to trigger a novel vision of urban planning. Geo-referenced data-driven models exist in different fields of civil and geotechnical engineering (Xie et al., 2020) often coupled with artificial intelligence, to optimize investigation (Crisp et al., 2020), predict the response to external inputs (Paolella et al., 2019). Geotechnical data sharing, encouraging operators to convey their information into common platforms, is a principle espoused in several countries (e.g. France - brgm; UK – British Geological Survey BGS and Geological Survey; Poland – Polish Geological Institute National

Seismic Risk assessment:
Overall Approach and Framework of Methodology

Research Institute; Norway – Geological Survey of Norway; Denmark – GEUS-Jupiter, Italy – ISPRA Ambiente) with the explicit scope of supporting the activity of technicians. Activated in 2016 as an extension of the database created in Christchurch after the 2011-2012 earthquake sequence, the New Zealand Geotechnical Database now contains to date about 130,000 geotechnical data points (boreholes, pits, penetrometer and geophysical logs) spread across the country. The geotechnical database of the British Geological Survey BGS covers the UK with nearly 450.000 laboratory tests and core descriptions. In Italy, the Geoportale dell'Emilia Romagna provides about 85.000 in situ investigations distributed over the region. Generally, geotechnical datasets are run voluntarily, aiming at reducing cost and improving the quality of investigation with information from the surrounding area. Conspicuous databases allow for detailed analyzes, performed with different methodologies, mainly grouped into two groups: *deterministic* or *probabilistic* studies. Probabilistic refers to studies that assess expected annual impacts by integrating across return periods based on a probabilistic stochastic event set. For droughts, volcanoes, and landslides, studies to date have used non-probabilistic approaches only. Studies on floods and earthquakes have seen a move towards more probabilistic studies in more recent years, and the two studies reviewed for tsunamis also use a probabilistic approach. A major difference between the studies of earthquakes and tsunamis, in comparison to the other hazards, is the extensive use of stochastic event sets in the former.

The outcome of a risk analysis is typically a synthetic indicator that incorporates the analysis of hazard, vulnerability and exposure. The most commonly used risk indicators (Ward *et al.*, 2020) are the number of affected people (i.e., Daniell, 2014; Daniell & Wenzel, 2014; Knorr *et al.*, 2016; Liu *et al.*, 2018), some indicators of direct economic damage (i.e., Chan *et al.*, 1998; UNISDR, 2013, 2015, 2017; Ward *et al.*, 2013, 2017), with fatalities (i.e., Dilley *et al.*, 2005; Peduzzi *et al.*, 2009; Dottori *et al.*, 2018) and affected gross domestic product (GDP) (i.e., Peduzzi *et al.* 2012; Daniell, 2014; Daniell & Wenzel, 2014). Fatalities have been much less commonly assessed in flood and drought risk studies than in studies of the other hazards, offering the potential for cross-hazard knowledge exchange on methods for fatality assessment.

The goals of risk assessment analysis are summarized in promoting a strengthening in community resilience, through multi-risk disaster management, as proposed during UNDRO 1979. Such a purpose has become a priority for the 180 member States which joined this challenge promoting new policies supported by financial plans with guided investments. In fact, the strengthening of disaster risk governance is a necessary element for the development of prevention, mitigation, and risk management activities

Seismic Risk assessment:
Overall Approach and Framework of Methodology

and international cooperation to contribute to the development of knowledge at all levels, particularly for developing countries.

Following these criteria, objectives and wishes, the Third United Nations World Conference on Disaster Risk Reduction, held from 14 to 18 March 2015 in Sendai (Japan) adopted the 2015-2030 Sendai Framework Disaster Risk Reduction. The Sendai Framework for Disaster Risk Reduction 2015-2030 outlines seven clear targets and four priorities for action (Figure 1.2) to prevent new and reduce existing disaster risks: (i) Understanding disaster risk; (ii) Strengthening disaster risk governance to manage disaster risk; (iii) Investing in disaster reduction for resilience and; (iv) Enhancing disaster preparedness for effective response, and to "Build Back Better" in recovery, rehabilitation and reconstruction. It aims to achieve a substantial reduction of disaster risk and losses in lives, livelihoods and health and the economic, physical, social, cultural and environmental assets of persons, businesses, communities and countries over the next years until 2030.

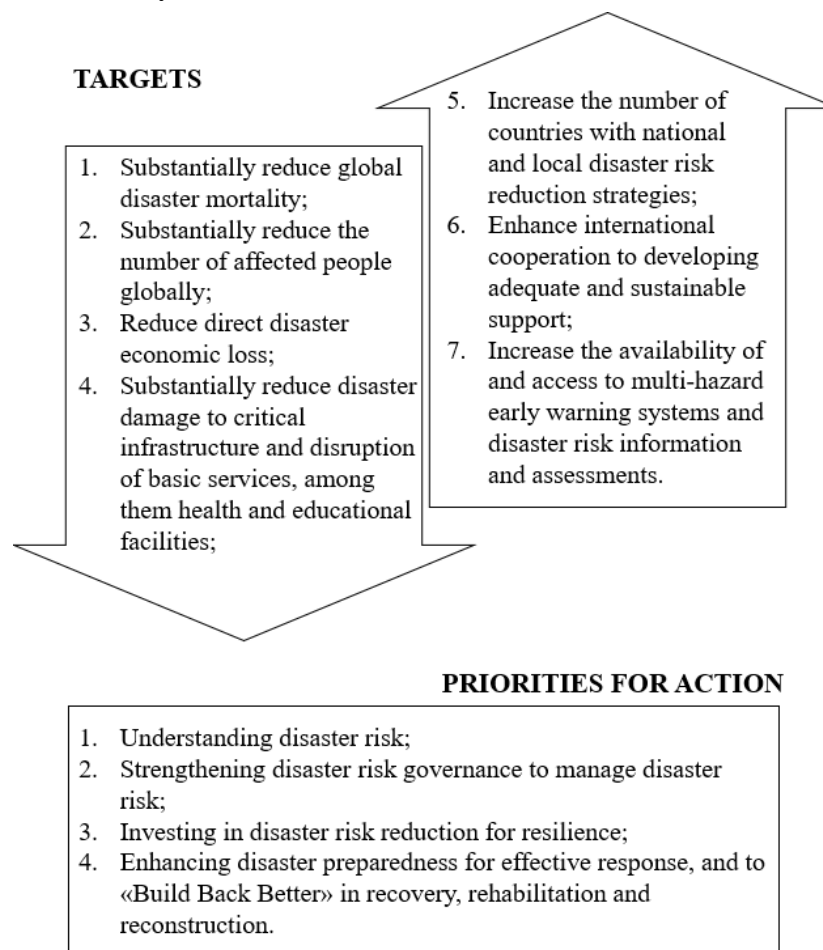


Figure 1.2 - Objective of the SENDAI Framework and priorities for action (UNISDR, 2015).

1.3 Principles for Seismic Risk Assessment

Seismic risk is defined as the probability of exceeding a certain level of damage, or losses occurring in economic-social terms, within a given time interval and area, due to a seismic event; these losses can include human lives, social and economic disruption as well as material damage.

The effects of earthquakes can vary from localized events to dramatic impacts on communities, infrastructure, the economy and the environment, across large regions. Occurrence of a major seismic event in an urban area can have a particularly severe impact, resulting in the complete disruption of economic and social functions in the community.

The assessment of earthquake risk constitutes the first step to support decisions and actions to reduce potential losses. The process involves developing (UNISDR, 2017):

- earthquake hazard models characterizing the level of ground shaking and its associated frequency across a region;
- vulnerability functions establishing the likelihood of loss conditional on the shaking intensity;
- exposure data sets defining the geographic location and value of the elements exposed to the hazards.

Hence, Equation 1.1 can be particularized for seismic hazard as follows:

$$\textit{Seismic Risk} = \textit{Seismic Hazard} \times \textit{Vulnerability} \times \textit{Exposure} \quad (1.2)$$

The development of a seismic risk analysis is a complex task involving many disciplines and actions. Bungum and Lang (2010) proposed a causal chain from basic research disciplines to preventive measures through earthquake loss estimation (Figure 1.3). The flowchart starts with a geophysical and geological study (to take in account past seismicity, seismo-tectonic framework, wave propagation), supported by surveys (i.e., reports about building stock and subsoil investigations), structural analysis (in order to assess the building response under seismic conditions) and social and economic sciences. The key to reducing earthquake damages is to reduce vulnerability, building-related as well as societal, based on an underlying knowledge of earthquake hazard. A number of well-proven preventive measures can be activated for this

Seismic Risk assessment:
Overall Approach and Framework of Methodology

mitigation purpose (i.e., strengthening of existing buildings, codes and provisions for new buildings, land use planning, preparedness and prevention measures).

The methodological chain of seismic risk assessment, from seismic hazard assessment to evaluation of potential losses, however, encompasses both aleatory and epistemic uncertainties associated with different sources.

Aleatory variability is the natural randomness in a process, and thus cannot be reduced with the collection of additional data. For discrete variables, the randomness is parameterized by the probability of each possible value. For continuous variables, the randomness is parameterized by the probability density function.

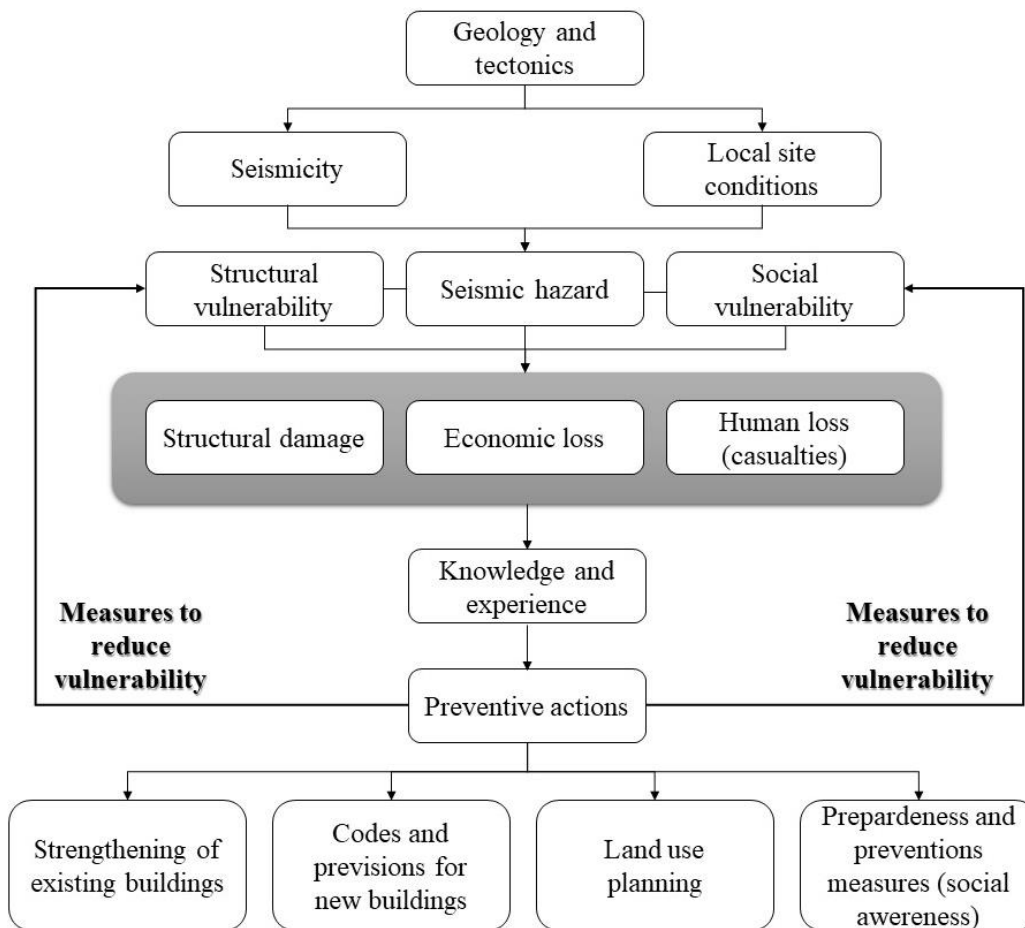


Figure 1.3 - The causal chain from basic research disciplines to preventive actions through earthquake loss estimation (adapted from Bungum and Lang, 2010).

Epistemic uncertainty is the scientific uncertainty in the model of the process and is related to the necessity to perform simplifications to simulate the complex nature or the response of the elements at risk. It is improvable with data and knowledge.

Seismic Risk assessment:
Overall Approach and Framework of Methodology

The epistemic uncertainty is characterized by alternative models. For discrete random variables, the epistemic uncertainty is modelled by alternative probability distributions. For continuous random variables, the epistemic uncertainty is modelled by alternative probability density functions. In addition, there is epistemic uncertainty in parameters that are not random by having only a single correct (but unknown) value (Pitilakis *et al.*, 2015; Crowley *et al.*, 2005; Tyagunov *et al.*, 2014). Treatment of epistemic uncertainty usually takes place in two complementary stages: quantification of uncertainty and sensitivity analysis. Quantification of epistemic uncertainty can be performed using methods such as Monte Carlo analyses (e.g. Cramer *et al.*, 1996; Sousa *et al.*, 2016), Bayesian methods (e.g. Bayraktarli *et al.*, 2011; Paoletta *et al.* 2022), fuzzy logic methods (e.g. Buratti *et al.*, 2012), and logic trees (e.g. Coppersmith *et al.*, 1986, Riga *et al.*, 2017).

Uncertainty is intrinsic in every phase of the risk analysis, as evidenced by the difficulty of forecasting the expected magnitude and the exact position in which an earthquake will occur. Here the two above categories of uncertainty are combined.

The current prediction of earthquake magnitude in a specific site is based on the statistical inference of historical data. Randomness is thus implicit in this prediction, being typically managed with the adoption of probabilistic models. However, one should admit that human experience is insufficient to predict all possible seismic scenarios and surprises must unavoidably be admitted beyond the expected range of situations. The uncertainty is also connected to the subsoil characterization. In this case, the degree of uncertainty can be reduced by increasing the number of available subsoil investigations: however, an increasing number of surveys will lead to an increase in costs and, anyhow, also in the ideal case of measures points distributed all over the analyzed area, there will always remain a component of uncertainty linked to the construction of subsoil geotechnical model, built introducing simplistic and generally conservative assumptions. Huge efforts are thus required to obtain the best subsoil geotechnical model with a limited number of investigations. The uncertainty encountered in the hazard analysis propagates to the subsequent levels of the risk assessment and is cumulated with the uncertainties related to vulnerability and exposure. In particular, vulnerability's uncertainty is dependent on the characteristics of engineering materials and systems, simplified model of structure and infrastructure and mechanical properties degradation over time. Last, exposure's uncertainty is principally associated to non-physical factors, like risk perception (e.g., expert versus

Seismic Risk assessment:
Overall Approach and Framework of Methodology

public), criteria (individual versus societal, or voluntary versus involuntary), political process, and risk communication (Tesfamariam & Goda, 2013).

All of the above considerations lead to the definition of a quantitative risk assessment. All of the above considerations lead to the execution of a quantitative risk assessment, taking into account all the possible uncertainty. This aim is pursued with a probabilistic approach. Probabilistic/statistical analyses rely on databases that quantify the probability and consequent values, provide a more objective and unanimously acknowledged understanding. Still their efficacy relies fundamentally on the quality of available information, i.e., numerosity and accuracy of data, representing various possible situations. Furthermore, these methods are useful for quantifying, or comparing, seismic risks for different options and facilitating informed decision-making. Reducing uncertainties within tolerable levels and evaluating reliability of conclusions is of paramount importance for a successful risk assessment and must be thus continuously considered as the reference goal along the whole process.

The Pacific Earthquake Engineering Research (PEER) Center (Cornell and Krawinkler, 2000) defined a performance-based earthquake engineering (PBEE) cascade methodology expressing the Eq. 1.2. The methodology is synthetically showed in Figure 1.4 and fully commented in the following paragraphs, in which the individual elements of risk analysis will be defined.

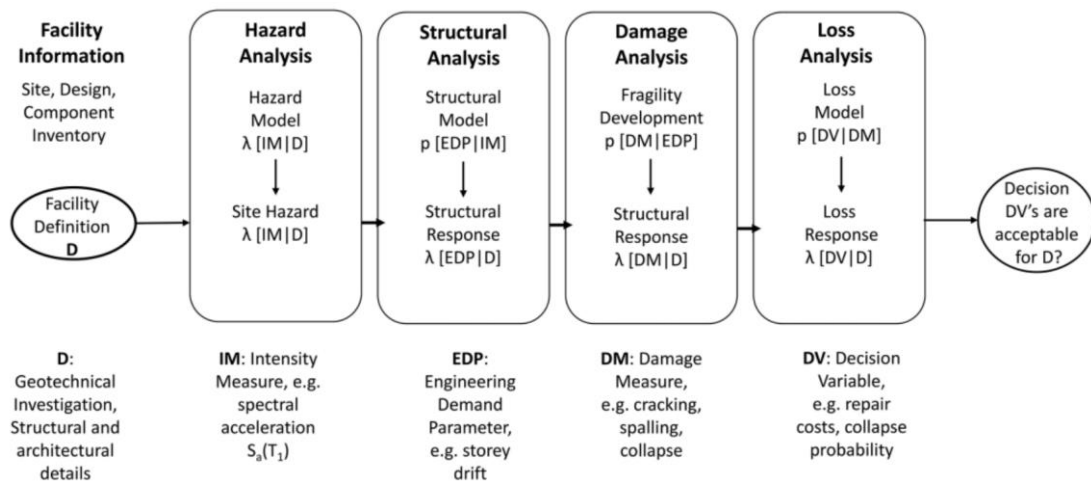


Figure 1.4 - Performance-based earthquake engineering (PBEE) cascade methodology proposed by the Pacific Earthquake Engineering Research (PEER) Center (modified after Cornell and Krawinkler, 2000).

1.3.1 Seismic hazard analysis

A key point in any seismic risk assessment is the provision of seismic ground motion (level and spectral characteristics of earthquake shaking). The seismic hazard analysis involves the identification and quantitative description of the earthquake that will be used as seismic input for the evaluation of losses (in economic and death terms). A ground-shaking hazard analysis can be carried out following different approaches:

- deterministic methods: based on the definition of deterministic earthquake scenarios and appropriate ground motion prediction equations (GMPE) in order to compute the spectral ordinates and supported by a strong hypothesis: if an earthquake has occurred once, it can occur again;
- probabilistic analysis: when a probabilistic approach is followed, the representation of the seismic hazard can lead to producing either the probability of exceeding a specified ground motion (in this case the output is generally a set of curves showing the exceedance probabilities of various ground motions at a site) or the ground motion that has a specified probability of being exceeded over a particular period (in this case the output is a set of maps showing the estimated magnitude distribution of ground motion that has a specific exceedance probability over a specified time period within a region).

Mualchin (2005) stated no seismic hazard analysis (SHA) is perfect and the key to performing this work successfully is understanding the fundamental differences and limitations of each, before then selecting one or both approaches for the study; advantages and disadvantages of each approach are exhaustively examined in Bommer 2002 and 2003.

Deterministic seismic hazard analysis (DSHA)

Deterministic seismic hazard analysis (DSHA) is an approach for evaluating site-specific seismic hazard, looks at multiple seismic sources and determines the Maximum Credible Earthquake to a specific fault from the single source which creates the largest hazard for the site. The magnitude and the epicentre of the expected earthquake are derived from historical data of past shocks and database of seismic sources (faults). A specific attenuation relationship is then assumed to determine the PGA at the project site based on the geographic location of the study region and the type of fault. The amplification of ground shaking to account for local site conditions is usually based on site classes and soil amplification factors. The main advantage is that both the intensity of ground shaking (PGA) and the duration of the motions are

Seismic Risk assessment:
Overall Approach and Framework of Methodology

known. The biggest drawback of DSHA is that the temporal characteristics (i.e., earthquake frequency of occurrence and the associated uncertainty) are often neglected; furthermore, the PGA values do not necessarily reflect the cumulative, or aggregate, hazard in the region, and assessing the influence of uncertainties in factors such as earthquake magnitude or source-to-site distance on the resulting PGA are accounted for by performing additional parametric studies of each variable. The DSHA has been widely used until 1970s.

Probabilistic seismic hazard analysis (PSHA)

In probabilistic seismic hazard analysis (PSHA), seismic hazard is defined as the ground motion with an annual probability of exceedance and calculated from a triple integration based on statistical relationships of earthquake and ground motion. Two approaches for PSHA were developed to estimate seismic risk in the late 1960s: the Cornell approach (1968) with a theoretical base, and the Milne-Davenport (1969) approach, empirical; the most commonly used is the Cornell approach or the so-called Cornell–McGuire method (Cornell, 1968,1971; McGuire, 2004). The Cornell’s 1968 theoretical approach is developed on the relationship between a ground motion parameter (i.e., MMI, PGA, or others) and annual probability of exceedance at a site of interest based on the statistical relationships of earthquakes and ground motion, i.e., Gutenberg–Richter relationship and GMPE. A primary advantage of probabilistic seismic hazard analysis is that by assigning locations and seismicity rates to all sources, the ground motion parameter of interest expected at a specific site can be determined along with its probability distribution, which is useful for illustrating uncertainty in the ground motion variable. Repeating the analysis for multiple locations, specified as grid points, throughout a region allows for the creation of contour maps of the ground motion parameters for specified exposure intervals. These maps have been referred to as “uniform” or “aggregate” hazard maps as all sources’ contributions have been incorporated into a single ground motion value. Once the Probabilistic Seismic Hazard Analysis (PSHA) has been completed, ground motion maps can be obtained for any specified exposure interval. This information forms the input of risk assessment.

1.3.2 Seismic vulnerability analysis

Seismic vulnerability is the proneness of some categories of elements at risk to undergo adverse effects induced by potential earthquakes. A vulnerability analysis involves the drawing up of an inventory of all the structures and services of interest. Once redacted, the elements identified are divided into different categories (for example: construction type, period, type of foundation, number of floors) in order to simplify the analysis. For each class identified, it must be established the relationships among intensity of ground shaking, resulting damage, and associated losses. This is generally represented in the form of fragility curves which show the relationship between the level of earthquake effect and the level of damage/loss of either one of the previously mentioned categories.

Fragility curves are a statistical tool, often constituted by a lognormal function, representing the probability of exceeding a given damage state (or performance) as a function of an engineering demand parameter (EDP). The EDP is a parameter that represents the demand on the structure or infrastructure, in terms of displacements in foundation (Fotopoulou *et al.*, 2018), seismic excitation at the base (Kircher and McCann, 1983) or, in case of liquefaction phenomena, liquefaction indicators (Baris *et al.*, 2020). Seismic Vulnerability analysis will be presented and examined in detail in Chapter 3.

1.3.3 Exposure

Risk exposure is the measure of potential future loss resulting from a specific activity or event. The first step in a risk exposure analysis is the definition of the element at risk. The elements at risk can be animate or inanimate. The firsts are humans and animals and their exposure is evaluated in terms of casualties and injured. The non-living risk elements are constituted by critical infrastructures, buildings and infrastructures. Furthermore, economic losses are a consequence of risk exposure, they can be direct or indirect.

There are different methodologies to estimate the number of casualties produced by an earthquake. One of the most popular is the one defined in HAZUS (FEMA, 2003): injuries are categorized into four different severity levels, from a slight (level #1) requiring paramedical assistance to instantaneous death (level #4). The code considers 36 different building types and for each of them, a given earthquake scenario defines four possible damage states depending on the building's vulnerability. The key point

Seismic Risk assessment:
Overall Approach and Framework of Methodology

for the calculation is the probability of injury level associated to the building damage, given in a series of tables.

Critical Infrastructures (CI) are the organizations delivering goods and services that are fundamental to the functioning of society. A potential list of CIs is proposed in Table 1.2 summarizing Murray and Grubestic (2007) and Macaulay (2009). A unique definition of the losses for all critical infrastructure is impossible as it depends on the type of infrastructure and its societal role. Broadly, the following categories of losses can be distinguished:

- direct social losses deriving from casualties;
- direct economic losses connected with the repair/replacement of the damaged component of the infrastructure;
- indirect economic losses connected with the shortage of supply (e.g. displaced households due to loss of housing habitability and short-term shelter needs, lack of service for users, reduced income for a company);
- indirect long-term economic losses connected with the reduced value of the critical infrastructure (e.g. the reduced value of building stocks located in a highly valuable area of the city, the loss of market share for a company).

The relative weight of each loss category cannot be uniquely defined as it depends on the relevance of the infrastructure function for the life of people and the adaptive capability of the critical infrastructure.

Table 1.2 - List of critical infrastructures.

Murray and Grubestic (2007)	Macaulay (2009)
National Monuments and Icons	Bank and finance
Nuclear Power Plants	Energy
Dams	Information and communication
Government Facilities	Transportation
Key Commercial Assets	Safety and security
-	Health service
-	Water supply
-	Government
-	Manufacturing
-	Food supply

Buildings affected by earthquakes and in particular by liquefaction undergo structural and non-structural repair costs caused by damage to the structural and non-structural components, damage of building contents and business inventory. The

restriction of the building's ability to function properly represents another (indirect) relevant source of losses. Direct and indirect losses of buildings are subdivided into the following categories:

- Casualties;
- Repair/replacement costs;
- Content losses;
- Inventory losses;
- Indirect economic losses for temporary housing (shelter).

An appropriate cost-benefit analysis of mitigation should consider that while the budget for countermeasures is sustained in a relatively short time, the advantage is spread over the entire lifecycle of the system (whether a structure, an infrastructure, a lifeline etc.). Hence expenses and saved repair costs must be expressed on an annual basis to become comparable. There are different criteria to compute the annualized cost of mitigation, one of the most adopted is to equally distribute the invested capital over the lifecycle of the structure adding the interest rate (fixed or variable). The question can be seen as equivalent to borrowing the capital necessary for mitigation from a bank at a fixed rate mortgage and paying it back with a constant annual amount. In this way the annualized cost sustained for mitigation is the amount paid by the borrower every year that ensures that the loan is paid off, in full of interest, at the end of its term. The annual payment can be computed with the following formula:

$$AC = C \cdot (1 + MR)^n \frac{MR}{(1+MR)^n - 1} \quad (1.3)$$

where AC is the annual cost sustained by the investor, C is the capital necessary to cover the expenses of mitigation, MR is the fixed mortgage rate, n is the lifecycle length expressed in years. This cost should be compared with the annualized benefit, i.e. the earthquake losses saved per year.

1.4 Scale and Resolution of Risk Studies

A key issue in risk studies is the choice of an appropriate scale for the analysis. Seismic hazard analyses are conducted at different scales (i.e., global, regional, local...) because the purpose of these studies is to characterize the seismic input present on the investigated area, whether populated or not. On the other hand, risk analyses have the mission of investigating not only the hazard, but also the exposure and vulnerability. This consideration implies that the extent of the risk analysis is strongly

Seismic Risk assessment:
Overall Approach and Framework of Methodology

related to the presence of vulnerable physical elements exposed to seismic input; this means that earthquake risk studies are restricted to those areas where physical assets are located, i.e. buildings and infrastructure components, and people are living. The minimum scale to perform an earthquake loss estimation (ELE) analysis is constituted by the single physical entity up to extending to an entire urban aggregate, a city or a region (or country). The transition from one scale to another does not only involve a modification in terms of geographic and geometric extension, but also an alteration of the used database, a different accuracy in the performing of the analysis and a change in the accepted level of uncertainty (Figure 1.5; Lang, 2012). The scale of the study is directly related to the needed resolution and level of detail of the end results. Needless to say the highest level of resolution would be to consider individual buildings and to predict damage for each and every building available.

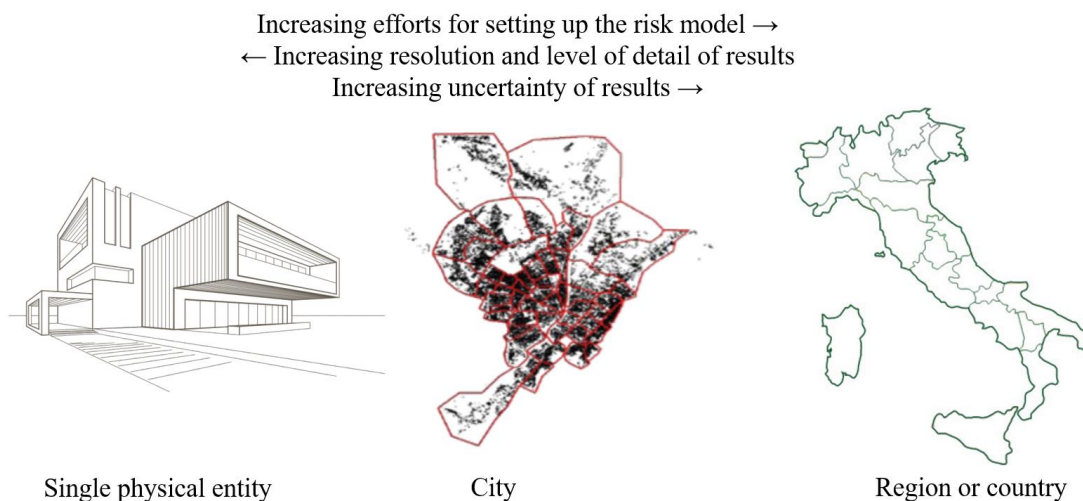


Figure 1.5 - Different levels of the study area's size. The extent of the study area affects the study's resolution and efforts to make (adapted after Lang, 2012).

Most ELE studies consider the minimum geographical unit (i.e., geounit, census tract) as the smallest area unit. The spatial extent of these geounits depends on different variables such as soil conditions, constant surface topography or level of building quality within the demarcated area (socio-economic aspects). In most cases, geounits are related to building blocks or to smaller city districts and damage and loss computations are conducted for aggregated data within each unit. Lang and Aldea (2011) remarks how the size of the geounits affect the study's resolution and level of effort required (Figure 1.6). Basically, three levels of resolution are defined: high, medium and coarse. The higher expected resolution takes place when geounits are

Seismic Risk assessment:
Overall Approach and Framework of Methodology

represented by building blocks; the medium one is attributable to the geounits constituted by city districts and the coarse resolution occurs when the size of geounits is enlarged to entire city sectors. Increasing numbers of geounits, and thus resolution, leads to an increase of efforts for setting up the risk model and of the detail of results, resulting in a reduction of uncertainties. In a practical situation, the size of the study area will be governed by the respective geographical conditions and how large the area of interest is. The resolution of the study and its results will however be decided by the level of detail of available inventory data or how much effort one is willing to spend while generating an inventory database. The resolution will further depend on the study's initial purpose and the end users of the derived results (strengthening and mitigation studies, emergency response, insurance).

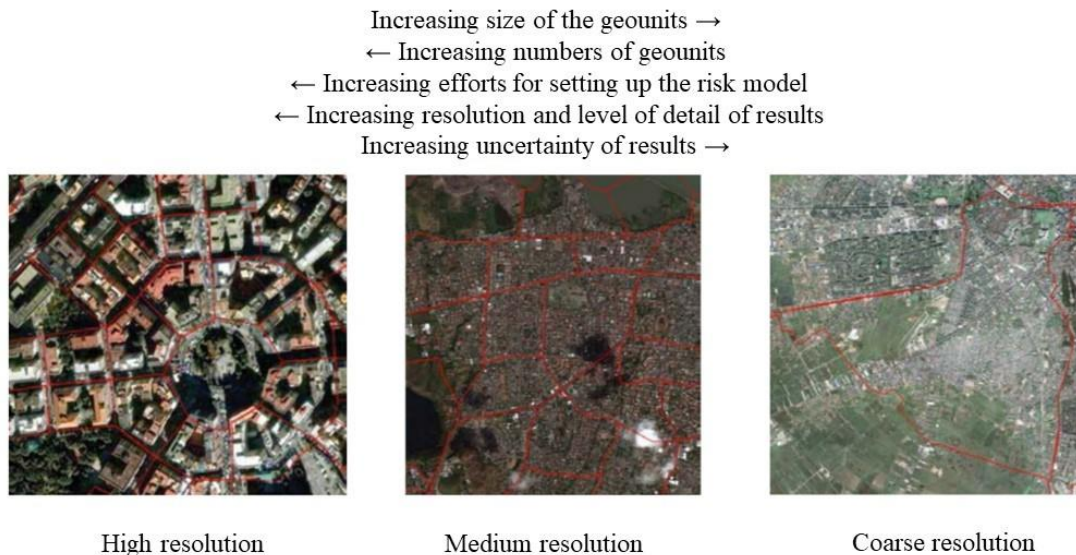


Figure 1.6 - Different ways to demarcate the geographical units (geounits). The size of the geounits affect the study's resolution and level of effort required (adapted from Lang and Aldea, 2011).

Chapter 2. SEISMIC LIQUEFACTION: PHENOMENON AND HAZARD ASSESSMENT

The term liquefaction was originally coined by Mogami and Kubo (1953) to indicate the manifestations of a complex phenomenon affecting loose, saturated, and cohesionless soils under seismic conditions. Liquefaction is a phenomenon wherein the shear resistance of soil decreases when subjected to monotonic, cyclic, or dynamic loading at constant volume and occurs in saturated sands, silts and quick clays; such soils typically have no to low plasticity, and low to moderate permeability. When liquefaction occurs, the mass tends towards the steady state of deformation in an essentially undrained condition. One of the most popular classifications (Kramer, 1996) groups liquefaction-related phenomena into two categories: flow liquefaction and cyclic mobility.

Flow failure occurs when the static shear stresses on sloping ground exceed the frictional shear strength of the soil deteriorated by the pore pressure build-up. The cyclic stress may bring the soil to an unstable state at which its strength drops sufficiently to allow the static stress to determine flow failure. Flow liquefaction is characterized by a sudden nature of the origin, the velocity of their development and the distance interested by such instability; displacements, in this case, can be very large, in the order of tens of metres or even more, and may disrupt buildings and infrastructure over wide areas.

In contrast, cyclic mobility occurs when the shear stress required for the static equilibrium is smaller than the shear stress of the soil in its liquefied state (e.g., gentle slopes). The deformation produced by cyclic mobility develops incrementally under the seismic load, driven by both cyclic and static shear stresses, causing lateral spreading, which is defined as the horizontal displacement of a soil layer riding on liquefied soil either down a gentle slope or toward a free face like a river channel

(Youd, 2018). In this case, when the underlying soil layer liquefies, the non-liquefied upper soil crust continues moving down until it reaches a new equilibrium position. Level ground liquefaction represents a special case of cyclic mobility, characterized by the absence of static shear stress capable of producing lateral deformation. Therefore, what happens during an earthquake is a chaotic movement of soil particles known as ground oscillation.

Seismic-induced liquefaction in sandy soil is the subject of the following research. From a mechanical viewpoint, this phenomenon determines a new grain asset caused by the upward flowing porewater generated by a rapid porewater pressure build-up during strong earthquakes, say having a $PGA \geq 0.15g$ and a Richter magnitude greater than 5.5 (NTC, 2018). These assumptions reflect both the laboratory tests of Seed *et al.* (1975) relating the equivalent number of cycles to the earthquake magnitude, and the empirical observations of Ambraseyes (1988) that correlated the epicentral distance to the earthquake magnitude for sites where liquefaction happened and did not. At the ground surface, the consequences of this mechanism are conical deposits of sand called sand boils and subsidence that can lead to low-moderate liquefaction-induced surficial damage, significant soil deformations, both horizontal (cracking) and vertical (settlements) capable of provoking severe damage to a variety of structures and infrastructures and lateral spreading.

The relevance of seismic-induced liquefaction over Europe is evident from the study carried out within the Work Package 2 (Deliverable D2.4 of LiquefACT Project) that counts 920 recorded cases of liquefaction induced by 196 earthquakes. Figure 2.1 reporting the GIS-based catalogue of historical occurrences shows that liquefaction is spread all over the seismic portion of the European territory practically with no exceptions. Fourteen countries are involved in total, with an obviously greater frequency for the most seismic regions, primarily Italy, Greece and Turkey, but with examples recorded also in the other countries.

However, the fact that soil is susceptible to liquefaction does not guarantee that liquefaction will occur during an earthquake event. It is also recognized that the stress conditions (confining pressure, cyclic shear and initial static shear stresses) play an important role in the liquefaction behaviour of soil, the type of failure mechanism and the mode of development of soil deformation, especially in the case of slopes of sandy deposits.

Bird *et al.* (2006) and NZGS (2016) summarize a simplified liquefaction risk assessment procedure as follows:

Seismic Liquefaction:
phenomenon and hazard assessment

1. definition of site characterization and seismic hazard evaluation;
2. evaluation of liquefaction susceptibility: it is a physical characteristic of soil that determines if it is able to liquefy or not, it is based solely on ground conditions with no earthquake-specific information;
3. definition of liquefaction triggering: liquefaction is triggered in soil when the seismic demand exceeds the resistance of the soil;
4. liquefaction-induced ground deformation: the scale of liquefaction can be predicted as a permanent ground deformation;
5. evaluation of effects of liquefaction on structures: it's important to develop an understanding of the correlation between liquefaction risk and physical damage to the built environment, similar to the fragility functions that are used to predict damage associated with ground shaking;
6. liquefaction mitigation.

Boulanger & Idriss (2014) remark the two main attributes of liquefaction analysis procedure:

1. The liquefaction analysis procedure applies to the full range of conditions important to practice; e.g., shallow lateral spreads, settlement of structures, stability failures or deformations in levees or earth dams. Practice often results in the need to extrapolate outside the range of the case history experiences, requiring the framework to be supported by sound experimental and theoretical bases for guiding such extrapolations.
2. The functional relationships used to describe fundamental aspects of soil behaviour and site response are consistent with those used in developing companion correlations for the other in-situ tests; e.g., SPT blow count, CPT penetration resistance, and shear wave velocity, V_s . Consistency in these functional relationships facilitates the logical integration of information from multiple sources and provides a rational basis for the calibration of constitutive models for use in nonlinear dynamic analyses.

Seismic Liquefaction: phenomenon and hazard assessment

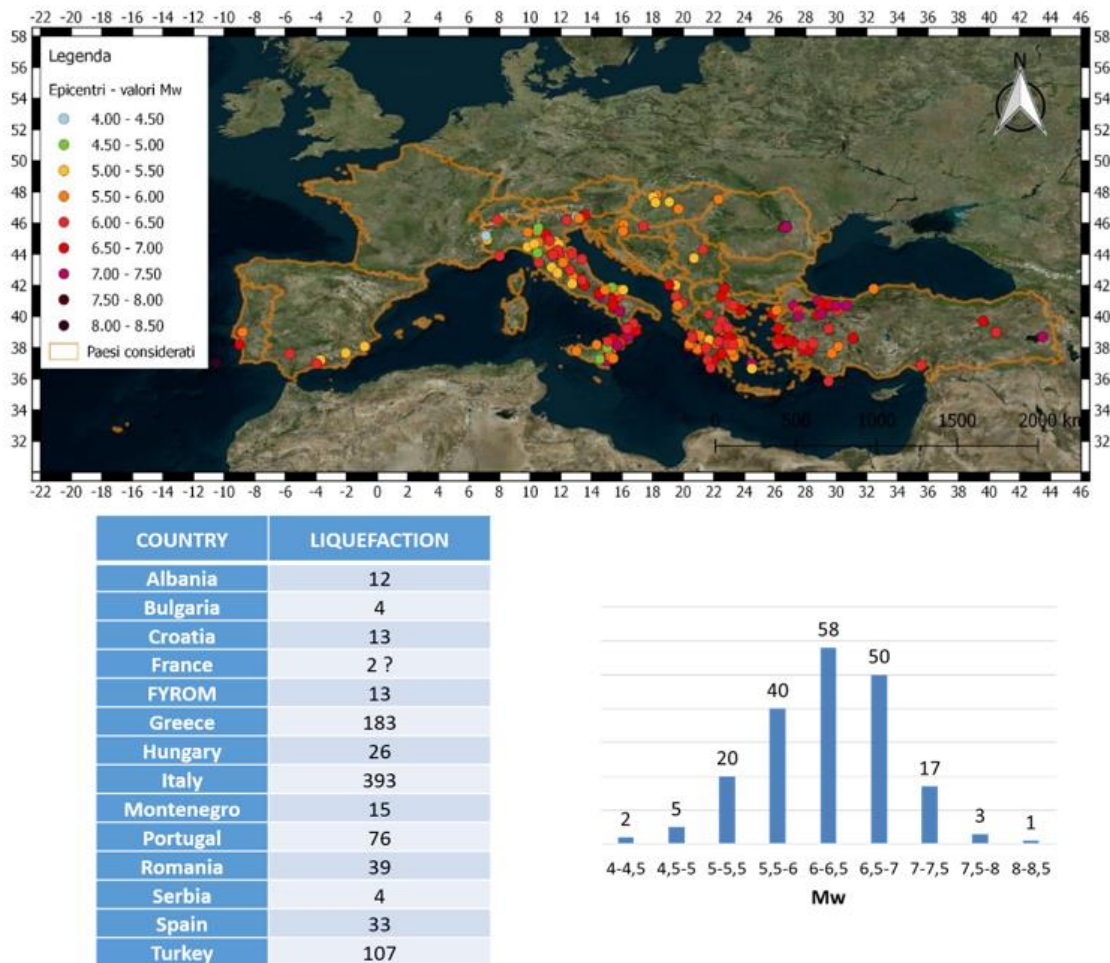


Figure 2.1 - Liquefaction evidences over Europe (extracted from the deliverable D2.4 of LiquefACT Project).

2.1 Susceptibility

A prodromic step for liquefaction hazard assessment consists ascertaining of the susceptibility, that is the proneness of subsoil to undergo liquefaction based on historical observation, earthquake magnitude, soil composition and groundwater table position, without introducing a specific seismic scenario. The evaluation of susceptibility is mainly carried out on two scales: the geological and the geotechnical level.

2.1.1 Geological factors controlling liquefaction susceptibility

At the geological level, liquefaction susceptibility is commonly pursued by characterizing larger portions of territory and collecting available historical and geological data, proving that liquefaction-induced phenomena are not randomly localized but are tightly related to the geology of the territory.

Youd and Hoose (1978) identify the environment of deposition, age of the deposit, water table depth and depth of burial as the main geologic and hydrologic factors that control liquefaction susceptibility. In particular, the most common deposits affected by liquefaction are in the fluvial environment, but also Deltaic, Colluvial eolian sand deposits and, more rarely, alluvial-fan, alluvial-plain, beach, terrace and estuarine undergo liquefaction. Glacial till and laterite deposits appear immune. Thus, the degree of sorting, amount of compaction during sedimentation and grain-size class are major factors controlling the phenomenon. Since it is ascertained that the liquefaction resistance increases with the soil aging (Schmertman, 1991), due to the cementing and compaction by natural processes, the most disturbed deposits by liquefaction are attributable to the Holocene era.

Water table position and depth of burial strongly condition the susceptibility: a water table near or within a few meters of ground surface increases the proneness to liquefaction and most episodes commonly occur at a relatively shallow depth of burial (less than 20m). These results are justified by the increase of overburden pressure and in sediment compactness with depth.

These findings are summarized in the qualitative subsoil classification introduced by Youd and Perkins (1978) and presented in Table 2.1.

Given these considerations, the preparatory step for the susceptibility assessment is the contemplation of geomorphological and surface geological maps since they describe the geomorphology of the area, highlighting the presence of sandy and silty lithologies and relevant geomorphological elements such as rivers, meanders, levees/paleo-levees, and paleochannels. Furthermore, information about the land use, thickness of human-made deposits and the existing survey maps may help understand the urban development of the study area and reconstruct the subsoil profiles. In Europe, a map of the potentially liquefiable lithologies shows a wide and heterogeneous distribution of liquefaction susceptibility over the continent, which characterizes the

Seismic Liquefaction:
phenomenon and hazard assessment

Iberian Peninsula, Italy, Balkan region, Greece, Turkey, and also part of the Baltic area, as confirmed by the historical observation reported in Figure 2.1.

The assessment of susceptibility at a geological level is not sufficient because it considers large areas, providing a regional scale evaluation and not a punctual analysis.

Table 2.1 - Liquefaction susceptibility of sedimentary deposits (Youd and Perkins, 1978).

Type of Deposit	General Distribution of Cohesionless Sediments in Deposits	Likelihood that Cohesionless Sediments when Saturated would be Susceptible to Liquefaction (by Age of Deposit)			
		< 500 yr Modern	Holocene < 11 ka	Pleistocene 11 ka - 2 Ma	Pre-Pleistocene > 2 Ma
(a) Continental Deposits					
River channel	Locally variable	Very High	High	Low	Very Low
Flood plain	Locally variable	High	Moderate	Low	Very Low
Alluvial fan and plain	Widespread	Moderate	Low	Low	Very Low
Marine terraces and plains	Widespread	---	Low	Very Low	Very Low
Delta and fan-delta	Widespread	High	Moderate	Low	Very Low
Lacustrine and playa	Variable	High	Moderate	Low	Very Low
Colluvium	Variable	High	Moderate	Low	Very Low
Talus	Widespread	Low	Low	Very Low	Very Low
Dunes	Widespread	High	Moderate	Low	Very Low
Loess	Variable	High	High	High	Unknown
Glacial till	Variable	Low	Low	Very Low	Very Low
Tuff	Rare	Low	Low	Very Low	Very Low
Tephra	Widespread	High	High	?	?
Residual soils	Rare	Low	Low	Very Low	Very Low
Sebka	Locally variable	High	Moderate	Low	Very Low
(b) Coastal Zone					
Delta	Widespread	Very High	High	Low	Very Low
Estuarine	Locally variable	High	Moderate	Low	Very Low
Beach					
High Wave Energy	Widespread	Moderate	Low	Very Low	Very Low
Low Wave Energy	Widespread	High	Moderate	Low	Very Low
Lagoonal	Locally variable	High	Moderate	Low	Very Low
Fore shore	Locally variable	High	Moderate	Low	Very Low
(c) Artificial					
Uncompacted Fill	Variable	Very High	---	---	---
Compacted Fill	Variable	Low	---	---	---

2.1.2 Geotechnical factors controlling liquefaction susceptibility

Portions of territory liquefiable at the geological scale need further analysis to identify areas prone to local instability and to quantify their susceptibility.

In 1982, the *Chinese criteria* were proposed by Seed and Idriss. These criteria are a function of percent clay (less than 15% by weight of particles < 0.005 mm), liquid limit ($LL < 35\%$), and with an in-situ water content greater than 0.9 multiplied by the LL.

With the aim of a more refined susceptibility assessment, carrying out more investigations at a more detailed scale allow for determining the co-existence of paramount factors influencing the properness for the liquefaction phenomenon (i.e., grain size distribution, plasticity, and water level) as well as to build a 3D stratigraphic model. In this case, quantitative criteria are required to identify areas prone to local instability. This implies the realization of geological and geotechnical models aimed at identifying source layers for liquefaction as much as the definition of zones having homogeneous stratigraphy, to evaluate the local site effects on ground motion. A geotechnical model must be defined based on topography (DEM, DTM), monitoring activities (piezometers, wells), in-situ geotechnical (e.g., Boreholes, SPT, CPT) and geophysical investigations (MASW, Cross-hole, Down-Hole, HVSR...) and laboratory tests. The availability of in situ and laboratory tests allows the development of increasingly detailed methods for the susceptibility assessment to seismic liquefaction. The University of Ferrara, in conjunction with the Group for the seismic microzonation of S. Agostino (FE), from the back-analysis of the 2012 earthquake in Emilia-Romagna, proposed a criterion for defining the level of susceptibility based on the thickness and depth of the liquefiable layer and crustal layer. In particular, five susceptibility levels are defined, summarized in the matrix shown in Table 2.2, level *LI* is the maximum and *N* stands for *null*.

At the geotechnical scale, the classification of susceptibility level passes by investigation of thickness, depth and strength of potentially liquefiable layers, granulometric distribution, groundwater depth modelling. This information can be extrapolated by in-situ and laboratory tests directly or indirectly.

Seismic Liquefaction:
phenomenon and hazard assessment

Table 2.2 - Level of liquefaction susceptibility defined at the scale of in-situ test ("CMS"- University of Ferrara, 2014).

Crust Thickness (m)	Thickness of liquefiable layer (m)	Susceptibility level
<5	>0.4	L1
5-10	>1	L2
10-15	>2	L3
15-20	≥2	L4
>20	0	N

Boreholes provide a direct stratigraphic recognition, but are rarely available all over the investigated area. Instead, CPTs cannot be expected to provide accurate predictions of soil type based on physical characteristics, such as grain size distribution, but offer a guide to the mechanical characteristics (strength, stiffness, compressibility) of the soil, attributable to several soil typologies.

Among the wide range of applications of CPT profiles, Robertson and Wride (1998) proposed a widely applicable criterion that combines the measured tip resistance and sleeve friction to the in-situ tensional state, providing a repeatable index of the aggregate soil behaviour, identifying nine zones (Figure 2.2a). Hence, the approximate boundaries of soil behaviour types are given in terms of the SBTn index, I_c , defined by Robertson (1986, 1990, 1998, 2010a, 2015). I_c is the radius of the essentially concentric circles that represent the boundaries between each SBTn zone. The soil behaviour type index does not apply to zones 1, 8 and 9 (obtainable in any case through normalized measured tip resistance and sleeve friction).

I_c can be defined as follows and obtained using the procedure depicted in Figure 2.2b:

$$I_c = ((3.47 - \log Q_t)^2 + (\log Fr + 1.22)^2)^{0.5} \quad (2.1)$$

Where:

$$Q_t = \text{normalized cone penetration resistance (dimensionless)} = (q_t - \sigma_{v0}) / \sigma'_{v0}$$

$$Fr = \text{normalized friction ratio, in \%} = \left(\frac{f_s}{q_t - \sigma_{v0}} \right) * 100\%$$

Seismic Liquefaction:
phenomenon and hazard assessment

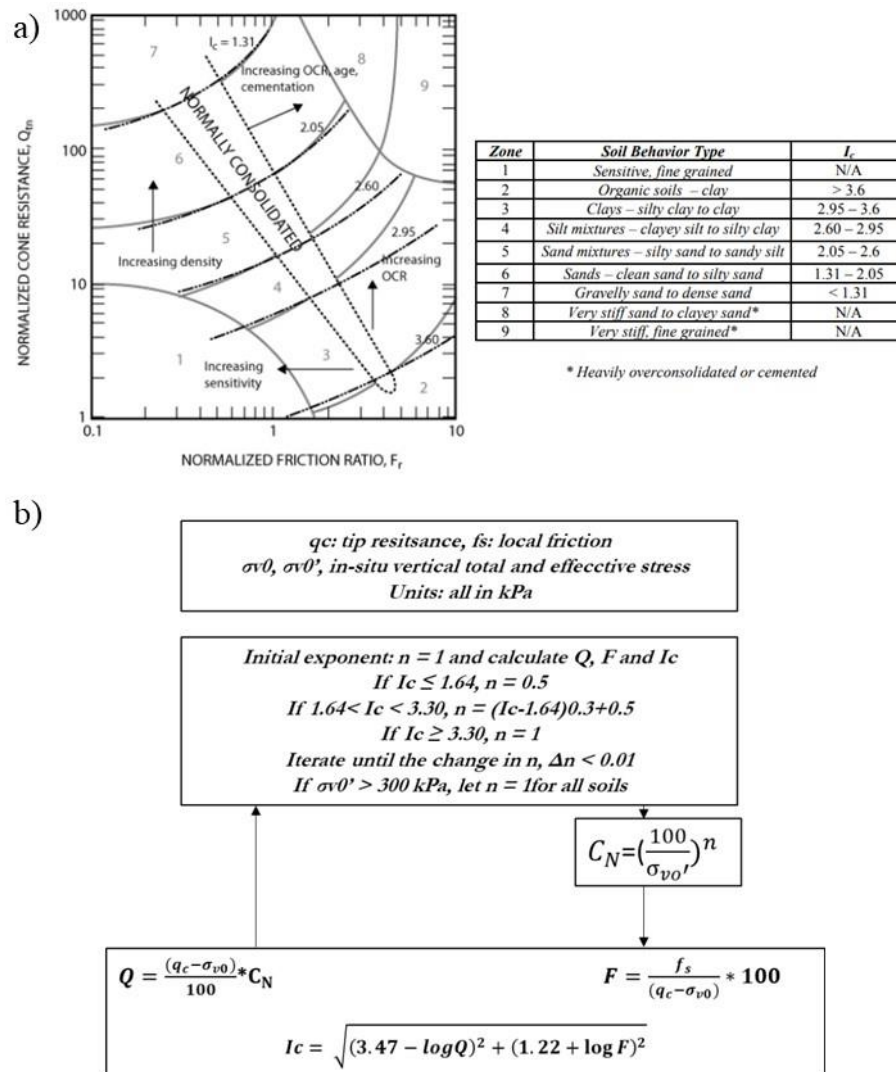


Figure 2.2 - (a) Normalized CPT Soil Behavior Type (SBTn) chart, $Q_t - F_r$ (Robertson, 1990, updated by Robertson, 2010 and 2015); (b) Schematic flowchart to evaluate the Soil Behaviour Type index (Robertson, 1998).

Classes 5 and 6 are qualitatively attributable to liquefiable soil. Accounting for the groundwater level, the non-liquefiable crust thickness and the cumulative thickness of the potentially liquefiable layers (i.e., as the summation of all the layers in Robertson SBT equal to 5 and 6), the previously presented criterion to assess the level of susceptibility can be applied. Unfortunately, this procedure is lithology based and does not consider the mechanical properties of soil.

Millen *et al.* (2020) propose the criterion of the Equivalent Soil Profile ESP, identified by the thickness of the crust and liquefiable layer and a mean Cyclic Resistance Ratio (CRR), then it introduces the mechanical properties of the soil into the susceptibility assessment. The procedure, articulated in four steps, is briefly

Seismic Liquefaction: phenomenon and hazard assessment

described in Figure 2.3 and defines 22 equivalent soil classes, finding the best combination of H_{crust} , H_{liq} , and C .

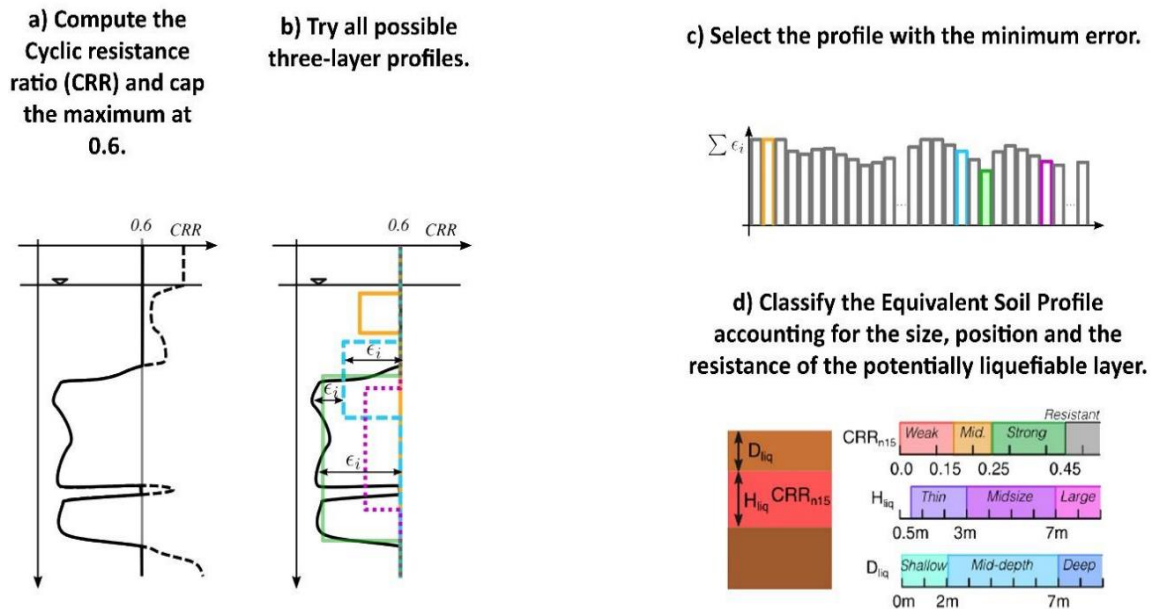


Figure 2.3 - Scheme of the procedure to implement the CRR-fitted method and equivalent soil profile classification criteria.

Italian NTC18 suggests omitting the liquefaction assessment when at least one of the following conditions is stated:

- maximum accelerations expected at ground level in free field conditions less than $0.1g$;
- average seasonal depth of the aquifer greater than 15 m from ground level, for sub-horizontal ground level and structures with superficial foundations;
- deposits consisting of clean sands with normalized resistance $(N_1)_{60} > 30$ or $q_{c1N} > 180$, where $(N_1)_{60}$ is the normalized resistance value determined in dynamic penetration tests (Standard Penetration Test) and q_{c1N} is the normalized resistance value determined in static penetrometer tests (Cone Penetration Test);
- granulometric distribution outside the areas indicated in Fig. 7.11.1(a) of NTC18 in the case of soils with uniformity coefficient $Uc < 3.5$ and in Fig. 7.11.1(b) of NTC18 in the case of soils with $Uc > 3.5$.

In conclusion, ascertaining the geological proneness to liquefaction, a next level of investigation is requested. At the geotechnical scale, five main factors must be

inspected and defined: granulometric classification (or stratigraphic recognition), burial depth, relative density, fine content and depth of the water table. In a nutshell, a soil layer is susceptible to liquefaction if constituted of loose sand, from clean to silty, deposited in the first 20 m of depth and saturated. This conclusion can be pursued by following the procedures and considerations listed in paragraphs 2.1.1 and 2.1.2 herein presented.

2.2 Triggering

The subsoil susceptibility is not a guarantee of liquefaction under seismic events. The next step in the liquefaction hazard assessment procedure consists of the evaluation of the factor of safety (FS_L) against liquefaction for a given seismic hazard or a deterministic earthquake scenario. This approach for liquefaction triggering, named the stress-based approach, initiated by Seed and Idriss (1967), compares the cyclic resistance ratios (CRR) of the soil with the earthquake-induced cyclic stress ratios (CSR) and their ratio is the FS_L .

Following this approach, liquefaction is triggered at a given depth if FS_L is found less than 1.

$$FS_L(z) = \frac{CRR(z)}{CSR(z)} \quad (2.2)$$

This comparison was made possible thanks to the application of a standardized procedure according to the theory of Idriss and Boulanger (2014).

The earthquake-induced CSR , at a given depth, z , within the soil profile, is usually expressed as a representative value (or equivalent uniform value) equal to 65% of the maximum cyclic shear stress ratio, i.e.:

$$CSR_{M,\sigma'v} = 0.65 \frac{\tau_{max}}{\sigma'v} \quad (2.3)$$

where τ_{max} is the maximum earthquake induced shear stress, $\sigma'v$ is the vertical effective stress, and the subscripts on the CSR indicate that it is computed for a specific earthquake magnitude (moment magnitude, M) and in-situ $\sigma'v$.

The factor 0.65 was selected by Seed and Idriss (1967) and represents the reference stress level.

A simplified method to estimate the *CSR* profile was developed by Seed and Idriss (1971) based on the maximum ground surface acceleration (*a max*) at the site. An update of this simplified approach is described in detail elsewhere (Youd and Idriss, 1997).

$$CSR_{M,\sigma v} = 0.65 \frac{a \max}{g} \frac{\sigma v}{\sigma v'} rd \quad (2.4)$$

Where *a max* is the maximum horizontal acceleration at the ground surface; $g = 9.81 \text{ m/s}^2$ is the gravity acceleration; σv and $\sigma v'$ are the total and effective vertical overburden stresses, respectively; *rd* is a stress-reduction factor dependent on depth that accounts for the dynamic response of the soil profile. Evaluation of stress-reduction factor, *rd*, according to Idriss (1999), in extending the work of Golesorkhi (1989):

$$rd = \exp(\alpha(z) + \beta(z) * M) \quad (2.5)$$

$$\alpha(z) = -1.012 - 1.126 \sin\left(\frac{z}{11.73} + 5.133\right) \quad (2.6)$$

$$\beta(z) = 0.106 + 0.118 \sin\left(\frac{z}{11.28} + 5.142\right) \quad (2.7)$$

On the other hand, the *CRR* represents the cyclic resistance ratio and was correlated to CPT and SPT penetration resistances after application of procedural and overburden stress corrections. The *CRR* of sand increases with increasing relative density (*Dr*), it also depends on the effective confining stress, which reflects the fact that the tendency of sand to dilate or contract depends on confining stress. *CRR* evaluation procedures are summarized in Figure 2.4a for SPTs-based-approach (Idriss and Boulanger 2008, 2010) and in Figure 2.4b for the CPTs-based procedure (Boulanger and Idriss, 2014).

The cyclic resistance ratio of soils is strictly related to the soil fine content (*FC*), this dependence is widely investigated and detailed presented in Boulanger and Idriss (2014). The soil's *CRR* is also dependent on the duration of shaking and effective overburden stress. The correlation for *CRR* is therefore developed by adjusting the case history *CSR* values to a reference $M = 7.5$ and $\sigma'v = 1 \text{ atm}$ as:

$$CSR_{M=7.5,\sigma'v=1} = \frac{CSR_{M,\sigma v}}{MSF * K_{\sigma}} \quad (2.8)$$

The MSF is used to account for duration effects (i.e., number and relative amplitudes of loading cycles) on the triggering of liquefaction, the MSF for sands used by Idriss and Boulanger (2008) was developed by Idriss (1999), who derived the following relationship:

$$MSF = 6.9 \exp\left(-\frac{M}{4}\right) - 0.058 \leq 1.8 \quad (2.9)$$

The K_σ relationship used was developed by Boulanger (2003b) and expresses the dependence on effective overburden stress:

$$K_\sigma = 1 - C_\sigma \ln\left(\frac{\sigma'v}{Pa}\right) \leq 1.1 \quad (2.10)$$

the coefficient C_σ can be limited to its maximum value of 0.3 and is a function of the normalized cone tip resistance or the normalized number of blows count.

The equation that is obtained to calculate the value of the CSR by applying the corrections MSF and K, is as follows:

$$CSR_{M=7.5, \sigma'v=1} = \frac{0.65 \frac{a \max \sigma v}{g} rd}{MSF * K_\sigma} \quad (2.11)$$

Alternatively, Andrus and Stokoe (2000) propose a method for calculating CRR that requires shear-wave velocity, v_s (Figure 2.5). When using liquefaction triggering methods based on v_s values to calculate the earthquake-induced CSR (e.g., Andrus and Stokoe, 2000; Cetin *et al.*, 2004), v_s should be measured directly and not estimated by correlations with the SPT or the CPT. v_s measurements are economical and non-invasive.

In conclusion, the stress-based liquefaction analysis framework for cohesionless soil includes the evaluation of the factor of safety (FS_L), which comprises four functions that describe fundamental aspects of dynamic site response, penetration resistance, and soil characteristics and behaviour. These four functions, along with the major factors affecting each, are:

- $rd = f(\text{depth; earthquake and ground motion characteristics; dynamic soil properties});$
- $CN = f(\sigma'v; Dr; FC);$
- $K_\sigma = f(\sigma'v; Dr; FC);$

Seismic Liquefaction:
phenomenon and hazard assessment

- $MSF = f(\text{earthquake and ground motion characteristics; } Dr; FC)$.

Triggering and susceptibility analysis investigating the subsoil proneness and resistance against the phenomenon, neglecting the assessment of liquefaction-induced surficial manifestations in free-field conditions.

a)

$(N_1)_{60} = C_N \cdot N_{60}$ $C_N = \left(\frac{pa}{\sigma'_v}\right)^m \leq 1.7$ $m = 0.784 - 0.0768 \cdot \sqrt{(N_1)_{60cs}}$
<p>Fine Content evaluation (FC)</p> $Fc = 80 \cdot (Ic + C_{FC}) - 137$ $C_{FC} = -0.29, 0, +0.29$ <p>CFC is a fitting parameter, while Ic is evaluated according to Mayne (2006)</p> $Ic = -0.7174 \cdot \ln\left(\frac{Vs^2}{9.81 \cdot z}\right) + 6.3211$ $Vs = 100.59 \cdot N_{SPT}^{0.302}$ <p>Modified after Palmer and Stuart (1957)</p>
$\Delta(N_1)_{60} = \exp\left(1.63 + \frac{9.7}{Fc + 0.01} - \left(\frac{15.7}{Fc + 0.01}\right)^2\right)$ $(N_1)_{60cs} = (N_1)_{60} + \Delta(N_1)_{60}$
$CRR = \exp\left(\frac{(N_1)_{60cs}}{14.1} + \left(\frac{(N_1)_{60cs}}{126}\right)^2 - \left(\frac{(N_1)_{60cs}}{23.6}\right)^3 + \left(\frac{(N_1)_{60cs}}{25.4}\right)^4 - 2.8\right)$

$$CSR = 0.65 \cdot \left(\frac{a_{max}}{g}\right) \cdot \left(\frac{\sigma_v}{\sigma'_v}\right) \cdot rd \cdot \left(\frac{1}{MSF}\right) \cdot \left(\frac{1}{K\sigma}\right)$$

$$\ln(rd) = \alpha + \beta M$$

$$\alpha = -1.012 - 1.126 \operatorname{sen}\left(\frac{z}{11.73} + 5.133\right)$$

$$\beta = 0.106 - 0.118 \operatorname{sen}\left(\frac{z}{11.28} + 5.142\right)$$

$$K\sigma = 1 - C\sigma \ln\left(\frac{\sigma'_v}{pa}\right) \leq 1.1$$

$$C\sigma = \frac{1}{18.9 - 2.55 \cdot (N_1)_{60cs}^{0.5}} \leq 0.3$$

$$MSF = 6.9 \exp\left(-\frac{M}{4}\right) - 0.058$$

Idriss and Boulanger (2008)

$$FSL = \frac{CRR}{CSR}$$

b)

$q_{c1} = C_N \cdot q_c$ $q_{c1N} = q_{c1}/pa$ $C_N = \left(\frac{pa}{\sigma'_v}\right)^m \leq 1.7$ $m = 1.338 - 0.249 \cdot (q_{c1N})^{0.264}$ <p>Pa = atmospheric pressure having same units as qc</p>
<p>Fine Content evaluation (FC)</p> $Fc = 80 \cdot (Ic + C_{FC}) - 137$ <p>Where: Ic is evaluated according to Robertson, 1998</p> $C_{FC} = -0.29, 0, +0.29$ <p>(where CFC is a fitting parameter that can be adjusted based on site-specific data when available)</p>
$\Delta q_{c1N} = \left(11.9 + \frac{q_{c1N}}{14.6}\right) \exp\left(1.63 - \frac{9.7}{Fc + 2} - \left(\frac{15.7}{Fc + 2}\right)^2\right)$ $(q_{c1N})_{CS} = q_{c1N} + \Delta q_{c1N}$
$CRR = \exp\left(\frac{q_{c1Ncs}}{113} + \left(\frac{q_{c1Ncs}}{1000}\right)^2 - \left(\frac{q_{c1Ncs}}{140}\right)^3 + \left(\frac{q_{c1Ncs}}{137}\right)^4 - 2.8\right)$

$$CSR = 0.65 \cdot \left(\frac{a_{max}}{g}\right) \cdot \left(\frac{\sigma_v}{\sigma'_v}\right) \cdot rd \cdot \left(\frac{1}{MSF}\right) \cdot \left(\frac{1}{K\sigma}\right)$$

$$\ln(rd) = \alpha + \beta M$$

$$\alpha = -1.012 - 1.126 \operatorname{sen}\left(\frac{z}{11.73} + 5.133\right)$$

$$\beta = 0.106 - 0.118 \operatorname{sen}\left(\frac{z}{11.28} + 5.142\right)$$

$$K\sigma = 1 - C\sigma \ln\left(\frac{\sigma'_v}{pa}\right) \leq 1.1$$

$$C\sigma = \frac{1}{37.3 - 8.27 \cdot q_{c1Ncs}^{0.264}} \leq 0.3$$

$$MSF = 6.9 \exp\left(-\frac{M}{4}\right) - 0.058$$

Idriss and Boulanger (2008)

$$FSL = \frac{CRR}{CSR}$$

Figure 2.4 - Flowchart of the Boulanger & Idriss (2008, 2010) SPT-based procedure for liquefaction triggering analysis.; Flowchart of the Boulanger & Idriss (2014) CPT-based procedure (b).

Seismic Liquefaction: phenomenon and hazard assessment

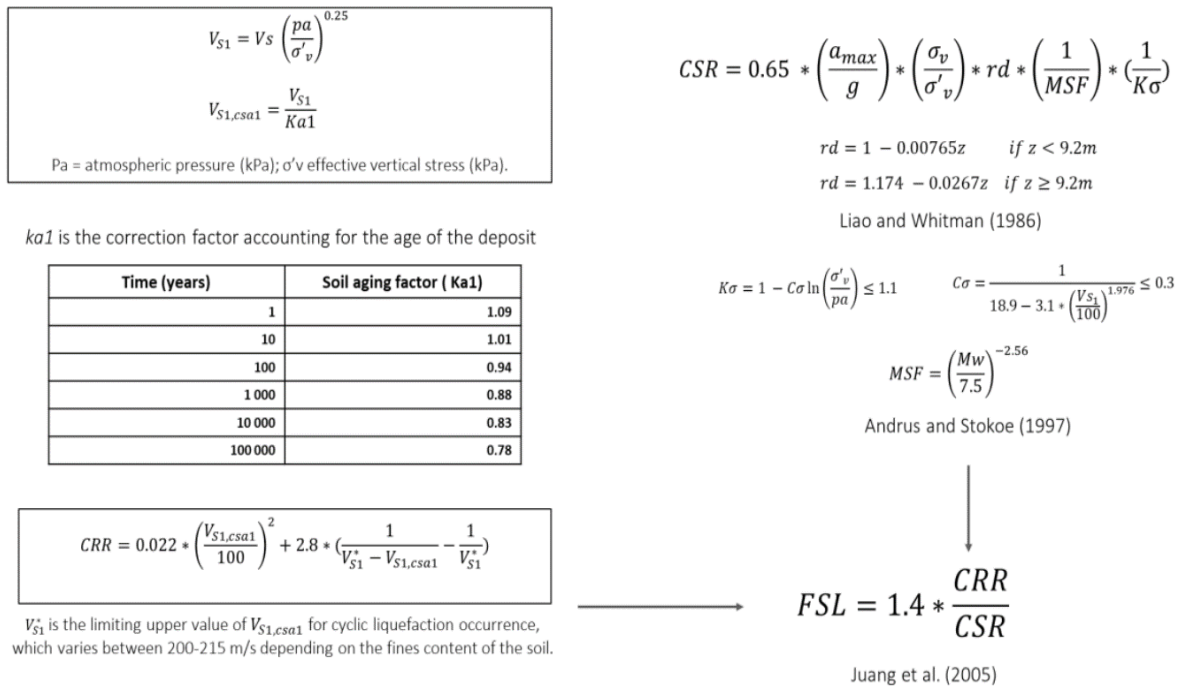


Figure 2.5 - Flowchart of the Andrus & Stokoe (2000) procedure for liquefaction triggering evaluation.

2.3 Liquefaction-induced surficial manifestations

Once the evaluation of liquefaction triggering is completed and triggering is predicted in the analysis, it is important to understand the potential effects of liquefaction that may occur at the site.

The possible effects due to the liquefaction phenomenon are listed below:

- Sand boils:

if the sand is saturated and there is no possibility for drainage, so that constant volume conditions are maintained, the primary cause of the shaking is the generation of excess pore water pressures. excess pore water is commonly dissipated by travelling upwards to the ground surface. The velocity of these flows may be sufficient to carry sand particles through cracks and channels. Sand boils are formed when these sand particles are ejected onto the ground surface;

Seismic Liquefaction:
phenomenon and hazard assessment



Figure 2.6 - Sand Boils from 2011 Christchurch, New Zealand Earthquake (Musson, 2011).

- Lateral spreading:
lateral spreading is the finite, lateral movement of gently to steeply sloping, saturated soil deposits caused by earthquake-induced liquefaction (Kramer, 2016).



Figure 2.7 - Effect of lateral spreading on the roadway after the 2011 earthquake series in Christchurch (New Zealand).

- Settlement:
sands tend to settle and densify when they are subjected to earthquake shaking. If the sand is saturated and there is no possibility for drainage, so that constant volume conditions are maintained, the primary cause of the shaking is the generation of excess pore water pressures. Settlement then occurs as the excess pore pressures dissipate. When post-liquefaction settlement occurs, buildings may sink, tilt, or even tip over.

Seismic Liquefaction:
phenomenon and hazard assessment

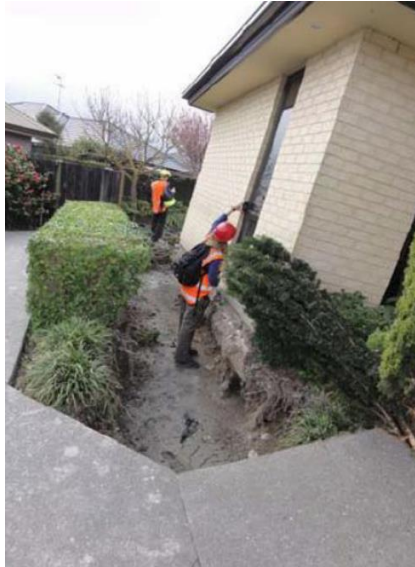


Figure 2.8 - Differential settlement on building (Taipei in Taiwan, 2010)

- Loss of bearing capacity:
liquefaction can also greatly reduce the shear strength of the liquefied soil, which will lead to the loss of bearing capacity;



Figure 2.9 - Loss of Bearing Capacity due to Soil Liquefaction from Niigata, Japan 1964 Earthquake (Niigata Earthquake, 1964).

Liquefaction-induced effects can cause significant damage to infrastructure. Understanding and correctly predicting these effects will improve engineers' ability to minimize damage resulting from liquefaction.

The huge impact caused by liquefaction during past earthquakes has raised the need for predictive formulas applicable at the large scale to forecast liquefaction-induced ground evidences in free-field conditions. To this aim, the geotechnical community has developed indicators of severity to liquefaction. These commonly used tools are computed as integral over fixed depths of a function of the factor of safety against liquefaction $f1(FS_L)$ weighted with a function of depth from the ground level $w(z)$, Eqn. 2.12.

$$INDEX = \int_{z_{min}}^{z_{max}} f1(FS_L) * w(z) dz \quad (2.12)$$

Table 2.3 reports a list of the most common indexes to predict liquefaction-induced surficial manifestations.

Table 2.3 - Liquefaction severity indexes proposed in literature

Index	Reference	$f1(FS_L)$	$w(z)$	z
LPI	Iwasaki <i>et al.</i> , 1978	$1 - FS_L$ if $FS_L < 1$ 0 if $FS_L \geq 1$	$10 - 0.5 * z$	$z_{min} = 0$ m $z_{max} = 20$ m
Wv	Zhang <i>et al.</i> , 2002	$\varepsilon_v = \varepsilon_v(FS_L, q_{c1Ncs})$	-	$z_{min} = 0$ m z_{max} = max depth
LSN	van Ballegoo <i>y et al.</i> , 2014	$\varepsilon_v = \varepsilon_v(FS_L, q_{c1Ncs})$	$1000/z$	$z_{min} = 0$ m $z_{max} = 20$ m
LPIISH	Maurer, 2015	$\begin{cases} 1 - FS_L & \text{if } FS_L \leq 1 \cap H1 * m(FS_L) \leq 3 \\ 0 & \text{otherwise} \end{cases}$	$25.56/z$	$z_{min} = H1$ $z_{max} = 20$ m
IAM	Chiarado nna <i>et al.</i> , 2020	$r_u = r_u(FS_L, Dr, FC)$	$\frac{1}{(1 + z_{min})^{0.3}}$	z_{min}, z_{max} depth of the uppermost liquefiable layer
GLSN	Paoletta <i>et al.</i> , 2022	$TF \int_0^1 \gamma_{max}$	$\arctan\left(\frac{z}{z_{max}}\right)$	$z_{min} = 0$ m $z_{max} = 20$ m

2.3.1 LPI: Liquefaction Potential Index

The liquefaction potential index (LPI) was developed by Iwasaki et al. (1978, 1981, 1982), is a measure of the liquefaction effects based on the width and depth of the liquefiable areas and historical cases of liquefaction.

LPI is derived from the expression:

$$LPI = \int_0^{20} F(z) \cdot w(z) dz \quad (2.13)$$

where:

$$\begin{cases} F = 1 - FS_L & \text{if } FS_L \leq 1 \\ F = 0 & \text{if } FS_L > 1 \end{cases} \quad \text{and } w(z) = 10 - 0.5 \cdot z \quad (2.14)$$

It is the summation of liquefaction severity in each layer of liquefiable soils, it is directly proportional to FS_L and weighted by a function $w(z)$ that decreases with depth. LPI value ranges between 0 and 100 and it was interpreted as follows:

Table 2.4 – LPI based risk classes

LPI	Liquefaction risk
LPI = 0	Very low
$0 < LPI \leq 5$	Low
$5 < LPI \leq 15$	High
$15 < LPI$	Very high

2.3.2 Settlement (W_v) Indicator

The Settlement indicator integrates the volumetric densification strains, ϵ_v , calculated using the Zhang et al. (2002) method, over the total depth of the CPT profile, Z , using:

$$w = \int_0^Z \epsilon_v(z) dz \quad (2.15)$$

Where:

- $\epsilon_v(z)$ is the volumetric densification strain at depth, z , based on Zhang et al. (2002);
- Z is the total depth of the CPT profile;
- z is the depth in meters below the ground surface.

There are always volumetric densification strains when the excess pore pressure rises during shaking, so strains are included for all factors of safety up to $FS_L = 2.0$ (i.e. including non-liquefied layers).

Settlements calculated using this method for deeper CPT profiles are typically greater than settlements calculated for shallower CPT profiles. The calculated values are therefore not strictly comparable between CPT profiles.

2.3.3 Volumetric Densification (Zhang *et al.*, 2002)

At each layer, the Factor of Safety, FS_L , and the normalized tip resistance, qc_{1Ncs} , are used to calculate the post-liquefaction volumetric densification strain, ϵ_v . These strains are interpolated from the curves proposed by Zhang *et al.* (2002) and summarized in Eq. 2.17, except that the CPT tip resistance is corrected to remove the effect of overburden stress using the iterative Idriss and Boulanger (2008) procedure.

$$\left\{ \begin{array}{ll} \text{if } FS \leq 0.5, \epsilon_v = 102(qc_{1N})cs - 0.82 & \text{for } 33 \leq (qc_{1N})cs \leq 200 \\ \text{if } FS = 0.6, \epsilon_v = 102(qc_{1N})cs - 0.82 & \text{for } 33 \leq (qc_{1N})cs \leq 147 \\ \text{if } FS = 0.6, \epsilon_v = 2411(qc_{1N})cs - 1.45 & \text{for } 147 \leq (qc_{1N})cs \leq 200 \\ \text{if } FS = 0.7, \epsilon_v = 102(qc_{1N})cs - 0.82 & \text{for } 33 \leq (qc_{1N})cs \leq 110 \\ \text{if } FS = 0.7, \epsilon_v = 1701(qc_{1N})cs - 1.42 & \text{for } 110 \leq (qc_{1N})cs \leq 200 \\ \text{if } FS = 0.8, \epsilon_v = 102(qc_{1N})cs - 0.82 & \text{for } 33 \leq (qc_{1N})cs \leq 80 \\ \text{if } FS = 0.8, \epsilon_v = 1690(qc_{1N})cs - 1.46 & \text{for } 80 \leq (qc_{1N})cs \leq 200 \\ \text{if } FS = 0.9, \epsilon_v = 102(qc_{1N})cs - 0.82 & \text{for } 33 \leq (qc_{1N})cs \leq 60 \\ \text{if } FS = 0.9, \epsilon_v = 1430(qc_{1N})cs - 1.48 & \text{for } 60 \leq (qc_{1N})cs \leq 200 \\ \text{if } FS = 1.0, \epsilon_v = 64(qc_{1N})cs - 0.93 & \text{for } 33 \leq (qc_{1N})cs \leq 200 \\ \text{if } FS = 1.1, \epsilon_v = 11(qc_{1N})cs - 0.65 & \text{for } 33 \leq (qc_{1N})cs \leq 200 \\ \text{if } FS = 1.2, \epsilon_v = 9.7(qc_{1N})cs - 0.69 & \text{for } 33 \leq (qc_{1N})cs \leq 200 \\ \text{if } FS = 1.3, \epsilon_v = 7.6(qc_{1N})cs - 0.71 & \text{for } 33 \leq (qc_{1N})c \leq 200 \\ \text{if } FS = 2.0, \epsilon_v = 0.0 & \text{for } 33 \leq (qc_{1N})cs \leq 200 \end{array} \right. \quad (2.16)$$

Table 2.5 - The following additional constraints are applied to the volumetric densification calculations using the equations given in Appendix A of Zhang *et al.* (2002).

CALCULATION ISSUE	DESCRIPTION OR REFERENCE
Strain equations are only provided for $q_{c1} / q_{c1ncs} \geq 33$	For $q_{c1ncs} < 33$, the strain is bounded by the limiting strain, calculated using $q_{c1ncs} = 33$
Strain equations are only provided for specific Factors of Safety	Linear interpolation is used between the published equations
Limits on values	Maximum strain = $102 q_{c1ncs}^{-0.82}$

2.3.4 LSN: Liquefaction Severity Number

The LSN indicator was developed to assess the performance of residential land in Canterbury (New Zealand) in future earthquakes and was validated against the residential land damage observed herein. The LSN depends on the seismic load, groundwater depth and geological profile. The LSN is defined as:

$$LSN = 1000 \cdot \int_0^{20 \text{ m}} \frac{\epsilon_v(z)}{z} dz \quad (2.17)$$

Where:

- $\epsilon_v(z)$ is the volumetric densification strain at depth, z , based on Zhang *et al.* (2002);
- z is the depth in metres below the ground surface.

LSN is calculated as the summation of the post-liquefaction volumetric reconsolidation strains calculated for each soil layer divided by the depth to the midpoint of that layer. The value of LSN is theoretically between 0 (representing no liquefaction vulnerability) to a very large number (representing extreme liquefaction vulnerability). The hyperbolic depth weighting function can yield a very large value only when the groundwater table is very close to the ground surface and soil layers immediately below the ground surface liquefy.

LSN is an extension of the LPI philosophy. It attempts to quantify the effects of liquefaction and consequent land damage using volumetric strains (adopted in conventional settlement calculations, e.g., Zhang *et al.* 2002).

The hyperbolic function gives much greater weight to liquefaction at shallow depths and considers shallow liquefaction (<6 m) to be the key contributor to the overall

damage to land and relatively light residential buildings supported on shallow foundations.

Table 2.6 - LSN Ranges and observed land effects (NGS, 2016).

LSN Range	Performance
0-10	Little to no expression of liquefaction, minor effects
10-20	Minor expression of liquefaction, some sand boils
20-30	Moderate expression of liquefaction, with sand boiling and some structural damage
30-40	Moderate to severe expression of liquefaction, settlement can cause structural damage
40-50	Major expression of liquefaction, undulations and damage to ground surface, severe total and differential settlement of structures
50+	Severe damage, extensive evidence of liquefaction at surface

2.3.5 LPI_{ISH}: LPI Ishihara inspired

After Ishihara (1985) experience, who recognized the important role of the upper non-liquefiable crust's thickness (H_1) in mitigating the surficial liquefaction manifestations, Maurer *et al.* (2015a) derived a new index to assess liquefaction-induced ground manifestations: the Ishihara inspired LPI, LPI_{ISH}. The modifications proposed to the LPI framework try better to capture the trends in the Ishihara boundary curves, including the influence of the thickness of the non-liquefied crust (i.e., H_1) on the surficial liquefaction manifestations. Maurer *et al.* (2015a) defined LPI_{ISH} as:

$$LPI_{ISH} = \int_0^{20m} F(FS_L) \frac{25.56}{z} dz \quad (2.18)$$

Where:

$$F(FS_L) = \begin{cases} 1 - FS_L & \text{if } FS_L \leq 1 \cap H_1 * m(FS_L) \leq 3 \\ 0 & \text{otherwise} \end{cases} \quad (2.19)$$

$$m(FS_L) = \exp\left(\frac{5}{25.56(1-FS_L)}\right) - 1 \quad (2.20)$$

Where: H_1 is defined in the Ishihara (1985) procedure; z is the depth to the layer of interest in meters below the ground surface FS_L is the factor of safety against liquefaction at a given depth, z . The new LPIISH framework has been developed as a result of the rebuilding efforts in Christchurch and tested against a total of 60 liquefaction case studies from the 1989 Loma Prieta (USA), 1994 Northridge (USA), 1999 Kocaeli (Turkey), 1999 Chi-Chi (Taiwan), 2010 Darfield (New Zealand) and 2011 Christchurch (New Zealand) earthquakes, showing a better performance in reducing false-positive predictions (cases where manifestations were predicted but not observed).

2.3.6 IAM: Induced dAmage parameter

The Induced dAmage parameter (IAM) is strictly related to the free-field post-volumetric consolidation settlement and therefore based on the estimate of liquefaction induced excess pore pressure. The IAM has been developed for a reference site located in the area struck by the 2012 Emilia seismic sequence by means of simplified and 1D effective stress dynamic analyses (Chiaradonna *et al.*, 2020). This cumulative indicator of the severity of liquefaction effects at the ground surface takes into account the thickness and the depth of the uppermost liquefiable layer, the induced excess pore water pressure and is directly correlated to the settlement ($w_{c,FF}$) and is computed as:

$$IAM = \frac{1}{(1+z_{min})^{0.3}} (w_{c,FF}) \quad (2.21)$$

Where:

$$w_{c,FF} = \int_{z_{min}}^{z_{max}} \frac{r_u(z)\sigma'_{vo}(z)}{E_{oed}(z)} dz \quad (2.22)$$

r_u is the ratio between the excess pore pressure and lithostatic effective stress. The quantification of r_u can be done with a rigorous approach by means of effective stress dynamic analyses (e.g., using a computer code) or in a simplified way by indirectly computing r_u with the empirical relationship between r_u and the stress-based safety factor against liquefaction recently proposed by Chiaradonna and Flora (2019). Four damage levels are identified and associated with the thresholds reported in Table 2.7.

Table 2.7 - Suggested limit states for rigid body settlements due to earthquake induced ground deformation (modified after Chiaradonna et al., 2020).

Damage state	IAM
Low	$IAM \leq 0.1$
Moderate	$0.1 < IAM \leq 0.3$
Extensive	$0.3 < IAM \leq 1.0$
Severe	$IAM > 1.0$

2.3.7 GLSN: generalized severity number to predict liquefaction damage with lateral spreading

Paolella *et al.* (2022) introduce a generalization of the classical one-dimensional liquefaction severity indexes to extend their predictive capability for the occurrence of lateral spreading.

The efficacy of the new index is demonstrated with a performance based study on two cases, the earthquakes of May 20th 2012 (M_w 6.1) at Terre del Reno (Emilia-Romagna, Italy) and of February 11th 2011 (M_w 6.2) at Christchurch (New Zealand). Stratigraphic attributes including thickness, depth, composition and relative density the liquefiable layers, obtained over the whole territories from rich datasets of Cone Penetration Tests (CPT) are coupled with topographic information derived from the digital elevation model to provide the input for the analysis. The proposed index is defined as follows:

$$GLSN = TF \int_0^1 \gamma_{max} * w\left(\frac{z}{z_{max}}\right) d\left(\frac{z}{z_{max}}\right) \quad (2.23)$$

γ_{max} is the maximum shear strain, dependent on the normalized CPT resistance $(q_{c1N})_{cs}$ and the liquefaction safety factor (Figure 2.6).

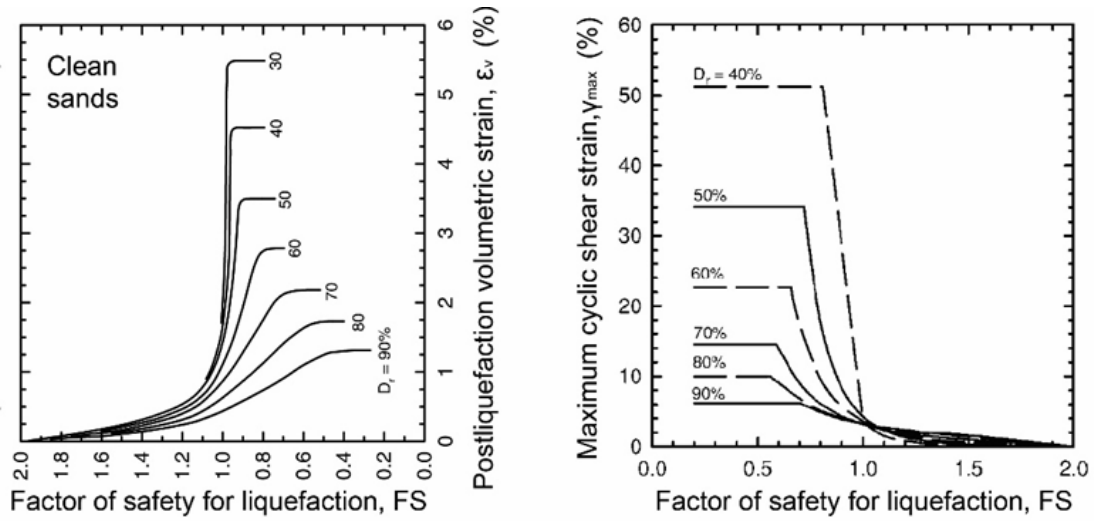


Figure 2.10 - Post liquefaction maximum cyclic shear strain (b) as function of relative density and Liquefaction Safety Factor (FS) (modified from Ishihara & Yoshimine, 1992).

The function $w\left(\frac{z}{z_{max}}\right)$ expresses the relative weight that defines the ground effects of liquefaction occurring at various depths. Concerning this issue, Iwasaki *et al.* (1978) propose a smooth linear attenuation law from one at ground level to zero at 20 m depth, while van Ballegooy *et al.* (2014) and Maurer *et al.* (2015a) propose a much faster decay with a hyperbolic attenuation function. An intermediate flexible function is proposed by the authors, expressed by the following formula:

$$w\left(\frac{z}{z_{max}}\right) = 10 \cdot \left(1 - \frac{\pi}{2} \cdot \left(\arctan\left(\frac{z}{z_{max}}\right)\right)^{n_1}\right)^{n_2} \quad (2.24)$$

In the proceedings z_{max} has been put equal to 20 m following the suggestion of most authors (see Table 2.3). The TF factor expresses the influence of the local topographical conditions on the effects of liquefaction. It introduces a dependency on the steepness of potential sliding surfaces, the latter obtained joining the given calculation point to the toe of the considered free face. Hence TF is a function of the slope S , computed as the ratio between the vertical and horizontal distances between the two points (H/L).

$$TF = 1 + \frac{LD}{LDI} = 1 + 6 \cdot (S)^{0.8} \quad (2.25)$$

The function, calibrated with the experimental observation provided by Zhang *et al.* (2004), aims to cover all possible situations. It provides the maximum correction for points located near the top edge of the free face and progressively decreases to one

Seismic Liquefaction:
phenomenon and hazard assessment

with the horizontal distance between the two points. The formula also includes the case of sloped ground, i.e. without a cut, being S in this circumstance equal to the local ground steepness and, of course, the case of the horizontal ground surface ($S=0$) for which $TF=1$.

Chapter 3. VULNERABILITY

ASSESSMENT

Economic losses caused by natural disasters is dramatically increased in the last couple of decades (Glaister *et al.*, 2013); among these natural disasters, earthquake has been the most catastrophic phenomena. A detailed report of the economic losses due to earthquakes from 1972 to 1990 has been drafted by Coburn and Spence (2002).

The 1994 Northridge (California, US) earthquake caused US\$14 billion earthquake loss, and the US\$150 billion cost of the 1995 Kobe (Japan) earthquake was the highest ever absolute earthquake loss (Calvi *et al.*, 2006). Besides the population losses that occurred in the 2011 Tohoku earthquake, the economic loss was US\$140 billion. Furthermore, the financial loss caused in Turkey was US\$2.2 billion after the occurrence of the Van earthquake event in 2011, and was estimated as US \$1.7 billion when the Sikkim earthquake event struck India in 2011 (Daniell *et al.*, 2011).

Although the dollar value of economic losses in other parts of the world may be far lower than in Japan and the US, the impact on the national economy may be much greater due to losses being a larger proportion of the gross national product (GNP) in that year. The Central American country of Nicaragua (1972) recorded the biggest loss in proportions of the GNP, which was about 40% GNP. The second and the third largest losses in terms of the GNP are in Guatemala (1976, 18% GNP) and El Salvador (1986, 31% GNP).

The huge impact caused by earthquakes has raised the need for predictive formulas to quantify the earthquake-related damages to structures and infrastructures, applicable at large scale.

Models capable of estimating losses in future earthquakes are of fundamental importance for reduction of injuries and fatalities, emergency planners and the insurance industries.

Seismic vulnerability assessment at urban scale is a useful tool for both prevention and management. In particular, seismic vulnerability means the tendency of a structure, subject to possible seismic events, to suffer damage.

Damage grade and damage type depend on the year and place of construction, on structural and material features and on the presence of nearby buildings. Seismic vulnerability assessment is performed on the basis of a reliable earthquake loss model for the region under consideration. The nature of a loss model is not only related to economic considerations, but it allows to have a positive impact in the management and forecasting of risk emergencies by national authority. In particular, knowledge of the expected losses for a future earthquake implies the possibility of establishing risk mitigation measures both in terms of structural interventions and the stipulation of insurance coverage. A consistent and site specific model can be used to adequate the seismic codes for the design of new buildings. Furthermore, fragility models can be formulated by including a single hazard element or by incorporating several secondary effects at the same time: amplified ground shaking, landslides, liquefaction, surface fault rupture, and tsunamis.

A crucial aspect of earthquake loss models theorization consists in the definition of a methodology to assess the vulnerability of the built environment.

Basically, the aim of a vulnerability assessment is to obtain the probability of a given level of damage to a given building type due to a scenario earthquake. In literature, several methods have been proposed using three different approaches: empirical, analytical and hybrid.

A preliminary step in defining the damage level consists in the hazard assessment. In particular, it is necessary to identify a seismic property representative of the ground shaking and capable of correlating the same to the damage on the structure; the use of peak ground acceleration (PGA), peak ground velocity (PGV) and response spectra obtained from the ground motions is a common practice. Furthermore, recent research links the damage to structures and infrastructures to indicators calibrated on specific hazards, for example there are studies that provide fragility curves as a function of the hazard indicators to liquefaction (Toprak *et al.*, 2017; Baris *et al.*, 2020).

Each vulnerability assessment method models the damage on a discrete damage scale; frequently used examples include the MSK scale (Medvedev and Sponheuer, 1969), the Modified Mercalli scale (Wood and Neumann, 1931), the Japanese Meteorological Agency Scale (JMA 1996, 2009) and the EMS98 scale (Grünthal, 1998). The existence of many different scales is a demonstration of the complexity of the problem of describing earthquake effects.

Calvi *et al.* (2006) summarize the vulnerability assessment procedure in an easy to understand and comprehensive flowchart, depicted in Figure 3.1.

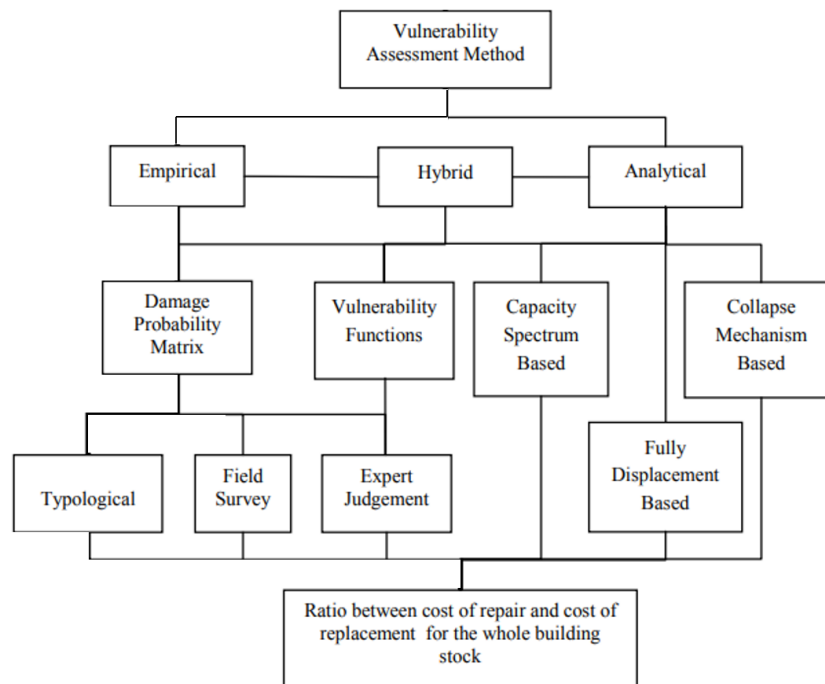


Figure 3.1 - Choices for the vulnerability assessment procedure (adapted from Calvi et al., 2006).

3.1 Intensity scales

Intensity scales are historically widely diffused because no instrumentation is necessary, and useful measurements of an earthquake can be made by an unequipped observer. The earliest use of intensity scale was observed in the second part of 1700, with a simple quantification of damage proposed by Schiantarelli in 1783 (Sarconi 1784). The first scale to be used internationally was the ten-degree Rossi-Forel Scale of 1883. However, it was only in the 20th century that the use of intensity became widespread; The first proposed seismic intensity scales are Sieberg (1912,1923), Davison (1900, 1921, 1933), a later study can be found in Medvedev (1962).

The scale of Sieberg (1912,1923) became the foundation of all modern twelve-degree scales. A later version of it became known as the Mercalli-Cancani-Sieberg Scale, or MCS Scale (Sieberg 1932), still in use in Southern Europe. The 1923 version was translated into English by Wood and Neumann (1931), becoming the Modified Mercalli Scale (MM). In 1964 the first version of the MSK Scale was published by Medvedev, Sponheuer and Karník (Sponheuer and Karník 1964). This scale became widely used in Europe. In 1988, the European Seismological Commission agreed to start a renewal of the MSK Scale. Grünthal (1998) published the final version of the revision in 1998, this new scale was renamed the European Macroseismic Scale (EMS). Since its publication it has been widely adopted inside and also outside Europe

(Musson *et al.*, 2012). In Japan is widespread the seven-degree Japanese Meteorological Agency Scale (JMA Scale, 1996, 2009). The three most important intensity scales in current use are the European Macroseismic Scale (EMS-98), the Modified Mercalli Scale (MM or MMI) and the JMA scale (Musson *et al.*, 2012).

European Macroseismic Scale (EMS)

The Europeans Macroseismic Scale (EMS-98; Grünthal, 1998) is made up of six vulnerability classes of decreasing vulnerability, from A to F (Figure 3.2), that directly represent the strength and takes into account the type of construction, the processing of construction and the conditions. These vulnerability classes allow a flexible and robust approach to assessing intensity from damage. The damage is defined with a scale of five levels, differentiated according to structural and non-structural damage and building type. The five grades damage system involves the following levels: negligible to slight; moderate; substantial to heavy; very heavy, and destruction; the damage levels are defined and depicted (reported in Figure 3.3, 3.4 for masonry and reinforced concrete buildings). It is the first intensity scale that uses the drawings to graphically and accurately show the meaning of the different levels of damage and the photographic examples in *Section 5* can be used in the field as a comparison with real cases. The scale counts twelve degree of intensity, from “*I - not felt*” to “*XII – Completely devastating*” describing the effects on three different categories:

- (a) Effects on people.
- (b) Effects on objects and the environment (Ground effects and land subsidence are dealt with in particular in *Section 7*).
- (c) Damage to buildings.

The EMS-98 scale recognizes the statistical nature of the intensity, i.e. that in any place it is likely that a certain effect will be observed only in a certain number of cases, the entity of which provides an indication of the severity of the shaking. Previous scales described only the effects, without the quantities, implicitly meaning that the same effect was universal on all sensors when the intensity reached that value. Furthermore, the EMS-98 scale provides extensive support material, including guidelines, tabular and graphical material explaining the classification of buildings and quantities used, illustrations and examples.

Type of Structure	Vulnerability Class					
	A	B	C	D	E	F
MASONRY	○					
	○—					
	○—					
	○—					
	○—					
	○—					
	○—					
REINFORCED CONCRETE (RC)	○—					
	○—					
	○—					
	○—					
	○—					
	○—					
STEEL				○—		
WOOD				○—		

○ most likely vulnerability class; — probable range;
range of less probable, exceptional cases

Figure 3.2 - Vulnerability classes in EMS-98.






Classification of damage to masonry buildings	
	<p>Grade 1: Negligible to slight damage (no structural damage, slight non-structural damage) Hair-line cracks in very few walls. Fall of small pieces of plaster only. Fall of loose stones from upper parts of buildings in very few cases.</p>
	<p>Grade 2: Moderate damage (slight structural damage, moderate non-structural damage) Cracks in many walls. Fall of fairly large pieces of plaster. Partial collapse of chimneys.</p>
	<p>Grade 3: Substantial to heavy damage (moderate structural damage, heavy non-structural damage) Large and extensive cracks in most walls. Roof tiles detach. Chimneys fracture at the roof line; failure of individual non-structural elements (partitions, gable walls).</p>
	<p>Grade 4: Very heavy damage (heavy structural damage, very heavy non-structural damage) Serious failure of walls; partial structural failure of roofs and floors.</p>
	<p>Grade 5: Destruction (very heavy structural damage) Total or near total collapse.</p>

Figure 3.3 - Damage classification for masonry buildings in the European Macroseismic Scale.

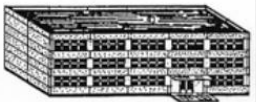




Classification of damage to buildings of reinforced concrete	
	<p>Grade 1: Negligible to slight damage (no structural damage, slight non-structural damage) Fine cracks in plaster over frame members or in walls at the base. Fine cracks in partitions and infills.</p>
	<p>Grade 2: Moderate damage (slight structural damage, moderate non-structural damage) Cracks in columns and beams of frames and in structural walls. Cracks in partition and infill walls; fall of brittle cladding and plaster. Falling mortar from the joints of wall panels.</p>
	<p>Grade 3: Substantial to heavy damage (moderate structural damage, heavy non-structural damage) Cracks in columns and beam column joints of frames at the base and at joints of coupled walls. Spalling of concrete cover, buckling of reinforced rods. Large cracks in partition and infill walls, failure of individual infill panels.</p>
	<p>Grade 4: Very heavy damage (heavy structural damage, very heavy non-structural damage) Large cracks in structural elements with compression failure of concrete and fracture of rebars; bond failure of beam reinforced bars; tilting of columns. Collapse of a few columns or of a single upper floor.</p>
	<p>Grade 5: Destruction (very heavy structural damage) Collapse of ground floor or parts (e. g. wings) of buildings.</p>

Figure 3.4 - Damage classification for reinforced concrete buildings in the European Macroseismic Scale.

Modified Mercalli (MM) Scale

The Modified Mercalli intensity scale has been developed over the last hundred years to evaluate the effects of earthquakes, it is the one currently used in the United States. It was developed in 1931 by the American seismologists Harry Wood and Frank Neumann, after modification carried out on several intensity scales proposed since 1883 with the ten-degree Rossi-Forel scale. The MM scale, composed of ten increasing levels of intensity that range from imperceptible shaking to catastrophic destruction, is designated by Roman numerals. It is theorized based on observed effects and does not have a mathematical basis. The scale counts ten degree of intensity, from “I - Not felt shaking” to “X - Extreme shaking” describing the effects on four different categories (Figures 3.5, 3.6):

- (a) Effects on people.

- (b) Effects on furnishings.
- (c) Built environment.
- (d) Natural environment.

The lower numbers of the intensity scale generally deal with the manner in which the earthquake is felt by people. The higher numbers of the scale are based on observed structural damage.

Intensity	Shaking	Description/Damage
I	Not felt	Not felt except by a very few under especially favorable conditions.
II	Weak	Felt only by a few persons at rest, especially on upper floors of buildings.
III	Weak	Felt quite noticeably by persons indoors, especially on upper floors of buildings. Many people do not recognize it as an earthquake. Standing motor cars may rock slightly. Vibrations similar to the passing of a truck. Duration estimated.
IV	Light	Felt indoors by many, outdoors by few during the day. At night, some awakened. Dishes, windows, doors disturbed; walls make cracking sound. Sensation like heavy truck striking building. Standing motor cars rocked noticeably.
V	Moderate	Felt by nearly everyone; many awakened. Some dishes, windows broken. Unstable objects overturned. Pendulum clocks may stop.
VI	Strong	Felt by all, many frightened. Some heavy furniture moved; a few instances of fallen plaster. Damage slight.
VII	Very strong	Damage negligible in buildings of good design and construction; slight to moderate in well-built ordinary structures; considerable damage in poorly built or badly designed structures; some chimneys broken.
VIII	Severe	Damage slight in specially designed structures; considerable damage in ordinary substantial buildings with partial collapse. Damage great in poorly built structures. Fall of chimneys, factory stacks, columns, monuments, walls. Heavy furniture overturned.
IX	Violent	Damage considerable in specially designed structures; well-designed frame structures thrown out of plumb. Damage great in substantial buildings, with partial collapse. Buildings shifted off foundations.
X	Extreme	Some well-built wooden structures destroyed; most masonry and frame structures destroyed with foundations. Rails bent.

Figure 3.5 - Modified Mercalli intensity scale: level of shaking and description of damage.

CIIM Intensity	People's Reaction	Furnishings	Built Environment	Natural Environment
I	Not felt			Changes in level and clarity of well water are occasionally associated with great earthquakes at distances beyond which the earthquakes felt by people.
II	Felt by a few.	Delicately suspended objects may swing.		
III	Felt by several; vibration like passing of truck.	Hanging objects may swing appreciably.		
IV	Felt by many; sensation like heavy body striking building.	Dishes rattle.	Walls creak; window rattle.	
V	Felt by nearly all; frightens a few.	Pictures swing out of place; small objects move; a few objects fall from shelves within the community.	A few instances of cracked plaster and cracked windows within the community.	Trees and bushes shaken noticeably.
VI	Frightens many; people move unsteadily.	Many objects fall from shelves.	A few instances of fallen plaster, broken windows, and damaged chimneys within the community.	Some fall of tree limbs and tops, isolated rockfalls and landslides, and isolated liquefaction.
VII	Frightens most; some lose balance.	Heavy furniture overturned.	Damage negligible in buildings of good design and construction, but considerable in some poorly built or badly designed structures; weak chimneys broken at roof line, fall of unbraced parapets.	Tree damage, rockfalls, landslides, and liquefaction are more severe and widespread with increasing intensity.
VIII	Many find it difficult to stand.	Very heavy furniture moves conspicuously.	Damage slight in buildings designed to be earthquake resistant, but severe in some poorly built structures. Widespread fall of chimneys and monuments.	
IX	Some forcibly thrown to the ground.		Damage considerable in some buildings designed to be earthquake resistant; buildings shift off foundations if not bolted to them.	
X			Most ordinary masonry structures collapse; damage moderate to severe in many buildings designed to be earthquake resistant.	

Figure 3.6 - Modified Mercalli intensity scale: people's perception and effects on environment.

Japan Meteorological Agency (JMA) Scale

The JMA scale has evolved over the years from the seven-degree scale of Omori (1900). The revision of 1996 added two new degrees, but to try and maintain consistency with older data sets, the new scale divided degree 5 into “5 Lower” and “5 Upper”, and similarly for degree 6 (Musson *et al.*, 2012). The latest revision, proposed in 2009, provides a set of three tables depicting the effects of different levels of seismic intensity on humans, buildings, infrastructures and environment. In particular, the human perception and reaction is divided in outdoor and indoor situations (Figure 3.7).

The effects on structures are divided into two categories according to the building types, providing two tables: one for wooden houses (Figure 3.8a) and one for reinforced concrete buildings (Figure 3.8b). The JMA scale establishes effects on structures upper the 5 level of intensity scale. The two tables have two subcategories according to their earthquake resistance (low and high).

Influence on infrastructures and utilities highlights that in the event of shaking with a seismic intensity of 6 upper or more, gas, water and electric supplies may stop over wide areas (Figure 3.9).

Vulnerability assessment

Seismic intensity	Human perception and reaction	Indoor situation	Outdoor situation
0	Imperceptible to people, but recorded by seismometers.	—	—
1	Felt slightly by some people keeping quiet in buildings.	—	—
2	Felt by many people keeping quiet in buildings. Some people may be awoken.	Hanging objects such as lamps swing slightly.	—
3	Felt by most people in buildings. Felt by some people walking. Many people are awoken.	Dishes in cupboards may rattle.	Electric wires swing slightly.
4	Most people are startled. Felt by most people walking. Most people are awoken.	Hanging objects such as lamps swing significantly, and dishes in cupboards rattle. Unstable ornaments may fall.	Electric wires swing significantly. Those driving vehicles may notice the tremor.
5 Lower	Many people are frightened and feel the need to hold onto something stable.	Hanging objects such as lamps swing violently. Dishes in cupboards and items on bookshelves may fall. Many unstable ornaments fall. Unsecured furniture may move, and unstable furniture may topple over.	In some cases, windows may break and fall. People notice electricity poles moving. Roads may sustain damage.
5 Upper	Many people find it hard to move; walking is difficult without holding onto something stable.	Dishes in cupboards and items on bookshelves are more likely to fall. TVs may fall from their stands, and unsecured furniture may topple over.	Windows may break and fall, unreinforced concrete-block walls may collapse, poorly installed vending machines may topple over; automobiles may stop due to the difficulty of continued movement.
6 Lower	It is difficult to remain standing.	Many unsecured furniture moves and may topple over. Doors may become wedged shut.	Wall tiles and windows may sustain damage and fall.
6 Upper	It is impossible to remain standing or move without crawling. People may be thrown through the air.	Most unsecured furniture moves, and is more likely to topple over.	Wall tiles and windows are more likely to break and fall. Most unreinforced concrete-block walls collapse.
7		Most unsecured furniture moves and topples over, or may even be thrown through the air.	Wall tiles and windows are even more likely to break and fall. Reinforced concrete-block walls may collapse.

Figure 3.7 - Human perception and reaction according to JMA scale.

a)

Seismic intensity	Wooden houses	
	High earthquake resistance	Low earthquake resistance
5 Lower	—	Slight cracks may form in walls.
5 Upper	—	Cracks may form in walls.
6 Lower	Slight cracks may form in walls.	Cracks are more likely to form in walls. Large cracks may form in walls. Tiles may fall, and buildings may lean or collapse.
6 Upper	Cracks may form in walls.	Large cracks are more likely to form in walls. Buildings are more likely to lean or collapse.
7	Cracks are more likely to form in walls. Buildings may lean in some cases.	Buildings are even more likely to lean or collapse.

b)

Seismic intensity	Reinforced-concrete buildings	
	High earthquake resistance	Low earthquake resistance
5 Upper	—	Cracks may form in walls, crossbeams and pillars.
6 Lower	Cracks may form in walls, crossbeams and pillars.	Cracks are more likely to form in walls, crossbeams and pillars.
6 Upper	Cracks are more likely to form in walls, crossbeams and pillars.	Slippage and X-shaped cracks may be seen in walls, crossbeams and pillars. Pillars at ground level or on intermediate floors may disintegrate, and buildings may collapse.
7	Cracks are even more likely to form in walls, crossbeams and pillars. Ground level or intermediate floors may sustain significant damage. Buildings may lean in some cases.	Slippage and X-shaped cracks are more likely to be seen in walls, crossbeams and pillars. Pillars at ground level or on intermediate floors are more likely to disintegrate, and buildings are more likely to collapse.

Figure 3.8 - Effects on wooden houses (a) and reinforced concrete buildings (b) according to JMA scale.

Suspension of gas supply	In the event of shaking with a seismic intensity of about 5 Lower or more, gas meter with safety devices are tripped, stopping the supply of gas. In the event of stronger shaking, the gas supply may stop for entire local blocks*.
Suspension of water supply, electrical blackouts	Suspension of water supply and electrical blackouts may occur in regions experiencing shaking with a seismic intensity of about 5 Lower or more*.
Suspension of railroad services, regulation of highways, etc.	In the event of shaking with a seismic intensity of about 4 or more, services on railroads or highways may be stopped for safety confirmation. Speed control and traffic regulations are performed according the judgment of the relevant bodies. (Standards for safety confirmation differ by organization and area.)
Disruption to lines of communication such as telephones	In the event of an earthquake, telephone line congestion may occur as a result of increased use related to safety confirmation around regions of strong shaking. To combat this, telecommunications providers offer message boards and message dial services for use in disasters resulting from earthquakes with a seismic intensity of about 6 Lower or more.
Suspension of elevator services	In the event of shaking with a seismic intensity of about 5 Lower or more, elevators with earthquake control devices will stop automatically for safety reasons. Resumption of service may be delayed until safety is confirmed.

Figure 3.9 - Influence on infrastructures and utilities according to JMA scale.

3.2 Damage States

The damage is divided into two classes, structural and non-structural, that are described separately. The structural damage is defined as “Slight, Moderate, Extensive, or Complete and Collapse”, with collapse being the subset of complete structure damage according to EQ’s HAZUS loss estimation. Similar damage grades have been defined for non-structural damage. Figure illustrates and describes the four structural damage states.

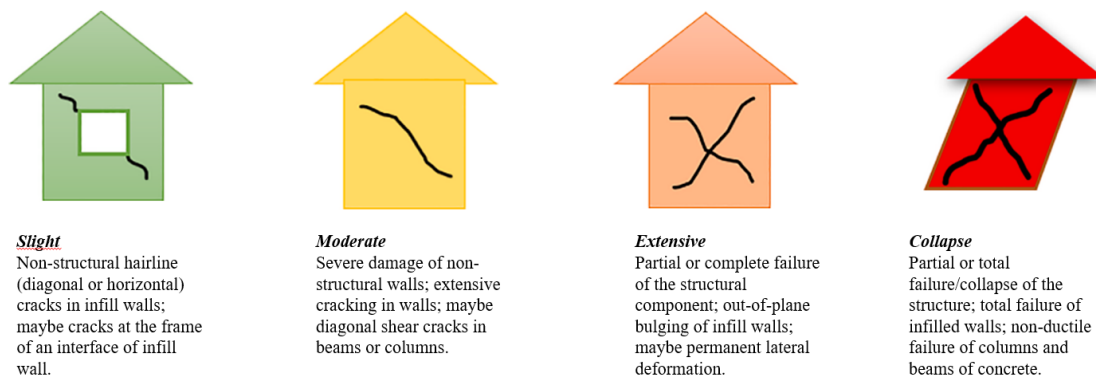


Figure 3.10 - Structural damage States (adapted from Rajkumari et al., 2022)

3.3 Seismic vulnerability assessment

In the following paragraph a short excursus about the methods proposed for the theorization of earthquake loss models is presented. In literature, several methods have been proposed using three different approaches: empirical, analytical and hybrid.

3.3.1 Empirical methods

The earliest empirical methods, formulated and calibrated as a function of macroseismic intensities, have been used since the ‘70s to perform seismic vulnerability assessment of buildings at large geographical scales. There are four main types of empirical methods that are based on the damage observed after earthquakes, which can be termed “damage-motion relationships”:

- 1) damage probability matrices (DPM);
- 2) vulnerability functions;
- 3) vulnerability index method.

Damage probability matrix (DPM)

Damage probability matrices express in a discrete form the conditional probability of obtaining a damage level j , due to a ground motion of intensity i , $P[D=j|i]$. Basically,

the DPM attributes to a building typology the same damage state for a given seismic intensity. Whitman *et al.* (1973) first proposed the use of damage probability matrices for the probabilistic prediction of damage to buildings from earthquakes. DPMs proposed by Whitman *et al.* (1973) were developed for several building typologies and calibrated on more than 1600 structures damaged during the 1971 San Fernando earthquake and provide the damage level (divided into structural and non-structural) as a function of the seismic intensity, attributing a damage ratio value. The damage ratio is the ratio of cost of repair to cost of replacement.

Table 3.1- Damage Probability Matrix Proposed by Whitman *et al.* (1973).

Damage State	Structural Damage	Non-structural Damage	Damage Ratio (%)	Intensity of Earthquake				
				V	VI	VII	VIII	IX
0	None	None	0-0.05	10.4	-	-	-	-
1	None	Minor	0.05-0.3	16.4	0.5	-	-	-
2	None	Localised	0.3-1.25	40.0	22.5	-	-	-
3	Not noticeable	Widespread	1.25-3.5	20.0	30.0	2.7	-	-
4	Minor	Substantial	3.5-4.5	13.2	47.1	92.3	58.8	14.7
5	Substantial	Extensive	7.5-20	-	0.2	5.0	41.2	83.0
6	Major	Nearly total	20-65	-	-	-	-	2.3
7	Building condemned		100	-	-	-	-	-
8	Collapse		100	-	-	-	-	-

In Italy, DPMs were widely used until the early 2000s and, in Europe, one of the first examples is due to an Italian study carried out in the earliest '80s. The study proposed by Braga *et al.* (1982) was based on the data of Italian buildings damaged after the 1980 Irpinia earthquake, introducing the binomial distribution to describe damage distributions of any class for different seismic intensities. The used method was defined as '*direct*' by Corsanego and Petrini (1990) because there is a direct link between the type of building and the observed damage. In particular, three vulnerability classes are defined (A, B and C) and for each class a DPM based on the MSK scale has been postulated. In the following years, modifications were suggested to the method proposed by Braga *et al.* (1982), introducing the MCS scale (Mercalli-Cancani-Sieberg) (Di Pasquale *et al.*, 2005) and applying the matrices to a case study for the ENSERVES (European Network on Seismic Risk, Vulnerability and Earthquake Scenarios) (Dolce *et al.*, 2003).

In the early years of the century, Giovinazzi and Lagomarsino proposed a macroseismic method (2001, 2004) which leads to the definition of damage probability

functions based on the macroseismic scale EMS-98 (Grünthal, 1998) for each vulnerability class, relating the damage to the building stock through the use of an empirical vulnerability index that depends on the type of building, the characteristics of the building stock (e.g. number of floors, irregularities, etc.) and regional construction practices.

The use of damage probability matrices has some disadvantages. Giovinazzi and Lagomarsino (2004) highlight the lack of information for all damage grades for a given level of intensity and their weakness due to a qualitatively, and not quantitative, description of vulnerability. Furthermore, in Calvi *et al.* (2006) underline the following main disadvantages of this method:

- A macroseismic intensity scale is defined by considering the observed damage of the building stock and thus in a loss model both the ground motion input and the vulnerability are based on the observed damage due to earthquakes.
- The derivation of empirical vulnerability functions requires the collection of post-earthquake building damage statistics at sites with similar ground conditions for a wide range of ground motions: this will often mean that the statistics from multiple earthquake events need to be combined. In addition, large magnitude earthquakes occur relatively infrequently near densely populated areas and so the data available tends to be clustered around the low damage/ground motion end of the matrix thus limiting the statistical validity of the high damage/ground motion end of the matrix.
- Seismic hazard maps are now defined in terms of PGA (or spectral ordinates) and thus PGA needs to be related to intensity; however, the uncertainty in this equation is frequently ignored.
- When PGA is used in the derivation of empirically-defined vulnerability, the relationship between the frequency content of the ground motions and the period of vibration of the buildings is not taken into account.

Vulnerability functions

Fragility functions are defined as functions describing the probability of exceeding different limit states (such as damage or injury levels) given a level of ground shaking. It relates earthquake intensities with the probability of exceeding certain limit states. The empirical vulnerability functions are developed on the basis of the historical data of damage collected after seismic events. Different levels of damage are observed and related to the seismic intensity. Usually, Log-normal functions are used for this purpose. The literature on empirical vulnerability functions is very rich. Below is a

brief summary of the early studies and latest publications from the most influential authors in this field. The empirical vulnerability functions have been formulated over the past thirty years. The main obstacle to their derivation consists in the discontinuity of the macroseismic intensity as a variable. In 1992, Spence *et al.* bypass the problem through the use of their Parameterless Scale of Intensity (PSI). Sabetta *et al.* (1998) used post-earthquake surveys of approximately 50000 buildings damaged by destructive Italian earthquakes in order to derive vulnerability curves. The above functions define the damage levels according to the MSK macroseismic scale. Rossetto and Elnashai (2003) propose vulnerability point distribution using the observations of low and mid-rise building damages after the 1995 Aegion (Greece) earthquake for different ground motion parameters: PGA, and Spectral displacement at the elastic fundamental period. Similar study, relating probability of damage to the spectral acceleration or spectral displacement at the fundamental elastic period of vibration, are developed in Japan (Scawthorn *et al.*, 1981; Shinozuka *et al.*, 1997).

Del Gaudio *et al.* (2019) develop empirical fragility curves for masonry buildings, focusing on the damages survey of the 2009 L'Aquila earthquake. A geo-referenced database of 32,520 masonry residential buildings was compiled in the aftermath of the earthquake under the coordination of the Italian Department of Civil Protection through the AeDES survey form.

Rosti *et al.* (2021) derive a set of PGA based empirical fragility curves for reinforced concrete buildings (Figure 3.10), by taking advantage of a huge amount of post-earthquake data (more than 300,000 residential buildings), collected in the aftermath of the Italian earthquakes occurred in the period 1976–2012 and available in the online platform Da.D.O. (Dolce *et al.*, 2019a). The set of curves are differentiated in function of rise class of the buildings and design code (Figure 3.10). The proposed fragility model complies with the framework of the Italian national seismic risk platform (Borzi *et al.*, 2020b) and it was used, together with other vulnerability models (i.e. Borzi *et al.*, 2020a; Donà *et al.*, 2020; Lagomarsino *et al.*, 2020; Rosti *et al.*, 2020a; Zuccaro *et al.*, 2020), for national seismic risk assessment (NDPC 2018; Dolce *et al.*, 2019b, 2020; Masi *et al.*, 2020).

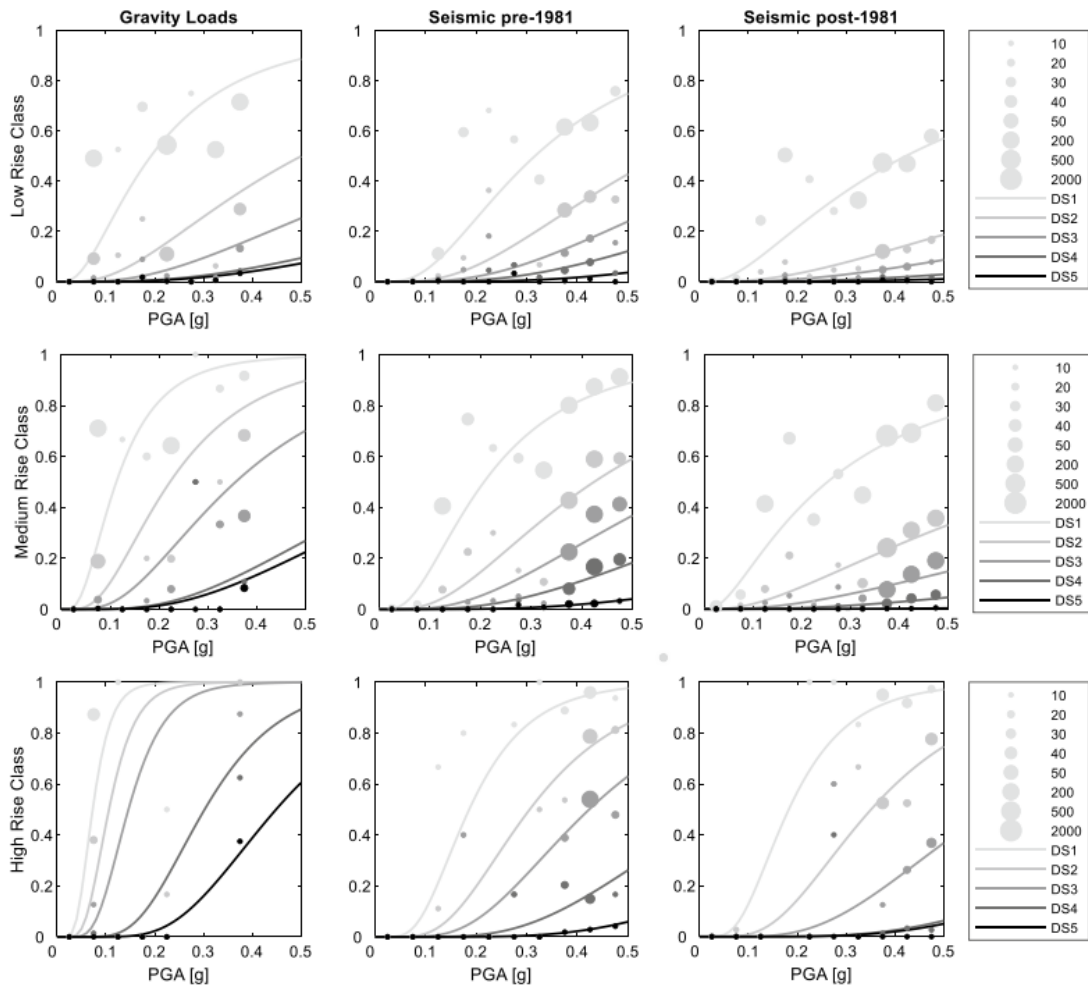


Figure 3.11 – Example of empirical fragility curves for RC building typologies proposed by Rosti et al. (2021). Numbers in the legend refer to the sample size.

Vulnerability index method

Vulnerability index method, proposed by Benedetti and Petrini (1984) is known as “indirect” method because a relationship between the seismic action and the response is established through an index. The index, I_v , is defined as (Eq. 3.1):

$$I_v = \sum_{i=1}^{11} K_i W_i \tag{3.1}$$

where K_i and W_i are qualification coefficients. These qualification coefficients are attributed in accordance with the quality conditions – from A (optimal) to D (unfavourable) – and are related to the *i-esim* parameter. In particular, eleven

parameters are taken into account as information about the building which could influence its vulnerability (i.e. materials, type of foundation, elevation configuration, structural and non-structural elements, state of conservation...). The vulnerability index ranges from 0 to 382.5, but frequently is expressed in the normalized form ranging from 0 to 100. The I_v is related to the earthquake intensity through historical data, providing a global damage factor (d) of buildings with the same typology, for the same macroseismic intensity or PGA. The damage factor ranges between 0 and 1 and defines the ratio of repair cost to replacement cost. An example of damage factor obtained with the vulnerability index is presented in Figure ..., with vulnerability functions (Guagenti and Petrini, 1989) for old masonry buildings calibrated to the damage observed after the 1976 Friuli and the 1984 Abruzzo earthquakes.

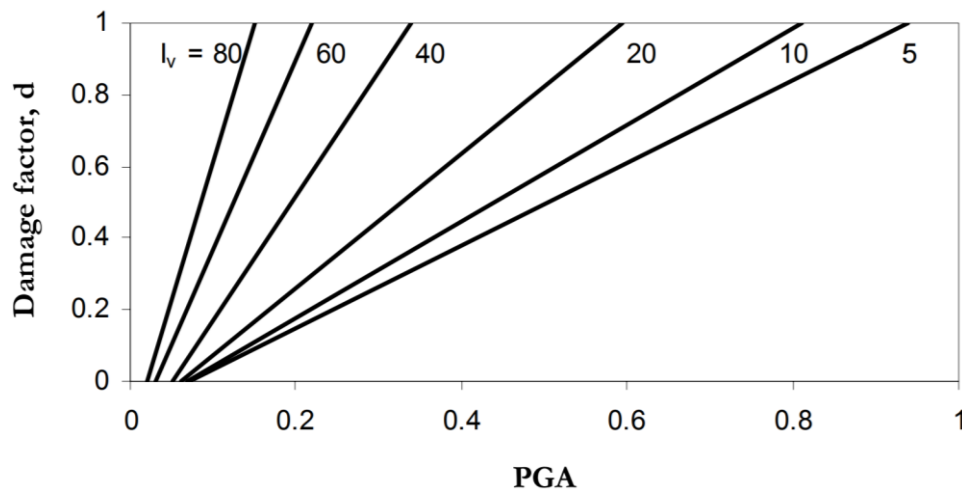


Figure 3.12 -Vulnerability functions to relate damage factor (d) and peak ground acceleration (PGA) for different values of vulnerability index (I_v) (adapted from Guagenti and Petrini, 1989).

3.3.2 Analytical methods

The progress of increasingly advanced computational methods and tools for calculation with ever greater capacities led to the development of analytical methods for the assessment of structures vulnerability. Analytical methods are based on more detailed and transparent vulnerability assessment algorithms than empirical methods, with direct physical significance. Figure 3.13 shows the flowchart to describe the components of the calculation of analytical vulnerability curves and damage probability matrices; the methodology is based on the selections of: earthquake intensity indicator, computational model of structure and model for the definition of damage and damage states.

A crucial aspect of the selection of the computational model of structure consists in the choice of the methodology for analysis. In the following lines a brief excursus on the mostly used procedures is presented.

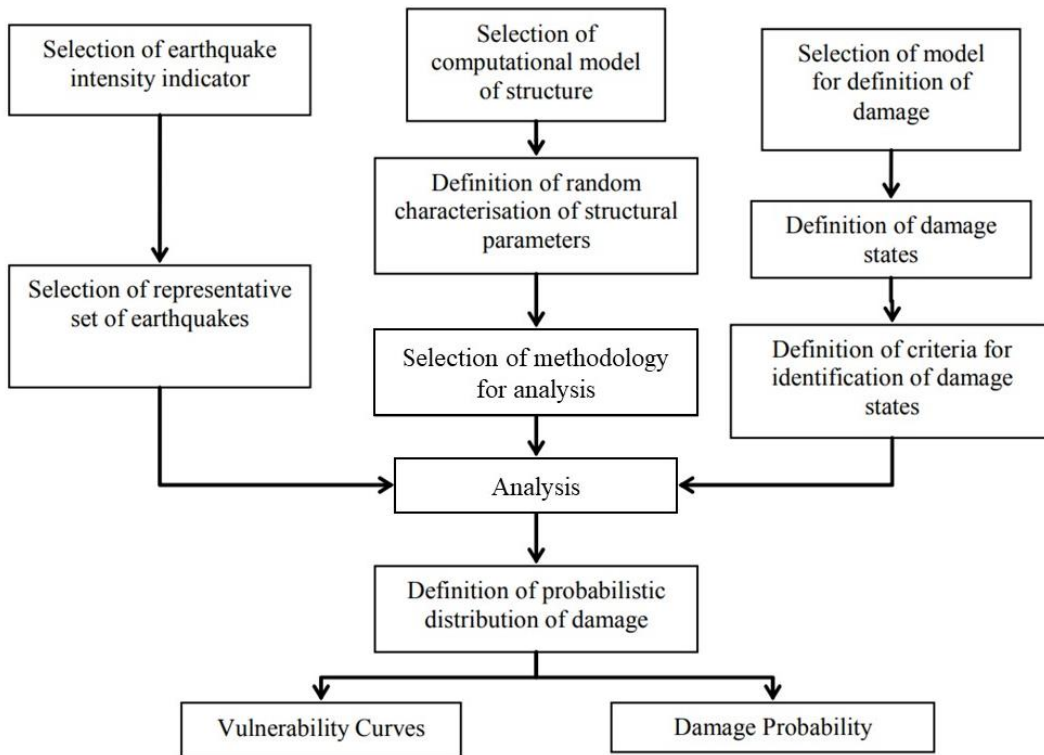


Figure 3.13 - Flowchart to describe the components of the calculation of analytical vulnerability curves and damage probability matrices (modified after Dumova-Jovanoska, 2004).

Non-linear static pushover analysis (PA)

Pushover analysis (PA), a fragment of the performance based design, is a method for evaluating inelastic strength and deformation demands in the structure, and for exposing design weaknesses (ATC 40, 1996). The use of non-linear static analysis is suggested for typical structures, without torsional irregularity, due to its simplification and because it does not take into account for complex properties such as hysteresis or higher participation mode.

The main output of the pushover analysis is the pushover curve, a plot of the base shear (total lateral load) versus the lateral displacement at some point at the roof level, including all the stages of lateral load/displacement increments. The main advantage of this type of analysis is the ability to identify the weak element of the structure and provides realistic prediction of demand models.

Dynamic time history analysis

Dynamic time history analysis (DTHA) provides the structure response over time, both before and after imposed loads. DTHA can be linear or non-linear, the inputted time history is alternatively constituted by force or acceleration and offers a full assessment of the structure's behaviour under load, even in complex building typology. The systemic response is derived at multiple time points, through the resolution of equation of motion of the structure. The Nonlinear THA permits the influence of nonlinearity of geometry and inelasticity of materials under the dynamic loading to estimate the behaviour of displacement and collapse load of a structure. A basic outline of NLDTHA is constituted by six consecutive steps (Muntasir, 2015):

- Definition of ground motion suite;
- Performance of the finite element model;
- Estimation of the component responses;
- Development of the probabilistic Seismic Demand Models (PSDM);
- Definition of the components limit states;
- Development of Fragility Curves.

Response history analysis (RHA)

Nonlinear response history analysis (NRHA) is used in both engineering industry and academia to assess the seismic performance of structures and to validate simpler analysis methods used in design or assessment (Grant, 2014). NRHA is the most general and most detailed analytic modelled approach in the earthquake engineer's toolkit, involving the numerical solution of the equation of the motion allowing for both material and geometric nonlinearity. The NRHA is carried out for a newly constructed structure, validation of a new proposed design or existing structure's performance-based vulnerability assessment. The structure's response as a function of time is determined when the structural system is subjected to ground motion intensity.

3.3.3 Hybrid methods

As suggested by the name, hybrid vulnerability functions and damage probability matrices are derived by combining post-earthquake damage statistical data with simulated, analytical damage from a mathematical numerical model of the building typology under consideration. The hybrid method is widely used to fill the lack of historical data of past seismic events in some areas, for some intensities or building types, integrating the empirical data with numerical simulations. Furthermore, it can also be used to reduce computational efforts in case of the construction of a complete

analytical vulnerability methods. On the other hand, these methods are difficult to calibrate because it is complicated to manage the uncertainties deriving from two different sources, therefore they are not directly comparable: historical data have intrinsic uncertainties related to their collection and classification, while analytical procedure contains uncertainties quantified and defined during the generation of the models.

3.4 Liquefaction vulnerability assessment

It has long been recognized that sands tend to settle and densify when they are subjected to earthquake shaking. If the sand is saturated and there is no possibility for drainage, so that constant volume conditions are maintained, the primary cause of the shaking is the generation of excess pore water pressures. Settlement then occurs as the excess pore pressures dissipate.

Based on the earliest studies (Lee and Albaisa, 1974; Silver and Seed, 1971; Tatsuoka et al., 1984; Tokimatsu and Seed, 1987) it appears that the primary factors controlling earthquake-induced settlement are the cyclic stress ratio for saturated sands with pore pressure generation and the cyclic shear strain for dry or partially saturated sands, together with the N-value for the sand and the magnitude of the earthquake.

The liquefaction induced soil movements are the main cause of damage on buildings. Dashti and Bray (2013) provide a comprehensive list of the several mechanisms spreading in the ground that induces different movements to the structure. The expected movements collected by Dashti and Bray (2013) are categorized as either volumetric-induced or shear-induced deformations (Figure 3.14).

The primary volumetric-induced displacement mechanisms are (Dashti and Bray, 2013):

- Localized volumetric strains during partially drained cyclic loading controlled by 3-D transient hydraulic gradients (Figure 3.14a);
- Downward displacement due to sedimentation or solidification after liquefaction or soil structure break-down;
- Consolidation-induced volumetric strains as excess pore water pressures dissipate and the soil's effective stress increases.

The primary shear-induced displacement mechanisms are:

- Partial bearing failure under the static load of structures due to strength loss in the foundation soil resulting in punching settlements or tilting of the structure (Figure 3.14b);

- Cumulative ratcheting foundation displacement due to SSI-induced cyclic loading near the edges of the foundation (Figure 3.14c).

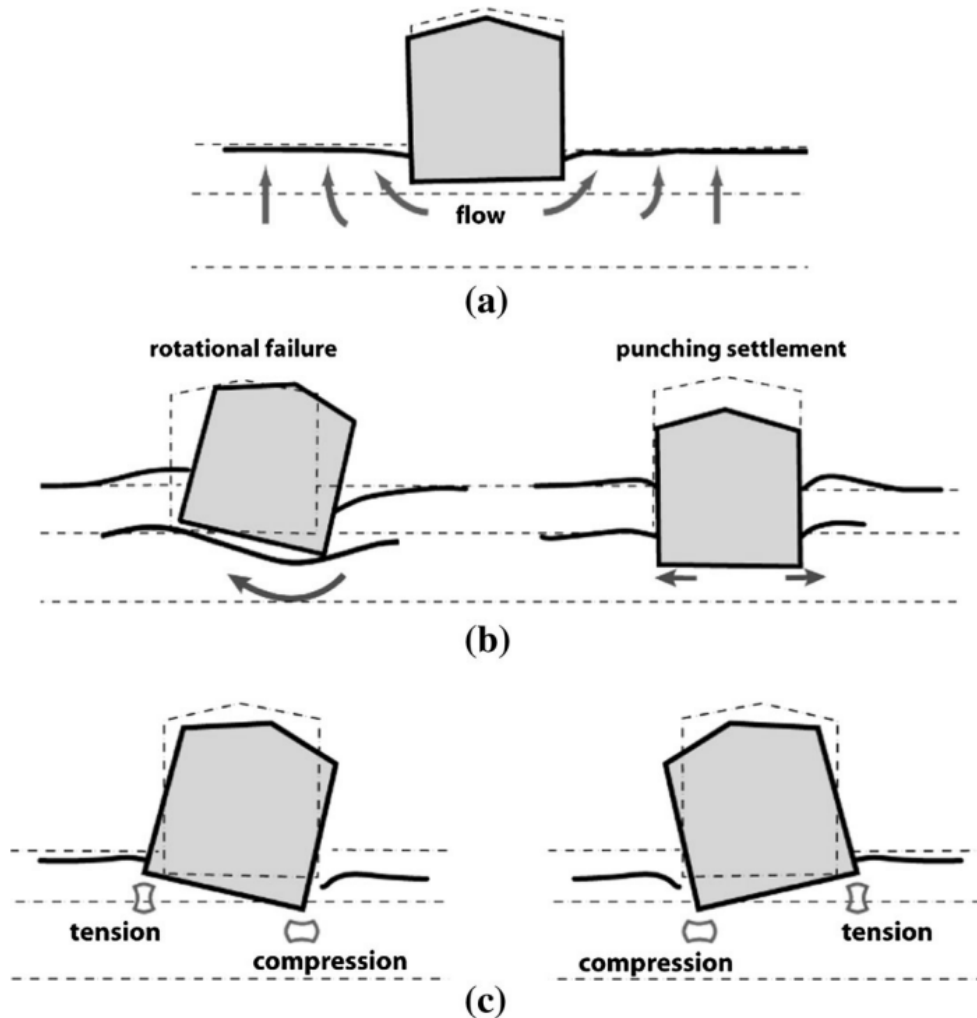


Figure 3.14 - Liquefaction-induced displacement mechanisms: a) volumetric strains caused by water flow in response to transient gradients; b) partial bearing failure due to soil softening; and c) SSI-induced building ratcheting during earthquake loading (from Dashti and Bray 2013).

For liquefaction, several methods are proposed to predict absolute settlements. The state-of-the-art practice for this evaluation largely relies on empirical procedures developed to estimate post-liquefaction, one dimensional consolidation settlement in free-field conditions (e.g., Tokimatsu and Seed, 1987; Ishihara and Yoshimine, 1992). According to Ishii and Tokimatsu (1988), this assumption can be reasonably accepted only if the width of the foundation is at least twice or three times larger than the thickness of the liquefiable soil layer.

However, the main limitation of these empirical procedures is that none of them considers the soil-structure interaction and the resulting complex mechanisms, for example the SSI-induced building ratcheting during earthquake loading (Dashti and Bray, 2013). Based on the results of numerical analyses and attributing liquefaction induced settlements to the seismic excitation characteristics and the post-shaking degraded static factor of safety, Karamitros *et al.* (2013) provide a simplified analytical formula for the estimation of absolute settlement of strip and rectangular footings with a clay crust. Such settlement is associated with a "sliding-block" type of punching failure through the clay crust and within the liquefied sand layer. Bray and Macedo (2017) performed a large number of parametric numerical analyses and proposed to express the total settlement as a sum of three contributions respectively induced by shear, volume deformation and sand ejecta; in particular, the shear-induced rate is related to several properties, including the unitary contact pressure on the foundation, the thickness of the liquefiable layer and the lower planimetric dimension of the building footprint and the cumulative absolute velocity (Campbell & Bozorgnia, 2011). Performing a rich and various parametric numerical, fully coupled three-dimensional analyses of the soil–structure interaction, Bullock *et al.* (2018, 2019) define two relations to predict the statistical distribution of settlements and tilts for shallow-founded structures on liquefiable soil induced by volumetric and distortional strains. This formula has the advantage of capturing the role of most soil, ground motion and building properties.

For liquefaction assessment of low-rise buildings, Bird *et al.* (2006) distinguish the case of rigid from flexible foundation, with absolute settlements being the principal damage factor for the former, differential settlement for the latter case. In this circumstance, differential settlements induced by liquefaction on framed buildings cause a drift of columns that the authors propose to cumulate to that produced by shaking. The differential settlement is also adopted as a demand variable by Fotopoulou *et al.* (2018) in their probabilistic definition of vulnerability for low-grade structures. In general, the structural damage induced by foundation movements on a building depends on the stiffness and fragility of the structure-foundation system.

3.4.1 Karamitros *et al.* (2013)

Based on the results of numerical analyses, Karamitros *et al.* (2013) provide a simplified analytical formula for the computation of the seismic settlements of strip and rectangle footings resting on liquefiable soil with a clay crust. Such settlement is associated to a “sliding-block” type of punching failure through the clay crust and

within the liquefied sand layer. The basic idea supporting their study is that liquefaction-induced settlements are correlated to the seismic excitation characteristics and the post-shaking degraded static factor of safety. At the same time, the effect of shear-induced dilation of the liquefied subsoil is also considered. The proposed expression for the dynamic settlement ρ_{dyn} (i.e. the settlement during shaking) is shown in Eqn. 3.2, being c a foundation aspect ratio correction (where $c'=0.003$), a_{max} the peak bedrock acceleration, T the representative period of the motion, N the number of cycles of the excitation, Z_{liq} the thick liquefiable sand layer, B the structure width and FS_{deg} the degraded static factor of safety of the foundation.

$$\rho_{dyn} = c a_{max} T^2 N \left(\frac{Z_{liq}}{B} \right)^{1,5} \cdot \left(\frac{1}{FS_{deg}} \right)^3 \quad (3.2)$$

$$c = c' \left(1 + 1,65 \cdot \frac{L}{B} \right) \leq 11,65 c' \quad (3.3)$$

$$a_{max} T^2 N = \int_{t=0}^t |v(t)| dt \quad (3.4)$$

FS_{deg} in Eq. 3.2 can be calculated as the degraded bearing capacity ($q_{ult,deg}$) divided by the bearing pressure (q) (Eq. 3.6). The foundation bearing capacity failure mechanism is simulated by the Meyerhof and Hanna (1978) model for a crust on a weak layer using the degraded friction angle in (Eq. 3.5) where r_u is the average excess pore pressure ratio of the liquefied sand and φ_0 is the initial friction angle. The superficial crust is beneficial, and there is an upper bound beyond where failure occurs entirely within the crust and does not get affected by the liquefiable layer.

$$\varphi_{deg} = \tan^{-1}(1 - r_u) \tan(\varphi_0) \quad (3.5)$$

$$FS_{deg} = \frac{q_{ultdeg}}{q} \quad (3.5)$$

Such methodology was evaluated against results from many relevant centrifuge and large-scale experiments, as well as against observations of the performance of shallow foundations in the City of Adapazari, during the 1999 Kocaeli Earthquake. Even if good agreement was found among analytical predictions and liquefaction-induced settlements, the authors suggest respecting the parameters of numerical analysis in future applications.

3.4.2 Bray & Macedo (2017)

Moving from the idea that a significant amount of settlements is induced by the distortional strains generated close to the foundation toe, Bray and Dashti (2014) proposed to express the total settlement (w_{\max}) as a sum of three contributions, shear-induced (w_s), volume-induced (w_v) and ejecta-induced (w_e):

$$w_{\max} = w_s + w_e + w_v \quad (3.7)$$

In the following study, Bray and Macedo (2017) performed a large number of parametric numerical analyses and inferred analytical formulas into the calculation results. They suggest computing the different terms as follows:

- integrate with depth the volumetric strain computed with the procedure suggested by Zhang et al. (2002) to compute w_v ;
- estimate the settlement due to sand ejecta (w_e) with an empirical function, built from case histories, of liquefaction indicators like the Liquefaction Severity Number LSN (van Ballegooy et al., 2014), the Liquefaction Potential Index LPI defined by Iwasaki et al. (1978);
- compute the shear-induced settlement using the following equation Bray and Macedo (2017):

$$\begin{aligned} \ln(w_s) = & c1 + 4.59 \cdot \ln(Q) - 0.42 \cdot \ln(Q)^2 + c2 \cdot LBS \\ & + 0.58 \cdot \ln(\tanh(HL/6)) - 0.02 \cdot B + 0.84 \\ & \cdot \ln(CAV_{dp}) + 0.41 \cdot \ln(S_{a1}) + \varepsilon \end{aligned} \quad (3.8)$$

where w_s is expressed in mm, Q is the unitary contact pressure on the foundation (kPa), HL (m) the thickness of the liquefiable layer and B (m) the lower planimetric dimension of the building footprint. CAV_{dp} ($g \cdot s$) is the cumulative absolute velocity (Campbell & Bozorgnia, 2011) and S_{a1} is the spectral acceleration at $T = 1.0$ s (g). The use of CAV for the characterization of the seismic signal responds to the concept that liquefaction is more dictated by the energy released by the earthquake rather than by its peak intensity.

Particular relevance is assumed by the index $LBS = \int \frac{\varepsilon_{shear}}{z} dz$ computed integrating with depth the shear deformation ε_{shear} (Zhang et al., 2002) below the

foundation plane. It also dictates the two coefficients c_1 and c_2 , equal respectively to -8.35 and 0.072 for $LBS \leq 16$, -7.48 and 0.014 otherwise.

The term computed by Eq. 3.8 represent the median of the results of numerical analyses. In fact, the authors suggest quantifying the uncertainty connected with the use of a simplified formulation with a probabilistic normal function having a variation coefficient $\varepsilon=0.5$ in the natural logarithmic units.

3.4.3 Bullock et al. (2018)

In a recent study, Bullock et al. (2018) present a comprehensive predictive relation for the settlement of shallow-founded structures on liquefiable ground during earthquakes. The relation is derived interpolating with a non-linear regression and latent variable analysis the results of an extensive fully coupled three-dimensional numerical parametric study of soil–structure systems, validated with centrifuge experiments and adjusted with case history observations to capture all mechanisms of settlement below the foundation, including volumetric and deviatoric strains as well as ejecta. The resulting probabilistic building settlement model incorporates the influence of the soil profile, the presence and properties of the structure and the characteristics of the ground motion, thus providing engineers with a comprehensive procedure for predicting liquefaction-induced settlement of a mat-founded building. The formula is written as:

$$\ln(\bar{S})_{\text{num}} = f_{\text{so}} + f_{\text{fnd}} + f_{\text{st}} + s_0 \ln(\text{CAV}) \quad (3.9)$$

where $\ln(\bar{S})_{\text{num}}$ is the natural logarithm of the median predicted numerical foundation settlement (mm) and f_{so} , f_{fnd} and f_{st} are functions that capture effects due to the characteristics of the soil profile, foundation and the structure, respectively.

The first term is computed as:

$$f_{\text{so}} = [\sum_i H(H_{S,i} - 1 + \varepsilon) f_{S,i} f_{H,i}] + [c_0 + c_1 \ln(\text{CAV})] F_{LPC} \quad (3.10)$$

$$S, i_{(SPT)} = \begin{cases} a_0 & N_{1,60,i} < 12.6 \\ a_0 + a_{1,SPT}(N_{1,60,i} - 12.6) & 12.6 \leq N_{1,60,i} < 17.2 \\ a_0 + 4 a_{1,SPT} & 17.2 \leq N_{1,60,i} \end{cases}$$

$$S, i_{(CPT)} = \begin{cases} a_0 & q_{c1N,i} < 112.4 \\ a_0 + a_{1,CPT}(q_{c1N,i} - 112.4) & 112.4 \leq q_{c1N,i} < 140.2 \\ a_0 + 27.8 a_{1,CPT} & 140.2 \leq q_{c1N,i} \end{cases}$$

$$f_{H,i} = b_0 H_{S,i} \exp [b_1 (\max(DSI)^2 - 4)]$$

H(-) is the Heaviside step function; ε is an infinitesimal positive quantity to make H(-) equal to 1 for an argument of zero; FLPC is a flag that is equal to 1 if a low-permeability layer is present above the uppermost susceptible layer; $N_{1;60}$ is the corrected standard penetration test (SPT) blow count in the i^{th} layer; $q_{c1N;i}$ is the corrected, normalized cone penetration test (CPT) tip resistance in the i^{th} layer; $H_{S;i}$ is the thickness of the i^{th} susceptible layer; and $D_{S;i}$ is the depth from the bottom of the foundation to the center of the i^{th} susceptible layer. The term related to the presence of a low-permeability cap indicates that its influence is dependent on motion intensity.

The second term is computed as:

$$f_{fnd} = f_q + f_{B,L} \quad (3.11)$$

$$f_q = \{d_0 + d_1 \ln[\min(CAV, 1000)]\} \ln(q) \exp\{d_2 \min[0, B - \max(D_{S,1}, 2)]\}$$

$$f_{B,L} = \{e_0 + e_1 \ln[\max(CAV, 1500)]\} [\ln(B)]^2 + e_2(L/B) + e_3 D_f$$

where q is the bearing pressure of the foundation (in kPa), B is the width of a rectangular foundation (m); $L=B$ is its unitless length-to-width ratio, and D_f is the depth from the surface to the bottom of the foundation (m). $D_{S,1}$ is the depth to the centre of the uppermost susceptible layer with $N_{1;60}$ less than 17.2 blows (q_{c1N} less than 140.2). The exponential decay term included in f_q reduces the influence of q for profiles where there are no loose susceptible layers within the foundation's depth of influence. This decay term, determined to maximize model performance with respect to the numerical database, engages for layer depths greater than B (taken here as the depth of influence), rather than $1.2 B$ (per Tokimatsu et al., 2019) or $1.5B$ (per Boussinesq's solution), which were based on the size of stress bulbs beneath a square footing. Using a threshold of B rather than either of these values offered improved model R2 and reduced bias for models with deep layers and multiple layers. This slight difference may be the result of a highly non-linear and elastoplastic soil response

considered in this numerical study, which contradicts simplifying assumptions used by previous researchers in their formulation of the foundation's zone of influence.

The form and intensity threshold captured the effects of the foundation dimensions well (as demonstrated later in this paper). The orders of scaling (natural logarithm squared for B and linear for L=B and D_f) were determined by inspection to minimize residuals.

The third term is:

$$f_{st} = \{f_0 + f_1 \ln[\min(CAV, 1000)]\} h_{eff}^2 + f_2 \min[(M_{st}/10^6, 1)] \quad (3.12)$$

where h_{eff} is the effective height of the structure (m), and M_{st} is the inertial mass of the structure (kg). The orders of the terms in this equation reflect the expectation that the building's effective moment of inertia should affect its ratcheting behaviour, which in turn influences settlement. An upper and a lower bound are given to CAV are included to allow the functional form to capture the trends discussed in points (e), (f), and (i) in the previous section describing trends in the numerical model.

3.4.4 Bullock *et al.* (2019)

The paper proposes two probabilistic models for predicting the residual tilt of mat-founded structures on liquefiable ground. The first is a completely empirical model describing residual tilt or foundation's angular distortion, expressed in degrees, as a function of settlement, based on case histories. As settlement is unknown for future earthquake scenarios, the use of this model requires implementation in tandem with a probabilistic model for building settlement (Bullock *et al.*, 2019). Second, a semiempirical model for residual tilt is developed based on an extensive numerical parametric study of soil–foundation–structure systems in 3D with more than 63,000 simulations, centrifuge tests performed by several researchers, and case history observations from several earthquakes.

Simplified empirical model for Residual Tilt

The empirical model for residual tilt is based solely on case history observations. This model depends on the width of the mat foundation (B), the thickness of the non-liquefiable crust above the topmost susceptible layer in the soil profile ($D_{S,T}$), and the average settlement experienced by the foundation (S). Because of its development from case history observations, this model inherently includes the effects of SFSI-

induced building ratcheting, 3D heterogeneity in soil, and ejecta on foundation tilt, to the extent that these phenomena occurred in the case history database. The advantage of the proposed empirical model is the simple approach for predicting residual tilt, requiring only a prediction of settlement (Bullock *et al.*, 2018) and minimal additional information (foundation size and profile geometry). The case history database of buildings with mat foundations on liquefiable soils used in this study is the same that was used as part of the development of the Bullock *et al.* (2018) model for foundation settlement.

Equation 3.13 shows the form selected for the base model:

$$\ln(\theta)_r = a_1 \ln(S) + a_2 \ln(B) + a_3 D_{S,T} + \varepsilon_{r^e} \quad (3.13)$$

Table 3.2 - Coefficient values for the empirical model

Parameter	Value
a_1	0.509
a_2	-0.936
a_3	-0.102
σ_{r^e}	0.287
B_1^*	12
B_2^*	16
$\sigma_{r^e,1}$	0.342
$\sigma_{r^e,2}$	0.123
$\rho_{\theta_r^e,S}$	0.194

Semi-empirical model for residual tilt

This second model for residual tilt takes advantage of 3D, fully coupled, effective stress, dynamic numerical simulations conducted in the finite element program OpenSEES by Karimi *et al.* (2018). Over 420 models with varying soil, foundation, and structure properties were analysed under a suite of 150 ground motions, resulting in more than 63,000 numerical case histories.

The semi-empirical model for residual tilt has been developed in three phases:

1. regression of a base model on the numerical database;
2. primary adjustment of the model according to centrifuge test results;
3. secondary adjustment of the model according to the same case history observations.

All model coefficients are provided in Table 3.3 and were developed based on laboratory tests, but subsequently validated with National Center for Earthquake

Engineering Research (NCEER) field observations of liquefaction triggering (NCEER 1997). The following equation shows the form selected for the base model, using the numerical database alone.

$$\begin{aligned}
 \ln(\theta_r)_{\text{num}} = & \alpha_0 + \alpha_1 \ln(q) + \alpha_2 \ln(B)^2 + \alpha_3 L/B + \alpha_4 \ln\left(\frac{L}{B}\right) \\
 & + \alpha_5 \ln(D_f) + [\alpha_6 \ln(V_{gi}) + \alpha_7 \ln(\text{CAV})]H_{S,1.0B} \\
 & + \alpha_8 D_{S,1} + \alpha_9 H(17.2 - N_{1,60,1}) + \alpha_{10} \min\left(\frac{M_{st}}{10^6}, 1\right) \\
 & + \alpha_{11} (H/B) \left(\frac{M_{st}}{10^6}\right) + \alpha_{12} \ln(V_{gi}) + \alpha_{13} \ln(\text{CAV}) \\
 & + \varepsilon_{r,\text{num}}
 \end{aligned} \tag{3.14}$$

where $\varepsilon_{r,\text{num}}$ = logarithmic residuals following regression on the numerical database.

Equation 3.14 showed significant systematic underprediction when applied to the centrifuge test results. This underprediction is attributed to the phenomena observed in the centrifuge that are not captured sufficiently by the numerical models as described previously, especially ejection, sedimentation, and localized shear and volumetric deformations within grains below the edges of the foundation that lead to accumulated permanent rotation.

Equation 3.15 provides the adjustment using the centrifuge database:

$$\ln(\theta_r)_{\text{num}} + \gamma_0 + \gamma_1 \ln(h_{\text{eff}}) + \varepsilon_{r,\text{adj}} \tag{3.15}$$

Subsequently, a wide range of proxies of vertical heterogeneity has been selected to inspect the influence of this aspect. Furthermore, a secondary adjustment based on case history observation has been pursued.

Equation 3.16 shows the final form selected for the semi-empirical model for residual tilt.

$$\begin{aligned}
 \ln(\theta_{r^{se}}) = & \ln(\theta_r)_{\text{adj}} + \kappa_0 + \kappa_1 F_{\text{LPC}} + \kappa_2 D_{S,T} + \kappa_3 \max(H_S)_{1.0B} \\
 & + \kappa_4 (N_{NS,1.0B}/N_{S,1.0B}) + \varepsilon_{r^{se}}
 \end{aligned} \tag{3.16}$$

Table 3.3 - Coefficients for the semiempirical model of residual tilt (from Bullock et al., 2019)

Parameter	Value
α_0	-4.353
α_1	-0.329
α_2	-0.252
α_3	-0.036
α_4	-0.430
α_5	-0.121
α_6	0.003
α_7	0.026
α_8	-0.082
α_9	0.314
α_{10}	0.472
α_{11}	-0.020
α_{12}	0.234
α_{13}	0.404
γ_0	0.066
γ_1	0.165
κ_0	2.383
κ_1	1.491
κ_2	-0.168
κ_3	-0.327
κ_4	0.087
$\sigma_{r^{se}}$	0.548
$\rho_{\theta_r^{se}, S}$	0.500

3.4.5 Fotopoulou *et al.* (2018)

Fotopoulou *et al.* (2018) propose a vulnerability assessment of low-code reinforced concrete frame buildings subjected to liquefaction-induced differential displacements. The methodology proposed by Fotopoulou *et al.* (2018) results in the development of lognormally distributed fragility curves for different structural damage states as a function of the liquefaction-induced differential displacements. The layout of the proposed methodology for the vulnerability assessment of RC frame buildings subjected to liquefaction-induced differential displacements is illustrated in Figure 3.15. It involves a comprehensive set of nonlinear parametric numerical computations and statistical analysis.

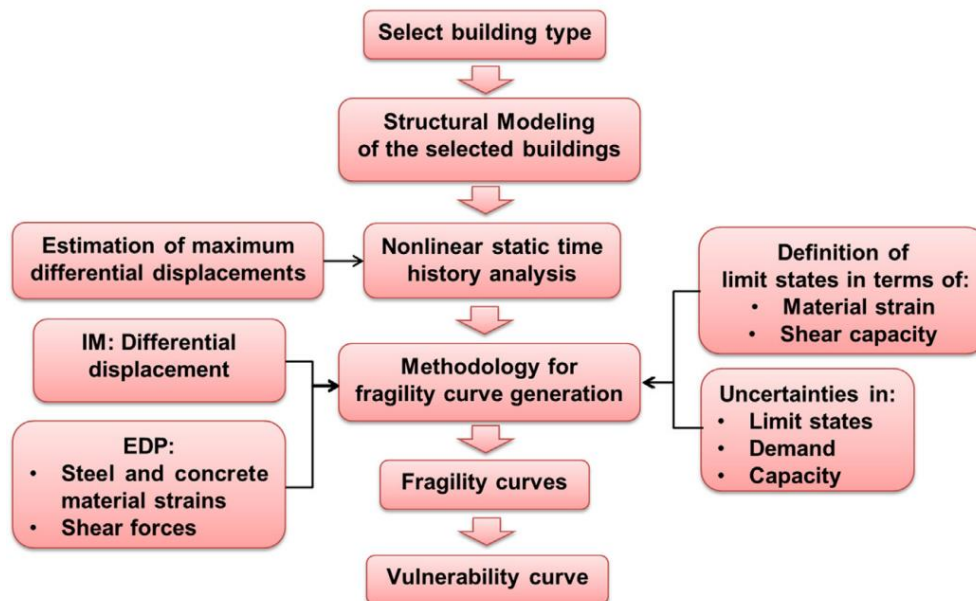


Figure 3.15 - Flowchart of the framework for vulnerability assessment of RC frame buildings subjected to liquefaction-induced differential displacements (from Fotopoulou et al., 2018).

In the method, the focus is on the differential component of liquefaction-induced ground deformation, which commonly occurs due to the heterogeneity in soil stiffness and stratigraphy both laterally and with depth. The vulnerability is assessed through probabilistic fragility functions, which describe the probability of exceeding each limit state under a range of liquefaction-induced differential displacements. Log-normally distributed fragility curves for the selected RC frame buildings subjected to settlements and lateral spreading differential deformation are constructed considering the most adverse failure mechanism (due to flexure or shear). The differential displacement is used as intensity measure (IM) that adequately correlates with structural deformation and damage. They have been obtained from statistical analyses of the results of non-linear numerical calculation considering two possible failure mechanisms, flexural damage of beams and shear failure of columns, induced by random differential displacements applied at the foundation. The formulated fragility curves are given in Figure 3.16, with the detail of median and dispersion values of the log-normal distribution for 2, 4 and 9- storey buildings.

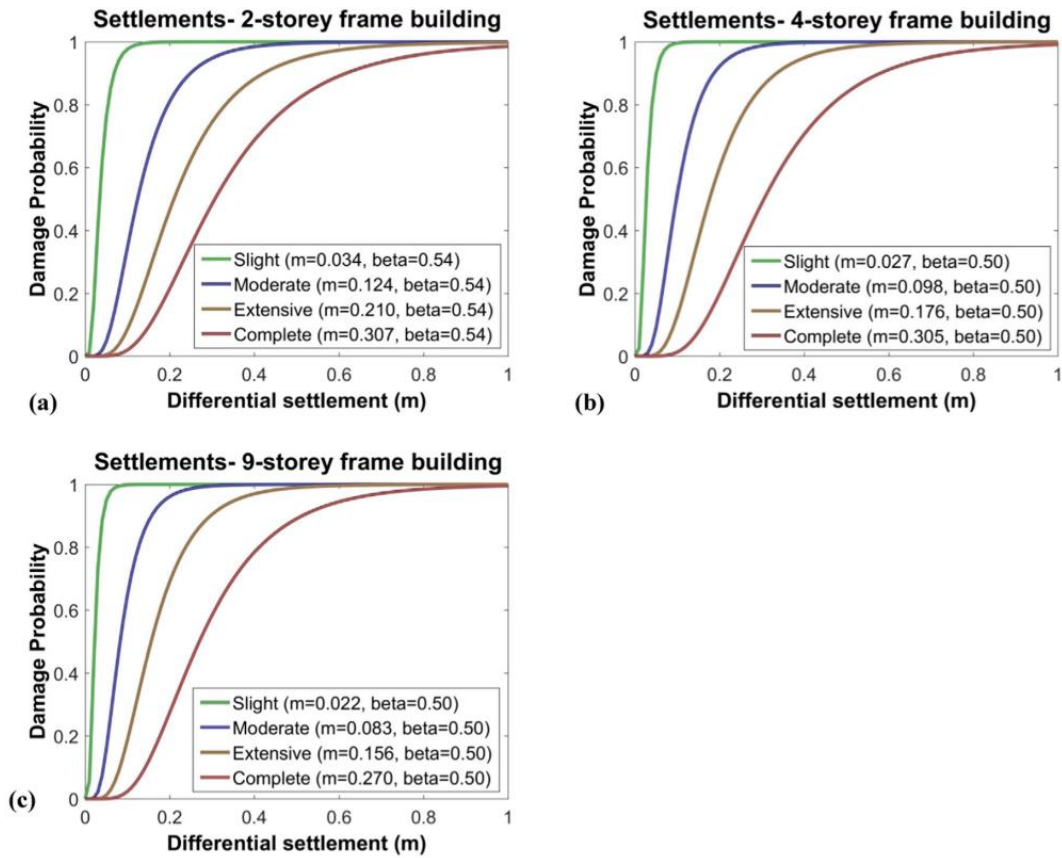


Figure 3.16 - Fragility curves formulated by Fotopoulou et al. (2018) for the (a) 2-storey, (b) 4-storey and (c) 9-storey frame buildings subjected to differential settlements due to liquefaction (from Fotopoulou et al., 2018).

Chapter 4. SUBSOIL CHARACTERIZATION AT URBAN SCALE

A crucial aspect of liquefaction risk assessment consists in the subsoil characterization, with the stratigraphic classification into homogeneous soil layers and the identification of the susceptible volumes, with the aim of constructing 2D and 3D geo-mechanical models. In the current practice, the CPT-based soil behaviour type (SBT) and the soil behaviour type index (I_c), are widely used to identify soil boundary discontinuities (Robertson, 2016).

Sometimes, the interpretation of subsoil profile is not immediate and unique, due to the lack of evident boundary changes. In these cases, the need is felt for sound, widely applicable tools that provide univocal identification of subsoil strata. Statistical procedure, developed over the years, provides a less subjective interpretation of the subsoil and, in conjunction with artificial intelligence, can lead to improving the current methodology obtaining an objective and extensive site characterization. This chapter exposes a data-driven analysis for the subsoil stratigraphic recognition combining geostatistical tools and AI genetic algorithms.

The presented procedure is calibrated and validated on the case study of Terre del Reno (Italy), homogeneously covered by about 1700 geognostic surveys available in the “PERL” database. “PERL” (stand for “Protocollo Emilia-Romagna Liquefazione”) is research project, carried out by the Emilia Romagna Region (RER), CNR-IGAG and UniCas-DiCeM, aiming to provide a reliable procedure for liquefaction risk assessment and a seismic microzonation.

From the geodatabase, 130 pairs of complementary CPT and boreholes were extracted to calibrate the method, defined as the couples of surveys located at a relative distance less than 30m, considered for this purpose as spatially correlated. Starting from the information available from the boreholes, a geologic-sedimentologic study has been carried out to define the main stratigraphic units.

In parallel, CPT profiles are processed with a statistical method based on the spatial variability analysis of the measured parameters, identifying statistically homogeneous layers and associating to each of them the correspondent stratigraphic unit reported in the complementary borehole. At this stage, an artificial intelligence algorithm has been calibrated merging the outcomes derived from couples of CPTs and boreholes. Subsequently, the procedure has been applied to the remaining CPTs, combining the geological and geotechnical knowledge of the subsoil in an efficient and automatic way to enable a large-scale reconstruction of the subsoil stratigraphy.

4.1 Methodology

The proposed approach aims to define a methodology for the subsoil stratigraphic recognition, applicable at the urban scale. In practice, this operation is based on the interpretation of a considerable amount of data coming from different sources. The most diffused approach is to combine the borehole logs stratigraphy and Cone Penetration Test results in a deterministic way with a consequent subjectivity of the interpretation of available data.

The proposed procedure, summarized in Figure 4.1, identifies the main lithologies from borehole log stratigraphies, the layer discontinuities from the sectioning with statistical test of the CPT profiles and the automatized stratigraphic classification of each statistically homogeneous layer from AI.

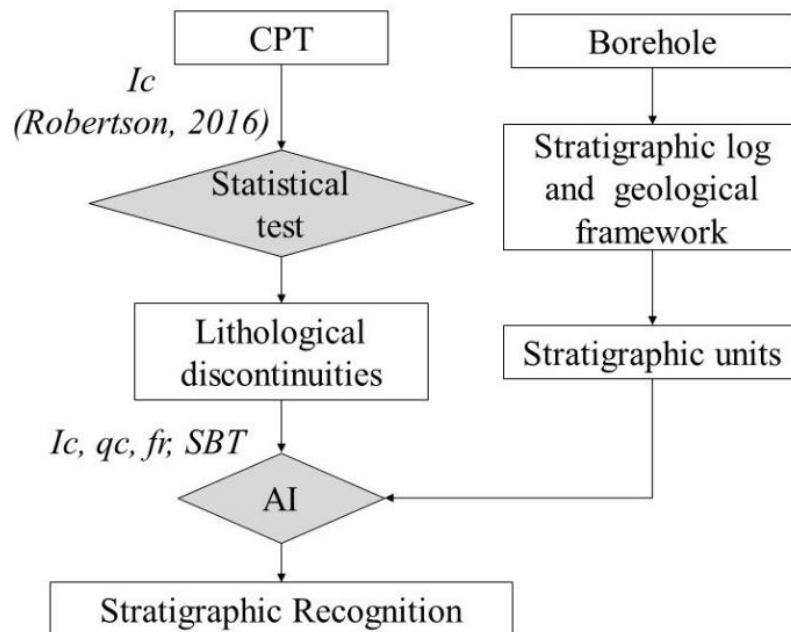


Figure 4.1 - Proposed methodology for the subsoil stratigraphic recognition.

4.1.1 Definition of stratigraphic units

The definition of the main stratigraphic units detectable in the studied area requires a detailed geological, hydrogeological, geomorphological and sedimentological framework.

The stratigraphic reference units for the selected case study are defined by combining the information from the geological framework and the borehole log stratigraphy.

The detail of the stratigraphic model, its extension and stratigraphic classification are strictly related to the typology of the performed analysis (i.e. subsidence, liquefaction, design of structures and infrastructures).

Therefore, the model (depth and thickness of the strata) and the stratigraphic units are defined according to the analyzed phenomenon (i.e., for a liquefaction risk assessment, the liquefiable layers).

4.1.2 Soil boundaries discontinuities

The homogeneous soil layers within the CPT profiles are identified based on the soil behaviour type index I_c (Robertson, 2016). The automatic procedure provides an accurate interpretation of the CPT tests considering the spatial correlation of the measured values along the vertical profile.

This statistical test verifies the equality of the means and the variance of two subsets of data. The two subsets of data (namely Ω_1 and Ω_2 , with size respectively equal to n_1 and n_2 , average \bar{Q}_1 and \bar{Q}_2 , and variance σ_{12} and σ_{22}) are identified along with the vertical CPT profile with a moving window W_{d0} divided by d_0 .

The T ratio (Eq. 4.1) and the intra-class correlation coefficient ρ_I (Eq. 4.2) are calculated along with the vertical CPT profile.

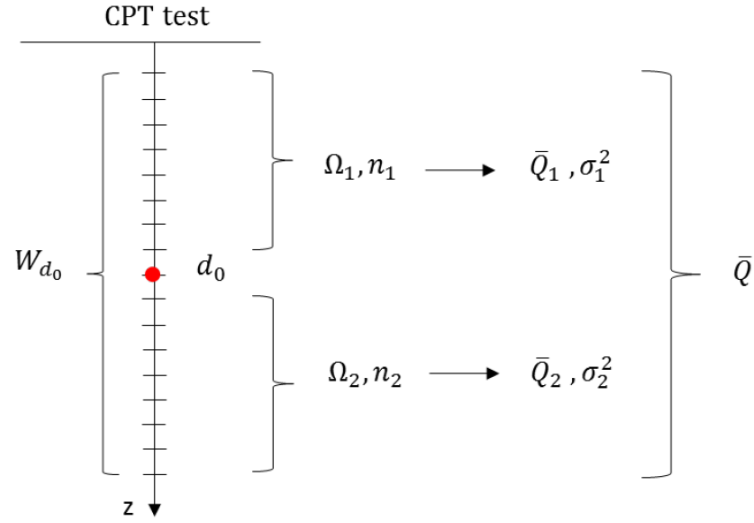


Figure 4.2 - Definition of the two subsets of relevant parameters along the vertical axis of CPT test (from Spacagna et al, 2015).

$$T = \frac{\bar{Q}_1 - \bar{Q}_2}{\gamma_w} \sqrt{\frac{n_1 n_2}{n_1 + n_2}} \quad (4.1)$$

Where:

$$\gamma_w = \frac{n_1}{n_1 + n_2 - 1} \sigma_1^2 + \frac{n_2}{n_1 + n_2 - 1} \sigma_2^2 \quad (4.2)$$

$$\sigma_1^2 = \frac{1}{(n_1 - 1)} \sum_{i=1}^{n_1} (Q_i - \bar{Q}_1)^2 \quad (4.3)$$

$$\sigma_2^2 = \frac{1}{(n_2 - 1)} \sum_{i=1}^{n_2} (Q_i - \bar{Q}_2)^2 \quad (4.4)$$

$$\rho_l = \frac{\gamma_b^2}{\gamma_b^2 + \gamma_w^2} \quad (4.5)$$

Where:

$$\gamma_b^2 = \frac{1}{n_1 + n_2 - 1} \sum_{i=1}^{n_1 + n_2} (Q_i - \bar{Q})^2 \quad (4.6)$$

where \bar{Q} is the average of the data Q_i belonging to the window w_{d_0} , with $i=1, 2, \dots, (n_1 + n_2)$.

To define the window W_{d_0} , the geostatistical approach proposed by Spacagna *et al.* (2015) suggests to calculate the one-dimensional experimental variogram of the variable (Chilès & Delfinet 2012), with a lag equal to the minimum distance of measured point, following the Equation 4.7.

$$\gamma(h) = \frac{1}{2N(h)} \sum_{i=1}^{N(h)} (z(i) - z(i+h))^2 \quad (4.7)$$

where $z(i)$ is the value of the considered variable at a location, $z(i+h)$ is the value of the variable at the distance h , and $N(h)$ is the number of couples of points with a distance equal to h . This spatial correlation of the variable is modelled with a theoretical function. In the present study, the spherical model (Chilès & Delfinet 2012) is adopted to interpolate the spatial correlation (Eq. 4.8).

$$\gamma(h) = \begin{cases} C \left(\frac{3h}{2a} - \frac{1}{2} \left(\frac{h}{a} \right)^3 \right) & 0 \leq h \leq a \\ C & h > a \end{cases} \quad (4.8)$$

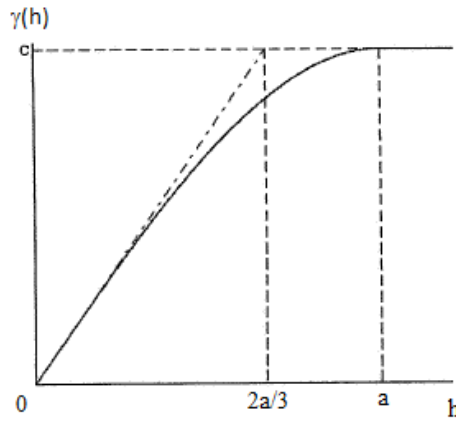


Figure 4.3 – Spherical variogram.

In general, the variogram $\gamma(h)$ is an increasing function with the distance h . The model introduces two parameters. The sill C describes the level of spatial variability, and the range a represents the maximum distance at which spatial correlation is observed.

The amplitude of w_{d_0} used for the statistical test is defined as a ratio of the range a . The Tratio and ρ_I are calculated for each point d_0 , implementing two new vertical

profiles. The higher values of T ratio and ρ_I correspond to a change of behaviour of the CPT-based parameters I_c .

The critical value of the parameter T ratio (t_c) is evaluated considering the 90% confidence interval of the T ratio distribution and is calculated following Equation 4.9.

$$t_c = \mu_{T_{ratio}} \pm 1,65 \sigma_{T_{ratio}} \quad (4.9)$$

where $\mu_{T_{ratio}}$ and $\sigma_{T_{ratio}}$ are respectively mean and standard deviation of the distribution of the T ratio values along the vertical profile. The depth to which T ratio values fall outside the confidence interval represents a change of behaviour along the CPT profile.

The critical value of ρ_{Ic} is calculated following the Equation 4.10 proposed by Herzagy, Mayne, and Rouhani (1996).

$$\rho_{Ic} = \mu_{\rho_I} + 1,65 \sigma_{\rho_I} \quad (4.10)$$

where μ_{ρ_I} and σ_{ρ_I} are respectively the mean and standard deviation of the distribution of the ρ_I values along the vertical profile. The depth to which ρ_I values are higher than ρ_{Ic} represents a change of behaviour along the CPT profile.

The transition between two different homogeneous layers is assumed at the d_0 depth points where both critical conditions occur simultaneously.

The described algorithm is implemented with open-source R software (R Core Team, 2021) and reported in Appendix B.

An example of a sectioned CPT profile is presented in Figure 4.4.

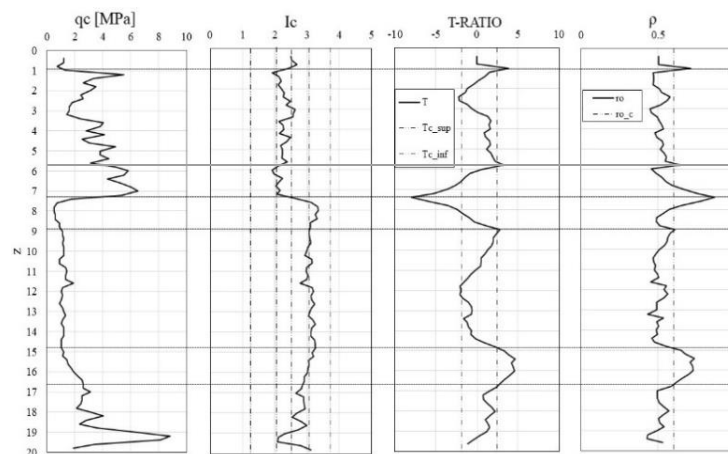


Figure 4.4 - Example of sectioned CPT profile.

4.1.3 Stratigraphic recognition with AI

In the proposed methodology, the attribution at each statistically homogeneous layer the correspondent stratigraphic unit, is automatically carried out with artificial intelligence (AI), studying the underlying relation between cone penetration tests information and stratigraphic properties.

Reale *et al.* (2018) proposed an automatic classification of fine-grained soils using CPT measurements and Artificial Neural Network. Ching, Wu & Phoon (2020) and Ching *et al.* (2020) proposed a Hierarchical Bayesian Model (HBM) to construct transformation models for soil and rock properties.

The algorithms are trained comparing the outcomes derived from couples of CPT-boreholes considered spatially correlated, providing a complementary description of the subsoil. The CPT-borehole distance has been chosen based on the analysis of the spatial structure of cone tip resistance in the horizontal direction. A measure of the spatial correlation is the scale of fluctuation, representing the maximum distance over which the points are significantly related (Chilès & Delfinet, 2012).

The calibration procedure is structured as follows: first, the couples of complementary CPT and boreholes are extracted from the geodatabase; once CPT profiles are processed, to each statistically homogeneous layer is associated the stratigraphic unit reported in the complementary borehole; last, the CPT output parameters and their correspondent stratigraphic recognition are used to train, test and validate various algorithms.

The artificial classifier characterized by the highest efficiency is selected and applied to automatically assign the stratigraphic units to the remaining sectioned cone penetration test profiles distributed over the studied area.

4.2 Considerations

The proposed methodology has a simple logical structure: it is based on the comparison of data coming from two different geotechnical surveys, which are processed thanks to powerful artificial intelligence algorithms, maintaining spatial information thanks to geostatistical tools. This research attempts to fill a gap still present in civil and geotechnical engineering: the construction of subsoil models over a large area. In particular, the study provides a valid tool that must be understood as a further piece to add to the knowledge achieved so far. The proposed procedure has the

advantage of being totally automated and therefore repeatable in similar contexts with a click of the mouse. However, the use of the proposed methodology is recommended in case studies where a rich database of geotechnical investigations is available. In particular, there must be copious areal coverage of CPT tests and boreholes.

In any case, in future studies, it is possible to calibrate the same procedure on other types of surveys, in order to make the methodology universally valid and applicable even in contexts where the availability of geotechnical and geological surveys is limited.

Chapter 5. LIQUEFACTION VULNERABILITY OF BUILDINGS: THE PROPOSED TOOL FOR A PRELIMINARY ASSESSMENT

5.1 Abstract

From the present chapter, has been extracted the paper “*Settlements and angular distortions of shallow foundations on liquefiable soil*” (Baris *et al.*, 2022). The study proposes a rapid calculation for the prediction of the angular distortion induced by liquefaction on shallows founded low-rise buildings. This method is applicable for the preliminary screening of risk at the large scale, e.g. cities, districts. To this aim, a large number of two-dimensional coupled numerical analyses are performed, parametrically varying the stratigraphic and mechanical conditions of the subsoil, the ground motion characteristics and the equivalent structural properties of the building. The analysis leads to infer a relation with the relevant properties by means of artificial neural networks.

5.2 Numerical analysis

5.2.1 Definition of the model

The implemented numerical model simulates with a Finite Difference code (FLAC v8, Itasca, 2016) the two-dimensional layout depicted in Figure 4.1 developed over a width of 40 meters and a depth of 20 meters. Luque and Bray (2015 and 2017) showed that the primary aspects of the dynamic response of a 3D system in terms of liquefaction-induced building settlements can be captured by 2D analyses when tributary masses

Liquefaction Vulnerability of Buildings: the proposed tool for a preliminary assessment

and stiffnesses are given to the buildings. The three-layer subsoil model, that includes an upper low-permeability cap (Layer #1), an intermediate liquefiable layer (Layer #2) and a stiffer base (Layer #3), has been chosen as one of the most frequent subsoil conditions, where the predominant role is played by the intermediate liquefiable layer. Tests are available in the literature (e.g. Millen et al., 2020) to assess whether real conditions conform to this scheme characterized by a single liquefiable layer or alternative models including multiple liquefiable layers are needed. The calculation mesh consists of 13,980 rectangular elements of 0.8m width and variable heights (0.5 m for the above and below layers, 0.4 for the liquefiable layer), these dimensions chosen after the suggestion of Kuhleimeyer & Lysmer (1973), who found that propagation of seismic waves in continuum media can be simulated with sufficient accuracy if the element's dimension is smaller than 1/10 of the minimum propagating wavelength.

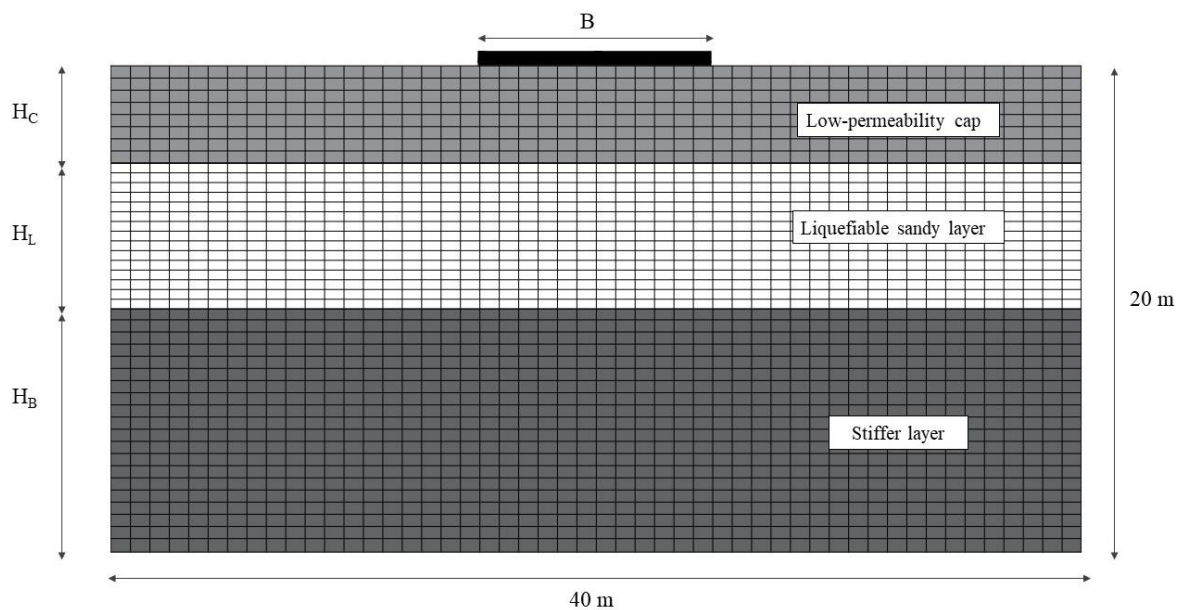


Figure 5.1 - Layout of the implemented numerical model.

The stress-strain response of the liquefiable soil has been simulated with PM4Sand Version 3.1 (Boulangier and Ziotopoulou, 2017) chosen thanks to its capability to capture the cyclic behavior of saturated sand, while the stress-strain response of the shallow and deepest layers is simulated using Mohr-Coulomb hysteretic model, considering the stress state induced into the subsoil by the above building. In principle, upper and lower layers affect the seismic excitation of the whole system and concur to determine the settlements of foundation. Thus, more refined constitutive models would be preferable for these layers too. For instance, the pore pressure build-up in the upper

Liquefaction Vulnerability of Buildings:
the proposed tool for a preliminary assessment

crust could reduce shear strength and eventually increase settlements. To this aim an interesting analysis is provided by Dahl et al., 2011, who compared the cyclic undrained shear strength τ_{cyc} of materials with different plasticity to the static undrained shear strength s_u . Their study shows that τ_{cyc} is lower than s_u with differences in the order of 30 or 40% (with respectively 10 or 30 cycles) for low plasticity soils ($PI < 10\%$). For higher plasticity materials, differences are less relevant, being in the order of 10 to 20 % for respectively 10 or 30 cycles. Therefore, the use of more complex models (e.g. PM4Silt - Zytoupolou et al., 2018) would be justified for low plasticity soil, while would introduce an unnecessary complexity for more plastic soils. In the present study, crust broadly indicates a category of plastic soils. Furthermore, the adopted simplification, made in the spirit of a preliminary calculation, has the advantage that the constitutive parameters of Mohr-Coulomb model can be determined with routine in-situ or laboratory tests. Nevertheless, the variability of seismic excitation in the intermediate layer is investigated considering largely different seismic inputs in the parametric analysis.

The constitutive parameters for each model (see Table 5.1) have been set from the back analysis of a case study in Terre del Reno (Italy) (Fioravante et al., 2013; Sinatra and Foti, 2015; Facciorusso et al., 2016). In this scheme, the upper crust is made of a silty-clayey soil ($PI = 15 \div 20\%$), while the lower base is made of relatively stiff clays. The availability of data on a such well-documented case study enabled to validate the adopted mechanical schematization versus observation (see *Appendix A*). The calibration on this specific case study does not affect generality, as the role of the most relevant soil properties has been explored systematically modifying them in a parametric analysis.

Starting from the natural unit weights and the void ratios reported for the different strata by Fioravante et al. (2013), the solid phase and dry unit weights are assigned in Table 1. In the same table, permeability for each stratum is derived from the work of Sinatra and Foti (2015) based on the analysis of CPTU tests. The small strain elastic stiffness parameters are inferred from the shear wave propagation velocity computing the small strain shear modulus before and computing the bulk modulus by imposing a Poisson's ratio equal to 0.3.

$$G_0 = \rho V_s^2 \quad (5.1)$$

$$E = 2G(1 + \nu) \quad (5.2)$$

$$K = \frac{E}{3(1-2\nu)} \quad (5.3)$$

Stiffness degradation and damping for the lower base and crust have been simulated by means of a cubic equation with two parameters c_0 and c_1 calibrated by fitting the experimental G/G_0 and D vs γ curve provided by Fioravante et al. (2013) and Sinatra and Foti (2015) (Figure 5.2). In this particular calculation, cyclic simple shear tests have been simulated with the numerical code and c_0 and c_1 have been fixed with a trial-and-error procedure looking for the best match between numerical and experimental results.

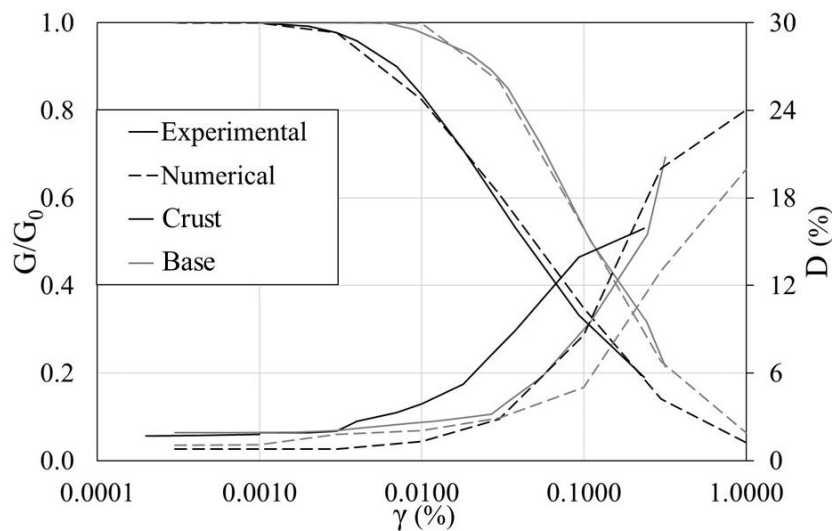


Figure 5.2 - Shear modulus degradation and damping curves numerically and experimentally (Fioravante et al., 2013 and Sinatra and Foti, 2015) obtained for the different subsoil layers.

The strength parameters for the Mohr Coulomb model, namely friction angle (ϕ'), cohesion (c') and undrained shear strength (s_u) are extracted from the work of Sinatra and Foti (2015) that provides them from the analysis of laboratory and CPT tests. The effective strength values and the large strain stiffness parameters for the cohesive soils are taken from the literature (Itasca Consulting Group, Inc., 2016).

The *PM4Sand* Version 3.1 (Boulanger and Ziotopoulou, 2017) adopted for the liquefiable layer represents an evolution of the Dafalias and Manzari (2004) formulation, being a stress-ratio controlled, critical state compatible, bounding surface plasticity model developed primarily for earthquake engineering applications (Boulanger and Ziotopoulou, 2013 and 2015). In *PM4Sand* the Jefferies state variable $\psi = e - e_{cs}$ is modified as proposed by Boulanger (2003):

Liquefaction Vulnerability of Buildings: the proposed tool for a preliminary assessment

$$\xi_R = D_{R,CS} - D_R \quad (5.4)$$

where D_R and $D_{R,CS}$ are the relative densities at respectively current and critical state. Deformation is regulated by the stress-ratio and developing according to multiple bounding surfaces. In particular, the model incorporates the bounding, dilation and critical surfaces of Dafalias and Manzari (2004) but removes the Lode angle dependency of friction angle. Thus the bounding (M^b) and dilation (M^d) ratios are related to the critical stress (M) ratio by the following simpler expressions:

$$M^b = M \exp(-n^b \xi_R) \quad (5.5)$$

$$M^d = M \exp(n^d \xi_R) \quad (5.6)$$

Where n^b and n^d are calibration parameters and M is computed as a function of the critical state friction angle.

The PM4Sand model has been calibrated capturing the cyclic undrained behaviour of the liquefiable sandy layer seen by Facciorusso et al. (2016). In particular, four triaxial undrained cyclic tests have been numerically simulated with the adopted code (FLAC v8, Itasca, 2016) matching the liquefaction resistance curve (CSR vs N_{liq}). The calibrated parameters are listed in Table 5.1 while the comparison of the numerical and experimental results is shown in Figure 5.3.

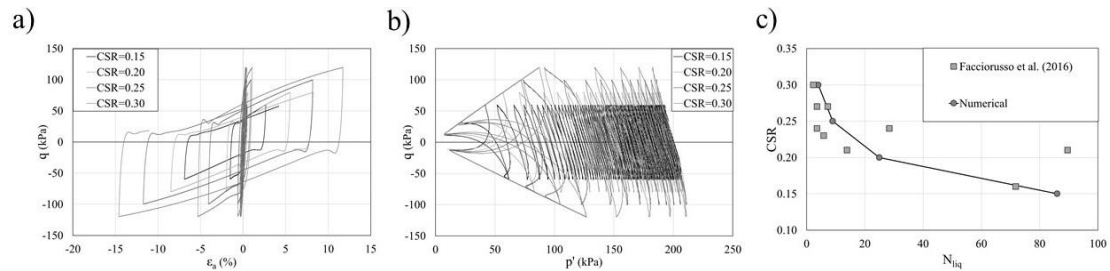


Figure 5.3 - Results of the numerical liquefaction tests in terms of a) deviatoric stress against axial strain curves; b) deviatoric stress against main effective stress curves; c) liquefaction curves.

Table 5.1 - Subsoil parameters assigned in the calculation.

Stratum	Model	n	γ_{nat}	γ^s	Permeability	ϕ' (°)	c' (kPa)	c_u (kPa)	K (MPa)	G (MPa)	c0	c1	Dr	G0	hp0	nb	Nd
			(kN/m ³)	(kN/m ³)													
Crust	Mohr-Coulomb hysteretic	0.5	16.5	22.5	1.00E-07	28	2	34	2.67	1.6	-3	0.2	/	/	/	/	/
Liquefiable sand	PM4Sand	0.5	18.5	27.2	7.00E-06	33	0	/	16.7	10	/	/	0.4	507	20	0.5	0.1
Stiffer base	Mohr-Coulomb hysteretic	0.4	18	24.6	6.00E-08	20	8	45	0.67	0.4	-2	0.2	/	/	/	/	/

The superstructure is modeled with an equivalent beam characterized with a flexural stiffness (EI) and a contact pressure (q). The EI modulus summarizes the flexural stiffness of the foundation-superstructure complex but, for the sake of simplicity, this modulus can be conservatively computed for the sole foundation. The contact pressure q summarizes the contribution of all building floors and can be computed multiplying the number of floors times the overall unit load, i.e. the load per unit area including the self-weight of structural and non-structural elements and the accidental loads.

In Appendix A, calculation has been performed for the considered case study, on one side showing a typical output of the numerical analysis, on the other side validating the calculation scheme with reference to a case where seismic input, subsoil and building conditions are known together with the surveyed settlements induced by liquefaction.

5.2.2 Parametric study

The physical, mechanical and geometrical factors varied in the parametric analysis have been chosen following Karimi *et al.* (2018), who observed that the mean permanent settlements of buildings are affected by contact pressure, seismic input, thickness, relative density and depth of the liquefiable layer, but also by the presence of a low-permeability cap. In this calculation, the parameters for the stiffer base (Layer #3) have been set equal to the reference case (Table 1), while the crust's strength has been varied parametrically giving values of undrained shear strength equal to 25, 50 and 100 kPa. This choice has been made featuring the three typical situations of respectively normally to slightly, moderately, and highly consolidated soils. Accordingly, E_u/s_u ratios equal to 550, 300 and 150 have been respectively assigned following the suggestion of Duncan and Buchignani (1976). In any case, the effects on seismic excitation have been considered assigning largely different inputs, i.e. varying Arias Intensity and PGV.

The complete list of varied parameters is summarized in Table 5.2, positioning the water table at the ground level for all calculations. The structure-foundation system has been modeled with an equivalent continuous foundation system characterized by width (B), flexural stiffness modulus (EI) and embedment depth (H_d). The choice of continuous foundation is considered to simulate strip footings and mat foundations, which are frequently used for low rise buildings on relatively weak soils. The assumed EI values (Table 5.2) correspond to reinforced concrete beams of different flexural stiffness, with the maximum value ($EI=260MN/m$) corresponding to a beam of

Liquefaction Vulnerability of Buildings:
the proposed tool for a preliminary assessment

rectangular section 1.0x0.5 m (width x height), spanned with 4 m distance. Finally, the embedment depth has been varied between 1 and 3 m, which are typical values for shallow foundation (see Table 5.2). In addition, a set of six numerical analysis has been performed to evaluate relevance of the structure's inertial mass, simulating height/width ratio (H/B) ranging between 0.5 and 1.5. Finally, considering the fundamental role played by the earthquake magnitude, four waveforms have been applied in the analysis, extracting them from the PEER Strong Ground Motion Databases. The velocity time history of these events, chosen thanks to their largely different Arias intensity (Table 5.3), have been scaled by three amplitude factors, respectively 0.7, 1.0 and 1.6 in order to explore the influence of wider range of ground motions examining the influence of the intensity of the ground motion on liquefaction induced foundation movements. Thus, a total number of twelve time-histories were assigned. Combining the seismic input with the parameters reported in Table 5.1, a total number of 353 analyses have been carried out. The sample calculation performed in Appendix A shows that settlements start to develop for maximum r_u values larger than 0.6÷0.8 in the liquefiable material (Layer #2). This observation, coupled with the summary of results reported in Appendix B that shows maximum $r_u > 0.8$ for all cases, leads to conclude that the computed settlements are in all cases induced by liquefaction.

The typical output of calculation consists of the displacements profile below the foundation (Figure 5.4) from which the following characteristic variables are extracted:

- maximum, minimum and mean settlement: w_{Max} , w_{min} and w_{av} ;
- angular distortion: β ;
- horizontal displacement: S_{hi} ;
- horizontal deformation: ε_h .

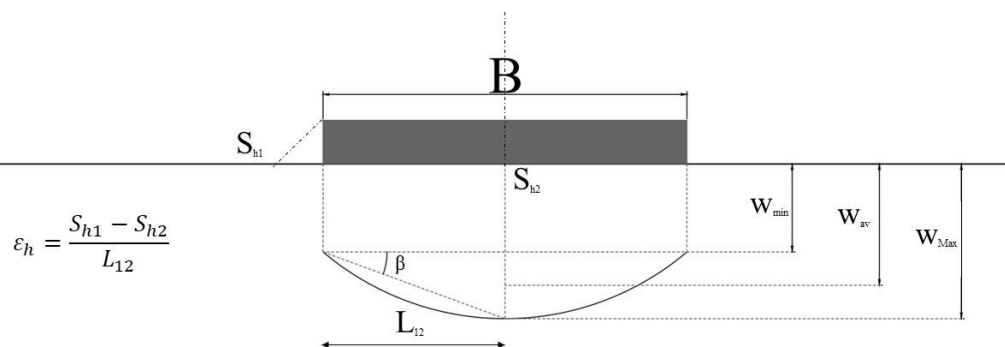


Figure 5.4 - Typical output and definition of the characteristic variables.

Liquefaction Vulnerability of Buildings:
the proposed tool for a preliminary assessment

Table 5.2 - Parameters for sensitivity analyses.

Parameter	Description	Range of variation
Hc	Layer #1 (non-liquefiable crust) thickness (m)	2 to 6 m
HL	Layer #2 (liquefiable layer) thickness (m)	4 to 12 m
Hb	Layer #3 (lower clay) thickness (m)	20 m-HL-Hc
Hd	Embedment depth (m)	1 to 3 m
Dr	Relative density of the liquefiable layer (%)	20 to 60%
s_u	Undrained shear strength of crust and lower clay (kPa)	25 to 100 kPa
B	Foundation base width (m)	10 to 30 m
Q	Contact pressure at the building foundation (kPa)	25 to 100 kPa
EI	Equivalent stiffness of the building foundation system (MN*m)	0 to 260 MN*m
PGV	Peak ground velocity (m/s)	0.23 to 0.63 m/s

Table 5.3 - Selected seismic input.

Earthquake	Mw	PGV (m/s)	Ia (m/s)
Emilia-Romagna	6.1	0.33	0.64
Northridge	6.7	0.42	4.5
Imperial Valley	6.5	0.47	1.6
Northridge	7.1	0.63	2.8

5.2.3 Sensitivity study

A sensitivity study has been initially performed to understand the relative influence of the varied parameters on the kinematic variables defined in Figure 5.4. Firstly, the relation between mean and maximum settlements (w_{av} and w_{MAX}) has been investigated as their equivalence is needed for the following analyses where their outputs are alternatively related to the angular distortion of the building-foundation system. Figure 5.5 shows a proportionality between these two variables, being the ratio w_{av}/w_{max} equal on average to 0.84, with minimum and maximum values equal to respectively 0.73 and 0.98.

Liquefaction Vulnerability of Buildings: the proposed tool for a preliminary assessment

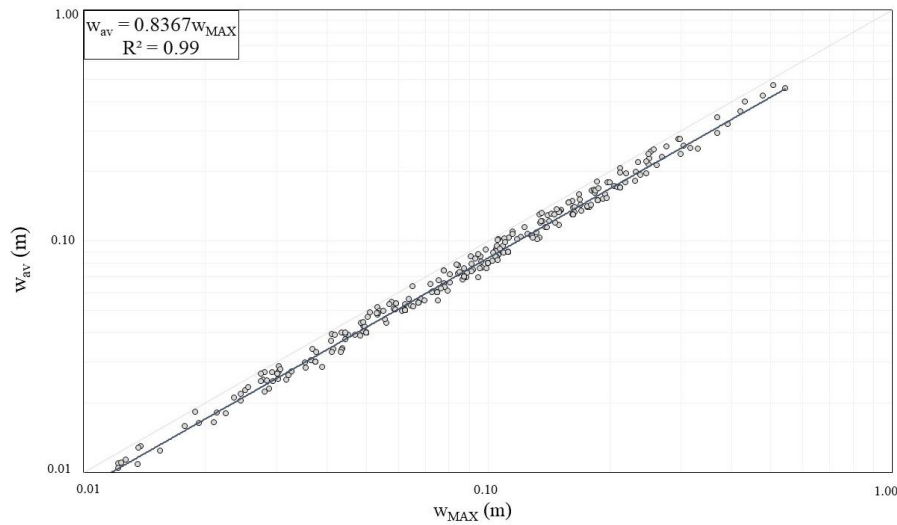


Figure 5.5 - Absolute versus mean settlement obtained in all numerical analyses.

The results of calculation are then summarized looking at the dependency of maximum, differential settlement and angular distortion (respectively w_{MAX} , $\delta = w_{MAX} - w_{MIN}$ and β defined in Figure 5.4) on the most relevant parameters varied in the analysis. Noting that, within the investigated range (1÷3 m), embedment depth H_d plays a lesser influence on the absolute and differential settlements, the role of upper crust (Figures 5.6 and 5.7), liquefiable layer (Figure 5.8 and 5.9) and structural characteristics (Figure 5.10, 5.11 and 5.12) is separately examined. In all Figures results are obtained assigning the seismic input of Emilia Romagna scaled for the different amplifying factors (0.7, 1.0 and 1.6). Figures 5.6 and 5.7 point out the influence of the upper impervious crust characterized with its thickness (H_c) and undrained shear strength (s_u). The curves show the positive role of both parameters on all the considered components of the foundation movement, attenuation rates being more remarkable for the stronger seismic events. Settlements reduce almost linearly within the considered thickness range ($H_c \leq 6$ m) for the higher seismic intensities ($f=1.0$ and 1.6), while reduction is smoother for the lower intensity earthquake ($f=0.7$) (Figure 5.6); attenuation rate is very high for undrained shear strength s_u increasing up to 50 kPa, then drops progressively for increasing s_u (up to 100 kPa and more) (Figure 5.7). In summary, despite preventing the excess pore pressure exhaust, the impervious crust forms a bridge below the foundation that contributes with its strength to limit the buildings settlements.

Liquefaction Vulnerability of Buildings: the proposed tool for a preliminary assessment

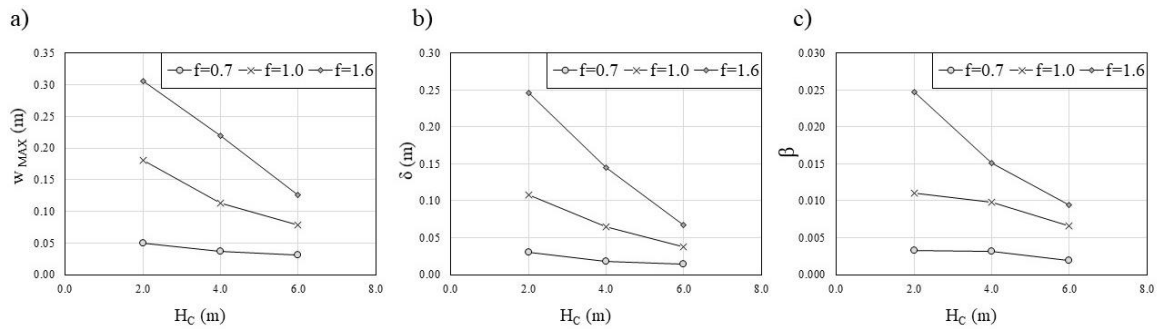


Figure 5.6 - Absolute settlement (a), differential settlement (b), and angular distortion (c) for variable thicknesses of the crust (H_C) (calculation has been performed assigning the Emilia Romagna earthquake, $H_L=6m$, $D_r=40\%$, $s_u=50kPa$, $B=10m$, $q=50kPa$, $EI=0 MN*m$).

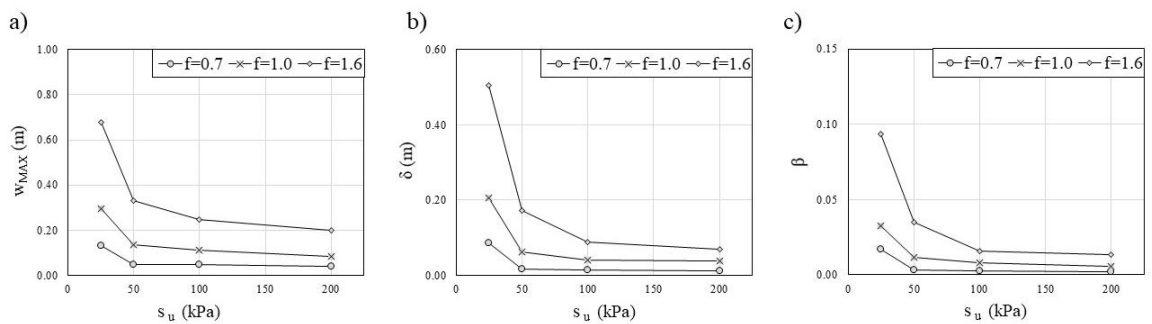


Figure 5.7 - Absolute settlement (a), differential settlement (b), and angular distortion (c) for variable undrained shear strength (s_u) of the crust (calculation has been performed assigning the Emilia Romagna earthquake, $H_L=6m$, $H_C=4m$, $D_r=40\%$, $B=10m$, $q=50kPa$, $EI=0 MN*m$).

Figures 5.8 and 5.9 point out the influence of the liquefiable layer. Here settlements and deformation increase rather continuously with thickness (H_L), being rates dependent on the earthquake intensity (Figure 5.8). On the contrary, the variation determined by soil density is sharper. Effects are particularly critical for the lowest considered density ($D_r=20\%$) with w_{MAX} reaching values as high as 2.5m (for $f=1.6$), then sharply reduce for $D_r=40\%$ and moreover for $D_r=60\%$. The latter result can be explained by the higher stiffness and lower tendency to contract seen on denser cohesionless materials (e.g. Modoni et al., 2000), while the coupled dependency on thickness and relative density justifies the assumptions made in the definition of liquefaction severity indexes (e.g. Iwasaki et al., 1978; van Ballegooy et al., 2014; Paolella et al., 2022).

Liquefaction Vulnerability of Buildings: the proposed tool for a preliminary assessment

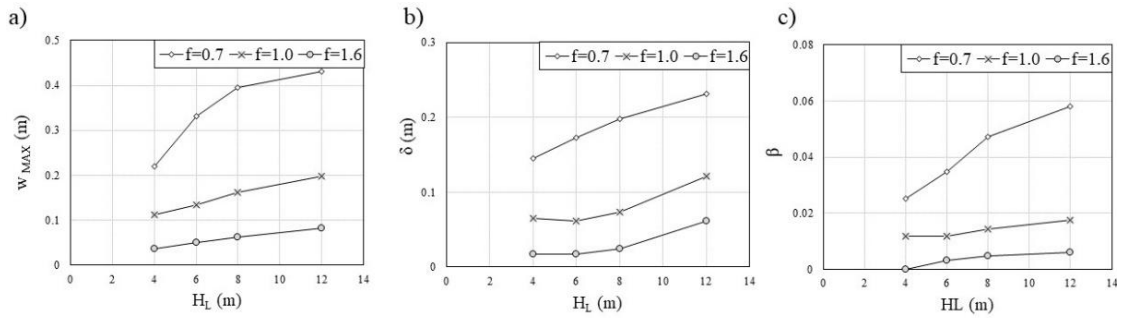


Figure 5.8 - Absolute settlement (a), differential settlement (b), and angular distortion (c) for variable thickness of liquefiable layer (HL) (calculation has been performed assigning the Emilia Romagna earthquake, $H_C = 4m$, $Dr = 40\%$, $su = 50kPa$, $B = 10m$, $q = 50kPa$, $EI = 0 M$).

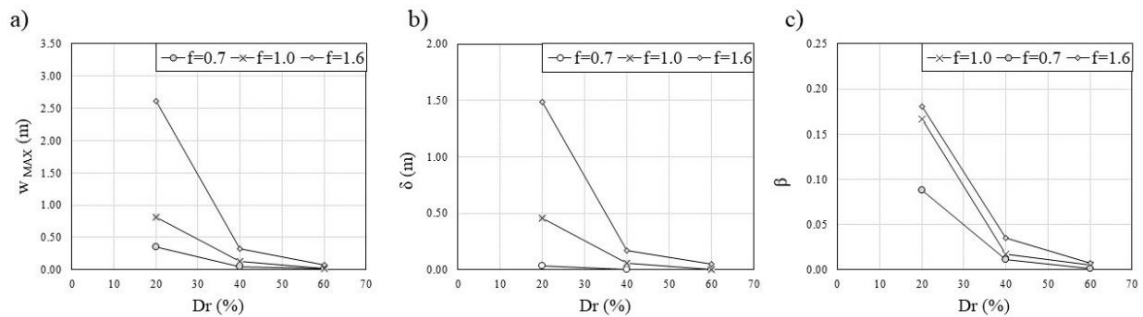


Figure 5.9 - Absolute settlement (a), differential settlement (b), and angular distortion (c) for variable relative density (Dr) of the liquefiable layer (calculation has been performed assigning the Emilia Romagna earthquake, $HL = 6m$, $H_C = 4m$, $su = 50kPa$, $B = 10m$, $q = 50kPa$, $EI = 0 MN*m$).

Finally, Figures 5.10, 5.11 and 5.12 summarize the effect of the building-foundation system. As expected, higher loads produce larger absolute and differential settlements (Figure 5.10), while foundations width B produces a reduction on the absolute settlements throughout the considered range (Figure 5.11.a), less evident on the differential component (Figure 5.11.b and c). This effect, also seen by Bray and Macedo (2017), is somehow surprising if compared with the dependency of settlements induced by static loading. It can be explained considering the relevance of the shear stresses initially activated by the foundation loads in the subsoil on the triggering of liquefaction. This effect becomes progressively marginal with the foundation width, as this solution tends to the one-dimensional scheme characterized by lower shear stresses and higher mean effective stresses. Finally, flexural stiffness EI produces a continuous reduction on the differential settlements and angular distortion (Figure 5.12.b and c) but has negligible effects on the absolute settlements (Figure 5.12.a). As will be shown later, the above sensitivity analysis and the observed dependencies have been used to infer functional relations among foundation

Liquefaction Vulnerability of Buildings: the proposed tool for a preliminary assessment

settlements, distortion and characteristic variables grouped in dimensionless parameters.

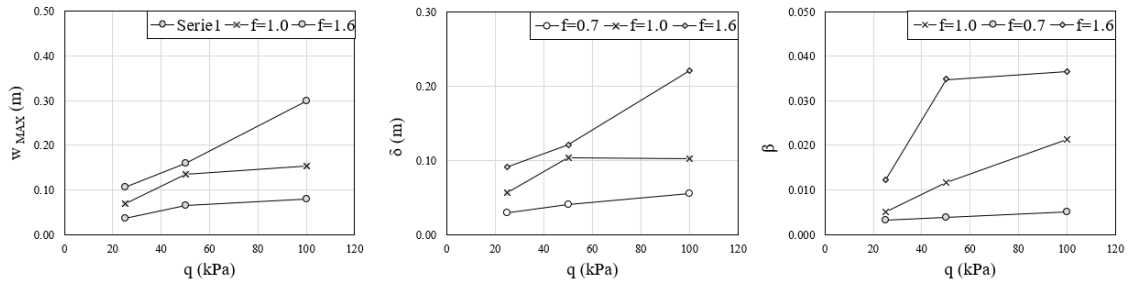


Figure 5.10 - Absolute settlement (a), differential settlement (b), and angular distortion (c) for variable relative foundation loads (q) (calculation has been performed assigning the Emilia Romagna earthquake, $HL=6m$, $HC=4m$, $Dr=40\%$, $su=50kPa$, $B=10m$, $EI=0MN^*m$).

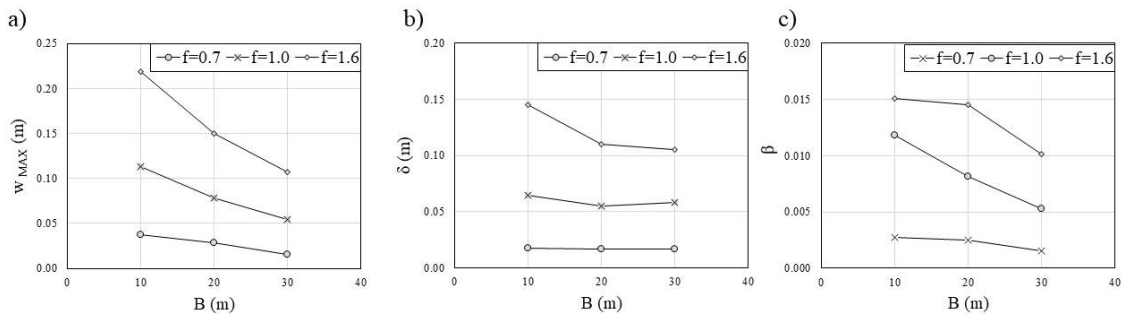


Figure 5.11 - Absolute settlement (a), differential settlement (b), and angular distortion (c) for variable relative foundation width (B) (calculation has been performed assigning the Emilia Romagna earthquake, $HL=6m$, $HC=4m$, $Dr=40\%$, $su=50kPa$, $q=50kPa$, $EI=0MN^*m$).

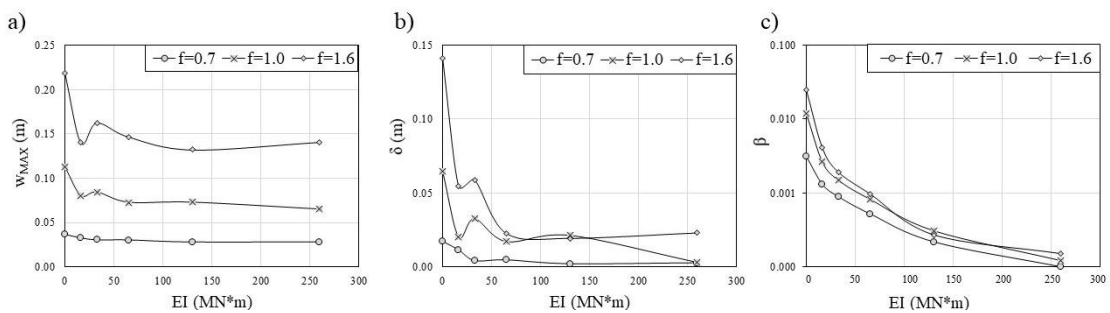


Figure 5.12 - Absolute settlement (a), differential settlement (b), and angular distortion (c) for variable stiffness (EI) (calculation has been performed assigning the Emilia Romagna earthquake, $HL=6m$, $HC=4m$, $Dr=40\%$, $su=50kPa$, $q=50kPa$, $B=10$).

5.2.4 Role of superstructure inertia

In the present study, the structure-foundation system has been simplified and modeled with an equivalent plate considering this case representative of low-rise buildings. This assumption has been made considering the observation of Karimi et al. (2018) on buildings of relatively limited height ($H/B \leq 3$), who found a negligible role on the foundation settlements played by the structure's inertial mass and height/width ratio. For the sake of completeness, the consistency of this assumption has been herein verified performing numerical analyses with B fixed equal to 10 m and varying the height/width ratio of the building (H/B) between 0.5 and 1.5. In this calculation, buildings have been simulated with equivalent linear elastic-perfectly plastic frames with pillars of 0.5x0.5 m section and beams of 0.3x0.5 m (width x height) section set at an inter-storey height equal to 2.5 m. A self-weight has been assigned to the beams equivalent to the unit load given in the simplified analysis. The effect of simplification is thus presented in Figure 5.10, showing the ratio (ρ) between the foundation movements computed with the equivalent beam (setting a distributed load equal to the sum of the weights of each floor and nil EI) and the framed structure. The comparison in terms of absolute, differential settlements and angular distortion (Figure 5.13) reveals a negligible role of the superstructure inertia, with variation between simplified and complete calculation ranging between -4% and +7% for all examined cases. This outcome was also seen with numerical calculation by Karamitros *et al.* (2013b), who gave a deviation lower than $\pm 5\%$. Both observation combine with the field evidence gained by Yoshida et al. (2001) in Adapazarı (Turkey) during the 1999 Kocaeli earthquake, where a limited influence of the height was noticed on the buildings damaged by liquefaction. On the contrary, a relevant role of height was seen on the buildings damaged by shaking in the non-liquefied areas of the city. This result has been explained by Karamitros *et al.* (2013b) considering that the seismic isolation induced at the upper levels by the liquefied layer (see also Appendix A), inhibits building oscillation and reduce inertial effects.

Liquefaction Vulnerability of Buildings: the proposed tool for a preliminary assessment

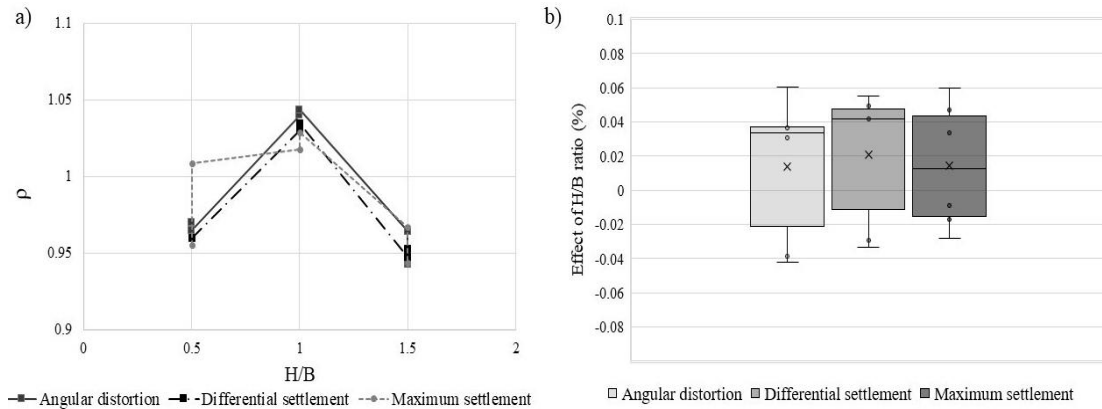


Figure 5.13 - Effect of superstructure in terms of ratio (ρ) between foundation movements computed with the model contemplating superstructure inertia and the corresponding results of the basic analysis (a); plot box of effect of H/B ratio for each foundation movement.

5.3 Prediction of settlement with the Bullock *et al.* (2018) formula

In the last decade several attempts have been made to produce predictive formulas with the purpose of massively estimate the performance of buildings distributed over a territory. With this aim, the recent literature proposes a variety of relations to predict liquefaction induced settlements based on the main characteristics of the phenomenon, i.e. seismic input, subsoil properties and foundation bearing pressure (Dashti and Bray, 2013; Karamitros *et al.*, 2013b; Bray and Macedo, 2017; Bullock *et al.*, 2018). Among them, the physics-informed semi-empirical probabilistic formula proposed by Bullock *et al.* (2018) is the last and probably the most comprehensive.

The method, calibrated with the results of a 3D fully coupled numerical parametric study and validated with a database of field observations and centrifuge experiments, estimates the expected mean foundation settlement for a given set of input parameters. In this study, this formula has been applied to each analyzed condition comparing the results of numerical calculation with the value computed with the spreadsheet provided by the authors (<https://shidehdashti.com/geotech-links/>). The calculation requires to input the parameters listed in Table 5.4.

Liquefaction Vulnerability of Buildings:
the proposed tool for a preliminary assessment

Table 5.4 - Input parameters for the application of Bullock et al. (2018) semi-empirical formula.

IP	Description	U.M
CAV	Cumulative absolute velocity	cm/s
M _w	Moment magnitude of the earthquake	M _w
Rrup	Distance to rupture	Km
H	Focal depth	Km
N _{st}	Number of floors	-
Q	contact pressure of the foundation	kPa
B	Foundation width	M
D _f	Foundation embedment depth	M
H _L	Thickness of the liquefaction-susceptible layer	M
D _L	Depth from the foundation base to the center of the liquefaction-susceptible layer	M
H _C	Non-susceptible crust thickness	M
q _{c1N}	CPT normalized cone tip resistance of the liquefaction-susceptible layer	-

The cumulative absolute velocity (*CAV*) has been computed for each combination of seismic event (Table 5.2) and scaling factor, implementing the equation proposed by Bullock *et al.* (2017). Analogously, foundation contact pressure (*q*), width (*B*), depth of embedment (*D_f*), thickness of the non-susceptible crust (*H_C*) and liquefaction-susceptible layer (*H_L*), depth from the foundation base to the center of the liquefaction-susceptible layer (*D_L*) have been set equal to those given in the numerical calculation. The number of storeys (*N_{st}*) has been derived as a function of the bearing contact pressure, considering a ratio $q/N_{st} \approx 25$ kPa. Finally, the mean CPT normalized cone tip resistance (*q_{c1N}*) of the liquefiable sandy layer has been computed with the equation proposed by Boulanger & Idriss (2014), as function of the relative density (*D_r*):

$$q_{c1N} = 0.9 \left(\frac{D_r + 1.063}{0.465} \right)^{3.788} \quad (5.7)$$

The Bullock *et al.* (2018) method provides a cumulated probability curve of settlements having Log-normal distribution and standard deviation σ_{ln} equal to 0.67, these properties derived comparing the computed settlement with those observed from case history and centrifuge experiments. Finally, the mean settlement derived from the numerical calculation has been compared with the median value computed with the Bullock *et al.* (2018) formula into a one-to-one plot. The values reported in the bi-logarithmic plane of Figure 5.14 show a linear inference line (black continuous) with a regression coefficient approximately equal to one (1.067) and a correlation coefficient (R^2) equal to 0.90 that confirm a reasonably good fit. It is worth observing that all points in the plot but few fall in the area formed by 16th and 84th percentile of

the probability distribution, most of them positioning near the interpolating line. In conclusion, this result confirms a good predictive performance of the formula, similar to that noticed in their original work by Bullock *et al.* (2018).

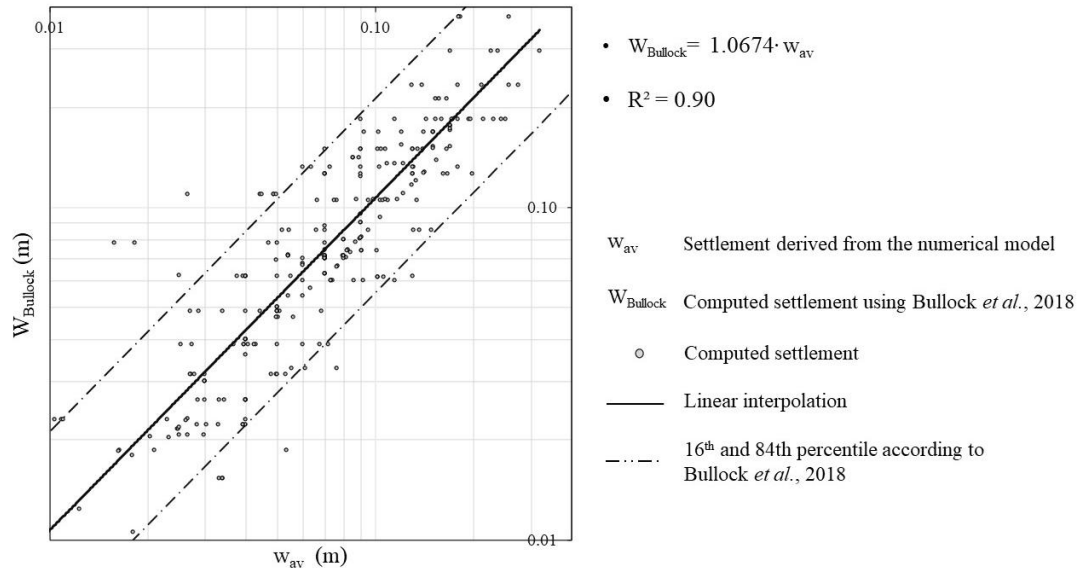


Figure 5.14 - Mean settlements predicted with the numerical calculation vs median settlements computed with the Bullock *et al.* (2018) semi-empirical method.

5.4 Prediction of angular distortion

The analysis of the angular distortion has been carried out looking at two classical studies on this subject for static loading, produced by Boscardin and Cording (1989) and Grant *et al.* (1974). The former authors proposed a vulnerability criterion applicable to brick bearing wall and small framed structures subjected to various underground events, from shallow and deep excavation to deformation induced by building construction. Their study focuses on the combination of angular distortion and horizontal strain at the foundation level, finding that the relative composition of these two kinematic components is dictated by the disturbing factor (see Figure 5.15). While underground excavation tends to produce larger horizontal strains, angular distortion is predominant in the case of foundation loading. The two quantities, computed for each simulation of the present parametric study, give an alignment of dots in Figure 5.15 on the line characteristic of deformation induced by the self-weight of buildings. This outcome implies that foundation movements occur with the same

Liquefaction Vulnerability of Buildings:
the proposed tool for a preliminary assessment

pattern, whether they are caused by static loading or liquefaction, being a possible explanation that subsoil deformation occurs at relatively shallow depths in both cases.

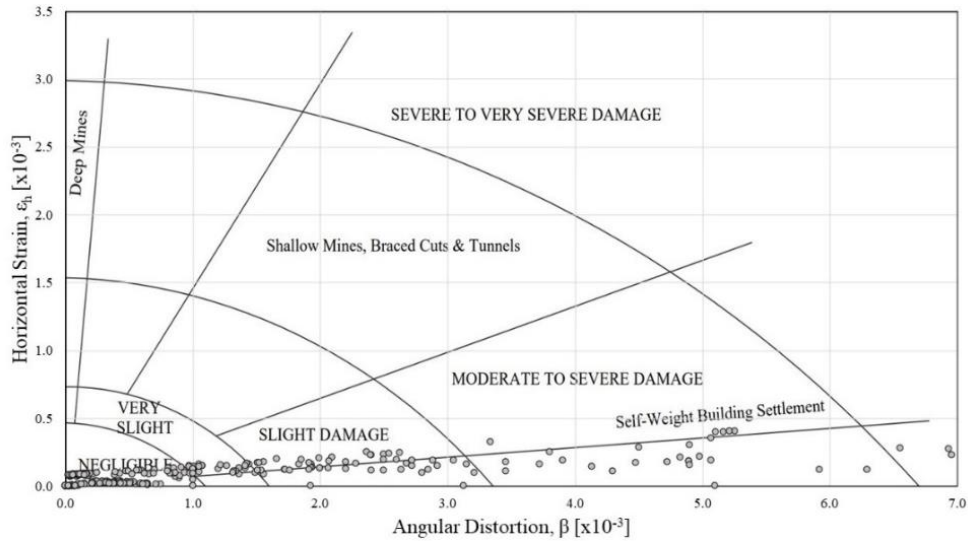


Figure 5.15 - Key evidence from the parametric study: ground horizontal strain vs angular distortion overlapped to the plot of Boscardin and Cording (1989).

Another interesting result is obtained reporting angular distortion and maximum settlement obtained from each numerical calculation on the bi-logarithmic plot of Figure 5.16, in analogy with the analysis performed by Grant *et al.* (1974). These authors collected observation on buildings founded on cohesive or cohesionless soils with shallow isolated or continuous footings and inferred an envelope curve for all monitoring data given by the following equation:

$$\beta_{MAX} = 7.8 \cdot 10^{-4} \cdot w_{MAX} \quad (5.8)$$

Interestingly, this curve reported with a continuous black line in Figure 5.16 represents the upper bound also for the angular distortion computed in the present study. This result highlights once more that, despite reaching different absolute values, liquefaction induced settlements on low-rise buildings possess similar characteristics as those induced by static loading. More particularly, this line interpolates quite closely the results obtained for nil bending stiffness. For increasing EI values, the angular distortion corresponding to the same maximum settlement tends progressively to diminish, consistently with the trend seen in Figure 5.12.c. Figures 5.15 and 5.16 suggest the possibility of adopting for liquefaction the same criteria used for the

Liquefaction Vulnerability of Buildings: the proposed tool for a preliminary assessment

vulnerability assessment upon static loading, i.e. assuming angular distortion as the demand variable for fragility and relating it to the maximum absolute settlements. However, to apply this strategy to the extensive assessment of building over large areas (e.g. urban systems), it is necessary to predict angular distortion with fast and reliable tools.

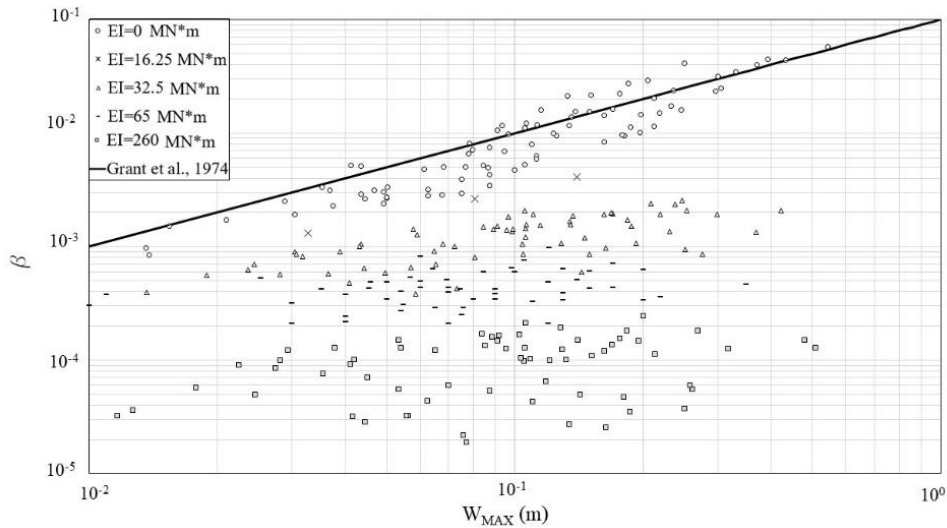


Figure 5.16 - Angular distortion vs maximum absolute settlement overlapped to the plot of Grant *et al.* (1974).

With this goal in mind, the trends shown in the examples of Figures 5.6-5.12 have been systematically interpreted with an analysis of variance (ANOVA, Fisher, 1918), determining the mutual influence of variables and separating those factors possessing a statistical relevance from others producing limited or random effects. Thereafter the relation between angular distortion and these variables has been sought training an artificial neural network, this tool preferred to the classical inference based on assigned mathematical functions thanks to its higher flexibility. Additionally, a minimum set of variables has been identified, grouping factors as much as possible, to render prediction more practical, e.g. in the form of graphical plots. After several trials, the median settlement computed with the Bullock *et al.* (2018) method, thickness and undrained shear strength of the crustal cap, bending stiffness of the building-foundation system have been identified as those compromising the lowest number of variables with an acceptable accuracy of prediction. Table 5.5 reports the results of the ANOVA test, where F is computed with the Fisher distribution and p measures the probability that a relation could be of random nature, i.e. p -value tending to zero means a greater statistical significance of the observed relation. The very low p -values computed for the assumed variables (Table 5.5), all lower than the suggested threshold

Liquefaction Vulnerability of Buildings:
the proposed tool for a preliminary assessment

($\alpha=0.05$), confirm the reliability of relations. Among variables, the median settlement computed with the Bullock *et al.* (2018) method has the virtue of including most of the relevant factors (see Table 4) and provides a good estimate of the mean settlement (Figure 14). This variable has been selected to group most factors, also considering the dependency of angular distortion on the maximum settlement seen in Figure 5.16 and the relation between mean and maximum settlement seen in Figure 5.5. The remaining variables (H_c , s_u and EI) have been chosen because the one-way ANOVA test gave a significant outcome, i.e. indicated a statistical significance of the relation between the selected variables and angular distortion.

Table 5.5 - ANOVA test showing the statistical significance of the relation between variables and angular distortion.

Parameter	F	Significance value ($\alpha=0.05$)
EI (MN*m)	75.3	9.97E-25
Hc (m)	18.0	5.90E-25
s_u (kPa)	3.9	5.05E-07
$w_{Bullock}$ (m)	48.4	7.37E-20

These variables have thus been assigned as input of an Artificial Neural Network (ANN), trained with the output of numerical calculation, and used to predict angular distortion in general cases (Figure 5.17.a). The ANN is a mathematical model that replicates the brain functioning, being composed of interconnected neurons (McCulloch and Pitts, 1943). The network herein assumed is a two-layer feed-forward type with sigmoid hidden neurons and linear output neurons, in which information moves only in one direction from the input nodes through the hidden nodes to the output nodes, avoiding loops or recursive programming. In this study, architecture has been chosen as the best performing one among several attempts. The Levenberg-Marquardt back-propagation algorithm has then been used for training as it minimizes the sum of squares of nonlinear functions. The developed network has 10 hidden layers and the fractions of the dataset used for training, validation and testing are respectively equal to 70%, 15%, 15%.

The prediction, evaluated in terms of mean squared error $MSE=5.98 \cdot 10^{-6}$ (Figure 5.17.b), reveals a good performance over the whole investigated range. The statistical analysis of error shows (Figure 5.17.c) a symmetric distribution well approximated with a gaussian probability density function ($PDF(terr)$) having zero mean and standard deviation $\sigma(terr)=0.0007$.

Liquefaction Vulnerability of Buildings: the proposed tool for a preliminary assessment

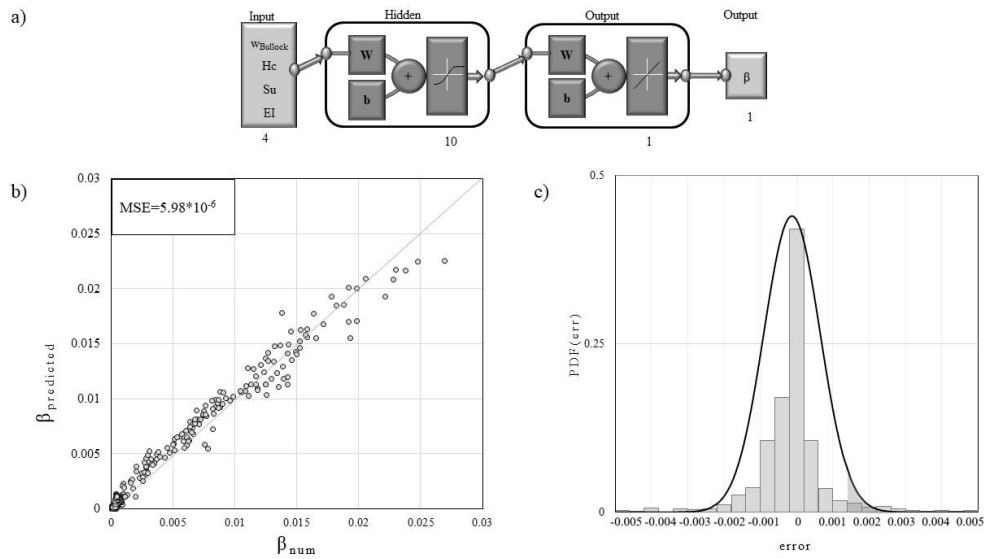


Figure 5.17 - Structure of the artificial neural network (a), regression (b), statistical analysis and frequency distribution of error (c).

The proposed tool can be used with the recommendation that prediction is reliable for values of the input variables included in the investigated range, i.e. $w_{Bullock} \leq 0.3$ m, $EI \leq 260$ MN*m, $H_c \leq 6$ m and $s_u \leq 150$ kPa. An example of ANN outcome is provided in Figure 5.18, where angular distortion β is plotted as function of median settlement $w_{Bullock}$ for selected values of flexural stiffness (EI equal to 0, 65 and 269 MN*m), undrained shear strength (s_u equal to 50 and 100 kPa) and crust thickness (H_c equal to 2, 4 and 6 m). The plots show the predominant role of equivalent bending stiffness of the foundation system, and the less relevant but still appreciable role of the upper crust layer.

Liquefaction Vulnerability of Buildings:
the proposed tool for a preliminary assessment

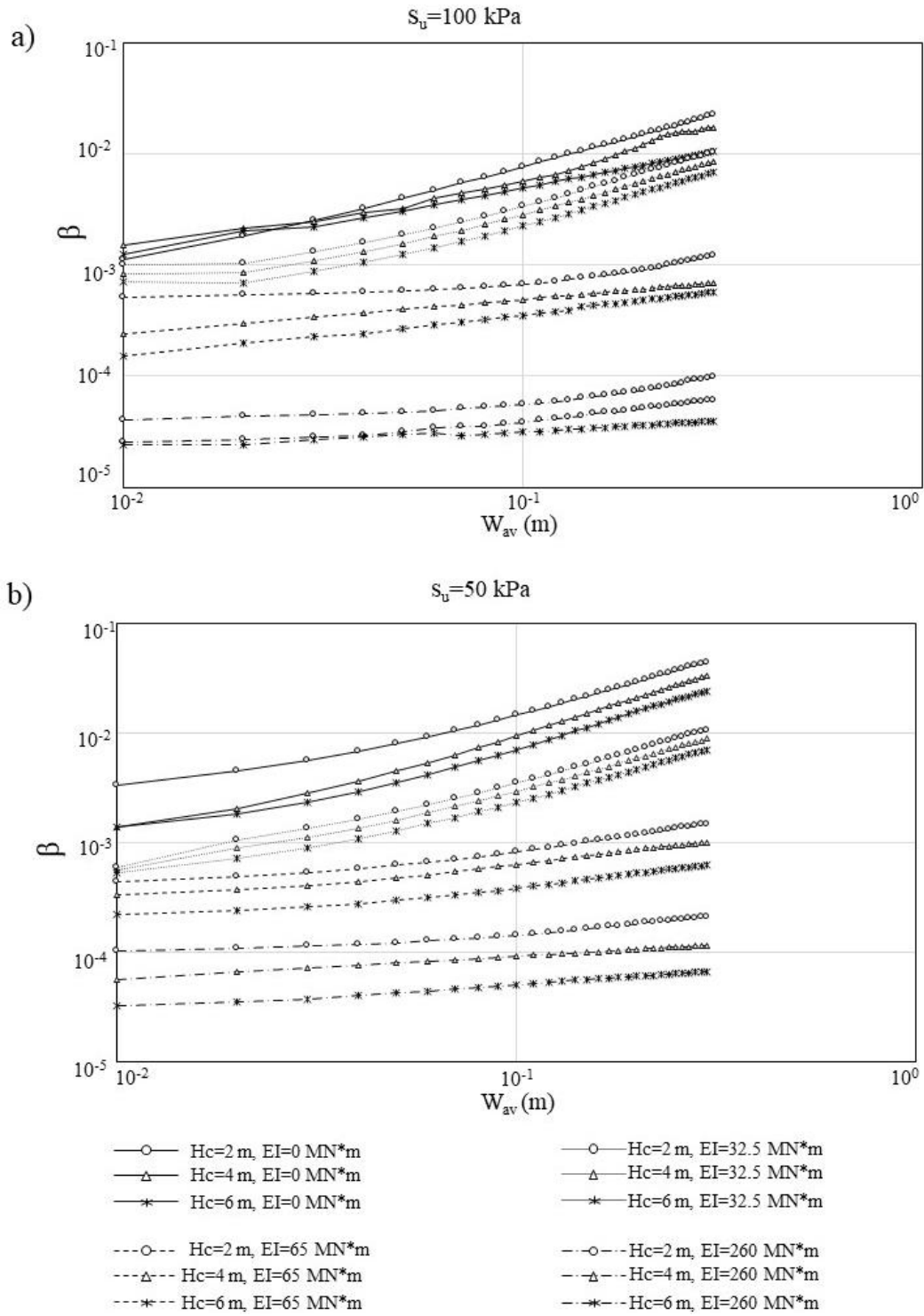


Figure 5.18 - Example of β prediction with ANN.

Chapter 6. THE CASE STUDY OF TERRE DEL RENO (FE)

6.1 Abstract

In May 2012, the Emilian Po Valley was struck by an intense seismic activity with two major earthquake sequences occurred respectively on May 20th and on May 29th. Widespread liquefaction was observed in areas located near old abandoned watercourses, especially in the municipality of Terre del Reno (FE). The municipality covers an area of 51 km², along a former branch of Reno River and is divided into three main districts: Sant’Agostino, San Carlo and Mirabello. The area of San Carlo, is the most emblematic location for the greatest concentration of liquefaction evidence (Fioravante *et al.*, 2013). In 2020, the municipality of Terre del Reno has been selected as a pilot site in the “PERL – Protocollo Emilia-Romagna Liquefazione”, a research project held by Emilia-Romagna Region (RER), CNR-IGAG and University of Cassino and Southern Lazio. This choice has been pursued due to the high density of surveys in the selected area and to the massive presence of liquefaction evidences.

Following these reasons, in the present study, Terre del Reno was selected to validate the tool for the assessment of liquefaction induced angular distortion on shallow foundations, presented and calibrated in *Chapter 5*.

In particular, the validation of the proposed tool has been automatically carried out in the district of San Carlo, because it is the area the area with the highest population density and the most affected by liquefaction phenomenon in the municipality of Terre del Reno. The validation consists in the evaluation of the robustness of the relation between recorded damages and predicted angular distortion in foundation, using the Receiver Operating Curve (ROC) method defined by Kongar *et al.* (2015).

6.2 The 2012 Emilia-Romagna seismic sequence

The Emilia-Romagna seismic sequence (Figure 6.1) lasted over two months and was characterised by more than 2,000 shocks, 8 of which had $M_L > 5$ (Fioravante *et*

al., 2013). The earthquakes were originated by the Ferrara folds, constituted by two main arcs. The inner arc (the Mirandola Arc) has its crest between Novi di Modena, Mirandola and Poggio Renatico. The outer arc (the Ferrara Arc) has its peak between Bondeno, Occhiobello and Ferrara. Two main events have been recorded during the seismic sequence: the first, occurred on May 20th, was characterised by a moment magnitude $M_w=6.1$ and hypocentre depth $d_h = 9.5$ km; the following main shock struck the region on May 29th with a moment magnitude equal to $M_w=5.6$ and hypocentre depth equal to $d_h = 8.1$ km (Fioravante *et al.*, 2013).

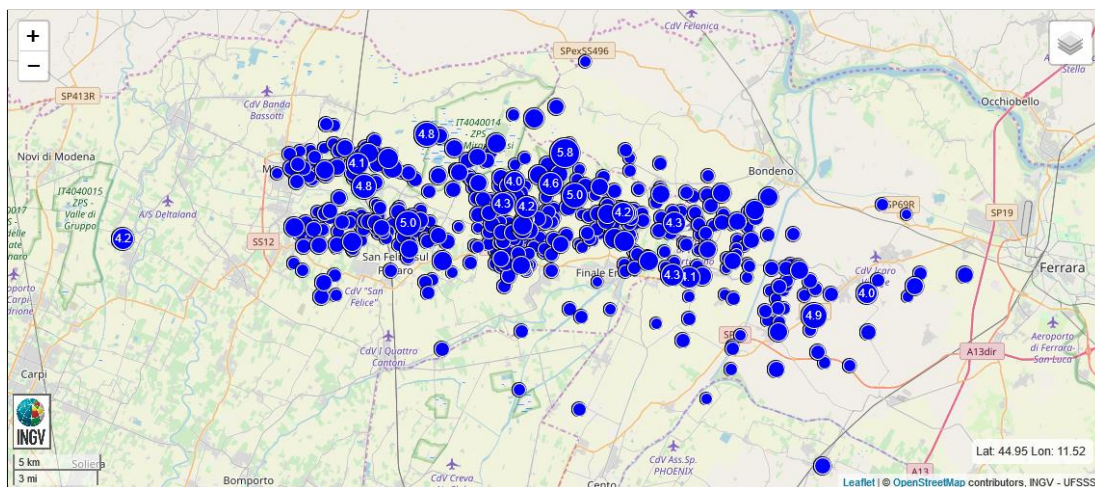


Figure 6.1 - Map reporting the epicentres of the Emilia Romagna 2012 seismic sequence (INGV database).

The two main shocks caused widespread liquefaction in various areas of the Emilia Romagna Region. In particular, following the 20th May 2012 event, the surficial effects were observed in the north-eastern area of the epicentre in San Martino Spino, Burana and Scortichino, and in the south-eastern area, in S. Felice sul Panaro, Dodici Morelli di Cento, Mirabello, San Carlo and San Agostino (Figure 6.2). Soon it appeared that liquefaction evidence was not evenly distributed over the area but tended to concentrate along preferential alignments, mostly dictated by the presence of paleo-riverbeds, levees, out-flow channels and fans that are characterized by the presence of sandy layers at relatively shallow depths. The maximum distance of observed liquefaction phenomena from epicentres is about 30 km, in agreement with the regional empirical relations proposed by Galli (2000). The spatial distribution reflects the combined effects of soil susceptibility (loose cohesionless soil with shallow water table) and ground motion intensity in terms of liquefaction hazard.

CONCLUSIONS

After the main shocks, the INGV Emergeo Working Group (2013) performed a systematic survey of the earthquake sequence area through field, aerial and interview approaches. Data regarding 1362 observations were collected, stored and online available in a [geographical information system](#). The surficial manifestations were grouped into three classes: (i) liquefaction; (ii) fracture/liquefaction; and (iii) fracture. Of the 1362 sites with coseismic effects identified and surveyed over more than 1200 km², 768 were classified as fracture/ liquefaction, 485 as liquefaction, and 109 as fracture (Figure 6.2).

The larger effects were observed during May 20th 2012 shake in the localities of San Carlo and Mirabello, in the municipality of Terre del Reno (Figure 6.2).

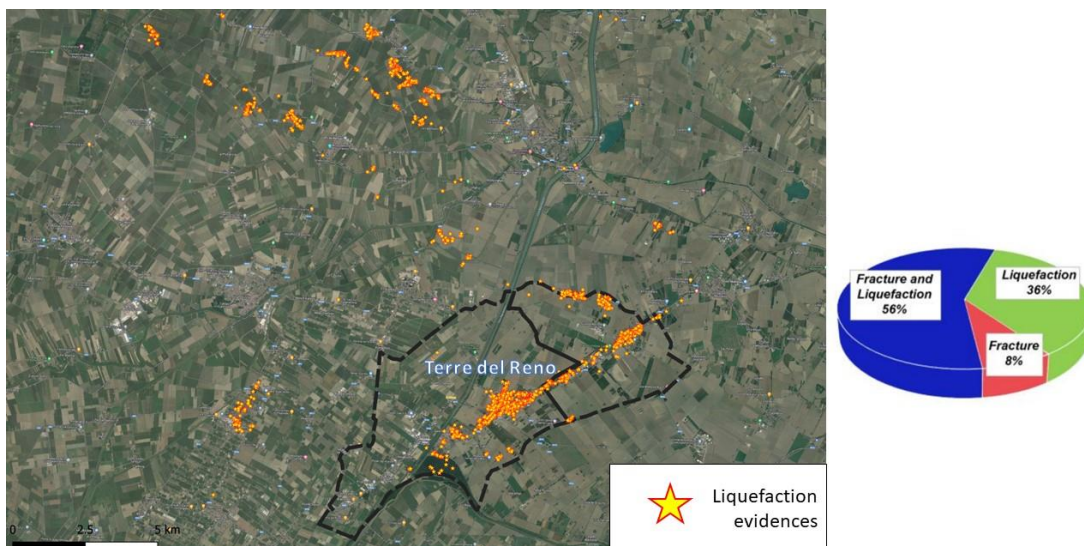


Figure 6.2 - Liquefaction ground evidences after the 2012 Emilia Earthquake Sequence.

The area struck by the 2012 earthquake sequence was declared as seismic only with the 2003 reclassification. Therefore, the 2012 shocks were very impactful on the community, causing deaths and considerable destruction of the building and cultural heritage. An amount of 27 people died, 13 of them due to the collapse of an industrial building; more than 12 000 structures were affected, including 147 collapsed or heavily damaged bell towers and churches (Fioravante *et al.*, 2013). The rebuilt has cost more than 6 billion euros, excluding the indirect costs of the loss of income and the inability to operate for several months, quite huge considering the importance of the entire industrial district on the regional gross domestic product. In fact, the area affected by liquefaction hosts a high concentration of agricultural production, agri-food, industrial and handicraft units. In particular, the earthquake-induced economic

losses leading to a decrease equal to 3.1 billion euros in the Regional Gross Domestic Product “GDP” in 2012-2013, from estimates of the Emilia-Romagna Region (Servizio geologico, sismico e dei suoli RER, 2012). In this context, the only district of S. Agostino (in the municipality of Terre del Reno) hosts a series of factories capable of producing 2% of the Regional GDP.

6.3 The Municipality of Terre del Reno

The Terre del Reno municipality is located in the southern Po river plain in the Emilia-Romagna Region (Italy). The area was struck by an intense seismic sequence associated with compression fault ruptures in 2012. The main shock of May 20th 2012 (Mw 6.1) produces extensive liquefaction phenomena due to subsoil composition, geologic history and the shallow depth of the groundwater table (Fioravante *et al.*, 2013). The municipality covers an area of 51 km², along a former branch of Reno River and is divided into three main districts: Sant’Agostino, San Carlo and Mirabello (Figure 6.3).

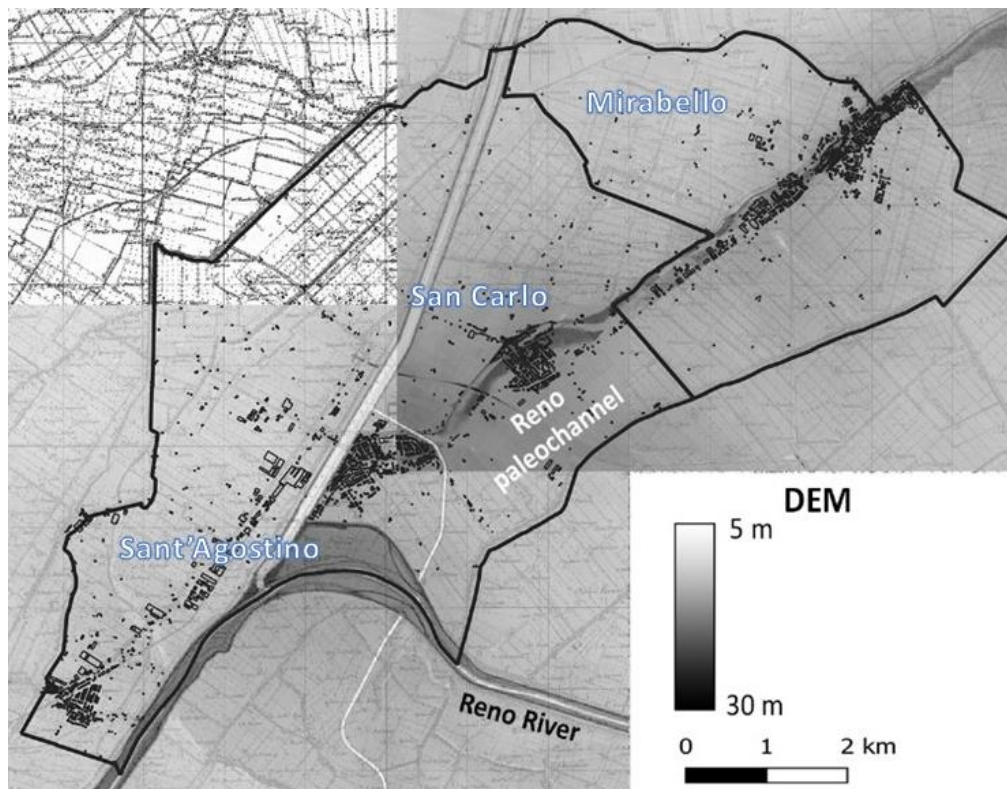


Figure 6.3 - The municipality of Terre del Reno (FE): main districts and Digital Elevation Model.

In the area of the municipality, Galli (2000) and Romeo *et al.* (2012) highlighted the presence of hidden paleochannels and paleo-levees. In particular, the San Carlo area is characterized by a complex stratigraphic context due to the depositional history of the Reno river, highlighted by the significant number of liquefactions induced surficial manifestations and damages.

6.3.1 Geological setting

The Municipality of Terre del Reno (FE), with its three main districts (Sant'Agostino, San Carlo and Mirabello), occupies an area along a former branch of Reno River (Figure 5.3), in the southern Po river Plain. The former branch of the Reno river was artificially created after 1457 to feed with water the Po river and dismissed in the period 1767-1795 to avoid silting of the Po riverbed and remediate the eastern area with landfill (Galli; 2000).

From the geological viewpoint, the plain is formed of sediments deposited by Apennine and Alpine rivers, interspersed with marine accretion, these alternated processes ruled by the regression and progression of the Adriatic Sea in the upper Pleistocene-Holocene (Romeo, 2012). The structural evolution of the Po foreland basin was mainly driven by the north-east verging Northern Apennines collisional system (Basili & Barba, 2007; Livani *et al.*, 2018; Malinverno & Ryan, 1986; Royden *et al.*, 1987). At present, the external sectors of the north-verging Northern Apennines are buried beneath the subsiding Po Plain and consists of three arcuate fold-and-thrust systems: the Monferrato Arc, the Emilia Arc and the Ferrara-Romagna Arc that became active since the Late Miocene (Boccaletti *et al.*, 2011; Ghielmi *et al.*, 2013; Picotti & Pazzaglia, 2008; Scrocca *et al.*, 2007). In particular, the faults of the Ferrara–Romagna Arc have been tectonically active since the Early Pliocene (Boccaletti *et al.*, 2011; Toscani *et al.*, 2009) and are still considered seismogenic. In particular, the 2012 earthquakes were originated by the Ferrara Arc.

Furthermore, the geological history of the Southern Po Plain is strongly influenced by the evolution of the Po, Panaro and Reno rivers and regulated by anthropic modification with the diversion and abandonment of channels and the erection of levees (Figure 6.4a; Galli and Meloni, 1993; Romeo, 2012). In particular, the geological and stratigraphic setting in the area of Terre del Reno was significantly affected by the evolution of the Reno river, where the paleochannel and the paleo

levees are still visible (Figure 5.4b), as confirmed by the Digital Elevation Model (Figure 6.3).

Caputo *et al.* (2015), Caputo *et al.* (2016) and Stefani *et al.* (2018) reconstructed the regional drainage evolution of the paleo-Reno river during historical times.

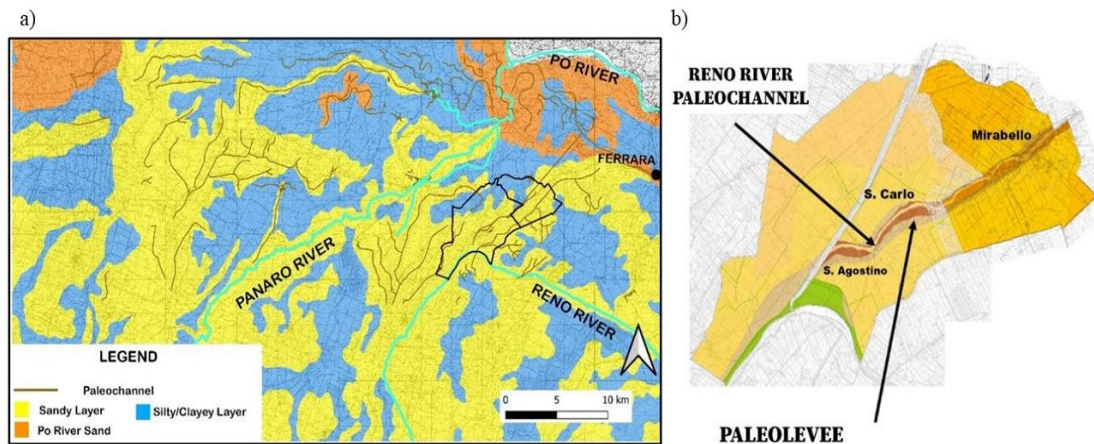


Figure 6.4 - a) In the map, the paleochannels and the different types of alluvial deposits are shown; b) geomorphology of the study area.

In particular, the area of San Carlo and Mirabello was dominated by a poorly drained floodplain and marshy environments since the latest Pleistocene and throughout most of the Holocene, reaching the Roman period. During the Middle Ages, the area of San Carlo and Mirabello was affected by heavy floods, which generated new aggrading channel body elevated above the surrounding plain and advancing into elongated lakes and swampy environments (Bondesan, 2001; Caputo *et al.*, 2016). In this period, attempts were made to limit the floods by building embankments, still visible today in the municipality of Terre del Reno. During the last decade of the XVIII century and after the unsuccessful efforts to artificially force the Reno water to reach the Adriatic Sea, the course was deviated through an abandoned distributary channel of the Po River just south of the municipality (Cazzola, 1995; Franceschini 1983).

The manmade embankments are mainly constituted by fine sand and silty materials and are characterized by a height of about 4÷5m (Figure 6.5). The shallowest layers of the alluvial plain are attributable to the Olocene era, with an alternance of sandy silty and fine to medium sand in the upper meters, followed by a continuous clayey layer with a thickness of about 10m (Figure 6.5). The deepest formation consists of an alternation of sandy silt and silty sand, dating back to the Pleistocene era (Figure 6.5).

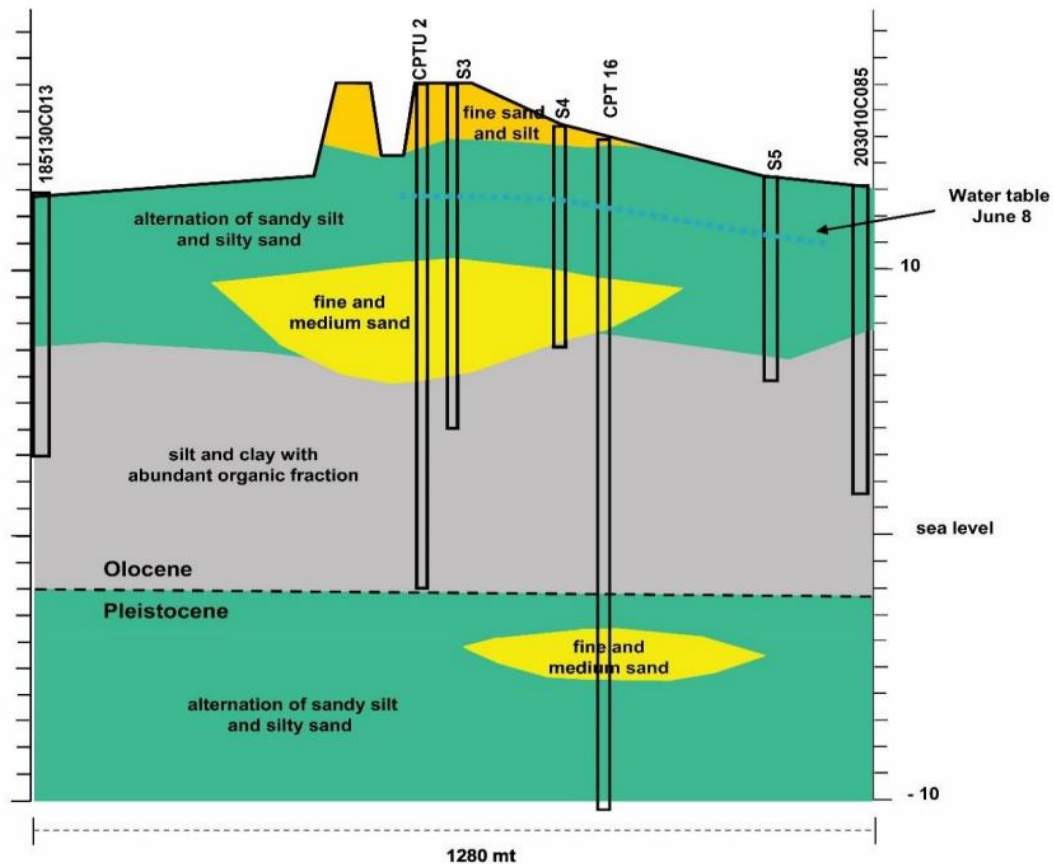


Figure 6.5 - Geological cross section WNW-ESE through the San Carlo area, (Martelli, 2012).

Over the years a conspicuous reconstruction of the hydro-stratigraphic setting has been carried out consulting hydrogeological maps, cross sections, seismic lines, stratigraphies, and water and oil wells (Emilia-Romagna Region and ENI – AGIP, 1998; Molinari *et al.*, 2007). Molinari *et al.* (2007) found three main groups of aquifers named A, B and C in the alluvial aquifers beneath the Ferrara province. Their hydro-stratigraphic architecture reflects the Pleistocene to Holocene depositional and tectonic evolution of the southern Po sedimentary basin (Regione Emilia-Romagna Region and ENI-AGIP, 1998). The aquifers from the shallower Group A consists of six hydro-stratigraphic units of lower hierarchical order belonging to fluvio-deltaic and alluvial depositional systems (Tentori *et al.*, 2022). Generally, the Group A aquifers are composed of sand dominated fluvial bodies (i.e., glacial) separated by mud dominated aquitards consisting of transgressive, finer-grained floodplain facies (i.e., interglacial). Minarelli *et al.* (2007) named A0 the shallowest hydro-stratigraphic unit and found out that it is mainly constituted by two sand-dominated aquifers units separated by floodplain mud. According to Papathanassiou *et al.* (2012), the water table of the A0

was at approximately 3÷4m depth beneath the earthen levee and 1-2 m in the alluvial plain, considering the surveys of the piezometric level during the summer 2012.

6.3.2 Liquefaction-induced surficial manifestations

After the 2012 Emilia Earthquake Sequence, an extensive liquefaction phenomenon was observed in the Municipality of Terre del Reno. Two types of liquefaction induced surficial manifestations were found: sand boils and fractures (Figure 6.6).

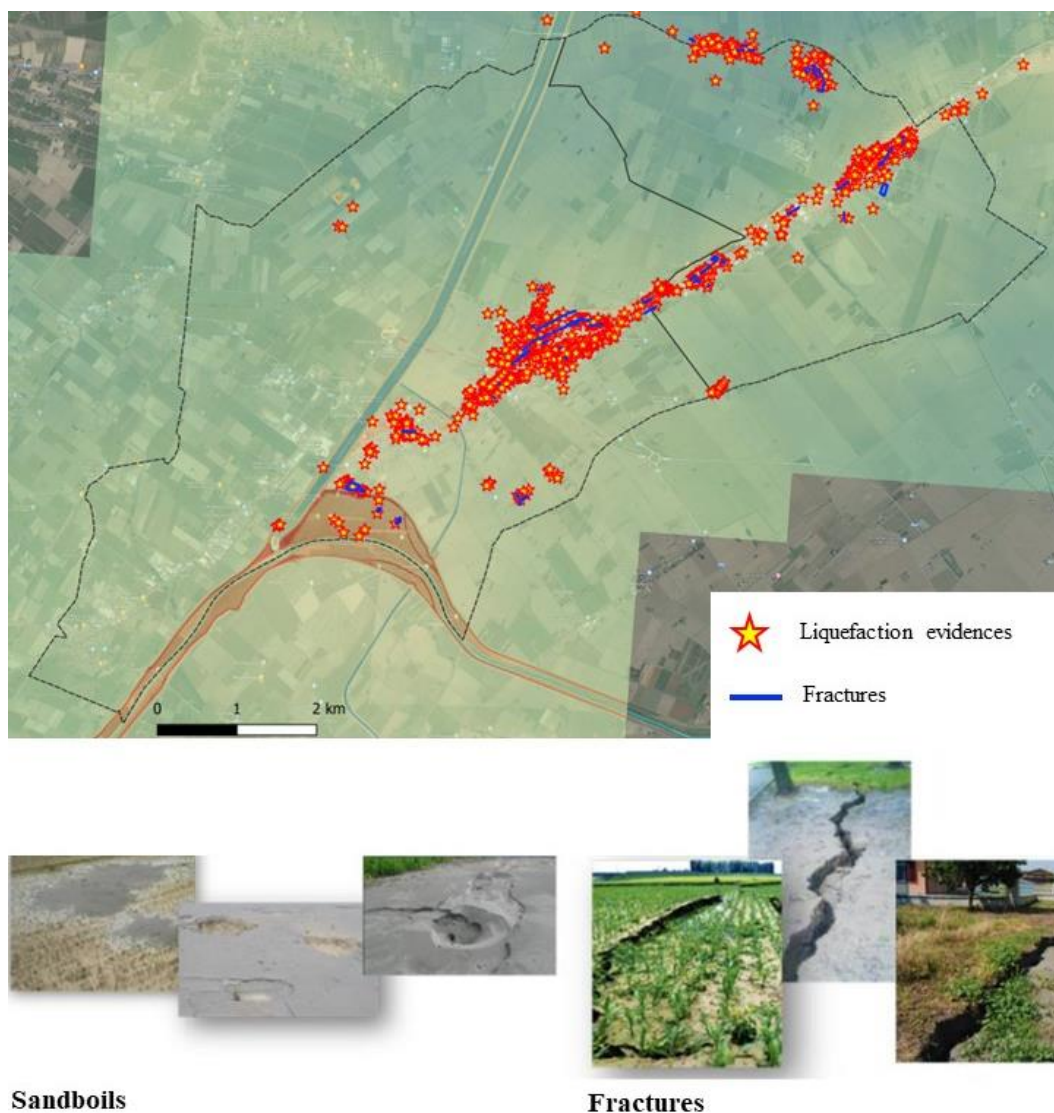


Figure 6.6 - Liquefaction ground observations after the 2012 Emilia Earthquake Sequence.

As shown in Figure 6.6, most of the surface liquefaction induced surficial manifestations were located along the paleochannel and the paleo-levee. In particular,

the higher density of sand boils and extended fractures was recorded in the populated area of the districts of Sant'Agostino and Mirabello, with few exceptions in the with few exceptions in the surrounding growing areas. In detail, the total number of sand boils in the municipality was equal to 1169, 56% of which were located in the districts of San Carlo and 23% in the urbanized area of Mirabello.

6.3.3 Urban development and damage on buildings

In the municipality of Terre del Reno, the urbanized areas are concentrated mainly along the paleochannel and paleo-levee. In total, there are 3981 buildings used for civil and industrial use.

Urban development

The year of construction of the buildings is a fundamental attribute for carrying out a vulnerability analysis, because it influences the construction characteristics and typology. In order to date the construction period of the buildings, a detailed analysis has been carried out consulting land-use maps and aerial photos taken over the years. In detail, the urban development has been reconstructed merging and comparing the information from:

- the aerial survey performed in 1954 (available on [Emilia-Romagna Region website](#));
- the land-use map drawn up in 1976 (accessible on [Emilia-Romagna Region website](#));
- the aerial survey of 1994 (downloaded from the [National Geoportal](#));
- the land-use map drawn up in 2003 (extracted from the [Emilia-Romagna Region website](#)).

Figure 6.7 shows the result of the study of the urban evolution of the Municipality of Terre del Reno, focusing on the districts of Sant'Agostino, San Carlo and Mirabello (Figure 6.7a, b and c, respectively). Most of the structures were built before 1954 (about 41% of the total number); a second conspicuous urban growth occurred before 1976 (29%). Between 1976 and 1994, urbanization interested only 25% of the buildings and the remaining 5% dates back to the period from 1994 to 2003. The detailed examination of the built heritage carried out by consulting [ISTAT databases](#), [National Geoportal](#) and the [Emilia-Romagna Region database](#), reveals that most of them are masonry, except in more recent cases where reinforced concrete constructions

prevail. Anyway, almost all buildings considered have been designed with seismic regulations not adequate for the latest standards.

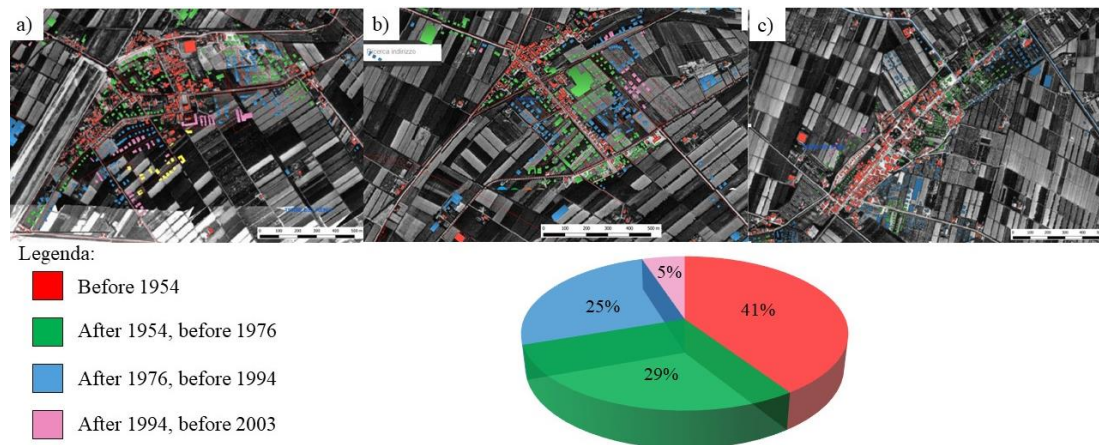


Figure 6.7 – Urban development of the municipality of Terre del Reno: aerial detail on the districts of Sant'Agostino (a) , San Carlo (b) and Mirabello (c).

Damage on buildings

Information on the totality of the structures is limited, but it was possible to build a detailed database of the buildings that suffered damage during the seismic sequence of May 2012 merging the Regional Database, aerial surveys, photographic documentation and the MUDE forms provided by the Emilia Romagna Region. The [MUDE form](#) is a model used for the implementation of commissioner orders 29, 51 and 86/2012 relating to reconstruction. MUDE combines in the same procedure both the building practice to carry out the repair, restoration or reconstruction of the buildings, and the practice relating to the request for contributions. Merging all information, each building is characterized by 20 voices to fill, listed below:

1. ID;
2. Request number;
3. Number of form;
4. Typology (masonry, reinforced concrete, steel, wood, etc.);
5. Number of storeys;
6. Number of floors underground;
7. Geographic coordinates;
8. Interstorey height;
9. Type of roof;

10. Type of foundation: the data is often not available;
11. Position of the housing unit with respect to adjacent structures;
12. Construction era;
13. Morphology (cresta, strong slope, light slope and plain)
14. Foundation seismic damage (absent, generated by the earthquake, increased by the earthquake or already existing);
15. Usability;
16. Surface (m²);
17. Type of damage;
18. Repair;
19. Use;
20. Costs.

Often, information about the type of foundations, inter-storey height and foundation seismic damage were missing.

Figure 6.8 shows the damaged buildings in the municipality (red crosses). Once the data was collected, a statistical analysis of the damage type and costs was carried out, considering separately the three districts of S. Agostino, S. Carlo and Mirabello.

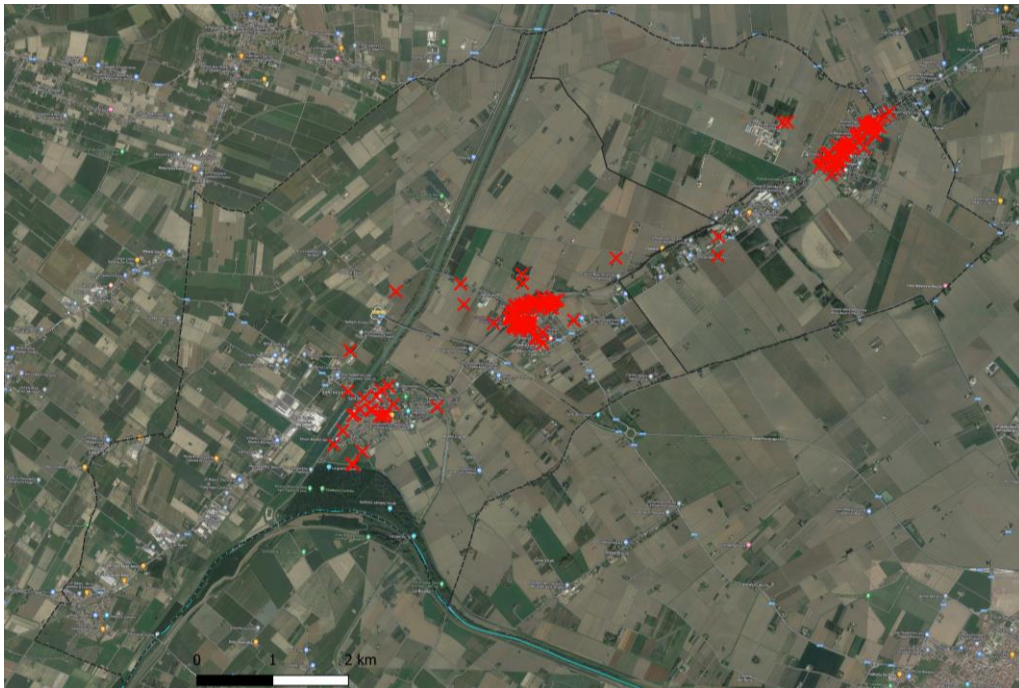


Figure 6.8 - Location of the damaged buildings in the municipality of Terre del Reno.

The cost for the reconstruction of private buildings in the municipality amounts to approximately 136 million euros: 55 million spent for the reconstruction of Sant’Agostino, 35 million for San Carlo and 46 million for Mirabello. By dividing the damage on buildings into three categories (liquefaction damage, seismic damage and combined damage), it is possible to evaluate the rates separately in the three districts (Figure 6.9).

In the San Carlo area, 89% of the cost of reconstruction (about 30 million) is attributable to the damage induced by the liquefaction phenomenon; the 8% is related to the seismic damage and the remaining 3% is a combined damage. Similar statistics were found in the Mirabello district where 56% of the damage was caused by the liquefaction phenomenon, 33% by the earthquake and 11% by the combination of liquefaction and seismic shock. The situation is different in Sant'Agostino: in this district the higher costs for reconstruction (72%) are attributable to the seismic damage, only the 4% of damage is combined and the manifestations of liquefaction is about 24%.

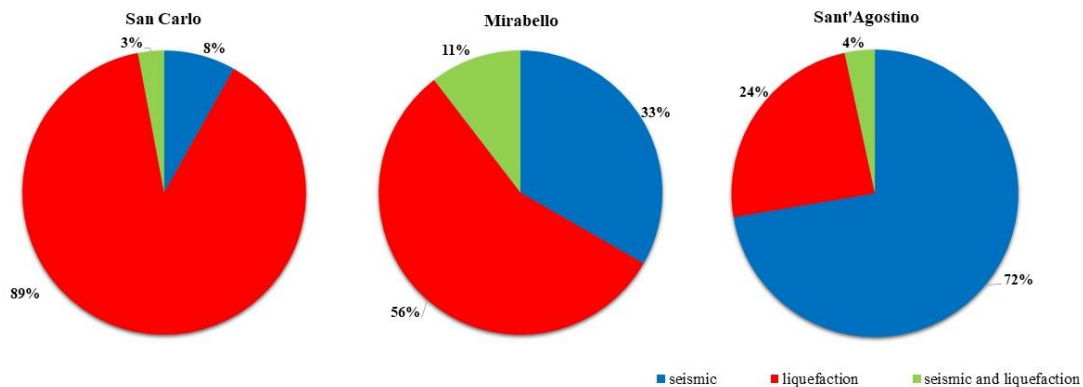


Figure 6.9 - Statistical analysis of the costs of reconstruction for the three districts of Terre del Reno.

6.4 Geodatabase

The subsoil reconstruction of the subsoil was carried out with the geognostic surveys contained in the “PERL” geodatabase.

The "PERL" database arises from the union of data available in three previous databases (RER, MUDE, MS), to which surveys carried out within the UrbiSIT7 and PERL projects have been added.

The first consulted database is the RER geodatabase. RER is the acronym of “Regione Emilia-Romagna” and is the database free available on the website of the Emilia-Romagna Region. The RER database is composed of 906 geo-localized,

punctual records, each of which has associated a set of key information (typology, date, coordinates, and maximum depth reached) and a scan of the investigation sheet. No parameter is available in a digital format; thus they were extracted by investigations sheets. This database is available at <https://servizimoka.regione.emilia-romagna.it/mokaApp/apps/geg/index.html>.

The second core is made up of 1284 surveys used in the previous study of microzonation in the old municipality of Sant'Agostino and Mirabello. The SM database included punctual as well as linear in-situ investigations. These investigations are geo-localized and organized in a standardized structure. The key information (typology, date, coordinates, etc.) of each investigation are stored in a dedicated table, while all the parameters measured are reported in chained tables. This database is available at <https://www.webms.it/>.

Finally, the MUDE database was consulted. This database consists of 384 geognostic surveys carried out after the compiling of the MUDE forms for requests for contributions for the reconstruction. Digital formats of these investigations are not available, thus geo-localization, key information and measured parameters were obtained from the digital scans of technical and geological reports.

Merging the three existing databases, 1749 geognostic surveys were obtained; in fact, about 32% of the already available data was redundant and therefore contained simultaneously in several databases. To avoid duplicates, a methodology to discern and verify the uniqueness of an investigation has been elaborated.

This methodology is based on the implementation of a series of multiple, progressive True/ False (TF) controls applied to various control parameters (CP) relative to all the investigations included in the pertinence area of the considered investigation. The pertinence area was defined as a circle with radius of 200 m and center corresponding to the considered investigation position. The progressively considered CP are: CP1) absence of another investigation within the area of pertinence; CP2) unmatching of the investigation typology; CP3) unmatching of the date of survey; CP4) matching of depth reached by the investigation. Each CP_m (m=1,2,3,4) is checked in a dedicated TF test (TF_n with n=1,2,3,4). Starting from TF 1, an investigation that verifies CP1 is moved to TF2 for CP2 verification up to TF4. Each time that a CP_m in a TF_n is not verified, the investigation is defined as “unique”. If an investigation verifies all the control parameters, it is defined as “redundant” and removed from the database.

Furthermore, during the PERL project investigation activities, a further 17 surveys were financed by the Emilia-Romagna Region, divided as follows:

- 1 Crosshole with tomography, with a depth of 30 m;
- 2 boreholes reaching 30m;
- 10 CPTU of various depths;
- 4 SCPTU of various depths.

The UrbiSIT project made a great contribution to the geophysical characterization of Terre del Reno, enriching the database of 176 surveys. In detail, the following tests were carried out during the UrbiSIT project:

- 116 HVSR;
- 29 ARRAY 2D;
- 31 MASW.

Hence, the total amount of data available after the “PERL” research project is equal to 1942 geognostic surveys (Figure 6.10).

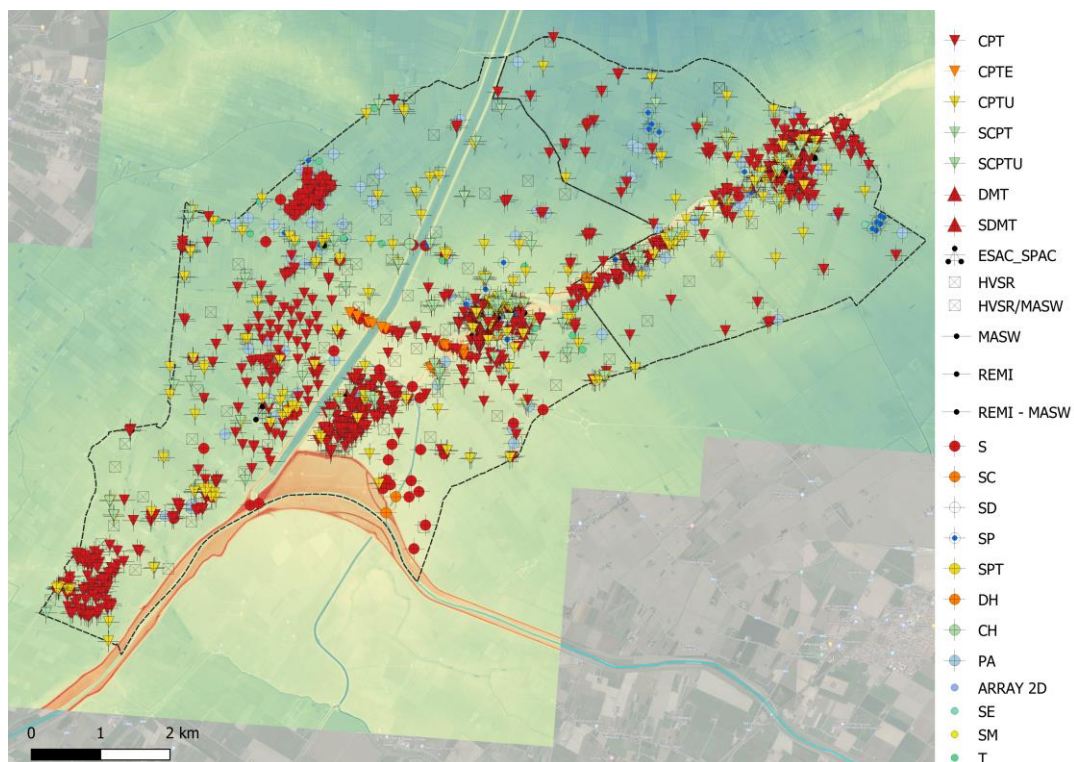


Figure 6.10 - Spatial distribution of the "PERL" geognostic surveys database, the acronym in the legenda are consistent with the guidelines for seismic microzonation.

Figure 6.11 shows the statistical distribution of the available survey in terms of typology (a), period of realization (b) and depth (c). It's worth noting that a conspicuous number of investigations were carried out after the 2012 earthquake sequence (Figure 6.11b). Penetrometer tests and boreholes makeup over 80% of the database. Furthermore, the reached depths make it possible to thoroughly investigate the first twenty meters of the subsoil, in order to identify the liquefiable volumes.

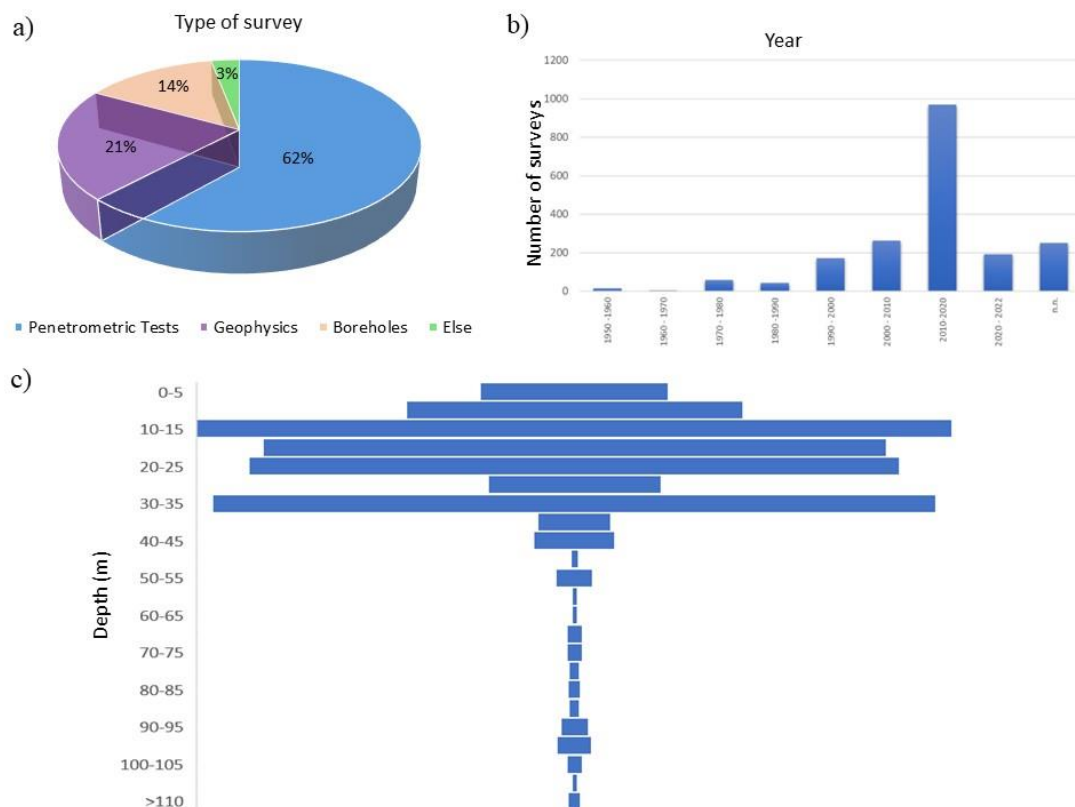


Figure 6.11 - statistical distribution of the available survey in terms of typology (a), period of realization (b) and depth (c).

6.5 Subsoil characterization with statistical methods and AI

The soil stratigraphic reconstruction of the municipality of Terre del Reno has been performed in order to identify the “Attention Zone” in the microzonation study chased during the PERL project. This aim has been pursued applying the procedure described in *Chapter 4* to the whole area of the selected case study.

In particular, in the following paragraphs is shown the processing of the cone penetration tests available in the urbanized land of San Carlo. The choice dropped on the San Carlo district for several reasons, herein listed:

- the high population density;
- the complex geological stratigraphic settings;
- the maximum density of liquefaction induced surficial manifestation (see par. 6.3.3);
- a homogeneous distribution of the geognostic surveys on the whole area;
- 89% of the collected damages to the buildings are attributable to the phenomenon of liquefaction (see par. 6.3.3).

6.5.1 Definition of stratigraphic units in the municipality of the Terre del Reno

The subsoil of San Carlo is characterized by a relatively recent geologic history, an intensive depositional sequence of the Reno river and a shallow groundwater table. The depositional activity of the river left superficial layers of loose sand with a thickness of a few meters. In the same period, the population constructed artificial levees mixing sand with silt to regulate the fluvial regime and limit flooding. The urban area is mainly built near those paleo-channel and paleo-levees.

The deepest layers are constituted of sediments deposited by Apennine and Alpine rivers, interspersed with marine accretion. These alternated processes are ruled by the regression and progression of the Adriatic Sea in the upper Pleistocene-Holocene (Romeo 2012).

The territory of Terre del Reno is covered by a conspicuous number of geognostic surveys. The definition of the stratigraphic units has been carried out analyzing the description reported in 252 boreholes logs distributed all over the municipality. From the geological and sedimentological characterization, four stratigraphic units have been identified in the upper 20 m of the subsoil:

- Unit #1: silt, silty clay, clayey silt;
- Unit #2: sandy silt, silty sand ;
- Unit #3: fine and medium clean sand;
- Unit #4: clay, organic clay, organic material.

6.5.2 CPT profiles processing

The soil boundaries discontinuities recognition (described in *paragraphs 4.1.2* and reported in Appendix C) has been applied to the district of San Carlo. In the selected region, there is a high density of surveys. For 369 investigation tests distributed over an area of 3 km², the available boreholes and cone penetration tests reach 82.5%. In particular, the mechanical CPTs correspond to 35.5% and the electrical ones to 32% of the total.

The implemented tool provides automatic sectioning of CPT profiles into statistically homogeneous layers.

From the CPT parameters, the I_c profile is computed. The statistical parameters $Tratio$ and ρ_I are calculated, and the critical thresholds are estimated. The horizontal dashed lines identify the transition between two different homogeneous layers.

For each stratum, the following parameters are computed:

- the Soil Behaviour Type SBT,
- the mean and standard deviation of the I_c values,
- the mean and standard deviation of the friction ratio, FR, defined as the ratio between sleeve friction and cone resistance.

6.5.3 Training and application of the Artificial intelligence algorithm

At this stage, data collected in boreholes and sectioned CPT must be cross-correlated to perform an automatic stratigraphic recognition. The calibration of the artificial intelligence algorithm has been performed comparing the outcomes derived from couples of CPT-borehole considered spatially correlated. Due to the complex stratigraphic context in the investigated area of Terre del Reno (Fe), each CPT profile has been considered representative of a circular area having a radius equal to 30 m. This distance has been chosen because the cone tip resistance of the selected site is characterized by a correlation length equal to $\Theta = 16.5$ m in the horizontal direction and a scale of fluctuation $\delta = 33$ m, representing the maximum distance over which the points are significantly related.

All boreholes located in the defined distance are classified as complementary of the cone penetration tests. The total number of couples CPT-boreholes is equal to 132. The 132 pairs constitute the starting point for the calibration of the algorithm. The sectioned CPT and the complementary boreholes have been compared.

CONCLUSIONS

Besides the output provided by the sectioning of CPTs, at each statically homogeneous layer has been attributed the stratigraphic unit recognized in the complementary boreholes. These parameters are the input values for the calibration of a classifier capable of identifying the corresponding stratigraphic unit.

The choice of the algorithm involves the estimation of the efficiency between 32 different artificial classifiers, implemented in the Classification Learner APP available in MATLAB R2021b, with a 10 folds cross-validation procedure (Stone, 1974).

This procedure is suggested to avoid overfitting and to estimate the accuracy obtained within the 10 iterations. Cross-validation divides the dataset into 10 folders of the same size: 9 folders are used to train the classifier while one is used to validate it. This procedure is iterated 10 times, training and testing each folder. The best classifier is a linear discriminant, characterized by an efficiency equal to 81.6%. Linear Discriminant Analysis (LDA) was been proposed by Fischer in 1918. It consists in finding the hyperplane projection that minimizes the interclass variance and maximizes the distance between the projected means of the classes.

In Figure 6.12a shows the efficiency of the algorithm to classify the four units, attributing the percentage of success and misclassification. The positive prediction is expressed as Positive Predicted Values (PPV), and the negative classification is expressed as False Discovery Rates (FDR). Figure 6.12b consists in a report showing a summary of prediction results of the mutual classification between classes, the grey cells correspond to the PPV and the sum of the remaining elements along the columns is equal to the FDR. For example, the first column summarizes the detail of the layers automatically classified as Unit #1: truly classified in 75.4% of occurrences; Unit #2 has been mistaken with Unit #1 in 15.8% of manifestations; Unit #1 has been attributed to the real Unit #3 in 1.2% and in the remaining 7.6%, Unit #4 has been classified as Unit #1.

In particular, the mutual misclassification between sands and clays never occurs. Furthermore, the lower PPV values are associated with Units #1 (silt, silty clay, clayey silt) and #2 (sandy silt, silty sand), located in the upper 10 m of the subsoil and characterized by a complex geological history.

Once the effectiveness was ascertained, the algorithm was applied to the remaining cone penetration tests, obtaining the stratigraphic recognition of the surveys disseminated on the investigated area (Fig. 6.13).

The script of the proposed algorithm is attached in the Appendix C.

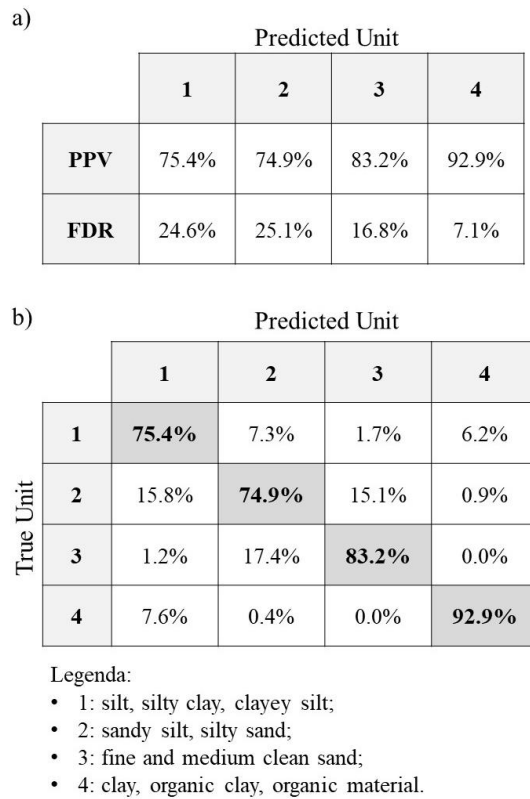


Figure 6.12 - Efficiency of the proposed LDA algorithm.

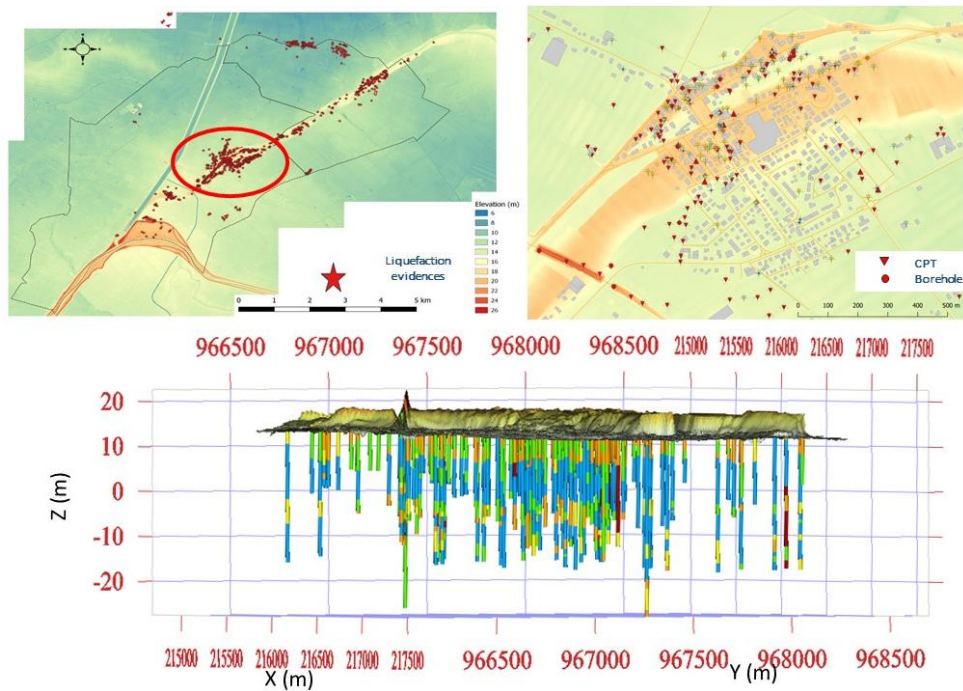


Figure 6.13 - Application of the LDA algorithm on the surveys disseminated all over the area of San Carlo.

6.5.4 3D subsoil stratigraphic reconstruction

The applied procedure allows a one-dimensional stratigraphic recognition. To evaluate the angular distortions in foundation caused by the liquefaction phenomenon, it is necessary to characterize the subsoil beneath the buildings. To this aim, a three-dimensional geotechnical model was built using the ISATIS software (Geovariances, 2022). ISATIS is the most comprehensive and advanced general-purpose geostatistics toolbox that allows addressing different issues from various industries, including mineral or life resource estimation, geomodeling, environmental mapping, risk analysis, and more.

A plurigaussian model was selected to build the 3D interpolation of the subsoil stratigraphy. The mathematical method called Plurigaussian Simulations was invented in France in the 1990s for simulating the internal architecture of oil reservoirs (Matheron *et al.*, 1987; Le Loc'h and Galli, 1994). Nowadays, the model is currently used for simulating geological domains (facies) in petroleum reservoirs and mineral deposits, with the aim of assessing the uncertainty in the domain boundaries and of improving the geological controls in the characterization of quantitative attributes. The principle of the method is to generate two (or more) Gaussian fields, using standard multi-Gaussian techniques, and then to truncate them in order to produce a map of discrete values representing the lithotypes (Le Loc'h and Galli, 1994). The model has been applied on several variables. The approach proposed by Le Loc'h and Galli (1994) for that purpose is to define the relations between the facies in a diagram called the lithotype rule. The lithotype rules are diagrams providing the proportion between facies and the possible contact between them. The choice of a lithotype rule is therefore a major step of the methodology. In practice, transition probabilities calculated from borehole logs provide good indications on which facies can and cannot be in contact. However, this is not sufficient since it is restricted to the vertical transitions. Therefore the lithotype rule is usually based on both the analysis of the borehole logs and on a geological conceptual model. In most practical cases, these proportions are

not constant over the domain, but vary vertically and laterally because of the existence of trends in the geological processes. This non-stationarity is modelled by providing variable proportions over the domain.

Another important feature of the plurigaussian technique is the inference of the variogram models for the underlying multi-Gaussian fields. Therefore, the variogram inference is based on an inverse procedure in which the ranges of the variograms of

the multi-Gaussian fields are adjusted iteratively through an inverse procedure (Freulon and Fouquet, 1993; Armstrong *et al.*, 2003).

In particular, the geostatistical interpolation with the truncated plurigaussian has been performed on the median value and the standard deviation of soil behaviour type index (I_c) and normalized cone tip resistance (q_{c1n}) of each strata on vertical CPT and boreholes profiles. Furthermore, in order to reduce the computational cost, two fixed surfaces and well identified in the subsoil have been introduced in the software analysis. The first surface is the groundwater table (in lightblue in Figure 6.14) and the second one is given by the top of alluvial clays (in blue in Figure 6.14).

Figure 6.14 shows the extension of the liquefiable volumes, depicted in yellow.

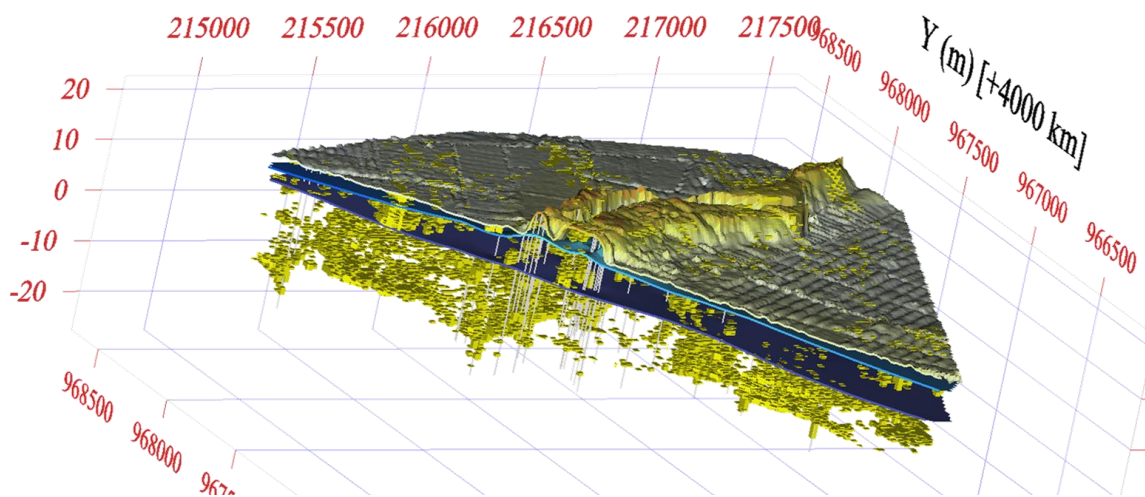


Figure 6.14 - Detail of the liquefiable volumes (in yellow) in the 3D stratigraphic reconstruction of the subsoil of San Carlo, performed with Isatis software.

6.6 Angular distortion assessment

The above analyses lead to the evaluation of the expected angular distortion in foundation induced by the liquefaction phenomenon. The aim is to relate the forecasted relative rotation to the observed damages occurred in the district of San Carlo after the 2012 Emilia-Romagna earthquake sequence, in order to define a method for a preliminary vulnerability screening at urban scale. The following results are a back analysis of the May 20th earthquake ($M_w=6.1$).

The angular distortion assessment has been carried out applying the procedure described above in *Paragraph 5.4* and performing the AI algorithm in Appendix C.

In detail, the methodology for the analysis of damage to buildings is based on the steps described below.

1. Subsoil characterization:
this step can be performed applying several procedure (i.e. the methodology described in *Chapter 3* or schematizing the subsoil in a the three-layer model through the application of the ESP method (Millen et al., 2020));
2. Characterization of building stock (geometry; number of stories; building type, based on the construction period; typology of foundation);
3. Evaluation of the expected liquefaction induced settlement in foundation with the semi-empirical method proposed by Bullock *et al.* (2018);
4. Assessment of the angular distortion applying the procedure described in Paragraph 5.4 and performing the AI algorithm in Appendix C.

The characterization of building stock and subsoil layers has been performed and described in paragraphs 6.3.3 and 6.5, respectively.

The following step consists in the evaluation of the average settlement in foundation with the comprehensive semi-empirical predictive relation for shallow-founded structures on liquefiable ground. The formula has been applied to each building in the district of San Carlo with the spreadsheet provided by the authors (<https://shidehdashti.com/geotech-links/>). The calculation requires inputting the parameters listed in Table 5.4, *Paragraph 5.3*.

The last step has been carried out with the MatLab function attached in Appendix C. The required input parameters are listed in Table 6.1. The non-liquefiable crust thickness (H_c) and the undrained shear strength of crust (s_u) are extracted beneath each structures from the 3D geotechnical model built in ISATIS, the average settlement ($w_{Bullock}$) has been derived in the third step and the equivalent stiffness of the building foundation system has been set equal to $EI = 0 \text{ MN} * m$ for the masonry buildings and individually characterized for the reinforced concrete buildings with the procedure described in *Paragraph 5.2.2*.

The obtained angular distortion are shown in Figure 6.15. Comparing the distribution of relative rotation (Figure 6.15), the observed liquefaction induced surficial manifestations (Figure 6.16) and the recorded damages (Figure 6.17), a good match between the forecasted values and the occurred liquefaction phenomenon is found.

Table 6.1 – Required input parameter for the assessment of the liquefaction induced angular distortion with the proposed ANN.

Parameter	
EI (MN*m)	Equivalent stiffness of the building foundation system
Hc (m)	non-liquefiable crust thickness
su (kPa)	Undrained shear strength of crust
WBullock (m)	Average settlement



Figure 6.15 - Forecasted liquefaction induced angular distortion in the district of San Carlo.

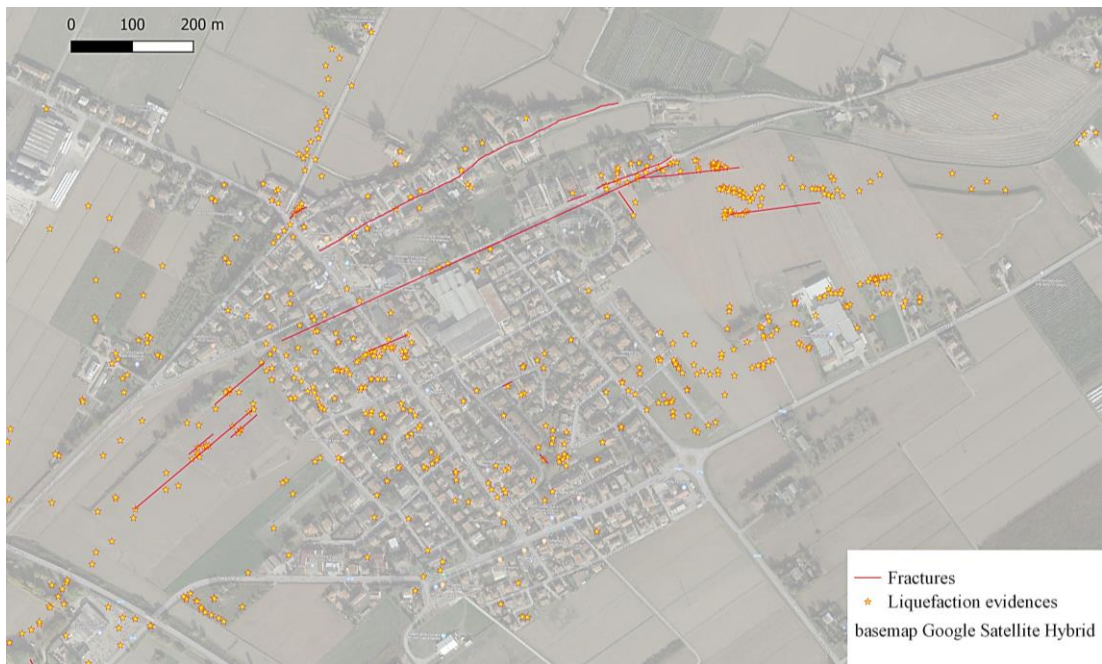


Figure 6.16 - Liquefaction induced surficial manifestations and fractures in the district of San Carlo.



Figure 6.17 - Liquefaction induced damages on buildings in the district of San Carlo.

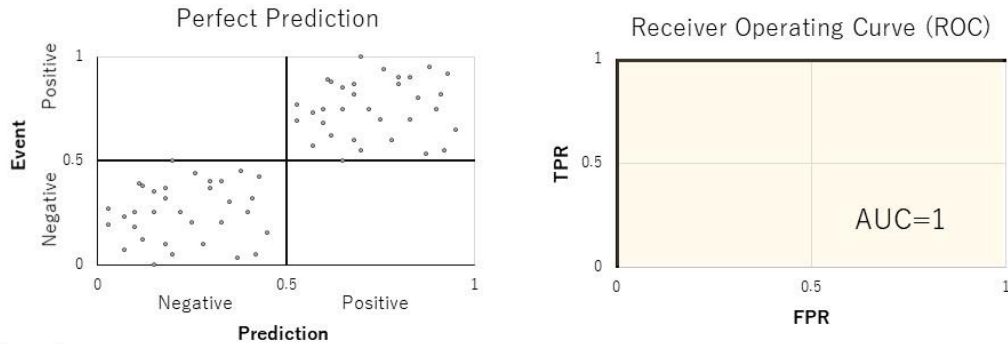
6.7 Validation

The robustness of the relation between damages and predicted angular distortion in foundation, is evaluated with the Receiver Operating Curve (ROC) method defined by Kongar *et al.* (2015) and illustrate in Figure 6.18 This method establishes a binary classification between prediction and observations. For a specific event and an associated prediction model, the comparison leads to summarize the results in a contingency table (2x2) distinguishing the different possible cases in true positives (PP), true negatives (NN), false positives (FP) and false negatives (FN). The true positives rate (TPR) (i.e. the fraction of positive events predicted as positive), and the false positive rate (FPR) (i.e. the fraction of negative events predicted as positive), can be computed from the above matrix. Considering increasing threshold values of the candidate predictive variable, it is possible to draw a curve in the FPR-TPR plane (Figure 6.18) whose shape represents the capability of the predictive method. In fact, for zero threshold, TPR and FPR are both equal to 1 (all events, positive or negative, are estimated as positive), then both variables tend to zero for increasing thresholds. At the maximum threshold all events, positive or negative, are predicted as negative (TPR and FPR are both equal to zero). If the predictive method is valid and a well-defined threshold can be set, the curve will pass near the upper-left corner of the plot (FPR=0 - TPR=1) (case A in Figure 6.18) which represent the ideal condition where all negative events are predicted as negative and all positive events are predicted as positive. On the contrary, in the case of poor prediction, the curve will move along the plane bisecting line (1:1) (case B in Figure 6.18), which means positive and negative events randomly predicted as positive or negative. With this representation, the extension of the Area Under the Curve (AUC) can be assumed as a proxy for the quality of prediction, 1 meaning good, 0.5 scarce predictive capability. Thereafter, the optimal threshold value, i.e. the decision value of the variable that defines the best separation between negative and positive events, can be computed as the one giving the maximum Mathews Correlation Coefficient (Mathews, 1975) defined as:

$$MCC = \frac{PP \cdot NN - NP \cdot PN}{\sqrt{(PP+NP) \cdot (PP+PN) \cdot (NN+NP) \cdot (NN+PN)}} \quad (6.1)$$

where TP, TN, FT and FN are the numbers of respectively true positive, true negative, false positive and false negative occurrences.

Case a:



Case b:

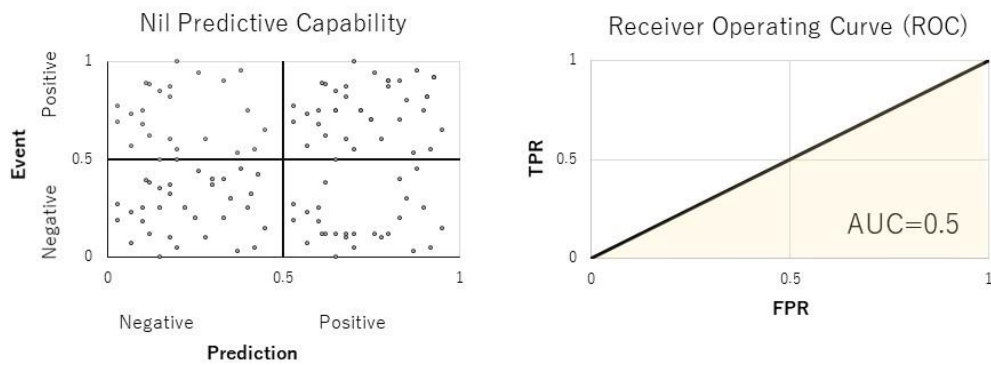


Figure 6.18 - Receiver Operating Curve (ROC) method.

The test based on ROC is thus applied to investigate the relation between the damage recorded during the event and angular distortion. This analysis gives $AUC=0.72$ and a first damage threshold of equal to $\beta = 1/500$, followed by two further peaks corresponding to $\beta = 1/300$ and $\beta = 1/200$.

For the sake of completeness, the ROC test has been also applied on the liquefaction settlement severity indicator (w_v) proposed by Zhang *et al.* (2002) and the average settlement computed with the semi-empirical formula proposed by Bullock *et al.* (2018).

In particular, the liquefaction settlement severity indicator (w_v) proposed by Zhang *et al.* (2002) has been computed in the proximity of each CPT test and, successively, has been interpolated with the ordinary kriging geostatistical tool. From the indicator's map, the values of the interpolated free-fields settlements have been extracted below each building.

The comparison between the proposed criterion, free-field settlement computed with Zhang *et al.* (2002) and average settlement evaluated with Bullock *et al.* (2018) is shown in Figure 6.19 and the obtained AUC are listed in Table 6.2.

Table 6.2 - AUC values

Parameter	AUC
β	0.72
w_v (m)	0.65
$w_{Bullock}$ (m)	0.65

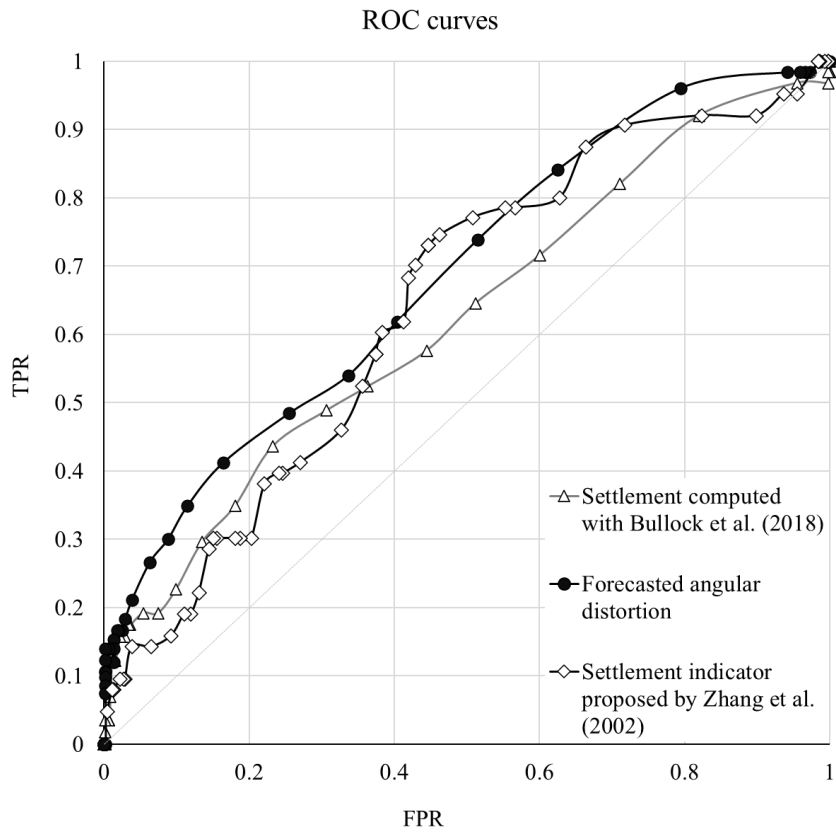


Figure 6.19 - Receiver Operating Curve test between damages on buildings and forecasted angular distortion, settlement computed with Bullock *et al.* (2018) and settlement indicator proposed by Zhang *et al.* (2002).

6.8 Analysis of results

The obtained result confirms the capability of the proposed procedure to capture damages on buildings and encourages to assume liquefaction induced angular distortion as indicator of damage on buildings.

Nevertheless, the performance with $AUC = 0.72$ suggests the possibility of an improvement in the procedure. The elements that contribute to the result are two: buildings and subsoil.

In order to test the goodness of the subsoil geotechnical model reconstruction, the performance in free-field conditions of the liquefaction settlement severity indicator (Zhang *et al.*, 2002) has been tested. In particular, the indicator has been compared with the liquefaction-induced surficial manifestations, neglecting the damage to buildings. The territory has been ideally subdivided with a grid of square cells of 25m side, classifying each cell as *True Positive* if the occurrence of sand boils or fractures is recorded and *True Negative* in case of nil manifestation. The performance of the indicator is thus verified with the criterion defined in *paragraph 6.7*.

Figure 6.20 shows the computed Receiver Operating Curve, characterized by an area under the curve equal to $AUC=0.79$. This result is confirmed by Paoletta *et al.* (2022) and allows to state that the subsoil is well modelled. Furthermore, the analysis highlights the better performance of the indicator on soil damage than on damages to buildings.

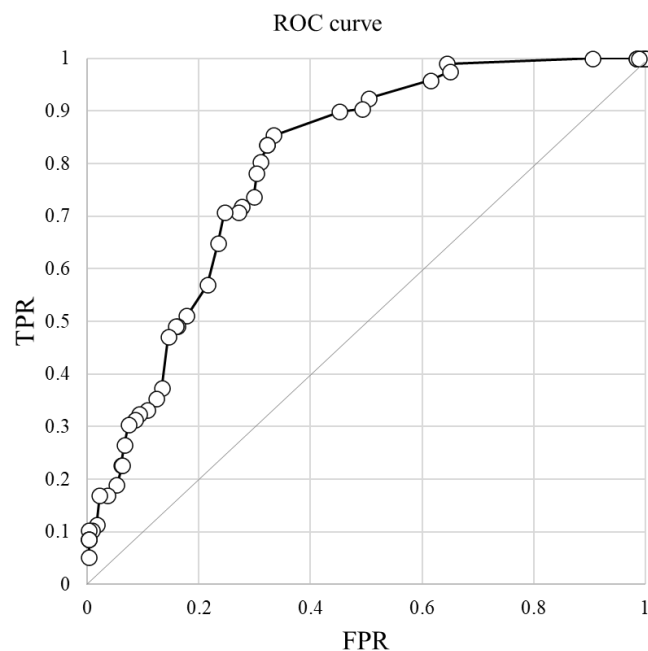


Figure 6.20 - Receiver Operating Curve test between liquefaction-induced surficial manifestations and free-field settlement indicator proposed by Zhang *et al.* (2002).

CONCLUSIONS

The buildings' features are the second element that contributes to the result. In particular, the angular distortion depends on the geometric characteristics and the construction typology, as well as on the stiffness of the building system. Furthermore, the ROC test is closely related to the number of damaged buildings.

In the proposed analysis, the recorded damaged buildings are only those for which the MUDE form has been filled-in for the request for financial assistance. This implies that there may be other structures that have suffered damage but have not been considered. If this were the case, there would be a reduction in the number of False Positives, leading to an increase in the value of the area under the curve (AUC).

The previous considerations attest that the proposed procedure can be made more efficient with an improvement of the building's description and if a more detailed aftershock survey is carried out.

CONCLUSIONS

The objective of the present study is to derive a simple yet comprehensive method to inspect buildings distributed over large areas against liquefaction risk. To this aim, several analyses have been performed investigating mainly two elements and their interactions: subsoil and structures.

First, CPT and boreholes are used to calibrate and validate a massive and automated site characterization by combining statistical tools and artificial intelligence algorithms (AI). The procedure is applied in the complex stratigraphic context of Terre del Reno (Italy). The proposed data-driven analysis allows to combine the geological and geotechnical knowledge of the subsoil in an efficient and automatic way based on site-specific data, obtaining reliable and indispensable results for the construction of a robust and coherent geotechnical model of the subsoil. The automatized methodology is easily replicable in other contexts for the stratigraphic recognition of the subsoil on a large scale. The data-driven analysis provides reliable and indispensable results for the construction of a robust and coherent geotechnical model of the subsoil.

Once the subsoil characterization has been accomplished, the attributes of liquefaction-induced settlements on low-rise buildings have been thoroughly examined with numerical Finite Difference analyses carried out with variable seismic, subsoil and structural conditions. The back-analysis of a documented case study has revealed that the pore pressure build-up and liquefaction occurring at certain depths inhibit propagation of the seismic signal to the upper levels, and thus liquefied soils act as an impedance to the shaking on the ground surface. This effect limits the role of inertia on the liquefaction assessment of buildings and justifies the herein adopted schematization of the structure with an equivalent beam. A specific calculation has shown a few percent influence of the inertia on the absolute and differential settlements computed with the simplified scheme. The parametric study has shown that, despite reaching larger values, movements induced by liquefaction present similar characters to those induced by static loading. Like for static loading, the horizontal deformation is negligible and the angular distortion β increases with the absolute settlement (mean or maximum), this relation being enveloped by the upper bound curve experimentally observed by Grant *et al.* (1989). This evidence has suggested to use a vulnerability

criterion for liquefaction assessment from the practice of foundation engineering under static conditions, i.e. adopting the angular distortion β as a demand variable. An Artificial Neural Network has thus been proposed to quantify β as a function of the fundamental characteristics of earthquake, building and subsoil. For the sake of simplicity, the number of input variables has been minimized by grouping most variables into the median settlement estimated with a semi-empirical method recently proposed by Bullock *et al.* (2018). The other considered input variables, selected based on their statistical relevance on β , are the flexural stiffness of the building-foundation system, the thickness and the undrained shear strength of the crust layer. The former complies with the observation of Bird *et al.* (2006) who distinguished absolute and differential settlement as damage factors for rigid and flexible foundations, respectively. The latter, in accordance with Karamitros *et al.* (2013a), who quantified the positive contribution on settlement reduction given by the non-liquefiable crust.

The proposed procedure for the prediction of the expected liquefaction-induced angular distortion have been validated on the case study of Terre del Reno (FE, Emilia-Romagna, Italy), severely struck by liquefaction during the 2012 earthquake sequence. In particular, the analysis has been performed on the districts of San Carlo, extensively covered by liquefaction-induced surficial manifestations and geognostic surveys. Due to the limited information about the structural typologies, the angular distortion has been assessed by assigning the conservative condition of nil equivalent stiffness in foundation. This choice gives the maximum value of angular distortion. The validation has been carried out with the binary test proposed by Kongar *et al.* (2015), characterized by two parameters of control: the receiver operating curve (ROC) and the area under the curve (AUC). The test based on ROC is thus applied to investigate the relation between the damage recorded during the event and angular distortion. This analysis gives AUC=0.72 and a first damage threshold of angular distortion equal to $\beta = 1/500$, followed by two further peaks corresponding to $\beta = 1/300$ and $\beta = 1/200$. The performance is consistent with the ones observed in past studies for other liquefaction indicators (Paolella *et al.*, 2022) and the obtained thresholds of angular distortion that optimize the detection of damages, remark the values observed in the serviceability limit state (SLS). However, the performance can be improved with a more detailed knowledge of the structures, in terms of structural typology and damages surveys.

Furthermore, the research highlights the importance of generating an inventory geodatabase. Thanks to georeferenced data and the availability of advanced tools, such as AI, it is possible to derive subsoil characterization always more detailed.

CONCLUSIONS

Finally, the results of numerical analyses prove that the shapes of the movements in the foundation due to static causes and due to seismic liquefaction are the same, keeping valid, in the seismic case, the theory widely applied in the serviceability limit state (i.e. Grant *et al.*, 1974 and Boscardin and Cording, 1989).

APPENDIX A

Calibration and validation of the numerical model

The prototype model has been firstly validated with the back-analysis of a building located in the Municipality of Terre del Reno, whose data are extracted from the Emilia-Romagna Regional database. In particular, the MUDE, an Italian post-earthquake survey form, were consulted to derive information related building typology and occurred damages. The building consists of a two storeys masonry building with a rectangular layout (length 13.10 m, width 11.10 m) founded on a shallow slab of poor structural characteristics. The liquefaction induced by the May 20th earthquake ($M_w=6.1$) caused significant differential settlements in the East-West direction, with an absolute settlement of 35 cm on the West side and 5 cm on the East side (Figure A1.b). Being the epicenter located about 15 km far from the building, at a depth approximately equal to 10 km below the ground level (Luzi *et al.*, 2019), the acceleration time history assigned for the back analysis (Figure 4.2.c) has been computed transferring to the considered site the signal recorded at the nearest seismic station (Mirandola, from the ITACA seismic catalogue) performing the procedure suggested by Sinatra & Foti (2015). These authors propose to deconvolve the acceleration time history recorded at the station to recover the signal the seismic bedrock, then apply the attenuation law proposed by Bindi *et al.* (2011) to move from the station to the studied site, then perform a local seismic response analysis to obtain the input at the model's base. In the analysis, the deeper subsoil model has been taken from Fioravante *et al.* (2013), while the top subsoil stratigraphy has been reconstructed considering various CPTU tests performed in the closest area around the building (Figure A1.a).

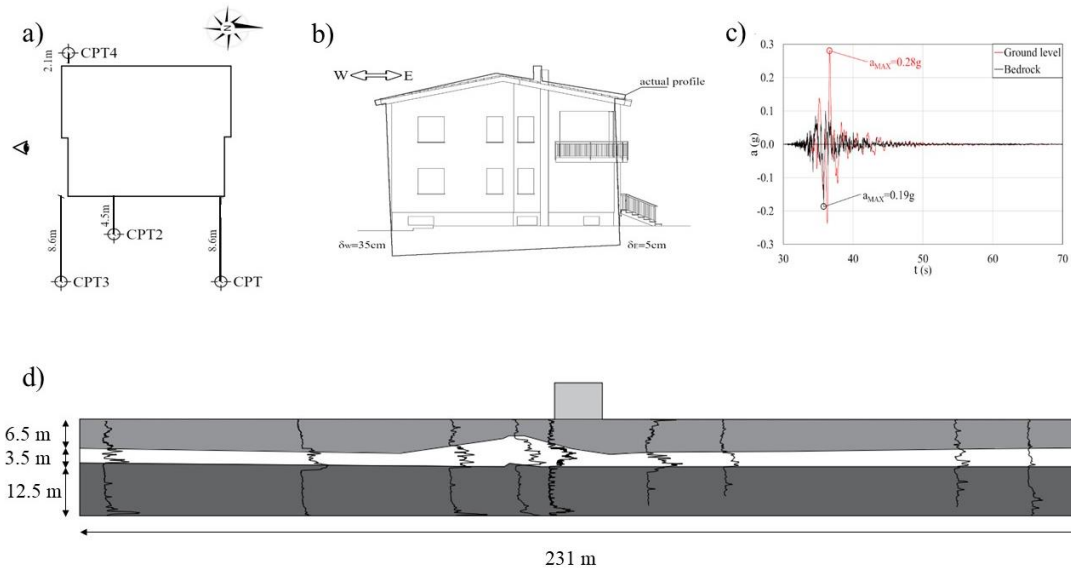


Figure A1- Building's plan and closest CPT tests (a), settlement profile (b), acceleration time history (c) and subsoil profile (d) of the selected case study.

Considering its known structural characteristics, the building has been simulated with an elastic body of given width ($B=12\text{m}$), flexural stiffness ($EI=60 \text{ MN}\cdot\text{m}$) and contact pressure ($q=35 \text{ kPa}$). The performed analysis returned a significant rotation of the building with a final vertical displacement at the west corner of 37 cm and at the east side corner of about 4 cm, these values in a close agreement with the post-earthquake surveyed deformation (Emilia-Romagna Regional database, [MUDE](#)) giving respectively 35 and 5 cm at the two corners (Figure A1).

The results of simulation are presented in Figure A2 as a typical output of calculation. Figure A2.c reports the acceleration time histories for the points A (at the foundation level), B (in the middle of the liquefiable layer) and C (at the bottom of model). During the first 36 seconds, the wave motion propagates upward with a slight signal's modification. After this time, the pore pressures in the sandy layer start to increase, as shown by the plot of $r_u = \Delta u / \sigma'_{zo}$ (Figure A2.e) and this effect progressively impedes the transmission from the sandy layer to the upper foundation, while acceleration is still conveyed from the clayey stratum. When r_u approaches relatively high values (say 0.8), after about 38 seconds, the sandy soil softens and becomes unable to further propagate motion upward. This effect proceeds until liquefaction fully develops (r_u approaching 1). Therefore, the increase of pore pressures and the liquefaction induced decay of stiffness in the sandy soil, prevents wave propagation and the liquefied soil acts as an isolator for the building shaking. From this viewpoint, this effect is positive as it should reduce structural damage. On the other hand, the

increase or pore pressure in the sandy soil determines (Figure A2.d) significant settlements that start to increase when r_u reaches values of about 0.6 and continues with the progress of liquefaction. The maps of Figure A4.a and b, that report the fields of pore pressure ratio R_u at the end of the shaking and of maximum shear deformation throughout the event, reveals that liquefaction does not occur uniformly in the sandy layer but starts principally near singularities of the subsoil. The settlements time histories of the foundation reported in Figure A2.c show a significant differential settlement between the left and right corners of the building, with vertical displacement respectively equal to 37 and 4 cm. This effect clearly depends on the higher thickness of the liquefiable layer on the left side of the building. In conclusion, the above results show the ability of the adopted numerical model to reproduce the phenomena taking place at buildings foundation upon seismic shaking and liquefaction. Despite calculation has been simplified (a two-dimensional model has been implemented) the results are fully consistent with the observed response of the building and, particularly, with the differential settlements experienced by the foundation at its two opposite corners.

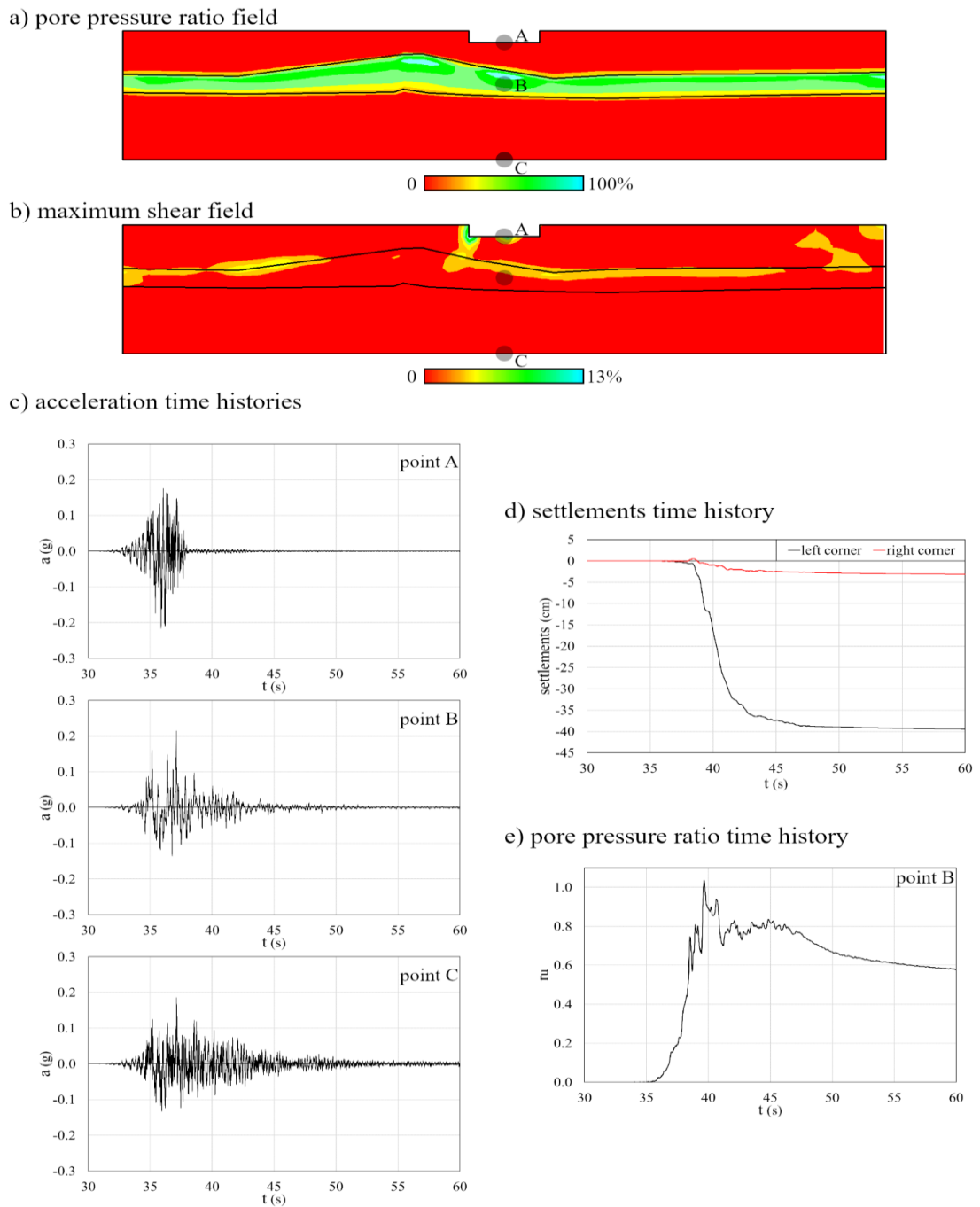


Figure A2 - Results of the simulation in terms of a) pore-pressure ratio field; b) maximum shear field; c) acceleration time histories at the bottom of the model (point C), in the middle of the liquefiable layer (point B) and at the foundation's level (point A); d) settlements time histories at the left corner of the foundation (in black) and at the right corner of the foundation (in red); e) pore-pressure ratio time history at the middle of the liquefiable layer.

APPENDIX B

Numerical results

Appendix B

ID	Earthquake	scaling facto	q (kPa)	Su (kPa)	B	HL	HC	EI	Hd	Dr	β	wmax (m)	wav (m)	eh	ru,max
1	Emilia-Romagna	0.7	50	50	10	4	2	0	1	40	0.00332	0.05	0.05	0.0013256	0.89
2	Emilia-Romagna	0.7	50	50	10	4	4	0	1	40	0.00312	0.04	0.03	0.0013523	0.93
3	Emilia-Romagna	0.7	50	50	10	4	6	0	1	40	0.00192	0.03	0.03	0.0001594	0.98
4	Emilia-Romagna	0.7	50	50	10	4	2	32.5	1	40	0.00056	0.02	0.02	0.0000133	0.91
5	Emilia-Romagna	0.7	50	50	10	4	4	32.5	1	40	0.00089	0.03	0.03	0.0000600	0.96
6	Emilia-Romagna	0.7	50	50	10	4	6	32.5	1	40	0.00086	0.03	0.03	0.0000700	0.88
7	Emilia-Romagna	0.7	50	50	10	4	2	260	1	40	0.00006	0.02	0.02	0.0000081	0.95
8	Emilia-Romagna	0.7	50	50	10	4	4	260	1	40	0.00010	0.03	0.03	0.0000038	0.90
9	Emilia-Romagna	0.7	50	50	10	4	6	260	1	40	0.00012	0.03	0.03	0.0000103	0.97
10	Emilia-Romagna	1	50	50	10	4	2	0	1	40	0.00956	0.18	0.17	0.0000138	0.84
11	Emilia-Romagna	1	50	50	10	4	4	0	1	40	0.01181	0.11	0.10	0.0002992	1.02
12	Emilia-Romagna	1	50	50	10	4	6	0	1	40	0.00655	0.08	0.07	0.0002810	0.94
13	Emilia-Romagna	1	50	50	10	4	2	32.5	1	40	0.00100	0.07	0.07	0.0000495	0.95
14	Emilia-Romagna	1	50	50	10	4	4	32.5	1	40	0.00149	0.08	0.07	0.0001000	0.95
15	Emilia-Romagna	1	50	50	10	4	6	32.5	1	40	0.00141	0.06	0.05	0.0001300	0.99
16	Emilia-Romagna	1	50	50	10	4	2	260	1	40	0.00002	0.08	0.06	0.0000001	0.93
17	Emilia-Romagna	1	50	50	10	4	4	260	1	40	0.00012	0.07	0.06	0.0000102	0.91
18	Emilia-Romagna	1	50	50	10	4	6	260	1	40	0.00015	0.05	0.05	0.0000177	1.00
19	Emilia-Romagna	1.6	50	50	10	4	2	0	1	40	0.02477	0.31	0.26	0.0005506	0.89
20	Emilia-Romagna	1.6	50	50	10	4	4	0	1	40	0.01506	0.22	0.18	0.0003622	1.03
21	Emilia-Romagna	1.6	50	50	10	4	6	0	1	40	0.00948	0.13	0.11	0.0000072	0.98
22	Emilia-Romagna	1.6	50	50	10	4	2	32.5	1	40	0.00136	0.23	0.18	0.0000866	0.97
23	Emilia-Romagna	1.6	50	50	10	4	4	32.5	1	40	0.00193	0.16	0.14	0.0001594	0.96
24	Emilia-Romagna	1.6	50	50	10	4	6	32.5	1	40	0.00155	0.11	0.10	0.0000894	0.99
25	Emilia-Romagna	1.6	50	50	10	4	2	260	1	40	0.00004	0.19	0.18	0.0000001	0.95
26	Emilia-Romagna	1.6	50	50	10	4	4	260	1	40	0.00015	0.14	0.13	0.0000103	0.93
27	Emilia-Romagna	1.6	50	50	10	4	6	260	1	40	0.00010	0.12	0.10	0.0000103	1.03
28	Emilia-Romagna	0.7	50	50	10	6	2	0	1	40	0.00391	0.08	0.06	0.0001872	0.91
29	Emilia-Romagna	0.7	50	50	10	6	4	0	1	40	0.00305	0.05	0.04	0.0001874	0.95
30	Emilia-Romagna	0.7	50	50	10	6	6	0	1	40	0.00288	0.04	0.03	0.0001874	1.00
31	Emilia-Romagna	0.7	50	50	10	6	2	32.5	1	40	0.00065	0.04	0.04	0.0000081	0.93
32	Emilia-Romagna	0.7	50	50	10	6	4	32.5	1	40	0.00059	0.05	0.04	0.0000131	0.98
33	Emilia-Romagna	0.7	50	50	10	6	6	32.5	1	40	0.00090	0.04	0.03	0.0000768	0.90
34	Emilia-Romagna	0.7	50	50	10	6	2	260	1	40	0.00007	0.05	0.04	0.0000001	0.97
35	Emilia-Romagna	0.7	50	50	10	6	4	260	1	40	0.00009	0.04	0.04	0.0000718	0.92
36	Emilia-Romagna	0.7	50	50	10	6	6	260	1	40	0.00013	0.04	0.03	0.0000103	0.99
37	Emilia-Romagna	1	50	50	10	6	2	0	1	40	0.00972	0.18	0.14	0.0003556	0.87
38	Emilia-Romagna	1	50	50	10	6	4	0	1	40	0.01166	0.13	0.10	0.0004127	1.03
39	Emilia-Romagna	1	50	50	10	6	6	0	1	40	0.00693	0.09	0.07	0.0002739	0.98
40	Emilia-Romagna	1	50	50	10	6	2	32.5	1	40	0.00085	0.10	0.09	0.0000951	0.97
41	Emilia-Romagna	1	50	50	10	6	4	32.5	1	40	0.00154	0.12	0.11	0.0001153	0.96
42	Emilia-Romagna	1	50	50	10	6	6	32.5	1	40	0.00151	0.09	0.08	0.0001144	0.99
43	Emilia-Romagna	1	50	50	10	6	2	260	1	40	0.00004	0.11	0.10	0.0000713	0.95
44	Emilia-Romagna	1	50	50	10	6	4	260	1	40	0.00010	0.11	0.10	0.0000730	0.93
45	Emilia-Romagna	1	50	50	10	6	6	260	1	40	0.00016	0.09	0.07	0.0000747	1.02
46	Emilia-Romagna	1.6	50	50	10	6	2	0	1	40	0.04471	0.39	0.32	0.0013846	0.91
47	Emilia-Romagna	1.6	50	50	10	6	4	0	1	40	0.03480	0.33	0.25	0.0010931	1.05
48	Emilia-Romagna	1.6	50	50	10	6	6	0	1	40	0.01730	0.23	0.20	0.0005786	1.00
49	Emilia-Romagna	1.6	50	50	10	6	2	32.5	1	40	0.00094	0.25	0.23	0.0000975	0.99
50	Emilia-Romagna	1.6	50	50	10	6	4	32.5	1	40	0.00206	0.25	0.24	0.0001307	0.98
51	Emilia-Romagna	1.6	50	50	10	6	6	32.5	1	40	0.00172	0.18	0.16	0.0001206	1.01
52	Emilia-Romagna	1.6	50	50	10	6	2	260	1	40	0.00004	0.25	0.24	0.0000711	0.97
53	Emilia-Romagna	1.6	50	50	10	6	4	260	1	40	0.00018	0.27	0.23	0.0000754	0.95
54	Emilia-Romagna	1.6	50	50	10	6	6	260	1	40	0.00018	0.18	0.17	0.0000753	1.04
55	Emilia-Romagna	0.7	50	50	10	8	2	0	1	40	0.00498	0.09	0.07	0.0002163	1.01
56	Emilia-Romagna	0.7	50	50	10	8	4	0	1	40	0.00483	0.06	0.05	0.0002120	1.04
57	Emilia-Romagna	0.7	50	50	10	8	6	0	1	40	0.00315	0.05	0.04	0.0001626	1.05
58	Emilia-Romagna	0.7	50	50	10	8	2	32.5	1	40	0.00038	0.06	0.05	0.0000813	1.03
59	Emilia-Romagna	0.7	50	50	10	8	4	32.5	1	40	0.00066	0.06	0.05	0.0000893	1.04
60	Emilia-Romagna	0.7	50	50	10	8	6	32.5	1	40	0.00105	0.04	0.04	0.0001009	1.05
61	Emilia-Romagna	0.7	50	50	10	8	2	260	1	40	0.00003	0.06	0.04	0.0000819	1.01
62	Emilia-Romagna	0.7	50	50	10	8	4	260	1	40	0.00006	0.05	0.05	0.0000833	1.02
63	Emilia-Romagna	0.7	50	50	10	8	6	260	1	40	0.00010	0.04	0.04	0.0000860	1.10
64	Emilia-Romagna	1	50	50	10	8	2	0	1	40	0.01457	0.20	0.18	0.0009454	1.02
65	Emilia-Romagna	1	50	50	10	8	4	0	1	40	0.01442	0.16	0.15	0.0009366	1.14
66	Emilia-Romagna	1	50	50	10	8	6	0	1	40	0.00989	0.12	0.11	0.0006676	1.09
67	Emilia-Romagna	1	50	50	10	8	2	32.5	1	40	0.00060	0.14	0.13	0.0001154	1.09
68	Emilia-Romagna	1	50	50	10	8	4	32.5	1	40	0.00120	0.15	0.13	0.0001274	1.06
69	Emilia-Romagna	1	50	50	10	8	6	32.5	1	40	0.00136	0.10	0.09	0.0001336	1.09
70	Emilia-Romagna	1	50	50	10	8	2	260	1	40	0.00003	0.13	0.13	0.0000811	1.03
71	Emilia-Romagna	1	50	50	10	8	4	260	1	40	0.00011	0.15	0.14	0.0000832	1.04
72	Emilia-Romagna	1	50	50	10	8	6	260	1	40	0.00015	0.09	0.09	0.0000844	1.13
73	Emilia-Romagna	1.6	50	50	10	8	2	0	1	40	0.02335	0.30	0.28	0.0007665	1.04
74	Emilia-Romagna	1.6	50	50	10	8	4	0	1	40	0.02738	0.18	0.17	0.0008849	1.16
75	Emilia-Romagna	1.6	50	50	10	8	6	0	1	40	0.01599	0.12	0.11	0.0005502	1.11
76	Emilia-Romagna	1.6	50	50	10	8	2	32.5	1	40	0.00086	0.28	0.26	0.0001052	1.10
77	Emilia-Romagna	1.6	50	50	10	8	4	32.5	1	40	0.00194	0.17	0.13	0.0001370	1.07
78	Emilia-Romagna	1.6	50	50	10	8	6	32.5	1	40	0.00192	0.11	0.10	0.0001366	1.10
79	Emilia-Romagna	1.6	50	50	10	8	2	260	1	40	0.00006	0.26	0.21	0.0000824	1.04
80	Emilia-Romagna	1.6	50	50	10	8	4	260	1	40	0.00016	0.18	0.14	0.0000867	1.05
81	Emilia-Romagna	1.6	50	50	10	8	6	260	1	40	0.00021	0.11	0.09	0.0000893	1.15
82	Emilia-Romagna	0.7	50	50	10	6	4	0	1	20	0.00983	0.10	0.08	0.0005065	0.92
83	Emilia-Romagna	1	50	50	10	6	4	0	1	20	0.02154	0.15	0.13	0.0001047	1.07
84	Emilia-Romagna	1.6	50	50	10	6	4	0	1	20	0.04106	0.25	0.21	0.0018620	1.02
85	Emilia-Romagna	0.7	50	50	10	6	4	32.5	1	20	0.00183	0.10	0.08	0.0001596	1.01
86	Emilia-Romagna	1	50	50	10	6	4	32.5	1	20	0.00166	0.13	0.12	0.0002017	1.00
87	Emilia-Romagna	1.6	50	50	10	6	4	32.5	1	20	0.00236	0.24	0.19	0.0002535	1.03
88	Emilia-Romagna	0.7	50	50	10	6	4	260	1	20	0.00013	0.10	0.08	0.0000893	0.99
89	Emilia-Romagna	1	50	50	10	6	4	260	1	20	0.00020	0.13	0.11	0.0000943	0.97
90	Emilia-Romagna	1.6	50	50	10	6	4	260							

Appendix B

98	Emilia-Romagna	1	50	50	10	6	4	260	1	60	0.00004	0.06	0.05	0.0000833	0.82
99	Emilia-Romagna	1.6	50	50	10	6	4	260	1	60	0.00005	0.09	0.08	0.0000840	0.96
100	Emilia-Romagna	0.7	25	50	10	6	4	0	1	40	0.00334	0.04	0.03	0.0003269	0.95
101	Emilia-Romagna	1	25	50	10	6	4	0	1	40	0.00507	0.07	0.06	0.0003538	1.03
102	Emilia-Romagna	1.6	25	50	10	6	4	0	1	40	0.01225	0.11	0.09	0.0007413	1.04
103	Emilia-Romagna	0.7	25	50	10	6	4	32.5	1	40	0.00082	0.03	0.03	0.0001240	0.94
104	Emilia-Romagna	1	25	50	10	6	4	32.5	1	40	0.00127	0.06	0.05	0.0001486	1.02
105	Emilia-Romagna	1.6	25	50	10	6	4	32.5	1	40	0.00144	0.11	0.10	0.0001580	1.03
106	Emilia-Romagna	0.7	25	50	10	6	4	260	1	40	0.00009	0.03	0.03	0.0000846	0.95
107	Emilia-Romagna	1	25	50	10	6	4	260	1	40	0.00013	0.05	0.05	0.0000869	1.02
108	Emilia-Romagna	1.6	25	50	10	6	4	260	1	40	0.00013	0.11	0.09	0.0000869	1.04
109	Emilia-Romagna	0.7	100	50	10	6	4	0	1	40	0.00510	0.04	0.03	0.0003964	0.97
110	Emilia-Romagna	1	100	50	10	6	4	0	1	40	0.02133	0.13	0.10	0.0014025	1.05
111	Emilia-Romagna	1.6	100	50	10	6	4	0	1	40	0.01554	0.14	0.11	0.0010436	1.07
112	Emilia-Romagna	0.7	100	50	10	6	4	32.5	1	40	0.00101	0.04	0.03	0.0001426	0.97
113	Emilia-Romagna	1	100	50	10	6	4	32.5	1	40	0.00108	0.13	0.11	0.0001467	1.04
114	Emilia-Romagna	1.6	100	50	10	6	4	32.5	1	40	0.00185	0.14	0.12	0.0001950	1.05
115	Emilia-Romagna	0.7	100	50	10	6	4	260	1	40	0.00003	0.04	0.03	0.0000820	0.97
116	Emilia-Romagna	1	100	50	10	6	4	260	1	40	0.00006	0.12	0.10	0.0000840	1.04
117	Emilia-Romagna	1.6	100	50	10	6	4	260	1	40	0.00010	0.13	0.11	0.0000862	1.06
118	Emilia-Romagna	0.7	50	25	10	6	4	0	1	40	0.01165	0.09	0.08	0.0008021	0.82
119	Emilia-Romagna	1	50	25	10	6	4	0	1	40	0.02232	0.18	0.14	0.0014638	0.84
120	Emilia-Romagna	1.6	50	25	10	6	4	0	1	40	0.02924	0.21	0.17	0.0018928	0.97
121	Emilia-Romagna	0.7	50	25	10	6	4	32.5	1	40	0.00081	0.08	0.07	0.0001301	0.82
122	Emilia-Romagna	1	50	25	10	6	4	32.5	1	40	0.00097	0.16	0.14	0.0001404	0.84
123	Emilia-Romagna	1.6	50	25	10	6	4	32.5	1	40	0.00107	0.19	0.15	0.0001464	0.98
124	Emilia-Romagna	0.7	50	25	10	6	4	260	1	40	0.00002	0.08	0.07	0.0000813	0.82
125	Emilia-Romagna	1	50	25	10	6	4	260	1	40	0.00003	0.16	0.13	0.0000816	0.84
126	Emilia-Romagna	1.6	50	25	10	6	4	260	1	40	0.00005	0.18	0.14	0.0000829	0.97
127	Emilia-Romagna	0.7	50	100	10	6	4	0	1	40	0.00240	0.05	0.04	0.0002288	0.80
128	Emilia-Romagna	1	50	100	10	6	4	0	1	40	0.00804	0.11	0.09	0.0005784	0.81
129	Emilia-Romagna	1.6	50	100	10	6	4	0	1	40	0.01595	0.25	0.20	0.0010688	0.93
130	Emilia-Romagna	0.7	50	100	10	6	4	32.5	1	40	0.00048	0.04	0.04	0.0001098	0.80
131	Emilia-Romagna	1	50	100	10	6	4	32.5	1	40	0.00143	0.10	0.08	0.0001685	0.81
132	Emilia-Romagna	1.6	50	100	10	6	4	32.5	1	40	0.00240	0.21	0.17	0.0002286	0.94
133	Emilia-Romagna	0.7	50	100	10	6	4	260	1	40	0.00003	0.04	0.04	0.0000818	0.80
134	Emilia-Romagna	1	50	100	10	6	4	260	1	40	0.00017	0.09	0.08	0.0000902	0.81
135	Emilia-Romagna	1.6	50	100	10	6	4	260	1	40	0.00025	0.20	0.18	0.0000953	0.93
136	Emilia-Romagna	0.7	50	50	20	4	4	0	1	40	0.00250	0.03	0.02	0.0002349	0.94
137	Emilia-Romagna	1	50	50	20	4	4	0	1	40	0.00813	0.08	0.06	0.0005841	0.96
138	Emilia-Romagna	1.6	50	50	20	4	4	0	1	40	0.01555	0.15	0.12	0.0010442	1.00
139	Emilia-Romagna	0.7	50	50	20	4	4	32.5	1	40	0.00070	0.02	0.02	0.0001234	0.94
140	Emilia-Romagna	1	50	50	20	4	4	32.5	1	40	0.00122	0.11	0.09	0.0001556	0.96
141	Emilia-Romagna	1.6	50	50	20	4	4	32.5	1	40	0.00156	0.14	0.12	0.0001764	1.00
142	Emilia-Romagna	0.7	50	50	20	4	4	260	1	40	0.00009	0.02	0.02	0.0000856	0.94
143	Emilia-Romagna	1	50	50	20	4	4	260	1	40	0.00010	0.11	0.09	0.0000860	0.96
144	Emilia-Romagna	1.6	50	50	20	4	4	260	1	40	0.00012	0.13	0.10	0.0000877	1.00
145	Emilia-Romagna	0.7	50	50	30	4	4	0	1	40	0.00151	0.02	0.01	0.0001736	0.94
146	Emilia-Romagna	1	50	50	30	4	4	0	1	40	0.00525	0.11	0.09	0.0004058	0.96
147	Emilia-Romagna	1.6	50	50	30	4	4	0	1	40	0.01013	0.20	0.15	0.0007078	1.00
148	Emilia-Romagna	0.7	50	50	30	4	4	32.5	1	40	0.00050	0.01	0.01	0.0001109	0.95
149	Emilia-Romagna	1	50	50	30	4	4	32.5	1	40	0.00105	0.10	0.09	0.0001452	0.97
150	Emilia-Romagna	1.6	50	50	30	4	4	32.5	1	40	0.00152	0.19	0.17	0.0001742	1.01
151	Emilia-Romagna	0.7	50	50	30	4	4	260	1	40	0.00006	0.01	0.01	0.0000840	0.94
152	Emilia-Romagna	1	50	50	30	4	4	260	1	40	0.00011	0.10	0.09	0.0000865	0.96
153	Emilia-Romagna	1.6	50	50	30	4	4	260	1	40	0.00012	0.16	0.13	0.0000875	1.00
154	Emilia-Romagna	0.7	50	50	10	12	4	0	1	40	0.00522	0.04	0.03	0.0004034	1.07
155	Emilia-Romagna	1	50	50	10	12	4	0	1	40	0.01087	0.09	0.07	0.0007350	1.15
156	Emilia-Romagna	1.6	50	50	10	12	4	0	1	40	0.01118	0.11	0.08	0.0007732	1.17
157	Emilia-Romagna	0.7	50	50	10	12	4	32.5	1	40	0.00058	0.04	0.03	0.0001189	1.06
158	Emilia-Romagna	1	50	50	10	12	4	32.5	1	40	0.00142	0.09	0.07	0.0001683	1.16
159	Emilia-Romagna	1.6	50	50	10	12	4	32.5	1	40	0.00209	0.11	0.09	0.0002097	1.17
160	Emilia-Romagna	0.7	50	50	10	12	4	260	1	40	0.00008	0.04	0.03	0.0000847	1.07
161	Emilia-Romagna	1	50	50	10	12	4	260	1	40	0.00014	0.09	0.07	0.0000884	1.16
162	Emilia-Romagna	1.6	50	50	10	12	4	260	1	40	0.00017	0.10	0.08	0.0000904	1.17
163	Imperial Valley	0.7	50	50	10	6	4	0	1	40	0.00085	0.01	0.01	0.0001327	0.91
164	Northridge (Ia=4.5)	0.7	50	50	10	6	4	0	1	40	0.02014	0.21	0.21	0.0013286	0.92
165	Imperial Valley	1	50	50	10	6	4	0	1	40	0.00262	0.04	0.04	0.0002427	0.94
166	Northridge (Ia=4.5)	0.7	50	50	10	6	4	32.5	1	40	0.00199	0.17	0.16	0.0002035	0.91
167	Imperial Valley	1.6	50	50	10	6	4	0	1	40	0.00516	0.08	0.08	0.0004002	0.99
168	Northridge (Ia=4.5)	0.7	50	50	10	6	4	260	1	40	0.00014	0.17	0.15	0.0000884	0.91
169	Imperial Valley	0.7	50	50	10	6	4	32.5	1	40	0.00039	0.01	0.01	0.0001045	0.91
170	Northridge (Ia=4.5)	1	50	50	10	6	4	0	1	40	0.03992	0.37	0.34	0.0025549	0.93
171	Imperial Valley	1	50	50	10	6	4	32.5	1	40	0.00056	0.03	0.02	0.0001150	0.91
172	Northridge (Ia=4.5)	1	50	50	10	6	4	32.5	1	40	0.00254	0.25	0.22	0.0002374	0.93
173	Imperial Valley	1.6	50	50	10	6	4	32.5	1	40	0.00091	0.06	0.05	0.0001366	0.98
174	Northridge (Ia=4.5)	1	50	50	10	6	4	260	1	40	0.00013	0.32	0.25	0.0000862	0.93
175	Imperial Valley	0.7	50	50	10	6	4	260	1	40	0.00003	0.01	0.01	0.0000816	0.91
176	Northridge (Ia=4.5)	1.6	50	50	10	6	4	0	1	40	0.05744	0.54	0.46	0.0028945	0.99
177	Imperial Valley	1	50	50	10	6	4	260	1	40	0.00005	0.02	0.02	0.0000824	0.91
178	Northridge (Ia=4.5)	1.6	50	50	10	6	4	32.5	1	40	0.00207	0.42	0.36	0.0001815	0.99
179	Imperial Valley	1.6	50	50	10	6	4	260	1	40	0.00006	0.07	0.06	0.0000830	0.98
180	Northridge (Ia=4.5)	1.6	50	50	10	6	4	260	1	40	0.00013	0.51	0.47	0.0000863	0.99
181	Imperial Valley	0.7	50	50	10	6	4	0	1	40	0.01387	0.14	0.13	0.0007599	0.97
182	Imperial Valley	0.7	50	50	10	6	4	32.5	1	40	0.00141	0.10	0.09	0.0001491	1.01
183	Imperial Valley	0.7	50	50	10	6	4	260	1	40	0.00017	0.08	0.08	0.0000883	1.02
184	Imperial Valley	1	50	50	10	6	4	0	1	40	0.02387	0.24	0.22	0.0012499	0.98
185	Imperial Valley	1	50	50	10	6	4	32.5	1	40	0.00191	0.22	0.20	0.0001738	1.01
186	Imperial Valley	1	50	50	10	6	4	260	1	40	0.00011	0.21	0.20	0.0000855	1.04
187	Imperial Valley	1.6	50	50	10	6	4	0	1	40	0.044				

Appendix B

196	Northridge (Ia=2.8)	1.6	50	50	10	6	4	0	1	40	0.03164	0.30	0.24	0.0007445	1.02
197	Northridge (Ia=2.8)	1.6	50	50	10	6	4	32.5	1	40	0.00191	0.30	0.28	0.0001202	1.04
198	Northridge (Ia=2.8)	1.6	50	50	10	6	4	260	1	40	0.00006	0.26	0.25	0.0000813	1.06
199	Emilia-Romagna	0.7	50	100	10	4	6	0	1	40	0.00220	0.03	0.03	0.0001262	0.93
200	Emilia-Romagna	0.7	50	35	10	4	6	0	1	40	0.01518	0.16	0.15	0.0003989	0.82
201	Emilia-Romagna	0.7	50	100	10	4	6	32.5	1	40	0.00489	0.06	0.05	0.0001827	0.93
202	Emilia-Romagna	0.7	50	35	10	4	6	32.5	1	40	0.00746	0.09	0.09	0.0002366	0.82
203	Emilia-Romagna	0.7	50	100	10	4	6	260	1	40	0.00132	0.03	0.02	0.0001077	0.93
204	Emilia-Romagna	0.7	50	35	10	4	6	260	1	40	0.00176	0.05	0.04	0.0001170	0.82
205	Emilia-Romagna	1	50	100	10	4	6	0	1	40	0.00774	0.08	0.07	0.0002425	0.96
206	Emilia-Romagna	1	50	100	10	4	6	32.5	1	40	0.00489	0.06	0.05	0.0001827	0.96
207	Emilia-Romagna	1	50	100	10	4	6	260	1	40	0.00372	0.06	0.06	0.0001581	0.96
208	Emilia-Romagna	1	50	35	10	4	6	260	1	40	0.01518	0.16	0.15	0.0003989	0.85
209	Emilia-Romagna	1.6	50	100	10	4	6	0	1	40	0.00695	0.11	0.09	0.0002260	0.99
210	Emilia-Romagna	1.6	50	100	10	4	6	32.5	1	40	0.00448	0.05	0.05	0.0001741	0.99
211	Emilia-Romagna	1.6	50	100	10	4	6	260	1	40	0.00774	0.08	0.07	0.0002425	0.99
212	Emilia-Romagna	1.6	50	35	10	4	6	260	1	40	0.01428	0.15	0.14	0.0002943	0.87
213	Emilia-Romagna	0.7	50	50	10	6	4	16.25	1	40	0.00132	0.03	0.03	0.0000997	1.02
214	Emilia-Romagna	1	50	50	10	6	4	16.25	1	40	0.00264	0.08	0.07	0.0001196	0.97
215	Emilia-Romagna	1.6	50	50	10	6	4	16.25	1	40	0.00413	0.14	0.11	0.0001420	1.02
216	Emilia-Romagna	0.7	50	50	10	6	4	65	1	40	0.00052	0.03	0.03	0.0000879	1.01
217	Emilia-Romagna	1	50	50	10	6	4	65	1	40	0.00082	0.07	0.06	0.0000923	1.00
218	Emilia-Romagna	1.6	50	50	10	6	4	65	1	40	0.00098	0.15	0.12	0.0000946	1.03
219	Emilia-Romagna	0.7	50	50	10	6	4	130	1	40	0.00028	0.00	0.00	0.0004992	0.99
220	Emilia-Romagna	1	50	50	10	6	4	130	1	40	0.00729	0.02	0.02	0.0011733	0.97
221	Emilia-Romagna	1.6	50	50	10	6	4	130	1	40	0.00101	0.02	0.02	0.0047040	1.06
222	Emilia-Romagna	0.7	50	200	10	6	4	0	1	50	0.00080	0.01	0.01	0.0001080	0.94
223	Emilia-Romagna	1	50	200	10	6	4	0	1	50	0.00200	0.03	0.03	0.0001300	1.04
224	Emilia-Romagna	1.6	50	200	10	6	4	0	1	50	0.00200	0.03	0.03	0.0001300	1.09
225	Emilia-Romagna	1	50	200	10	6	4	130	1	50	0.00250	0.03	0.02	0.0001925	0.94
226	Emilia-Romagna	1.6	50	200	10	6	4	130	1	50	0.00450	0.05	0.04	0.0002825	1.04
227	Emilia-Romagna	0.7	50	200	10	6	4	65	1	50	0.00100	0.01	0.01	0.0001250	1.09
228	Emilia-Romagna	1	50	200	10	6	4	65	1	50	0.00260	0.03	0.03	0.0001970	1.01
229	Emilia-Romagna	1.6	50	200	10	6	4	65	1	50	0.00490	0.05	0.05	0.0003005	1.04
230	Emilia-Romagna	0.7	50	100	10	6	4	16.25	1	50	0.00100	0.01	0.01	0.0001250	0.94
231	Emilia-Romagna	1	50	100	10	6	4	16.25	1	50	0.00220	0.03	0.02	0.0001790	0.98
232	Emilia-Romagna	1.6	50	100	10	6	4	16.25	1	50	0.00380	0.05	0.04	0.0002510	1.00
233	Emilia-Romagna	0.7	50	100	10	6	4	65	1	50	0.00100	0.01	0.01	0.0001250	0.94
234	Emilia-Romagna	1	50	100	10	6	4	65	1	50	0.00240	0.03	0.02	0.0001160	0.98
235	Emilia-Romagna	1.6	50	100	10	6	4	65	1	50	0.00490	0.05	0.05	0.0001535	1.00
236	Emilia-Romagna	0.7	50	100	10	6	4	130	1	50	0.00100	0.01	0.01	0.0000950	0.94
237	Emilia-Romagna	1	50	100	10	6	4	130	1	50	0.00250	0.03	0.03	0.0001175	0.98
238	Emilia-Romagna	1.6	50	100	10	6	4	130	1	50	0.00510	0.06	0.05	0.0002925	1.00
239	Emilia-Romagna	0.7	50	50	10	6	4	65	1	50	0.00100	0.01	0.01	0.0001250	0.94
240	Emilia-Romagna	0.7	50	50	10	6	2	65	1	40	0.00048	0.05	0.04	0.0000317	0.92
241	Emilia-Romagna	1	50	50	10	6	2	65	1	40	0.00064	0.08	0.06	0.0000198	1.01
242	Emilia-Romagna	1.6	50	50	10	6	2	65	1	40	0.00065	0.10	0.08	0.0000162	1.02
243	Emilia-Romagna	0.7	50	50	10	6	6	65	1	40	0.00031	0.06	0.05	0.0000285	0.95
244	Emilia-Romagna	1	50	50	10	6	6	65	1	40	0.00039	0.09	0.07	0.0000296	0.98
245	Emilia-Romagna	1.6	50	50	10	6	6	65	1	40	0.00042	0.11	0.09	0.0000330	1.01
246	Emilia-Romagna	0.7	50	100	10	6	4	65	1	40	0.00021	0.04	0.03	0.0000317	0.93
247	Emilia-Romagna	1	50	100	10	6	4	65	1	40	0.00024	0.05	0.04	0.0000338	0.96
248	Emilia-Romagna	1.6	50	100	10	6	4	65	1	40	0.00029	0.09	0.07	0.0000277	0.99
249	Emilia-Romagna	0.7	50	100	10	6	2	65	1	40	0.00054	0.06	0.05	0.0000285	0.91
250	Emilia-Romagna	1	50	100	10	6	2	65	1	40	0.00051	0.09	0.07	0.0000296	0.94
251	Emilia-Romagna	1.6	50	100	10	6	2	65	1	40	0.00060	0.11	0.09	0.0000182	0.96
252	Emilia-Romagna	0.7	50	100	10	6	6	65	1	40	0.00039	0.16	0.13	0.0000267	0.94
253	Emilia-Romagna	1	50	100	10	6	6	65	1	40	0.00043	0.19	0.15	0.0000288	0.97
254	Emilia-Romagna	1.6	50	100	10	6	6	65	1	40	0.00043	0.21	0.17	0.0000343	1.00
255	Emilia-Romagna	0.7	50	100	10	4	4	65	1	40	0.00042	0.05	0.04	0.0000296	0.92
256	Emilia-Romagna	1	50	100	10	4	4	65	1	40	0.00040	0.07	0.05	0.0000296	0.96
257	Emilia-Romagna	1.6	50	100	10	4	4	65	1	40	0.00042	0.09	0.07	0.0000330	0.99
258	Emilia-Romagna	0.7	50	100	10	4	2	65	1	40	0.00043	0.05	0.04	0.0000253	0.91
259	Emilia-Romagna	1	50	100	10	4	2	65	1	40	0.00049	0.08	0.06	0.0000268	0.95
260	Emilia-Romagna	1.6	50	100	10	4	2	65	1	40	0.00059	0.10	0.08	0.0000168	0.97
261	Emilia-Romagna	0.7	50	100	10	4	6	65	1	40	0.00025	0.06	0.05	0.0000359	0.93
262	Emilia-Romagna	1	50	100	10	4	6	65	1	40	0.00029	0.09	0.07	0.0000331	0.97
263	Emilia-Romagna	1.6	50	100	10	4	6	65	1	40	0.00033	0.11	0.09	0.0000376	1.00
264	Emilia-Romagna	0.7	50	75	10	6	4	65	1	40	0.00030	0.04	0.03	0.0000253	0.95
265	Emilia-Romagna	1	50	75	10	6	4	65	1	40	0.00034	0.05	0.04	0.0000268	0.98
266	Emilia-Romagna	1.6	50	75	10	6	4	65	1	40	0.00048	0.09	0.07	0.0000288	1.01
267	Emilia-Romagna	0.7	50	75	10	6	2	65	1	40	0.00063	0.06	0.05	0.0000187	0.92
268	Emilia-Romagna	1	50	75	10	6	2	65	1	40	0.00075	0.09	0.07	0.0000137	0.95
269	Emilia-Romagna	1.6	50	75	10	6	2	65	1	40	0.00038	0.11	0.09	0.0000273	0.98
270	Emilia-Romagna	0.7	50	75	10	6	6	65	1	40	0.00034	0.16	0.13	0.0000299	0.96
271	Emilia-Romagna	1	50	75	10	6	6	65	1	40	0.00034	0.19	0.15	0.0000222	0.99
272	Emilia-Romagna	1.6	50	75	10	6	6	65	1	40	0.00036	0.21	0.17	0.0000198	1.01
273	Emilia-Romagna	0.7	50	125	10	4	4	65	1	40	0.00038	0.05	0.04	0.0000221	0.90
274	Emilia-Romagna	0.7	50	125	10	4	4	0	1	40	0.00268	0.05	0.04	0.0001670	0.90
275	Emilia-Romagna	0.7	50	125	10	4	4	260	1	40	0.00003	0.05	0.04	0.0000002	0.90
276	Emilia-Romagna	1	50	125	10	4	4	65	1	40	0.00043	0.08	0.06	0.0000212	0.94
277	Emilia-Romagna	1	50	125	10	4	4	0	1	40	0.00292	0.08	0.06	0.0001478	0.94
278	Emilia-Romagna	1	50	125	10	4	4	260	1	40	0.00003	0.08	0.06	0.0000002	0.94
279	Emilia-Romagna	1.6	50	125	10	4	4	65	1	40	0.00034	0.10	0.08	0.0000226	0.97
280	Emilia-Romagna	1.6	50	125	10	4	4	0	1	40	0.00473	0.10	0.08	0.0001793	0.97
281	Emilia-Romagna	1.6	50	125	10	4	4	260	1	40	0.00005	0.10	0.08	0.0000002	0.97
282	Emilia-Romagna	0.7	50	125	10	4	2	65	1	40	0.00048	0.06	0.05	0.0000186	0.90
283	Emilia-Romagna	0.7	50	125	10	4	2	0	1	40	0.00321	0.06	0.05	0.0000990	0.90
284	Emilia-Romagna	0.7	50	125	10	4	2	260	1	40	0.00006	0.06	0.05	0.0000001	0.90
285	Emilia-Romagna	1	50	125	10	4	2								

Appendix B

294	Emilia-Romagna	1	50	125	10	4	6	65	1	40	0.00022	0.05	0.04	0.0000212	0.95
295	Emilia-Romagna	1	50	125	10	4	6	0	1	40	0.00272	0.05	0.04	0.0001478	0.95
296	Emilia-Romagna	1	50	125	10	4	6	260	1	40	0.00002	0.05	0.04	0.0000002	0.95
297	Emilia-Romagna	1.6	50	125	10	4	6	65	1	40	0.00021	0.09	0.07	0.0000226	0.98
298	Emilia-Romagna	1.6	50	125	10	4	6	0	1	40	0.00346	0.09	0.07	0.0001793	0.98
299	Emilia-Romagna	1.6	50	125	10	4	6	260	1	40	0.00003	0.09	0.07	0.0000002	0.98
300	Emilia-Romagna	0.7	50	125	10	6	4	65	1	40	0.00038	0.06	0.05	0.0000186	0.94
301	Emilia-Romagna	0.7	50	125	10	6	4	0	1	40	0.00280	0.06	0.05	0.0000990	0.94
302	Emilia-Romagna	0.7	50	125	10	6	4	260	1	40	0.00003	0.06	0.05	0.0000001	0.94
303	Emilia-Romagna	1	50	125	10	6	4	65	1	40	0.00043	0.09	0.07	0.0000191	0.97
304	Emilia-Romagna	1	50	125	10	6	4	0	1	40	0.00429	0.09	0.07	0.0001077	0.97
305	Emilia-Romagna	1	50	125	10	6	4	260	1	40	0.00004	0.09	0.07	0.0000001	0.97
306	Emilia-Romagna	1.6	50	125	10	6	4	65	1	40	0.00034	0.11	0.09	0.0000198	1.00
307	Emilia-Romagna	1.6	50	125	10	6	4	0	1	40	0.00592	0.11	0.09	0.0001201	1.00
308	Emilia-Romagna	1.6	50	125	10	6	4	260	1	40	0.00004	0.11	0.09	0.0000001	1.00
309	Emilia-Romagna	0.7	50	125	10	6	2	65	1	40	0.00064	0.16	0.13	0.0000122	0.91
310	Emilia-Romagna	0.7	50	125	10	6	2	0	1	40	0.00838	0.16	0.13	0.0001405	0.91
311	Emilia-Romagna	0.7	50	125	10	6	2	260	1	40	0.00007	0.16	0.13	0.0000001	0.91
312	Emilia-Romagna	1	50	125	10	6	2	65	1	40	0.00061	0.19	0.15	0.0000104	0.94
313	Emilia-Romagna	1	50	125	10	6	2	0	1	40	0.01127	0.19	0.15	0.0000881	0.94
314	Emilia-Romagna	1	50	125	10	6	2	260	1	40	0.00008	0.19	0.15	0.0000001	0.94
315	Emilia-Romagna	1.6	50	125	10	6	2	65	1	40	0.00071	0.21	0.17	0.0000113	0.98
316	Emilia-Romagna	1.6	50	125	10	6	2	0	1	40	0.01148	0.21	0.17	0.0001107	0.98
317	Emilia-Romagna	1.6	50	125	10	6	2	260	1	40	0.00008	0.21	0.17	0.0000001	0.98
318	Emilia-Romagna	0.7	50	125	10	6	6	65	1	40	0.00022	0.05	0.04	0.0000230	0.89
319	Emilia-Romagna	0.7	50	125	10	6	6	0	1	40	0.00272	0.05	0.04	0.0001879	0.89
320	Emilia-Romagna	0.7	50	125	10	6	6	260	1	40	0.00002	0.05	0.04	0.0000002	0.89
321	Emilia-Romagna	1	50	125	10	6	6	65	1	40	0.00027	0.07	0.05	0.0000198	0.92
322	Emilia-Romagna	1	50	125	10	6	6	0	1	40	0.00285	0.07	0.05	0.0001201	0.92
323	Emilia-Romagna	1	50	125	10	6	6	260	1	40	0.00002	0.07	0.05	0.0000001	0.92
324	Emilia-Romagna	1.6	50	125	10	6	6	65	1	40	0.00021	0.09	0.07	0.0000198	0.96
325	Emilia-Romagna	1.6	50	125	10	6	6	0	1	40	0.00346	0.09	0.07	0.0001073	0.96
326	Emilia-Romagna	1.6	50	125	10	6	6	260	1	40	0.00003	0.09	0.07	0.0000001	0.96
327	Emilia-Romagna	0.7	50	50	10	4	2	0	1.5	40	0.00329	0.05	0.05	0.0013143	0.88
328	Emilia-Romagna	0.7	50	50	10	4	2	0	2	40	0.00336	0.05	0.05	0.0013432	0.90
329	Emilia-Romagna	0.7	50	50	10	4	2	0	3	40	0.00332	0.05	0.05	0.0013256	0.89
330	Emilia-Romagna	0.7	50	50	10	4	2	32.5	1.5	40	0.00055	0.02	0.02	0.0000132	0.90
331	Emilia-Romagna	0.7	50	50	10	4	2	32.5	2	40	0.00056	0.02	0.02	0.0000135	0.92
332	Emilia-Romagna	0.7	50	50	10	4	2	32.5	3	40	0.00056	0.02	0.02	0.0000133	0.91
333	Emilia-Romagna	0.7	50	50	10	4	2	260	1.5	40	0.00006	0.02	0.02	0.0000080	0.94
334	Emilia-Romagna	0.7	50	50	10	4	2	260	2	40	0.00010	0.03	0.03	0.0000039	0.91
335	Emilia-Romagna	0.7	50	50	10	4	2	260	3	40	0.00012	0.03	0.03	0.0000103	0.97
336	Emilia-Romagna	1	50	50	10	4	2	0	1.5	40	0.00947	0.18	0.16	0.0000137	0.83
337	Emilia-Romagna	1	50	50	10	4	2	0	2	40	0.00968	0.18	0.17	0.0000140	0.85
338	Emilia-Romagna	1	50	50	10	4	2	0	3	40	0.00956	0.18	0.17	0.0000138	0.84
339	Emilia-Romagna	1	50	50	10	4	2	32.5	1.5	40	0.00099	0.07	0.06	0.0000491	0.94
340	Emilia-Romagna	1	50	50	10	4	2	32.5	2	40	0.00101	0.07	0.07	0.0000502	0.96
341	Emilia-Romagna	1	50	50	10	4	2	32.5	3	40	0.00100	0.07	0.07	0.0000495	0.95
342	Emilia-Romagna	1	50	50	10	4	2	260	1.5	40	0.00002	0.08	0.06	0.0000001	0.92
343	Emilia-Romagna	1	50	50	10	4	2	260	2	40	0.00002	0.08	0.06	0.0000001	0.94
344	Emilia-Romagna	1	50	50	10	4	2	260	3	40	0.00002	0.08	0.06	0.0000001	0.93
345	Emilia-Romagna	1.6	50	50	10	4	2	0	1.5	40	0.02456	0.30	0.26	0.0005459	0.88
346	Emilia-Romagna	1.6	50	50	10	4	2	0	2	40	0.02510	0.31	0.26	0.0005578	0.90
347	Emilia-Romagna	1.6	50	50	10	4	2	0	3	40	0.02477	0.31	0.26	0.0005506	0.89
348	Emilia-Romagna	1.6	50	50	10	4	2	32.5	1.5	40	0.00135	0.23	0.18	0.0000859	0.96
349	Emilia-Romagna	1.6	50	50	10	4	2	32.5	2	40	0.00138	0.23	0.18	0.0000878	0.98
350	Emilia-Romagna	1.6	50	50	10	4	2	32.5	3	40	0.00136	0.23	0.18	0.0000866	0.97
351	Emilia-Romagna	1.6	50	50	10	4	2	260	1.5	40	0.00004	0.18	0.18	0.0000001	0.95
352	Emilia-Romagna	1.6	50	50	10	4	2	260	2	40	0.00004	0.19	0.18	0.0000001	0.97
353	Emilia-Romagna	1.6	50	50	10	4	2	260	3	40	0.00004	0.19	0.18	0.0000001	0.95

APPENDIX C

Statistical method for soil boundaries discontinuities

```
##### carica la working directory e carica l'elenco delle prove
library(readxl)
library(RGeostats)
setwd("G:\\.shortcut-targets-by-
id\\16g5CoxmJUat13YHrdx0KrV9SigcPpKZK\\09-CNR-UNICAS\\Anna\\03-
Modello_Geotecnico\\Input")
#test_list_data <- read_excel("file.xlsx")
test_list_data <- read_excel("CPT_San_Carlo.xlsx")
dimension_test_list = dim(test_list_data)

# ----- ciclo su tutte le prove CPT-----
setwd("G:\\.shortcut-targets-by-
id\\16g5CoxmJUat13YHrdx0KrV9SigcPpKZK\\09-CNR-
UNICAS\\DB_PERL\\CPT_digitalizzate")
for (ii in (1:dimension_test_list[1])){
  file_exist = 0

  #numero cpt da cercare
  id = as.character(test_list_data[ii, 1])
  #creo il filename
  #####inserire doppio slash finale \\
  file_name_base = paste(id, sep="")
  file_name_to_find = paste("G:\\.shortcut-targets-by-
id\\16g5CoxmJUat13YHrdx0KrV9SigcPpKZK\\09-CNR-
UNICAS\\DB_PERL\\CPT_digitalizzate\\",file_name_base, ".txt", sep="")
  lastrow=0

  #File txt
  if(file.exists( file_name_to_find)){
    file_exist = 1
    whole_test <- read.table(file=file_name_to_find, header=FALSE,
fill = TRUE, skip = 1)
    dim_whole_test = dim(whole_test)
```

```

for (jj in (1:dim_whole_test[1])){
  if (whole_test[jj, 1] == "0:"){lastrow=jj}
}

if (lastrow!=0) {
  lastrow = lastrow -2
  test <- whole_test[(1:lastrow), (1:3)]}
else {test <- whole_test[, (1:3)]}
}

#-----variabili: Falda, Tipo di Prova-----#

setwd("G:\\.shortcut-targets-by-
id\\16g5CoxmJUat13YHrdx0KrV9SigcPpKZK\\09-CNR-UNICAS\\Anna\\03-
Modello_Geotecnico\\Output")

d<- as.numeric(test_list_data[ii,6])      #prof falda

PROVA<- test_list_data[ii,4]

if (PROVA == "SCPTUA"){
  z<- as.numeric(test[, 1])
  n<-length(z)
  PROFMAX<- z[n]
  if (z [n]<= 100) {n1 = n}
  for (i in (1:n)){
    if (z [i]<=100) {n1 = i}
    else {n1 = n1}}

  qc<-as.numeric(test[, 2])
  Ic<-as.numeric(test[, 3])

  z1<-1
  for ( i in (1:n1)){ z1 [i] = z[i]
  Ic[i] = Ic[i]}
  for (i in (1:n1)){
    if (qc[i]<=0){qc[i]=0.001}
    else {qc [i] = qc[i]}
  }

  #### gamma####
  Pa<- (0.1013)

```



```

gammaw<- 9.81
gama_m <- 19.2  ##gamma medio##

z2<-1
for ( i in (1:n1)){ z2 [i] = z[i]}

##### valutazione dello stato tensionale:sv,u,su#####
sv<-1
u<-1
su<-1

for( i in (1:n1)){sv[i]=(gama_m*z[i])}

for( i in (1:n1)){
  if (z[i]<=d)    {u[i]=0}
  else          {u[i]=9.81*(z[i]-d)}
}
su=sv-u

}

else{
  z<- as.numeric(test[, 1])
  n<-length(z)
  PROFMAX<- z[n]
  if (z [n]<= 100) {n1 = n}

  for (i in (1:n)){
    if (z [i]<=100) {n1 = i}
    else {n1 = n1}
  }

  qc<-as.numeric(test[, 2])
  fs<-as.numeric(test[, 3])
  #u<- as.numeric(test[, 4])

  d2<- 20.00  #profondit?? massima liquefazione
  dz<- z[2]-z[1] #distanza tra due misure successive in [m]

  z1<-1
  for ( i in (1:n1)){ z1 [i] = z[i]}
  for (i in (1:n1)){

```

```

    if (fs[i]<=0){fs[i]=0.001}
    else {fs [i] = fs[i]}
  }
for (i in (1:n1)){
  if (qc[i]<=0){qc[i]=0.001}
  else {qc [i] = qc[i]}
}

#### gamma####
Rf<- c(fs/qc)*100
Rf1<- abs(Rf)
Pa<- (0.1)
gammaw<- 9.81
gama
c((0.27*(log(x=Rf1,base=10))+0.36*(log(x=qc/0.0981,base=10))+1.236))
*gammaw

z2<-1
for ( i in (1:n1)){ z2 [i] = z[i]}

##### valutazione dello stato tensionale:sv,u,su#####
sv<-1
u<-1
su<-1

for( i in (1:n1)){
  if (i==1)      {sv[i]=(gama[i]*z[i])}
  else          {sv[i]=sv[i-1]+(gama[i]*(z[i]-z[i-1]))}
}

for( i in (1:n1)){
  if (z[i]<=d)    {u[i]=0}
  else          {u[i]=9.81*(z[i]-d)}
}

su=sv-u

DATA<-cbind(z, qc, fs, Rf, Rf1, gama, sv, u, su)
#write.table(DATA, (paste("dati_", id, ".txt")))

cn<-1
Qc<-1

```

```

cnb<-1
FF<-1
Ic<- 1
Ico<-1

##### Friction Ratio #####
FF<-1

for ( i in (1:n1)){
  if (qc[i]==0.001) {FF[i]=1}
  else {FF[i] = fs [i] *100/(qc[i] - 0.001*sv[i])}}
FF<-cbind(FF)
##plot(FF)
##### valutazione di Ic e qclnc #####

cn<-1
qcln<-1
cnb<-1
Ic<- 1
qclno<-1
Ico<-1
cnbo<-1

for (j in (1:n1)) {
  for( i in (1:20)){
    if (i==1){cn[i]=1}
    else {cn[i]=cnb[i-1]}
    qclno[i]=((qc[j]*1000-sv[j])/100)*((98.1/su[j])^cn[i])
    Ico [i]= sqrt((3.47-
log10(abs(qclno[i])))^2+(1.22+log10(abs(FF[j])))^2)
    if (Ico [i] <= 1.64)      {cnb [i] = 0.5}
    else if (Ico [i] < 3.3)  {cnb [i]=(Ico[i]-1.64)*0.3+0.5}
    else if (Ico [i] > 3.3)  { cnb [i] = 1} }
    qcln [j] = qclno [20]
    Ic [j] = Ic [20]
    cnbo[j]=cnb[20]
  }
IIC<-cbind(z1,Ic,PROVA)
####CORREZIONE sull'Ic CPTm_ Madaai et al. 2016 #####

for ( i in (1:n1)) {
  if ( PROVA == "CPT") { Ic [i] = 0.9464* Ic [i]}
  else { Ic [i] = Ic [i]}
}

```

```

}

IIC2<-cbind(z1,Ic,PROVA)
}

IIC3<-cbind(z1,Ic,PROVA)
ICa<-cbind(IIC,IIC2)
ICb<-cbind(ICa,IIC3)
#write.table(ICb,(paste("IC_",id,".txt")))

###correzione per il contenuto di fine #####
cfc<-0
Fc<-1

for (i in (1:n1)){
  Fc [i] = 80*(Ic[i]+cfc)-137
  if (Fc [i]<0) {Fc [i] =0}
  else {Fc[i] = Fc [i]}
}

c1n_cs=cbind(z2,Ic,Fc)

cn<-1
qc1n<-1
cnb<-1

for (j in (1:n1)) {
  for( i in (1:10)){
    if (i==1){cn[i]=1}
    else {cn[i]=cnb[i-1]}
    qc1n[j]=qc[j]*cn[i]/0.0981
    cnb[i]=(98.1/su[j])^(1.338-0.249*(qc1n[j])^0.264)
    if (cnb[i]<1.7) { cnb[i]=cnb[i]}
    else { cnb[i]=1.7}}
  cnb[j] = cnb [10]
  CNB<-cbind(cnb)}

Deltaqc1n<- (11.9+qc1n/14.6)*exp(1.63-9.7/(Fc+2)-
(15.7/(Fc+2))^2)

qc1ncs<- 1
Dr<-1

```

```

for (i in (1:n1)){
  qc1ncs[i] = qc1n[i]+Deltaqc1n[i]
}

c_cs=cbind(z2,qc1n,qc1ncs)

####CORREZIONE sulla qc1n,cs da CPTm (Madiari et al., 2016) ####

for ( i in (1:n1)) {
  if ( PROVA == "CPT") { qc1ncs [i] = 49.6590 + 0.0260* (qc1ncs
[i]^1.5611)}
  else { qc1ncs [i] = qc1ncs [i]}
}

for (i in (1:n1)){
  if (qc1ncs [i]> 254)      {qc1ncs [i]=254}
  else                    {qc1ncs [i]=qc1ncs [i]}
}

for (i in (1:n1)){
  if (qc1ncs [i]<= 200)    {Dr [i]=-85+76*log10(qc1ncs[i])}
  else                    {Dr [i]= 100}
}

for (i in (1:n1)){
  if (Dr [i]< 0)          {Dr [i]= 0}
  else                   {Dr [i]= Dr [i]}
}

ccs=cbind(id,z2,Ic,qc1n,Fc,Deltaqc1n,qc1ncs,Dr)

CCS<-cbind(ccs,c_cs)

#write.table(CCS,(paste("qc1n_", id,".txt")))
#####SEZIONAMENTO#####
#definizione del passo della prova
x1<- z[1]
dz<- round((PROFMAX - x1)/n1,digits = 2)

```

```

##### Wd0#####
data.db<-db.create(Ic,
                  flag.grid=TRUE,
                  x0=x1,
                  dx=dz,
                  nx=n1,
                  autoname=FALSE)

plot(data.db)
vario<- vario.calc(data.db,
                  lag=dz,
                  nlag=round((0.4*PROFMAX)/dz))
NLAG=(0.4*PROFMAX)/dz

jpeg(paste("variogramma_", id, ".jpeg"), quality = 75)

model <- model.auto(vario,
                   struct=melem.name(c(3)),
                   draw=TRUE,
                   wmode=1,
                   title="Variogram model",
                   ylab= "Variogram ",
                   xlab="distance [m]")

dev.off()
model

if(model$basics[[1]]$vartype==melem.name(3)){SILL=model$basics[[1]]$
sill;RANGE=model$basics[[1]]$range}
Wdo<-RANGE
#VARIO_model<-cbind(id,RANGE,SILL)
#write.table(VARIO_model, file =
"modell.txt", col.names=FALSE, append=TRUE)
Variogram<-cbind(vario$vardirs[[1]]$hh, vario$vardirs[[1]]$gg)
#write.table(Variogram, (paste("vario_", id, ".txt")))

##### TEST STATISTICO #####
omega=round((Wdo/4)/dz)
if(omega<5){omega=5}else{omega=omega}

t=1
ro=1
nsup=1

```

```

ninf=1
msup=1
minf=1
varsup=1
varinf=1
Ic_inf=1
Ic_sup=1
Ic_tot=1
mtot=1
vartot=1
gww=1
gw=1
gbb=1
p=1
p2=1

for(i in (1:n1)){

  nsup [i] = min(i:omega)
  ninf [i] =min(omega:(n1-i))
  Ic_sup <-cbind( Ic[(i-nsup[i]):(i)])
  lmsup=length(Ic_sup)
  Ic_inf<-cbind( Ic[(i):(i+ninf[i])])
  lminf=length(Ic_inf)
  Ic_tot<- cbind( Ic[(i-nsup[i]):(i+ninf[i])])
  lm<-length(Ic_tot)
  mtot[i] = mean(Ic_tot)
  msup [i] = mean(Ic_sup)
  varsup [i]=var(Ic_sup)
  minf [i] = mean(Ic_inf)
  varinf [i]=var(Ic_inf)
  p[i]= (Ic[i]-mtot[i])^2
  p2[i]=sum(p)
  gww[i]=((nsup[i]/(nsup[i]+ninf[i]-
1))*varsup[i])+((ninf[i]/(nsup[i]+ninf[i]-1))*varinf[i])
  gw[i]=sqrt(gww[i])
  gbb[i]=var(Ic_tot)
  if (i <=3) { t[i]=0
  ro[i]=0.5}
  else { t[i]=((msup[i]-
minf[i])/gw[i])*(sqrt((nsup[i]*ninf[i])/(nsup[i]+ninf[i])))
  ro[i]=gbb[i]/(gbb[i]+gww[i]) }
}

```

```

t<- t [ 1:n1-1]
ro<- ro [1:n1-1]
z<- z [1:n1-1]
TEST<- cbind(z,t,ro)
#plot(z,t)
#plot(z,ro)
#write.table(TEST,(paste("test_", id, ".txt")))

sint=cbind(z,qc,fs,Rf,Rf1,gama,sv,u,su,Ic,qc1n,Fc,Deltaqc1n,qc1ncs,D
r,t,ro)
SINT<- cbind(sint)
write.table(SINT,(paste("sintesi_", id, ".txt")))

Media_T<- mean(t)
Media_r<- mean(ro)
std_t<- (var(t))^0.5
std_r<- (var(ro))^0.5

fac<-1
if (dz >= 0.2) {fac=1}
if (dz < 0.2) {fac=1.65}
else fac=1
Tc<-round(mean(t)+ fac*std_t,digits=1)
Tcsup<-round(mean(t)+fac*std_t,digits=1)
Tcinf<-round(mean(t)-fac*std_t,digits=1)
rc<-round(fac*std_r+mean(ro), digits=1)

#
# Critic<-
cbind(id,PROVA,Tcsup,Tcinf,rc,Media_T,std_t,Media_r,std_r)
#write.table(Critic, file =
"Critic.txt",col.names=FALSE,append=TRUE)

Sintesi_prove<-cbind(id,PROVA,
PROFMAX,Tcsup,Tcinf,rc,Media_T,std_t,Media_r,std_r,RANGE,SILL,NLAG)
write.table(Sintesi_prove, file =
"Sintesi_prove.txt",col.names=FALSE,append=TRUE)

TT<-1

for (i in(2:(n1-2))) {

```



```

        if(((t[i]-t[i-1])*(t[i]-t[i+1]))>0 & (t[i]>Tcsup | t[i]<Tcinf)
&& (ro[i]-ro[i-1])*(ro[i]-ro[i+1])>0 & (ro[i]>=rc)) {TT[i]=1}
        else {TT[i]=0}
    }

TTT<-cbind(z,TT)
#plot(TTT)

AA<- cbind(z[TT==1],t[TT==1], ro [TT==1])
A<- cbind(z[TT==1])
A
fi<- length(A)
B<-1

for (i in (2:fi)) {
    #if(i==1) {A[i] = A[i] }
    if (A[i] - A[i-1] >= 0.50) {B[i] = A[i]}
    else {B[i] = 0}
}
B
C<- B[B>0]
C
C1<- C[-1]
cc<-length(C1)
C2<-C1[-cc]

z2<-1

#-----Calcolo input
LDA-----#

##---calcolo del valore di RF medio negli strati----#####
a<-1
Rf1_<-1
Rf_m<-1

for (j in (1:cc)){
    if (j==1) {
        for (i in (1:(n1-3))) {
            if (z[i] < C1[j]) {Rf1_ [i] = Rf1[i]
                a[i] = 1}
            else { Rf1_ [i] = 0

```

```

        a[i] = 0}}
if (j>=2) { for (i in (1:(n1-3))) {
  if (z[i] >= C1[j-1] & z[i] < C1[j]) { Rf1_[i] = Rf1[i]
  a[i] = 1
  }
  else {Rf1_ [i] = 0
  a[i] = 0}}

Rf_m [j] = sum(Rf1_)/sum(a)

##---calcolo del valore di Ic medio negli strati----#####
a<-1
Ic_<-1
Ic_m<-1

for (j in (1:cc)){
  if (j==1) {
    for (i in (1:(n1-3))) {
      if (z[i] < C1[j]) {Ic_ [i] = Ic[i]
      a[i] = 1}
      else { Ic_ [i] = 0
      a[i] = 0}}
  if (j>=2) { for (i in (1:(n1-3))) {
    if (z[i] >= C1[j-1] & z[i] < C1[j]) { Ic_ [i] = Ic[i]
    a[i] = 1
    }
    else {Ic_ [i] = 0
    a[i] = 0}}
  }

  Ic_m [j] = sum(Ic_)/sum(a)

##---calcolo del valore di qc1n medio negli strati----#####
a<-1
qc1n_<-1

qc1n_m<-1

for (j in (1:cc)){
  if (j==1) {
    for (i in (1:(n1-3))) {
      if (z[i] < C1[j]) {qc1n_ [i] = qc1n[i]
      a[i] = 1}
      else { qc1n_ [i] = 0

```

```

        a[i] = 0}}
if (j>=2) { for (i in (1:(n1-3))) {
  if (z[i] >= C1[j-1] & z[i] < C1[j]) { qc1n_[i] = qc1n[i]
  a[i] = 1
  }
  else {qc1n_[i] = 0
  a[i] = 0}}}

qc1n_m [j] = sum(qc1n_)/sum(a)}

##---calcolo del valore di qc1ncs medio negli strati----#####
a<-1
qc1ncs_<-1

qc1ncs_m<-1

for (j in (1:cc)){
  if (j==1) {
    for (i in (1:(n1-3))) {
      if (z[i] < C1[j]) {qc1ncs_ [i] = qc1ncs[i]
      a[i] = 1}
      else { qc1ncs_ [i] = 0
      a[i] = 0}}}
  if (j>=2) { for (i in (1:(n1-3))) {
    if (z[i] >= C1[j-1] & z[i] < C1[j]) { qc1ncs_[i] = qc1ncs[i]
    a[i] = 1
    }
    else {qc1ncs_[i] = 0
    a[i] = 0}}}

  qc1ncs_m [j] = sum(qc1ncs_)/sum(a)}

####---calcolo del valore di Dr medio negli strati----####
a<-1
Dr_<-1

Dr_m<-1

for (j in (1:cc)){
  if (j==1) {
    for (i in (1:(n1-3))) {
      if (z[i] < C1[j]) {Dr_ [i] = Dr[i]

```

```

        a[i] = 1}
        else { Dr_ [i] = 0
        a[i] = 0}}}
if (j>=2) {    for (i in (1:(n1-3))) {
  if (z[i] >= C1[j-1] & z[i] < C1[j]) { Dr_[i] = Dr[i]
  a[i] = 1
  }
  else {Dr_ [i] = 0
  a[i] = 0}}}}

Dr_m [j] = sum(Dr_)/sum(a)}

##---calcolo del valore di RF dev_st negli strati----#####
a<-1
Rf1_<-1
Rf_std<-1

for (j in (1:cc)){
  if (j==1) {
    for (i in (1:(n1-3))) {
      if (z[i] < C1[j]) {Rf1_ [i] = Rf1[i]
      a[i] = 1}
      else { Rf1_ [i] = 0
      a[i] = 0}}}}
  if (j>=2) {    for (i in (1:(n1-3))) {
    if (z[i] >= C1[j-1] & z[i] < C1[j]) { Rf1_[i] = Rf1[i]
    a[i] = 1
    }
    else {Rf1_ [i] = 0
    a[i] = 0}}}}

    Rf_std          [j]=          sqrt((sum(a)/(sum(a)-
1))*((sum(Rf1_^2)/(sum(a)))-(sum(Rf1_)/sum(a))^2))}

#####---calcolo del valore di deviazione standard di Dr negli
strati----#####
a<-1
Dr_<-1

Dr_std<-1

for (j in (1:cc)){

```

```

if (j==1) {
  for (i in (1:(n1-3))) {
    if (z[i] < C1[j]) {Dr_ [i] = Dr[i]
    a[i] = 1}
    else { Dr_ [i] = 0
    a[i] = 0}}}
if (j>=2) {  for (i in (1:(n1-3))) {
  if (z[i] >= C1[j-1] & z[i] < C1[j]) { Dr_[i] = Dr[i]
  a[i] = 1
  }
  else {Dr_ [i] = 0
  a[i] = 0}}}

  Dr_std [j]= sqrt((sum(a)/(sum(a)-1))*(((sum(Dr_^2)/(sum(a))))-
(sum(Dr_)/sum(a))^2))}

####---calcolo del valore di deviazione standard di Ic negli
strati----####
a<-1
Ic_<-1

Ic_std<-1

for (j in (1:cc)){
  if (j==1) {
    for (i in (1:(n1-3))) {
      if (z[i] < C1[j]) {Ic_ [i] = Ic[i]
      a[i] = 1}
      else { Ic_ [i] = 0
      a[i] = 0}}}}
  if (j>=2) {  for (i in (1:(n1-3))) {
    if (z[i] >= C1[j-1] & z[i] < C1[j]) { Ic_[i] = Ic[i]
    a[i] = 1
    }
    else {Ic_ [i] = 0
    a[i] = 0}}}

    Ic_std [j]= sqrt((sum(a)/(sum(a)-1))*(((sum(Ic_^2)/(sum(a))))-
(sum(Ic_)/sum(a))^2))}

####---calcolo del valore di deviazione standard di qcln negli
strati----####
a<-1

```

```

qc1n_<-1

qc1n_std<-1

for (j in (1:cc)){
  if (j==1) {
    for (i in (1:(n1-3))) {
      if (z[i] < C1[j]) {qc1n_ [i] = qc1n[i]
      a[i] = 1}
      else { qc1n_ [i] = 0
      a[i] = 0}}
    if (j>=2) { for (i in (1:(n1-3))) {
      if (z[i] >= C1[j-1] & z[i] < C1[j]) { qc1n_ [i] = qc1n[i]
      a[i] = 1
      }
      else {qc1n_ [i] = 0
      a[i] = 0}}}

    qc1n_std [j]= sqrt((sum(a)/(sum(a)-
1))*((sum(qc1n_^2)/(sum(a)))-(sum(qc1n_)/sum(a))^2))
    #####---calcolo del valore di deviazione standard di qc1ncs negli
strati----#####
    a<-1
    qc1ncs_<-1

    qc1ncs_std<-1

    for (j in (1:cc)){
      if (j==1) {
        for (i in (1:(n1-3))) {
          if (z[i] < C1[j]) {qc1ncs_ [i] = qc1ncs[i]
          a[i] = 1}
          else { qc1ncs_ [i] = 0
          a[i] = 0}}
        if (j>=2) { for (i in (1:(n1-3))) {
          if (z[i] >= C1[j-1] & z[i] < C1[j]) { qc1ncs_ [i] = qc1ncs[i]
          a[i] = 1
          }
          else {qc1ncs_ [i] = 0
          a[i] = 0}}}

        qc1ncs_std [j]= sqrt((sum(a)/(sum(a)-
1))*((sum(qc1ncs_^2)/(sum(a)))-(sum(qc1ncs_)/sum(a))^2))

```

```

##-----PERMEABILITÀ-----##

k_perm<-1

for( i in (1:n1)){
  if (Ic[i]<=3.27) {k_perm[i]=10^(0.952-3.04*Ic[i])}
  else {k_perm[i]=10^(-4.52-1.37*Ic[i])}

####---calcolo del valore di k_perm medio negli strati---####
a<-1
k_perm_<-1

k_perm_m<-1

for (j in (1:cc)){
  if (j==1) {
    for (i in (1:(n1-3))) {
      if (z[i] < C1[j]) {k_perm_ [i] = k_perm_[i]
      a[i] = 1}
      else { k_perm_ [i] = 0
      a[i] = 0}}}
  if (j>=2) { for (i in (1:(n1-3))) {
    if (z[i] >= C1[j-1] & z[i] < C1[j]) { k_perm_[i] = k_perm_[i]
    a[i] = 1
    }
    else {k_perm_ [i] = 0
    a[i] = 0}}}

  k_perm_m [j] = sum(k_perm_)/sum(a)

##### -----Soil Behaviour Type----- #####
R<-cbind(Ic, Ic_,a)

SBT<-1
for (i in (1:cc)) {
  if ( Ic_m [i] <=1.31) {SBT [i]=7}
  if ( Ic_m [i] >1.31 && Ic_m [i]<=2.05) {SBT [i]=6}
  if ( Ic_m [i] >2.05 && Ic_m [i]<=2.6) {SBT [i]=5}
  if ( Ic_m [i] >2.6 && Ic_m [i]<=2.95) {SBT [i]=4}
  if ( Ic_m [i] >2.95 && Ic_m [i]<=3.6) {SBT [i]=3}
  if ( Ic_m [i] >3.6) { SBT [i]=2}}

```

```

PC<-z[1]
BASE<-c(PC,C1)
mm<-length(BASE)
SP<-1
Zm<-1

for (i in (1:(mm-1))) {
  SP [i] = BASE [i+1] - BASE [i]
  Zm [i] = (BASE [i+1] + BASE [i])/2
}

#####output_sez sezionamento #####
output_sez<-cbind(id,C1,SP,Rf_m,          Rf_std,Ic_m,Ic_std,SBT,
Dr_m,Dr_std,qcln_m,qcln_std,qclncs_m,qclncs_std,k_perm_m )
write.table(output_sez,
file="output_sez.txt",col.names=FALSE,append=TRUE)
}

```

LDA for soil stratigraphic recognition

```

function      [trainedClassifier,      validationAccuracy]      =
trainClassifier(trainingData)
%      [trainedClassifier,      validationAccuracy]      =
trainClassifier(trainingData)
% Returns a trained classifier and its accuracy. This code recreates
the
% classification model trained in Classification Learner app. Use the
% generated code to automate training the same model with new data,
or to
% learn how to programmatically train models.
%
% Input:
%   trainingData: A table containing the same predictor and response
%   columns as those imported into the app.
%
% Output:
%   trainedClassifier: A struct containing the trained classifier.
The
%   struct contains various fields with information about the
trained
%   classifier.

```



```

%
%     trainedClassifier.predictFcn: A function to make predictions
on new
%     data.
%
%     validationAccuracy: A double containing the accuracy in percent.
In
%     the app, the History list displays this overall accuracy score
for
%     each model.
%
% Use the code to train the model with new data. To retrain your
% classifier, call the function from the command line with your
original
% data or new data as the input argument trainingData.
%
% For example, to retrain a classifier trained with the original data
set
% T, enter:
% [trainedClassifier, validationAccuracy] = trainClassifier(T)
%
% To make predictions with the returned 'trainedClassifier' on new
data T2,
% use
% yfit = trainedClassifier.predictFcn(T2)
%
% T2 must be a table containing at least the same predictor columns
as used
% during training. For details, enter:
%     trainedClassifier.HowToPredict

% Auto-generated by MATLAB on 24-Sep-2021 11:26:58

% Extract predictors and response
% This code processes the data into the right shape for training the
% model.
inputTable = trainingData;
predictorNames = {'Rf_m', 'Rf_std', 'Ic_m', 'Ic_std', 'SBT'};
predictors = inputTable(:, predictorNames);
response = inputTable.SEDOk;
isCategoricalPredictor = [false, false, false, false, false];

```

```

% Train a classifier
% This code specifies all the classifier options and trains the
classifier.
classificationDiscriminant = fitcdiscr(...
    predictors, ...
    response, ...
    'DiscrimType', 'linear', ...
    'Gamma', 0, ...
    'FillCoeffs', 'off', ...
    'ClassNames', categorical({'A'; 'L'; 'M'; 'S'}));

% Create the result struct with predict function
predictorExtractionFcn = @(t) t(:, predictorNames);
discriminantPredictFcn = @(x) predict(classificationDiscriminant, x);
trainedClassifier.predictFcn = @ (x)
discriminantPredictFcn(predictorExtractionFcn(x));

% Add additional fields to the result struct
trainedClassifier.RequiredVariables = {'Ic_m', 'Ic_std', 'Rf_m',
'Ic_std', 'SBT'};
trainedClassifier.ClassificationDiscriminant =
classificationDiscriminant;
trainedClassifier.About = 'This struct is a trained model exported
from Classification Learner R2021a.';
trainedClassifier.HowToPredict = sprintf('To make predictions on a
new table, T, use: \n yfit = c.predictFcn(T) \nreplacing ''c'' with
the name of the variable that is this struct, e.g. ''trainedModel''.
\n \nThe table, T, must contain the variables returned by: \n
c.RequiredVariables \nVariable formats (e.g. matrix/vector, datatype)
must match the original training data. \nAdditional variables are
ignored. \n \nFor more information, see <a
href="matlab:helpview(fullfile(docroot, ''stats'', ''stats.map''),
''appclassification_exportmodeltoworkspace'')">How to predict using
an exported model</a>.'.');

% Extract predictors and response
% This code processes the data into the right shape for training the
% model.
inputTable = trainingData;
predictorNames = {'Rf_m', 'Rf_std', 'Ic_m', 'Ic_std', 'SBT'};
predictors = inputTable(:, predictorNames);
response = inputTable.SEDOk;
isCategoricalPredictor = [false, false, false, false, false];

```

```
% Perform cross-validation
partitionedModel =
crossval(trainedClassifier.ClassificationDiscriminant, 'KFold', 10);

% Compute validation predictions
[validationPredictions, validationScores] =
kfoldPredict(partitionedModel);

% Compute validation accuracy
validationAccuracy = 1 - kfoldLoss(partitionedModel, 'LossFun',
'ClassifError');

%predictor
yfit = trainClassifier(inputpred)
```

APPENDIX D

ANN for angular distortion prediction

```
function [Y,Xf,Af] = NeuralNetworkbeta(X,~,~)
%NeuralNetworkbeta neural network simulation function.
% [Y] = NeuralNetworkbeta(X,~,~) takes these arguments:
%   X = 1xTS cell, 1 inputs over TS timesteps
%   Each X{1,ts} = Qx4 matrix, input #1 at timestep ts.
%
% and returns:
%   Y = 1xTS cell of 1 outputs over TS timesteps.
%   Each Y{1,ts} = Qx1 matrix, output #1 at timestep ts.
%
% where Q is number of samples (or series) and TS is the number of
timesteps.

%#ok<*RPMT0>

% ===== NEURAL NETWORK CONSTANTS =====

% Input 1
x1_step1.xoffset = [0.01;50;2;0];
x1_step1.gain =
[5.12820512820513;0.02666666666666667;0.5;0.00769230769230769];
x1_step1.ymin = -1;

% Layer 1
b1 = [-3.236569792087924835;-
7.6646071732020759626;3.0628473977897163749;-1.4477862908154592869;-
0.24728141327203143063;0.90142249604312529865;1.3965931720031481422;
3.3561985498653004178;4.3364720994551921862;2.8038127674947603829];
IW1_1 = [0.48128624163301370054 -4.1724844940385699132 -
0.044049853120027494813 1.3395590858823909208;0.74051229684378694351
-0.41335975249911832696 -0.39564308250732116434 -
6.3587738655369872021;-0.46306948065117820024 4.2303733811839023815
0.046353260562595040295 -
0.81338867519757396263;0.54325850522270269227 0.02130488669459856127
```

```

-0.080628461604423509734          -1.8072183364580942655;-
1.782299066340171434  2.0010369368995641892  0.20141938181699209354  -
0.60529883408225149122;-0.22787035705926328433          -
0.13478827559526235236          0.25511049316342776505
1.5939273736407244542;0.10251015679477319675  -0.09239885080556853314
0.3175743828944024294  2.242741037044835295;-0.69535912418672518598
4.9643372891814436798          0.11746811175105206781          -
0.17619856727213711878;0.72469357458320904364  0.9843981094778796459
-0.089211933703036969123          5.4210886811344991543;-
0.59947805138882748199  1.6326663416406856921  0.1203296086762239564  -
2.0255945796846805962];

% Layer 2
b2 = 0.37075592159757975175;
LW2_1 = [-1.431046512369281043  1.1179631080509704333  -
2.4482737736336601664  0.55665734347542261684  0.015676037245593375802
0.65727693319048774434  -0.47760664459531992909  1.151995682052583625
0.14961519766183670188  -0.16961749846561732791];

% Output 1
y1_step1.ymin = -1;
y1_step1.gain = 34.5492590071746;
y1_step1.xoffset = 2.298e-05;

% ===== SIMULATION =====

% Format Input Arguments
isCellX = iscell(X);
if ~isCellX
    X = {X};
end

% Dimensions
TS = size(X,2); % timesteps
if ~isempty(X)
    Q = size(X{1},1); % samples/series
else
    Q = 0;
end

% Allocate Outputs
Y = cell(1,TS);

```

```

% Time loop
for ts=1:TS

    % Input 1
    X{1,ts} = X{1,ts}';
    Xp1 = mapminmax_apply(X{1,ts},x1_step1);

    % Layer 1
    a1 = tansig_apply(repmat(b1,1,Q) + IW1_1*Xp1);

    % Layer 2
    a2 = repmat(b2,1,Q) + LW2_1*a1;

    % Output 1
    Y{1,ts} = mapminmax_reverse(a2,y1_step1);
    Y{1,ts} = Y{1,ts}';
end

% Final Delay States
Xf = cell(1,0);
Af = cell(2,0);

% Format Output Arguments
if ~isCellX
    Y = cell2mat(Y);
end
end

% ===== MODULE FUNCTIONS =====

% Map Minimum and Maximum Input Processing Function
function y = mapminmax_apply(x,settings)
y = psxfun(@minus,x,settings.xoffset);
y = psxfun(@times,y,settings.gain);
y = psxfun(@plus,y,settings.ymin);
end

% Sigmoid Symmetric Transfer Function
function a = tansig_apply(n,~)
a = 2 ./ (1 + exp(-2*n)) - 1;
end

% Map Minimum and Maximum Output Reverse-Processing Function

```

```
function x = mapminmax_reverse(y, settings)
x = psxfun(@minus, y, settings.ymin);
x = psxfun(@rdivide, x, settings.gain);
x = psxfun(@plus, x, settings.xoffset);
end

%predictor
w_av= %median settlement computed with Bullock et al. (2018) [m]
Cu= %undrained shear strength of the crustal cap[kPa]
Hc= % Crust thickness[m]
EI= %EI [MN*m]

input= [w_av Cu Hc EI]
beta = NeuralNetworkbeta(input);
```

REFERENCES

- ACUUS 2018, Integrated Underground Solutions for Compacted Metropolitan Cities, Proc of the Conference, 5 - 7 November 2018, Hong Kong. 2018 www.acuus2018.hk
- M.E. Allen, Z. Sibahi, E. Sohm, "Evaluation of the Office of the United Nations Disaster Relief Coordinator, Joint Inspection Unit", 1980. JIU/REP/80/11.
- N.N. Ambraseyes, "Engineering seismology". Earthquake Engineering and Structural Dynamics, Vol. 17, pp. 1 -105, 1988.
- R. D., Andrus, and II, K. H., Stokoe, Liquefaction resistance of soils from shear wave velocity, J. Geotech. Geoenviron. Eng., ASCE, 126 (11), 1015–1025, 2000.
- ATC 40, Applied Technology Council Seismic Evaluation and Retrofit of Concrete Buildings, California, 1996.
- M. Armstrong, A.G. Galli, G.L. Loc'h, F. Geoffroy, R. Eschard. Plurigaussian Simulations in Geosciences, Berlin Heidelberg New York, pp. 149. 2003.
- A. Baris, R.L. Spacagna, L. Paoella, J. Koseki, G. Modoni, Liquefaction fragility of sewer pipes derived from the case study of Urayasu (Japan). Bull Earthquake Eng 19, 3963–3986, 2021. <https://doi.org/10.1007/s10518-020-00957-2>
- R. Basili, S. Barba. Migration and shortening rates in the northern Apennines, Italy: implications for seismic hazard. Terra Nova, 19(6), 462–468, 2007.
- Y.Y. Bayraktarli, J.W. Baker, M.H. Faber, Uncertainty treatment in earthquake modeling using Bayesian probabilistic networks. Georisk;5:44–58, 2011.
- D. Benedetti, and V. Petrini, , "Sulla Vulnerabilità Di Edifici in Muratura: Proposta Di Un Metodo Di Valutazione", L'industria delle Costruzioni, Vol. 149, No. 1, pp. 66-74, 1984.
- J. Bird, J. Bommer, H. Crowley, R. Pinho, "Modelling liquefaction-induced building damage in earthquake loss estimation". Soil Dynamics and Earthquake Engineering 26 (2006) 15–30, 2006.
- L. Bjerrum. Discussion session IV. Proc, European Conf. on Soil Mech. and Found. Engr., Wiesbaden, Germany, II, 135-137, 1963.
- M. Boccaletti, G. Corti, L. Martelli. Recent and active tectonics of the external zone of the Northern Apennines (Italy). International Journal of Earth Sciences, 100(6), 1331–

- 1348, 2011. <https://doi.org/10.1007/s00531-010-0545-y>
- J.J. Bommer, Deterministic vs. probabilistic seismic hazard assessment: An exaggerated and obstructive dichotomy. *J. Earthq. Eng.* 6, 43–73, 2002.
- J.J. Bommer, Uncertainty about the uncertainty in seismic hazard analysis. *Eng. Geol.* 70, 165–168, 2003.
- M. Bondesan. L'evoluzione idrografica e ambientale della pianura ferrarese negli ultimi 3000 anni. *Storia Di Ferrara*, 1, 228–263, 2001.
- B. Borzi, M. Faravelli, A. Di Meo, Application of the SP-BELA methodology to RC residential buildings in Italy to produce seismic risk maps for the national risk assessment. *Bull Earthq Eng.*, 2020a. <https://doi.org/10.1007/s10518-020-00953-6>
- B. Borzi, M. Onida, M. Faravelli, D. Polli, M. Pagano, D. Quaroni, A. Cantoni, E. Speranza, C. Moroni, IRMA platform for the calculation of damages and risks of Italian residential buildings. *Bull Earthq Eng.*, 2020b. <https://doi.org/10.1007/s10518-020-00924-x>
- R. W. Boulanger, High overburden stress effects in liquefaction analyses. *J. Geotechnical and Geoenvironmental Engineering*, ASCE, 129(12), 1071-1082, 2003b.
- R. W. Boulanger, and K. Ziotopoulou. Formulation of a sand plasticity plane-strain model for earthquake engineering applications. *Journal of Soil Dynamics and Earthquake Engineering*, Elsevier, 53, 254-267, 2013. 10.1016/j.soildyn.2013.07.006.
- R. W. Boulanger, I. Idriss. CPT and SPT Based Liquefaction Triggering Procedures; Report No. UCD/CGM-14/01; Center for Geotechnical Modeling, Department of Civil and Environmental Engineering, University of California: Davis, CA, USA. 2014.
- R. W. Boulanger, and K. Ziotopoulou. PM4Sand (Version 3): A Sand Plasticity Model for Earthquake Engineering Applications Report No. UCD/CGM-15/01, Center for Geotechnical Modeling, Department of Civil and Environmental Engineering, University of California, Davis, CA, March, 114 pp. 2015.
- R. W. Boulanger, and K. Ziotopoulou. PM4Sand (version 3.1): A sand plasticity model for earthquake engineering applications. Report No. UCD/CGM-17/01, Center for Geotechnical Modeling, Department of Civil and Environmental Engineering, University of California, Davis, CA, 114 pp. March, 2017.
- R. W. Boulanger, and K. Ziotopoulou. PM4Silt (Version 1): A Silt Plasticity Model for Earthquake Engineering Applications. Report No. UCD/CGM-18/01, Center for Geotechnical Modeling, Department of Civil and Environmental Engineering, University of California, Davis, CA, 109 pp. January, 2018.
- F. Braga, M. Dolce, D. Liberatore, “A Statistical Study on Damaged Buildings and an Ensuing Review of the MSK-76 Scale”, *Proceedings of the Seventh European*

- Conference on Earthquake Engineering, Athens, Greece, pp. 431-450, 1982.
- J. Bray, S. Dashti. Liquefaction-induced building movements. *B Earthq Eng* 2014; 12:1129–56, 2014.
- J.M Bray, J. Cubrinovski, J. Zupan, and M. Taylor, “Liquefaction effects on buildings in the central business district of Christchurch.” *Earthquake Spectra* 30 (1): 85–109, 2014. <https://doi.org/10.1193/022113EQS043M>.
- J.M Bray, J. Macedo. 6th Ishihara lecture: Simplified procedure for estimating liquefaction-induced building settlement. *Soil Dynamics Earthquake Eng* 102, 215–231, 2017.
- J.M Bray, R. Sancio. Assessment of the Liquefaction Susceptibility of Fine-Grained Soils, *Journal of Geotechnical and Geoenvironmental Engineering*, Vol. 132., 2006. 10.1061/(ASCE)1090-0241(2006)132:9(1165)
- BRGM: <https://www.brgm.eu/scientific-output/digital-data-services/infoterre-portal-access-to-brgm-geoscientific-data>
- British Geological Survey: <https://www.bgs.ac.uk/geological-data/information-hub/>
- Z. Bullock, S. Dashti, A. Liel, K. Porter, Z. Karimi, B. Bradley. Ground motion prediction equations for Arias intensity, cumulative absolute velocity, and peak incremental ground velocity for rock sites in different tectonic environments. *Bulletin of the Seismological Society of America* 107(5), 2293–2309, 2017.
- Z. Bullock, Z. Karimi, S. Dashti, K. Porter, A. Liel, K. Franke. A Physics-Informed Semi-Empirical Probabilistic Model for the Settlement of Shallow-Founded Structures on Liquefiable Ground. *Geotechnique*, 2018. [<https://doi.org/10.1680/jgeot.17.P.174>].
- H. Bungum, D. H. Lang, Haiti vil rammes igjen, *aftenposten*, 20 January 2010. <http://www.aftenposten.no/fakta/innsikt/article3473823.ece>, <http://www.norsar.no/pc-70-99-Why-Haiti,-and-what-now.aspx>.
- N. Buratti, B. Ferracuti, M. Savoia, G. Antonioni, V. Cozzani, A fuzzy-sets based approach for modelling uncertainties in quantitative risk assessment of industrial plants under seismic actions. *Chemical Engineering Transactions*;26:105–10, 2012.
- J. B. Burland, C.P. Wroth. Settlement of buildings and associated damage. *Proc, Conf. on Settlement of Structures*, Pentech Press, London, England, 611-654, 1974.
- J. B. Burland, B.B. Broms, V.F.B. de Mello. Behaviour of foundations and structures. *State-of-the-Art Report. Proc, 9th Int'l. Conf. on Soil Mech. and Found. Engr., II, Tokyo, Japan*, 495-546, 1977.
- G. Calvi, R. Pinho, G. Magenes, J. Bommer, L. Restrepo-Vélez, H. Crowley, Development of seismic vulnerability assessment methodologies over the past 30 years. *ISET Journal of Earthquake Technology*. 43, 2006.
- K. W. Campbell, Y. Bozorgnia. Predictive equations for the horizontal component of

- standardized cumulative absolute velocity as adapted for use in the shutdown of U.S. nuclear power plants, *Nucl. Eng. Des.* 241, 2558–2569, 2011.
- R. Caputo, A. Pellegrinelli, C. Bignami, A. Bondesan, A. Mantovani, S. Stramondo, P. Russo. High-precision levelling, DInSAR and geomorphological effects in the Emilia 2012 epicentral area. *Geomorphology*, 235, 106–117, 2015. <https://doi.org/10.1016/j.geomorph.2015.02.002>
- R. Caputo, M.E. Poli, L. Minarelli, D. Rapti, S. Sboras, M. Stefani, A. Zanferrari. Palaeoseismological evidence for the 1570 Ferrara earthquake, Italy. *Tectonics*, 35(6), 1423–1445, 2016. <https://doi.org/10.1002/2016TC004238>
- M. Castiglia, T. Fierro, F. Santucci de Magistris. Pipeline Performances under Earthquake-Induced Soil Liquefaction: State of the Art on Real Observations, Model Tests, and Numerical Simulations. *Shock and Vibration*, 2020. 10.1155/2020/8874200.
- F. Cazzola. E la terra emerse dall'acqua. Le Fasi Storiche Della Grande Bonificazione Ferrarese. Dallo Scolo Naturale Al Sollevamento Meccanico. Consorzio Di Bonifica I Circondario Polesine Di Ferrara, Ferrara. 1995.
- A. Chiaradonna, A. Flora, On the estimate of seismically-induced pore water pressure increments before liquefaction. *Geotech. Lett.*, 2019. <https://doi.org/10.1680/jgele.19.00032>.
- A. Chiaradonna, S. Lirer, A. Flora, “A liquefaction potential integral index based on pore pressure build-up”. *Engineering Geology*, 2020.
- K. O. Cetin, T.L. Youd, R.B. Seed, J. D. Bray, R. Sancio, W. Lettis, M. Tolga Yilmaz, H. Turan Durgunoglu, Liquefaction-induced ground deformations at Hotel Sapanca during Kocaeli (Izmit), Turkey earthquake, *Soil Dynamics and Earthquake Engineering*, Volume 22, Issues 9–12, Pages 1083-1092, ISSN 0267-7261, 2002. [https://doi.org/10.1016/S0267-7261\(02\)00134-3](https://doi.org/10.1016/S0267-7261(02)00134-3).
- K. O. Cetin, R. B. Seed, A. Der Kiureghian, K. Tokimatsu, L.F. Harder, R.E. Kayen, R.E.S. Moss, “Standard penetration test-based probabilistic and deterministic assessment of seismic soil liquefaction potential”. *J. Geotechnical and Geoenvironmental Eng.*, ASCE 130(12), 1314–340, 2004.
- JP. Chilès, & P. Delfiner, P. *Geostatistics: modeling spatial uncertainty*. 2nd edn. Wiley, Hoboken, p 726, 2012. ISBN 978-0-470-18315-1.
- J. Ching, K.K. Phoon, Y. Ho, M.C. Weng. Quasisite-specific Prediction for Deformation Modulus of Rock Mass. *Canadian Geotechnical Journal*, 2020. doi:10.1139/cgj-2020-0168.
- J. Ching, S. Wu, K.K. Phoon, Constructing QuasiSite-specific Multivariate Probability Distribution Using Hierarchical Bayesian Model. *Journal of Engineering Mechanics*,

- under review computing. R Foundation for Statistical Computing, Vienna, Austria, 2020.
- R. Chung, January 17, 1995 Hyogoken-Nanbu (Kobe) Earthquake: Performance of Structures, Lifelines, and Fire Protection Systems (NIST SP 901), Special Publication (NIST SP), National Institute of Standards and Technology, Gaithersburg, MD, 1996 [online]. <https://doi.org/10.6028/NIST.SP.901>
- K.J. Coppersmith, R.R. Youngs, Capturing uncertainty in probabilistic seismic hazard assessments with intraplate tectonic environments. Proceedings of 3rd U.S National Conference on Earthquake Engineering, Charleston, South Carolina, USA, p. 301–12, 1986.
- C. A. Cornell, Engineering seismic risk analysis, Bull Seismol Soc Am 58, 1583–1606, 1968.
- C. A. Cornell, Probabilistic analysis of damage to structures under seismic loads. In Dynamic Waves in Civil Engineering (eds. Howells, D. A., Haigh, I. P., and Taylor, C.), Proceedings of a Conference Organized by the Society for Earthquake and Civil Engineering Dynamics (John Wiley, New York), 1971.
- C.A. Cornell, H. Krawinkler, “Progress and Challenges in Seismic Performance Assessment”. PEER Center News, 3, 1-3, 2000.
- A. Corsanego, V. Petrini, “Seismic Vulnerability of Buildings – Work in Progress”, Proceedings of the Workshop II on Seismic Risk Vulnerability and Risk Assessment, Trieste, Italy, pp. 577-598, 1990.
- C.H. Cramer, M.D. Petersen, M.S. Reichle. A Monte Carlo approach in estimating uncertainty for a seismic hazard assessment of Los Angeles, Ventura, and Orange Counties, California. Bulletin of the Seismological Society of America;86:1681–91, 1996.
- CRED & UNISDR, Economic losses, poverty & disasters 1998-2017, 2018.
- M. Crisp, M. Jaksa, Y. Kuo, Optimal Testing Locations in Geotechnical Site Investigations through the Application of a Genetic Algorithm. Geosciences, 10(7), 265, 2020.
- H. Crowley, J.J. Bommer, R. Pinho, J. Bird, The impact of epistemic uncertainty on an earthquake loss model. Earthquake Engineering and Structural Dynamics;34:1653–85. doi:10.1002/eqe.498, 2005.
- CSAPEISLA, "State of the Art and Practice in the Assessment of Earthquake Induced Soil Liquefaction and Its Consequences", 2016.
- M. Cubrinovski, J. D. Bray, M. Taylor, S. Giorgini, B. A. Bradley, L. Wotherspoon, and J. Zupan. “Soil liquefaction effects in the central business district during the February 2011 Christchurch earthquake.” Seismol. Res. Lett. 82 (6): 893–904, 2011b.

- M. Cubrinovski, S. van Ballegooy. System response of liquefiable deposits. 3rd International conference on performance based design in earthquake geotechnical engineering, 2017.
- Y.F. Dafalias, M.T. Manzari. Simple plasticity sand model accounting for fabric change effects. *J. Eng. Mech.* 130(6), 622–634, 2004.
- K. R. Dahl. Evaluation of seismic behavior of intermediate and fine-grained soils. Doctoral thesis, University of California, Davis, 2011.
- J. Daniell, A. Vervaeck, The CATDAT damaging earthquakes database–2010– year in review. *CEDIM Earthquake Loss Estimation Series* 2011:2011–101.
- J.E. Daniell, B. Khazai, F. Wenzel, A. Vervaeck, "The Worldwide Economic Impact of Earthquakes". *Proceedings of the 15th World Conference of Earthquake Engineering*, Lisbon, Portugal, 2012.
- J. E. Daniell, The development of socio-economic fragility functions for use in worldwide rapid earthquake loss estimation procedures, Doctoral Thesis, Karlsruhe Institute of Technology, Karlsruhe, 2014.
- J. E. Daniell, F. Wenzel, The production and implementation of socioeconomic fragility functions for use in rapid worldwide earthquake loss estimation, Paper No. 490, in: 15th ECEE, Istanbul, 2014.
- S. Dashti, J.D. Bray. Numerical simulation of building response on liquefiable sand. *J Geotech Geoenviron Eng ASCE* 139(8):1235–1249, 2013.
- C. Del Gaudio, G. DE Martino, M. Di Ludovico, G. Manfredi, A. Prota, P. Ricci, G. Verderame, Empirical fragility curves for masonry buildings after the 2009 L’Aquila, Italy, earthquake. *Bulletin of Earthquake Engineering*, 2019. 17. 10.1007/s10518-019-00683-4.
- M. Dilley, R. S. Chen, U. Deichmann, A. Lerner-Lam, M. Arnold, J. Agwe, P. Buys, O. Kjekstad, B. Lyon, and G. Yetman, *Natural Disaster Hotspots. A Global Risk Analysis*, The World Bank, Washington, D.C., 2005.
- G. Di Pasquale, G. Orsini, R.W. Romeo, “New Developments in Seismic Risk Assessment in Italy”, *Bulletin of Earthquake Engineering*, Vol. 3, No. 1, pp. 101-128, 2005.
- M. Dolce, A. Masi, M. Marino, M. Vona, “Earthquake Damage Scenarios of the Building Stock of Potenza (Southern Italy) Including Site Effects”, *Bulletin of Earthquake Engineering*, Vol. 1, No. 1, pp. 115-140, 2003.
- M. Dolce, E. Speranza, F. Giordan, B. Borzi, F. Bocchi, C. Conte, A. Di Meo, M. Faravelli, V. Pascale, Observed damage database of past Italian earthquakes: the Da.D.O. WebGIS. *Bollettino di Geofisica Teorica ed Applicata* 60(2):141–164, 2019°.
- M. Dolce, B. Borzi, F. da Porto, M. Faravelli, S. Lagomarsino, G. Magenes, C. Moroni, A.

- Penna, A. Prota, E. Speranza, G. Zuccaro, GM. Verderame. Seismic risk maps for the Italian territory. In: XVIII Italian conference on earthquake engineering (ANIDIS). Ascoli Piceno (Italy), 15–19 September 2019. (in Italian)
- M. Dolce, A. Prota, ..., Seismic Risk Assessment of residential buildings in Italy: methodology overview and main results. *Bull Earthq Eng*, 2020.
- M. Donà, P. Carpanese, V. Follador, L. Sbrogiò, F. da Porto, Mechanics-based fragility curves for Italian residential URM buildings. *Bull Earthq Eng.*, 2020. <https://doi.org/10.1007/s10518-020-00928-7>
- F. Dottori, W. Szewczyk, J.C. Ciscar, F. Zhao, L. Alfieri, Y. Hirabayashi, A. Bianchi, I. Mongelli, K. Frieler, R.A. Betts, L. Feyen, Increased human and economic losses from river flooding with anthropogenic warming, *Nat. Clim. Change*, 8, 781–786, <https://doi.org/10.1038/s41558-018-0257-z>, 2018.
- J. M. Duncan, and A. L. Buchignani. An engineering manual for settlement studies, University of California at Bekeley, Bekeley, California, 1976.
- EM-DAT International Disaster Database: <https://www.emdat.be/>
- FEMA/NIBS. “HAZUS-Earthquake – Technical Manual”. Federal Emergency, 2003.
- J. Facciorusso, C. Madiari, and G. Vannucchi. The 2012 Emilia earthquake (Italy): geotechnical characterization and ground response analyses of the paleo-Reno river levees. *Soil Dynamics and Earthquake Engineering*, 86, 71-88. 2016.
- V. Fioravante, D. Giretti, G. Abate, S. Aversa, D. Boldini, P.P Capilleri, J. Facciorusso, Earthquake geotechnical engineering aspects of the 2012 Emilia-Romagna earthquake (Italy), 2013.
- R. A. Fisher. The correlation between relatives on the supposition of mendelian inheritance. *Trans. R. Soc. Edinb.* 53: 399–433. 1918.
- A. Flora, E. Bilotta, A. Chiaradonna, *et al.* A field trial to test the efficiency of induced partial saturation and horizontal drains to mitigate the susceptibility of soils to liquefaction. *Bull Earthquake Eng* 19, 3835–3864, 2021. <https://doi.org/10.1007/s10518-020-00914-z>
- S. Fotopoulou, S. Karafagka, K. Pitilakis, Vulnerability assessment of low-code reinforced concrete frame buildings subjected to liquefaction-induced differential displacements. *Soil Dynamics and Earthquake Engineering* 110, 173-184, 2018.
- Foumier d'Albe, Earthquake Prediction and Risk Management. European Space Agency/Council of Europe Seminar on earthquake prediction, Strasbourg, France, 5 to 7 March 1979. Available from UNESCO's Earth Sciences Division on request, 1979.
- X. Freulon, C. Fouquet. Conditioning a Gaussian model with inequalities. In *Geostat Troia*

- '92. (ed. Soares), pp. 201-212. Kluwer, Dordrecht, 1993.
- P. Galli. New empirical relationships between magnitude and distance for liquefaction. *Tectonophysics* 324, 169-187, 2000.
- P. Galli, F. Meloni. Liquefazione Storica. Un catalogo nazionale. *Quat. Ital. J. Quat. Sci.* 6. Pagg. 271–292., 1993.
- Geological Survey: <https://www.gsi.ie/en-ie/data-and-maps/Pages/Geotechnical.aspx>
- Geological Survey of Norway: <https://www.ngu.no/en/topic/maps-and-data>
- Geoportale dell'Emilia-Romagna: <https://geoportale.regione.emilia-romagna.it>
- GEUS: <https://eng.geus.dk/products-services-facilities/data-and-maps/national-well-database-jupiter>
- M. Ghielmi, M. Minervini, C. Nini, S. Rogledi, M. Rossi. Late Miocene–Middle Pleistocene sequences in the Po Plain–Northern Adriatic Sea (Italy): the stratigraphic record of modification phases affecting a complex foreland basin. *Marine and Petroleum Geology*, 42, 50–81, 2013.
- S. Giovinazzi, S. Lagomarsino, “Una Metodologia per L’analisi Di Vulnerabilità Sismica Del Costruito”, Proceedings of the X Congresso Nazionale on L’Ingegneria Sismica in Italia, Potenza-Matera, Italy, Paper No. 121, 2001.
- S. Giovinazzi, S. Lagomarsino, “A Macroseismic Method for the Vulnerability Assessment of Buildings”, Proceedings of the 13th World Conference on Earthquake Engineering, Vancouver, Canada, Paper No. 896, 2004.
- S. Glaister, R. Pinho, Development of a simplified deformation-based method for seismic vulnerability assessment. *J Earthquake Eng*;7:107–40, 2003.
- R. Golezorkhi, “Factors Influencing the Computational Determination of Earthquake-Induced Shear Stresses in Sandy Soils,” Ph.D. thesis, University of California at Berkeley, 395 pp, 1989.
- D. N. Grant. Assessment of Existing Structures Using Response History Analysis. In: Beer, M., Kougioumtzoglou, I., Patelli, E., Au, IK. (eds) *Encyclopedia of Earthquake Engineering*. Springer, Berlin, Heidelberg, 2014. https://doi.org/10.1007/978-3-642-36197-5_202-1
- R. Grant, J. T. Christian, E. H. Vanmarcke. Differential settlement of buildings. *Journal of Geotechnical Engineering Division, ASCE*, 100(9), pp. 973-991, 1974.
- G. Grünthal, “Cahiers du Centre Européen de Géodynamique et de Séismologie: Volume 15 – European Macroseismic Scale 1998”, European Center for Geodynamics and Seismology, Luxembourg, 1998.
- E. Guagenti, and V. Petrini, “The Case of Old Buildings: Towards a Damage-Intensity Relationship”, Proceedings of the Fourth Italian National Conference on Earthquake

- Engineering, Milan, Italy, pp. 145-153, 1989.
- Hazus -MH MR5. 2010.
- Y. Herzagy, P. Mayne, S. Rouhani. Geostatistical assessment of spatial variability in piezocone tests. *Uncertainty in geologic environment: from theory to practice (GSP 58)*, ASCE, New York, 254-268, 1996.
- ICMS, 2008: "Indirizzi e Criteri generali per la Microzonazione Sismica", approvato da Dipartimento della Protezione Civile e Conferenza delle Regioni e Province Autonome in data 13 novembre 2008. The English version is: SM Working Group, *Guidelines for Seismic Microzonation, Conference of Regions and Autonomous Provinces of Italy—Civil Protection Department, Rome, 2015.*
- ICMS-LIQ, 2017: "Microzonazione sismica. Linee guida per la gestione del territorio in aree interessate da liquefazioni (LQ)". Versione 1.0. Commissione tecnica per la microzonazione sismica. Roma, 2017. The English version is: Technical Commission on Seismic Microzonation, *Land Use Guidelines for Areas Affected by Liquefaction (LQ)*, version 1.0, Rome, 2018.
- I. M. Idriss, "An update to the Seed-Idriss simplified procedure for evaluating liquefaction potential", *Proceedings, TRB Workshop on New Approaches to Liquefaction, Publication No. FHWARD- 99-165, Federal Highway Administration, January, 1999.*
- I.M. Idriss, R.W. Boulanger, "Soil Liquefaction During Earthquake", *Earthquake Engineering Research Institute, 2008.*
- I.M. Idriss, R.W. Boulanger, "SPT-Based Liquefaction Triggering Procedures", *Center for Geotechnical Modeling, 259, 2010.*
- I.M. Idriss, R.W. Boulanger, "CPT and SPT based liquefaction triggering procedures", *Department of Civil and Environmental engineering, University of California at Davis, 2014.*
- K. Ishihara. *Soil behaviour in earthquake geotechnics.* Oxford University Press Inc, New York, NY, 1996.
- K. Ishihara, "Stability of Natural Deposits During Earthquakes". *Proceedings of the 11th International Conference on Soil Mechanics and Foundation Engineering.* San Francisco, 1:321-376, 1985.
- K. Ishihara M. Yoshimine, "Evaluation of settlements in sand deposits following liquefaction during earthquakes". *Soils Found 1992;32(1):173–188, 1992.*
- Y. Ishii, K. Tokimatsu. Simplified procedures for the evaluation of settlements of structures during earthquakes. In: *Proceedings from the ninth world conference on earthquake engineering, Tokyo-Kyoto, Japan, vol 3, pp 95–100, 1988.*

ISPRA

Ambiente:

- http://sgi2.isprambiente.it/viewersgi2/?title=ITA_Indagini_sottosuolo464&resource=wms%3Ahttp%3A//sgi2.isprambiente.it/arcgis/services/servizi/indagini464/MapServer/WMSserver%3Frequest%3DGetCapabilities%26service%3DWMS
- Itasca Consulting Group, Inc. *FLAC - Fast Lagrangian Analysis of Continua*, Ver. 8.0. Minneapolis: Itasca. 2016.
- T. Iwasaki, F. Tatsuoka, K. Tokida, S. Yasuda, "A Practical method for assessing soil liquefaction potential based on case studies at various sites in Japan". [conference]: 2nd International conference on Microzonation. - 1978: 885-896, 1978.
- JMA (Japan Meteorological Agency), *Explanation Table of the JMA Seismic Intensity Scale* (February 1996), 4pp, 1996.
- JMA (Japan Meteorological Agency), *Explanation Table of JMA Seismic Intensity Scale*, 2009. <http://www.jma.go.jp/jma/kishou/known/shindo/kaisetsu.html> (in Japanese).
- D.K. Karamitros., G.D. Bouckovalas, Y.K. Chaloulos. Seismic settlements of shallow foundations on liquefiable soil with a clay crust. *Soil Dynamics and Earthquake Engineering*. 46. 64-76, 2013.
- D.K. Karamitros., G.D. Bouckovalas, Y.K. Chaloulos. Insight into the Seismic Liquefaction Performance of Shallow Foundations. *Journal of Geotechnical and Geoenvironmental Engineering* 139(4):599-607, 2013. 10.1061/(ASCE)GT.1943-5606.0000797
- Z. Karimi, S. Dashti, Z. Bullock, K. Porter, A. Liel. Key predictors of structure settlement on liquefiable ground: a numerical parametric study, *Soil Dynamics and Earthquake Engineering*, Volume 113, 2018, Pages 286-308, ISSN 0267-7261, 2018. <https://doi.org/10.1016/j.soildyn.2018.03.001>.
- C. Kircher, M. McCann, *Development of fragility curves for estimation of earthquake-induced damage*, USGS Report-437, Washington D.c., U.S.A, 1983.
- W. Knorr, A. Arneth, L. Jiang, Demographic controls of future global fire risk, *Nat. Clim. Change*, 6, 781–785, 2016.
- I. Kongar, T. Rossetto, S. Giovinazzi. Evaluating Desktop Methods for Assessing Liquefaction-Induced Damage to Infrastructure for the Insurance Sector. 12th International Conference on Applications of Statistics and Probability in Civil Engineering, ICASP12 Vancouver, Canada, July 12-15, 2015.
- S.L. Kramer, "Geotechnical Earthquake Engineering". Prentice Hall Publishers, 653 p, 1996.
- S.L. Kramer. Lateral Spreading. In: Bobrowsky, P.T. (eds) *Encyclopedia of Natural Hazards*. Encyclopedia of Earth Sciences Series. Springer, Dordrecht, 2013.

- https://doi.org/10.1007/978-1-4020-4399-4_215
- R. Kuhleimeyer, J. Lysmer. Finite element method accuracy for wave propagation problems. *Journal of the soil mechanics and foundations division, ASCE*, 99(SM5), 421-427, 1973.
- S. Lagomarsino, S. Cattari, D. Ottonelli, Macroseismic fragility curves for Italian residential URM buildings calibrated by observed damage. *Bull Earthq Eng*, 2020.
- K. L. Lee, A. Albaisa. Earthquake Induced Settlements in Saturated Sands, *Journal of the Soil Mechanics and Foundations Division, ASCE* 1 Vol. 100, No. GT4, April, 1974, pp. 387-406.
- G. Le Loc'h, A.G. Galli. Improvement in the truncated Gaussian method: combining several Gaussian functions. In *Ecmor 4, 4th European Conference on the Mathematics of Oil Recovery*, Roros, Norway, 1994.
- Liquefact D2.4, Deliverable 2.4: "GIS database of the historical liquefaction occurrences in Europe and European empirical correlations to predict the liquefaction occurrence starting from the main seismological information", 2019. www.liquefact.eu
- W. Liu, F. Sun, W. Ho Lim, J. Zhang, H. Wang, H. Shiogama, Y. Zhang, Global drought and severe drought-affected populations in 1.5 and 2.0 °C warmer worlds, *Earth Syst. Dynam.*, 9, 267–283, <https://doi.org/10.5194/esd-9-267-2018>, 2018.
- M. Livani, D. Scrocca, P. Arecco, C. Doglioni. Structural and stratigraphic control on salient and recess development along a thrust belt front: the Northern Apennines (Po Plain, Italy). *Journal of Geophysical Research: Solid Earth*, 123(5), 4360–4387, 2018.
- R. Luque, J. Bray. Dynamic analysis of a shallow-founded building in Christchurch during the Canterbury earthquake sequence. In *Proc., 6th Int. Conf. on Earthquake Geotechnical Engineering*. Christchurch, New Zealand. 2015.
- R. Luque, J. Bray. Dynamic analyses of two buildings founded on liquefiable soils during the Canterbury earthquake sequence. *J. Geotech. Geoenviron. Eng.* 143 (9): 04017067. 2017. [https://doi.org/10.1061/\(ASCE\)GT.1943-5606.0001736](https://doi.org/10.1061/(ASCE)GT.1943-5606.0001736).
- T. Macaulay, "Critical Infrastructures". Taylor & Francis, 342 pp, 2009.
- A. Malinverno, W. B. F. Ryan. Extension in the Tyrrhenian Sea and shortening in the Apennines as result of arc migration driven by sinking of the lithosphere. *Tectonics*, 5(2), 227–245, 1986.
- A. Masi, S. Lagomarsino, M. Dolce et al, Towards the updated 2020 Seismic Risk Assessment: definitions and developments. *Bull Earthq Eng* 5:977, 2020.
- G. Matheron, H. Beucher, A.G. Galli, D. Guérillot, C. Ravenne. Conditional simulation of the geometry of fluvio-deltaic reservoirs. In *62nd Annual Technical Conference and Exhibition of the Society of petroleum Engineers*, pp. 591-599. SPE Paper 16753,

- Dallas, 1987.
- B. W. Maurer, R. A. Green, S. Oliver, O. S. Taylor, “Moving Towards an Improved Index for Assessing Liquefaction Hazard: Lessons from Historical Data”. *Soils and Foundations*, 55(4): 778-787, 2015a.
- R. K. MCGUIRE, *Seismic hazard and risk analysis*, Earth-quake Engineering Research Institute, MNO-10, 240 pp, 2004.
- S. V. Medvedev, *Engineering seismology* (in Russian). Academy of Sciences, Inst. of Physics of the Earth, Publ. house for literature on Civil Engineering, Architecture and Building Materials, Moscow, 1962.
- S.V. Medvedev, and W. Sponheuer, “MSK Scale of Seismic Intensity”, *Proceedings of the Fourth World Conference on Earthquake Engineering*, Santiago, Chile, Vol. 1, p. A2, 1969.
- G. G. Meyerhof. Some recent foundation research and its application to design. *Struct. Engr.*, 31, 151-167, 1953.
- M. Millen, A. Viana da Fonseca, J. Quintero, C. Ferreira, S. Oztoprak, I. Bozbey, C. Oser, N. Aysal, M. Kotic, J. Logar, "Equivalent soil profiles to integrate in situ tests results and soil-structure interaction in liquefiable soils. The Adapazari case-study". *Bull Earthq Eng (Special issue)*, 2020.
- W. G. MILNE, A. G. DAVENPORT, Distribution of earthquake risk in Canada, *Bull Seismol Soc Am* 59, 729–754, 1969.
- T. Mogami, and K. Kubo, “The Behaviour of Soil during Vibration“ *Proceedings of the Third International Conference on Soil Mechanics and Foundation Engineering*, Vol. 1, pp. 152-153, 1953.
- L. Mualchin, *Seismic hazard analysis for critical infrastructures in California*. *Eng. Geol.* 79, 177–184, 2005.
- B. A. Muntasir. Performance-based seismic design and assessment of concrete bridge piers reinforced with shape memory alloy rebar. 2015. https://doi.org/10.1007/978-3-319-16964-4_7.
- A. Murray, T. Grubestic, “Critical Infrastructure: Reliability and Vulnerability”. Springer eds. 313 pp, 2007.
- T. Musson. flickr: <https://www.flickr.com/photos/37990418@N08/5476123346>, 2011.
- T. Musson, Roger & Cecić, Ina. *Intensity and Intensity Scales*. 10.2312/GFZ.NMSOP-2_ch12, 2012.
- NCEER (National Center for Earthquake Engineering Research). *Proc., NCEER Workshop on Evaluation of Liquefaction Resistance of Soils*. Technical Rep. No. NCEER-97-0022. New York: NCEER, 1997.

- New Zealand Geotechnical Database: <https://www.nzgd.org.nz/Registration/Login.aspx#t3>
- NTC 2018: "Norme Tecniche per le Costruzioni". Ministero delle Infrastrutture e dei Trasporti, Decreto Ministeriale del 17 gennaio 2018, Supplemento ordinario alla G.U. n. 8 del 20 febbraio 2018A.
- NZGS, "New Zealand Geotechnical Society, Earthquake geotechnical engineering practice-Module 3: identification, assessment and mitigation of liquefaction hazards", 2016.
- Office of the United States Disaster Relief Co-ordinator, "UNDRO", 1979: "Natural disasters and vulnerability analysis". Report of expert group meeting, 9-12 July 1979.
- F. Omori, Intensity scale. Earthquake Investigation Committee, vol 4, 137-141, 1990. (In Japanese)
- G. Papathanassiou, R. Caputo, D. Rapti-Caputo. Liquefaction phenomena along the paleo-Reno River caused by the May 20, 2012, Emilia (northern Italy) earthquake. *Annals of Geophysics*, 55(4), 2012.
- L. Paoella, E. Salvatore, R. L. Spacagna, G. Modoni, M. Ochmański, Prediction of liquefaction damage with artificial neural networks, VII Int. Conf. on Earthquake Geotechnical Engineering, Rome, 4309-4316, 2019.
- L. Paoella, G. Modoni, R. L. Spacagna, A. Baris, "A Generalized Severity Number To Predict Liquefaction Damage With Lateral Spreading". *Géotechnique*, 2022. 10.1680/jgeot.21.00006
- L. Paoella, R. L. Spacagna, A. Baris, G. Modoni, S. Fabozzi, Liquefaction damage assessment using Bayesian belief networks. CPT'22, 2022.
- P. Peduzzi, H. Dao, C. Herold, and F. Mouton, Assessing global exposure and vulnerability towards natural hazards: the Disaster Risk Index, *Nat. Hazards Earth Syst. Sci.*, 9, 1149–1159, <https://doi.org/10.5194/nhess-9-1149-2009>, 2009.
- P. Peduzzi, B. Chatenoux, H. Dao, A. De Bono, C. Herold, J. Kossin, F. Mouton, and O. Nordbeck, Global trends in tropical cyclone risk, *Nat. Clim. Change*, 2, 289–294, <https://doi.org/10.1038/NCLIMATE1410>, 2012.
- V. Picotti, F. J. Pazzaglia. A new active tectonic model for the construction of the Northern Apennines mountain front near Bologna (Italy). *Journal of Geophysical Research: Solid Earth*, 113(B8), 2008.
- K. Pitilakis, Earthquake risk assessment: Certitudes, fallacies, uncertainties and the quest for soundness. In: Ansal A, editor. *Perspectives on European Earthquake Engineering and Seismology*, Volume 2, Springer International Publishing; p. 59–952015.
- Polish Geological Institute, National Research Institute: <https://www.pgi.gov.pl/en/for-press/12707-the-cbdg-gis-application-informs-you-about-the-possibilities-of->

- accessing-spatial-data.html
- H.G. Poulos. Pile foundations. Ch. 10 of *Geotechnical and Geoenvironmental Handbook*, Ed. R.K. Rowe, Kluwer Academic Publishers, Boston, 261-304. Foundations and retaining structures - Research and practice, 2001.
- R Core Team . 2021. R: A language and environment for statistical.
- S. Rajkumari, K. Thakkar, H. Goyal, “Fragility analysis of structures subjected to seismic excitation: A state-of-the-art review”, *Structures Volume 40*, Pages 303-316, June 2022.
- C. Reale, K. Gavin, L. Librić, D. Jurić-Kačunić. Automatic classification of finegrained soils using CPT measurements and Artificial Neural Networks. *Advanced Engineering Informatics*, Volume 36, Pages 207-215, ISSN 1474-0346, 2018. <https://doi.org/10.1016/j.aei.2018.04.003>.
- P.K. Robertson, R.G. Campanella, D. Gillespie, and A. Rice, Seismic CPT to measure in-situ shear wave velocity. *Journal of Geotechnical Engineering Division, ASCE*, 112(8): 791-803. 1986.
- P.K. Robertson, “Soil classification using the cone penetration test”. *Canadian Geotechnical Journal*, 27(1):151–158, 1990.
- P.K. Robertson and C.E. Wride, “Evaluating Cyclic Liquefaction Potential Using the Cone Penetration Test”. *Canadian Geotechnical Journal* 35, 442– 459, 1998.
- P.K. Robertson, Soil behaviour type from the CPT: an update. 2nd International Symposium on Cone Penetration Testing, CPT’10, Huntington Beach, CA, USA, 2010a. www.cpt10.com
- P.K. Robertson, and K.L. Cabal, “Guide to Cone Penetration Testing for Geotechnical Engineering”. Gregg Drilling & Testing, Inc. 2015.
- P. K. Robertson. “Cone Penetration Test (CPT)-Based Soil Behaviour Type (SBT) Classification System – An Update.” *Canadian Geotechnical Journal* 53 (12): 1910–1927, 2016.
- R.W. Romeo. Emilia (Italy) M5.9 earthquake on 20 May 2012: an unusual pattern of liquefaction. *Italian Journal of Engineering Geology and Environment*, 2, 2012.
- T. Rossetto, and A. Elnashai, “Derivation of Vulnerability Functions for European-Type RC Structures Based on Observational Data”, *Engineering Structures*, Vol. 25, No. 10, pp. 1241-1263, 2003.
- A. Rosti, Del Gaudio, Rota, Ricci, Di Ludovico, Penna, Verderame, Empirical fragility curves for Italian residential RC buildings. *Bulletin of Earthquake Engineering* (2021) 19:3165–3183 <https://doi.org/10.1007/s10518-020-00971-4>
- A. Rosti, M. Rota, A. Penna, Empirical fragility curves for Italian URM buildings. *Bull*

- Earthq Eng., 2020a. <https://doi.org/10.1007/s10518-020-00845-9>
- L. Royden, E. Patacca, P. Scandone. Segmentation and configuration of subducted lithosphere in Italy: an important control on thrust-belt and foredeep-basin evolution. *Geology*, 15(8), 714–717, 1987.
- F. Sabetta, A. Goretti, and A. Lucantoni, “Empirical Fragility Curves from Damage Surveys and Estimated Strong Ground Motion”, Proceedings of the 11th European Conference on Earthquake Engineering, Paris, France, pp. 1-11, 1998.
- E. Salvatore, G. Modoni, M. C. Mascolo, D. Grassi, G. Spagnoli. Experimental Evidence of the Effectiveness and Applicability of Colloidal Nanosilica Grouting for Liquefaction Mitigation. *Journal of Geotechnical and Geoenvironmental Engineering*. 2020. 146. 04020108. 10.1061/(ASCE)GT.1943-5606.0002346.
- M. Sarconi, *Istoria dei fenomeni del terremoto avvenuto nelle Calabrie, e nel Valdemone nell’anno 1783*. Luce dalla Reale Accademia della Scienze, e delle Belle Lettere di Napoli, Naples, 1784.
- C. Scawthorn, H. Iemura, and Y. Yamada, “Seismic Damage Estimation for Low- and MidRise Buildings in Japan”, *Earthquake Engineering & Structural*, 1981.
- J. H. Schmertmann, “The mechanical aging of soils”. *J. Geotech. Engng*, ASCE 117, No. 9, 1288–1330, 1991.
- D. Scrocca, E. Carminati, C. Doglioni, D. Marcantoni. Slab retreat and active shortening along the central-northern Apennines. In *Thrust belts and foreland basins* (pp. 471–487). Springer, 2007.
- R.B. Seed, K.O. Cetin, R.E.S. Moss, A. Kammerer, J. Wu, J. Pestana, M. Riemer, R.B. Sancio, J.D. Bray, R.E. Kayen, A. Faris. Recent advances in soil liquefaction engineering: a unified and consistent framework. Keynote presentation, 26th Annual ASCE Los Angeles Geotechnical Spring Seminar, Long Beach, CA, April 30, 2003.
- H.B. Seed, I.M. Idriss, Analysis of soil liquefaction: Niigata earthquake. *Journal of the Soil Mechanics and Foundation Division*, ASCE, vol. XCIII, n. 3, pp. 83-108, 1967.
- H.B. Seed, I.M. Idriss, “Simplified procedure for evaluating soil liquefaction potential”. *Journal of the Soil Mechanics and Foundations Division*, ASCE, 97(SM9): 1249–1273, 1971.
- H.B. Seed, I.M. Idriss, F. Makdisi, N. Banerjee, "Representation of irregular stresses time histories by equivalent uniform stress series in liquefaction analyses". EERC 75-29, Earthquake Engineering Research Center, University of California Berkeley, 1975.
- M. Shinozuka, S.E. Chang, R.T. Eguchi, D.P. Abrams, H.H.M. Hwang, and A. Rose, “Advances in Earthquake Loss Estimation and Application to Memphis, Tennessee”, *Earthquake Spectra*, Vol. 13, No. 4, pp. 739-758, 1997.

- A. Sieberg, Über die makroseismische Bestimmung der Erdbebenstärke. *Gerl. Beitr.Geophys.*, 11, 227-239, 1912.
- A. Sieberg, *Geologische, physikalische und angewandte Erdbebenkunde*. Verlag Gustav Fischer, Jena, 572 S, 1923.
- A. Sieberg,. *Geologie der Erdbeben*. Handbuch der Geophysik, Gebrüder Bornträger, Berlin, vol. 2, pt 4, 550-555, 1932.
- M. L. Silver, H. B. Seed. Volume Changes in Sands during Cyclic Loading. *Journal of the Soil Mechanics and Foundations Division, ASCE*, Vol. 97, No. SM9, Sept., 1971, pp. 1171-1182.
- L. Sinatra, S. Foti. The role of aftershocks in the liquefaction phenomena caused by the Emilia 2012 seismic sequence. *Soil Dynamics and Earthquake Engineering*, 75, 234-245, 2015.
- A. W. Skempton, D. H. MacDonald. The allowable settlement of buildings. *Proc, Inst, of Civ. Engrs., Part III*, 5, 727-784, 1956.
- L. Sousa, V. Silva, M. Marques, H. Crowley, On the treatment of uncertainties in the development of fragility functions for earthquake loss estimation of building portfolios. *Earthquake Engineering & Structural Dynamics* 2016. doi:10.1002/eqe.2734.
- R.L. Spacagna, C. de Fouquet, G. Russo. Interpretation of CPTU tests with statistical and geostatistical methods. *ISGSR2015 Geotechnical Safety and Risk V T. Schweckendiek et al. (Eds.) © 2015 The authors and IOS Press. 13-16 October 2015.*
- R. Spence, A.W. Coburn, and A. Pomonis, “Correlation of Ground Motion with Building Damage: The Definition of a New Damage-Based Seismic Intensity Scale”, *Proceedings of the Tenth World Conference on Earthquake Engineering, Madrid, Spain, Vol. 1*, pp. 551-556, 1992.
- M. Stefani, L. Minarelli, A. Fontana, I. Hajdas. Regional deformation of late Quaternary fluvial sediments in the Apennines foreland basin (Emilia, Italy). *International Journal of Earth Sciences*, 107(7), 2433–2447, 2018. <https://doi.org/10.1007/s00531-018-1606-x>
- M. Stone. Cross-validatory choice and assessment of statistical predic-tions. *Journal of the Royal Statistical Society: Series B (Methodological)*, 36(2), 111-133, 1974. <https://doi.org/10.1111/j.2517-6161.1974.tb00994.x>
- F. Tatsuoka, T. Sasaki, S. Yamada, Settlement in Saturated Sand Induced by Cyclic Undrained Simple Shear, *Proceedings, 8th World Conference on Earthquake Engineering, San Francisco, Vol. 3*, pp. 95-102, July 1984.
- D. Tentori, M. Mancini, C. Varone, R. Spacagna, A. Baris, S. Milli, I. Gaudiosi, M.

- Simionato, F. Stigliano, G. Modoni, L. Martelli, M. Moscatelli. The influence of alluvial stratigraphic architecture on liquefaction phenomena: A case study from the Terre del Reno subsoil (southern Po plain, Italy). *Sedimentary Geology*, 2022. <https://doi.org/10.1016/j.sedgeo.2022.106258>
- S. Tesfamariam, K. Goda, Seismic risk analysis and management of civil infrastructure systems: an overview. In *Handbook of seismic risk analysis and management of civil infrastructure systems*, S. Tesfamariam and K. Goda editors, Woodhead Publishing Limited, pp.141-174, 2013.
- K. Tokimatsu, H. B. Seed. Simplified procedures for the evaluation of settlements in clean sands. Earthquake Engineering Research Center. REPORT NO. UCB/EERC-84/16 OCTOBER 1984.
- E. N. Toprak, Pipeline damage predictions in liquefaction zones using LSN. Santiago, Chile: In: 16th World conference on earthquake, 16WCEE 2017
- G. Toscani, P. Burrato, D. Di Bucci, S. Seno, G. Valensise. Plio-Quaternary tectonic evolution of the Northern Apennines thrust fronts (Bologna-Ferrara section, Italy): seismotectonic implications. *Bollettino Della Società Geologica Italiana*, 128(2), 605–613, 2009.
- S. Tyagunov, M. Pittore, M. Wieland, S. Parolai, D. Bindi, K. Fleming, et al. Uncertainty and sensitivity analyses in seismic risk assessments on the example of Cologne, Germany. *Natural Hazards and Earth System Science*;14:1625–40, 2014. doi:10.5194/nhess-14-1625-2014.
- United Nations Office for Disaster Risk Reduction, UNDRR: GAR 2013. From Shared Risk to Shared Value: the Business Case for Disaster Risk Reduction, UN Office for Disaster Risk Reduction, Geneva, 2013.
- United Nations Office for Disaster Risk Reduction, UNDRR: Global Assessment Report 2015, Making Development Sustainable: The Future of Disaster Risk Management, UN Office for Disaster Risk Reduction, Geneva, 2015a.
- United Nations Office for Disaster Risk Reduction, UNDRR: Sendai Framework for Disaster Risk Reduction 2015–2030 United Nations Office for Disaster Risk Reduction, Geneva, Switzerland, 2015b.
- United Nations Office for Disaster Risk Reduction, UNDRR. (2017). UNISDR: Annual report 2017, United Nations Office for Disaster Risk Reduction, Geneva, Switzerland, 2017.
- UNDRR: GAR 2019. Global Assessment Report on Disaster Risk Reduction, UN Office for Disaster Risk Reduction, Geneva, 2017.
- S. van Ballegooy, P. Malan, V. Lacrosse, M.E. Jacka, M. Cubrinovski, J.D. Bray, T.D.

- O'Rourke, S.A. Crawford, H. Cowan, "Assessment of Liquefaction-Induced Land Damage for Residential Christchurch". *Earthquake Spectra* (30) No. 1: pages 31–55, February 2014.
- P. J. Ward, B. Jongman, F. Sperna Weiland, A. Bouwman, R. Van Beek, M. F. P. Bierkens, W. Ligtoet, H. C. Winsemius, Assessing flood risk at the global scale: model setup, results, and sensitivity, *Environ. Res. Lett.*, 8, 044019, <https://doi.org/10.1088/1748-9326/8/4/044019>, 2013.
- P. J. Ward, B. Jongman, J. C. J. H. Aerts, P. D. Bates, W. J. W. Botzen, A. Diaz Loaiza, S. Hallegatte, J. M. Kind, J. Kwadijk, P. Scussolini, and H. C. Winsemius, A global framework for future costs and benefits of river-flood protection in urban areas, *Nat. Clim. Change*, 7, 642–646, <https://doi.org/10.1038/NCLIMATE3350>, 2017.
- P.J. Ward, V. Blauhut, N. Bloemendaal, J. E. Daniell, M.C. de Ruiter, M.J. Duncan, R. Emberson, S.F. Jenkins, ..., "Review article: Natural hazard risk assessments at the global scale". *Nat. Hazards Earth Syst. Sci.*, 20, 1069–1096, 2020. <https://doi.org/10.5194/nhess-20-1069-2020>
- H. E. Wahls. Tolerable settlement of buildings. *J. Geotech. Engrg.*, ASCE, 107(11), 1489-1504, 1981.
- R.V. Whitman, J.W. Reed, and S.T. Hong, "Earthquake Damage Probability Matrices", *Proceedings of the Fifth World Conference on Earthquake Engineering*, Rome, Italy, Vol. 2, pp. 2531-2540, 1973.
- H.O. Wood, and F. Neumann, "Modified Mercalli Intensity Scale of 1931", *Bulletin of the Seismological Society of America*, Vol. 21, No. 4, pp. 277-283, 1931.
- J. Xie, J. Huang, C. Zeng, S. Jiang, N. Podlich, Systematic Literature Review on Data-Driven Models for Predictive Maintenance of Railway Track: Implications in Geotechnical Engineering. *Geosciences*, 10(11), 425, 2020.
- S. Yasuda, K. Harada, K. Ishikawa, Y. Kanemaru, Characteristics of Liquefaction in Tokyo Bay Area by the 2011 Great East Japan Earthquake. *Soils Found* 52:793–810, 2012.
- N. Yoshida, K. Tokimatsu, S. Yasuda, T. Kokusho, T., Okimura. Geotechnical aspects of damage in Adapazari city during 1999 Kocaeli, Turkey earthquake. *Soils Foundation.*, 41(4), 25–45, 2001.
- T.L. Youd, "Application of MLR Procedure for Prediction of Liquefaction Induced Lateral Spread Displacement". *J. Geotech. Geoenvironmental Eng.*, 6, 144, 2018.
- T.L. Youd and I.M. Idriss (Editors), "Summary Report, Proceedings of the NCEER Workshop on Evaluation of Liquefaction Resistance of Soils", Salt Lake City: Technical Report NCEER-97-0022: National Center for Earthquake Engineering Research, Buffalo, NY, 1997.

- T.L. Youd and I.M. Idriss. Liquefaction resistance of soils: Summary report from the 1996 NCEER and 1998 NCEER/NSF workshops on evaluation of liquefaction resistance of soils. *J Geotech Geoenviron Eng* 127(10):817–833, 2001.
- T.L. Youd, and S.N. Hoose, "Historic Ground Failures in Northern California Associated with Earthquakes", Professional Paper 993, U.S. Geological Survey, 1978.
- T. L. Youd, and D. M. Perkins, "Mapping Liquefaction-induced Ground Failure Potential". *J. Geotech. Eng. Div., ASC E*, 104, 433–446pp, 1978.
- G. Zhang, P.K. Robertson, R.W.I. Brachman, "Estimating liquefaction-induced ground settlements from CPT for level ground". *Canadian Geotechnical Journal* 39: 1168–80, 2002.
- G. Zhang, P.K. Robertson, R.W.I. Brachman, "Estimating liquefaction-induced Lateral Displacements from CPT for level ground". *Journal of Geotechnical and Geoenvironmental Engineering*. AUGUST 2004.
- G. Zuccaro et al, Empirical fragility curves for Italian masonry buildings: evolution of the vulnerability model from DPM to curves as a function of acceleration. *Bull Earthq Eng* 6:137, 2020.